

~~CONFIDENTIAL~~

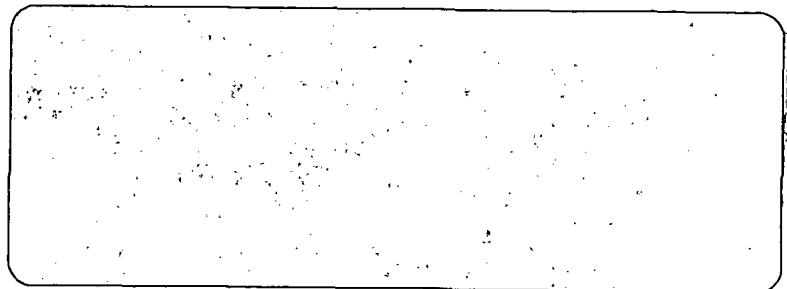
X72-10359

NASA TECHNICAL
MEMORANDUM



NASA TM X-2551

NASA TM X-2551



STATIC AERODYNAMIC
CHARACTERISTICS OF A MODEL
WITH A 17-PERCENT-THICK
SUPERCRITICAL WING

by James C. Ferris

Langley Research Center
Hampton, Va. 23365

NATIONAL AERONAUTICS AND SPACE ADMINISTRATION • WASHINGTON, D. C. • MAY 1972

~~CONFIDENTIAL~~

~~CONFIDENTIAL~~

1. Report No. NASA TM X-2551	2. Government Accession No.	3. Recipient's Catalog No.
4. Title and Subtitle STATIC AERODYNAMIC CHARACTERISTICS OF A MODEL WITH A 17-PERCENT-THICK SUPERCRITICAL WING (U)		5. Report Date May 1972
7. Author(s) James C. Ferris		6. Performing Organization Code
9. Performing Organization Name and Address NASA Langley Research Center Hampton, Va. 23365		8. Performing Organization Report No. L-8081
12. Sponsoring Agency Name and Address National Aeronautics and Space Administration Washington, D.C. 20546		10. Work Unit No. 742-73-02-01
15. Supplementary Notes		11. Contract or Grant No.
		13. Type of Report and Period Covered Technical Memorandum
		14. Sponsoring Agency Code
16. Abstract <p>An investigation was made of the static stability and control characteristics and air loads on the wing and aileron of a 0.09-scale model of an airplane with a 17-percent-thick supercritical wing. The longitudinal aerodynamic characteristics were determined over a lift-coefficient range sufficiently high to induce buffet onset at Mach numbers from 0.30 to 0.80. In addition, the lateral aerodynamic characteristics were determined as a function of sideslip angle and angle of attack at selected Mach numbers.</p>		
<p>CLASSIFICATION CHANGE</p> <p>To UNCLASSIFIED By authority of NASA HQ, T.D. 77-163 Changed by L Shirley Date 6-15-76 Classified Document Master Control Station, NASA Scientific and Technical Information Facility</p> <p>CLASSIFIED BY E/A/20254(10/3/72) DPLW-2431 SUBJECT TO GENERAL DECLASSIFICATION SCHEDULE OF EXECUTIVE ORDER 11652. AUTOMATICALLY DOWNGRADED AT TWO-YEAR INTERVALS</p>		
17. Key Words (Suggested by Author(s)) Thick supercritical wing Buffet onset Drag-divergence Mach number		

~~CONFIDENTIAL~~

STATIC AERODYNAMIC CHARACTERISTICS OF A MODEL WITH A 17-PERCENT-THICK SUPERCRITICAL WING*

By James C. Ferris
Langley Research Center

SUMMARY

An investigation was made of the static stability and control characteristics and air loads on the wing and aileron of a 0.09-scale model of an airplane with a 17-percent-thick supercritical wing. The longitudinal aerodynamic characteristics were determined over a lift-coefficient range sufficiently high to induce buffet onset at Mach numbers from 0.30 to 0.80. In addition, the lateral aerodynamic characteristics were determined as a function of sideslip angle and angle of attack at selected Mach numbers.

The results of the investigation indicate that the model was longitudinally and laterally stable with adequate control effectiveness through the Mach number range of the investigation. A comparison of these results with data from flight tests of the airplane with the conventional NACA 64₁A212 airfoil indicates that substantially higher lift coefficients at buffet onset were obtained with the 17-percent-thick supercritical airfoil at Mach numbers from 0.30 to 0.70. This new airfoil also slightly increased the drag-divergence Mach number (M_{DD} as defined by $\frac{\partial C_D}{\partial M} = 0.1$, where C_D is the drag coefficient and M is the free-stream Mach number) at lift coefficients greater than 0.30. A comparison of the wind-tunnel data with the flight data for the supercritical airfoil indicates good correlation for buffet onset and drag-divergence Mach number.

INTRODUCTION

Over the last several years research on supercritical airfoils at the Langley Research Center has been directed toward improving performance by increasing the drag-divergence Mach number and therefore the cruising speeds of airplanes that employ wings with this airfoil section. These airfoils accomplish this improvement by delaying the onset of shock-induced flow separation over the airfoil and, as a result, also delay buffet onset of the wing. Wind-tunnel models with extensive area-rule modifications have been investigated with supercritical wings, and the results from these investigations indicate that the area rule and the supercritical wing can be incorporated in the design of

*Title, Unclassified.

~~CONFIDENTIAL~~

~~CONFIDENTIAL~~

airplane configurations to obtain the additive performance improvements of both concepts. The research airplane configuration in references 1 and 2 is an excellent example of the application of both concepts to demonstrate the feasibility of a near-sonic commercial jet transport.

Other, unpublished data indicate that supercritical airfoil sections with substantial increases in thickness ratio can obtain drag-divergence Mach numbers equal to those of much thinner conventional sections. As a result, the advantages of more volume for fuel or boundary-layer-control high-lift devices, increased aspect ratio, and lower structural weight may be achieved by use of supercritical airfoil sections with high thickness ratios.

The purpose of the present paper is to present results of a wind-tunnel investigation of a 0.09-scale model of an airplane with an unswept wing employing a supercritical airfoil section with a thickness-chord ratio of 17 percent.

The investigation was conducted in the Langley 8-foot transonic pressure tunnel at Mach numbers from 0.30 to 0.80 to determine the basic longitudinal and lateral stability and control characteristics, effects of Reynolds number, aileron hinge moments, and effects of sealing the aileron gaps. Buffet-onset characteristics were also determined by use of the wing-root—bending-moment gage technique.

SYMBOLS

Longitudinal results are referred to the stability-axis system, and lateral-directional results are referred to the body-axis system. The origin of the stability and body axes is at the moment reference center, located at 25 percent of the reference length and 1.084 cm above the fuselage reference line. (See fig. 1.) All data presented herein are based on the planform dimensions of the wing.

The symbols used herein are defined as follows:

- b reference span, 98.618 centimeters
- c local chord
- \bar{c} model reference length, 20.318 centimeters
- c_a aileron average chord
- C_A axial-force coefficient, $\frac{\text{Axial force}}{qS}$
- C_D drag coefficient, $\frac{\text{Drag}}{qS}$

C_h	aileron hinge-moment coefficient (positive when load tends to cause a positive aileron deflection angle), $\frac{\text{Hinge moment}}{qS_a c_a}$
$C_{h\alpha}$	rate of change of aileron hinge-moment coefficient with angle of attack, $\frac{\partial C_h}{\partial \alpha}$, per degree
$C_{h\delta_a}$	rate of change of aileron hinge-moment coefficient with aileron deflection angle, $\frac{\partial C_h}{\partial \delta_a}$, per degree
C_L	lift coefficient, $\frac{\text{Lift}}{qS}$
$C_{L\alpha}$	lift-curve slope, $\frac{\partial C_L}{\partial \alpha}$, per degree
C_l	rolling-moment coefficient, $\frac{\text{Rolling moment}}{qS_b}$
$C_{l\beta}$	effective dihedral parameter, $\frac{\Delta C_l}{\Delta \beta}$, per degree
$C_{l\delta_a}$	lateral control parameter, $\frac{\Delta C_l}{\Delta \delta_a}$, per degree
C_m	pitching-moment coefficient, $\frac{\text{Pitching moment}}{qS_c}$
$C_m C_L$	longitudinal stability derivative, $\frac{\partial C_m}{\partial C_L}$
$C_{m,0}$	pitching-moment coefficient at zero lift
$C_{m\delta_e}$	longitudinal control parameter, $\frac{\Delta C_m}{\Delta \delta_e}$, per degree
C_n	yawing-moment coefficient, $\frac{\text{Yawing moment}}{qS_b}$
$C_{n\beta}$	directional stability parameter, $\frac{\Delta C_n}{\Delta \beta}$, per degree
C_Y	side-force coefficient, $\frac{\text{Side force}}{qS}$
$C_{Y\beta}$	side-force parameter, $\frac{\Delta C_Y}{\Delta \beta}$, per degree
i_h	horizontal-tail incidence angle, referred to fuselage reference line (positive when trailing edge is down), degrees

L/D	lift-drag ratio
M	free-stream Mach number
M_{DD}	drag-divergence Mach number, Mach number for which $\frac{\partial C_D}{\partial M} = 0.1$
M_{wsg}	root-mean-square output of wing bending gage
p_t	free-stream total pressure, newtons/square meter
q	free-stream dynamic pressure, newtons/square meter
$R_{\bar{C}}$	Reynolds number based on model reference length
S	reference wing area, 0.192 square meter
S_a	aileron area, 0.007 square meter
x,y	distance along X- and Y-axis, respectively
α	angle of attack, referred to fuselage reference line, degrees
β	angle of sideslip, referred to model plane of symmetry, degrees
δ_a	aileron deflection angle, referred to wing-chord plane (positive when trailing edge is down), degrees
δ_e	elevator deflection angle, referred to horizontal-tail plane (positive when trailing edge is down), degrees

Subscripts:

L	left
LER	leading-edge radius
max	maximum
R	right

APPARATUS AND PROCEDURES

Model Description

The model used in the present investigation was a sting-supported 0.09-scale model of an airplane with an unswept wing employing supercritical airfoil sections with a constant spanwise thickness ratio of 17 percent. Drawings and photographs of the model are shown in figures 1 and 2, respectively; the geometric characteristics are presented in table I. Coordinates of the supercritical airfoil are given in table II. The coordinates given in table II do not include the small extension (0.0075c) of the trailing edge from the aileron inboard to the wing-fuselage juncture shown in the planform view of figure 1(a) and the airfoil drawing of figure 1(b). This extension was used to form a step in the trailing edge for configuration 1 and a 0.0075c-thick (blunt) trailing edge for configuration 2.

Longitudinal control was provided by the elevator which extended from the 72-percent-chord line to the trailing edge of the horizontal tail. The incidence of the horizontal tail, which is fixed on the full-scale airplane, was made adjustable on the model in order to aid in measuring downwash characteristics. Lateral control and aileron hinge-moment data were obtained with only one aileron, located on the left wing.

Tunnel Description

The investigation was conducted in the Langley 8-foot transonic pressure tunnel, which is a single-return tunnel having a rectangular, slotted test section to permit continuous operation through the transonic speed range. This facility has the capability of independent variation of Mach number, density, temperature, and humidity. The stagnation temperature and dewpoint were maintained at values sufficient to avoid significant condensation effects.

Test Conditions

The model was investigated at Mach numbers from 0.30 to 0.80 through a lift-coefficient range sufficient to determine buffet onset. Table III presents the tunnel conditions at which the data were obtained. Some additional tests were made with the aileron gaps sealed, since the results of the investigation indicated the desirability of determining effects of the aileron gap on the flow characteristics over the wing. Fluorescent-oil film studies of the upper surface of the left wing and aileron were made at several sealed conditions of the aileron during these tests.

Boundary-Layer Transition

All the investigations were made with transition fixed on the model. Boundary-layer trips were applied to the upper and lower surfaces of the wing by use of the technique

described in references 3 and 4 to simulate full-scale Reynolds number boundary-layer thickness at the trailing edge of the wing. This technique requires that laminar flow be maintained ahead of the trips, and as a result, model surface regions ahead of the trips were maintained in an extremely smooth condition.

The location and the size of the grains used for the boundary-layer trips are shown in the following table:

Surface	Type of transition strip	Location
Fuselage	No. 150 carborundum grains	3.1 cm aft of nose apex
Wing upper surface	No. 120 carborundum grains	27 percent of local streamwise chord
Wing lower surface	No. 120 carborundum grains	37 percent of local streamwise chord
Wing-tip-mounted fuel tanks	No. 150 carborundum grains	3.3 cm aft of nose apex
Horizontal and vertical tails	No. 180 carborundum grains	10 percent of local streamwise chord

Measurements

Six-component force and moment data were obtained by use of an electrical strain-gage balance housed within the fuselage. A strain gage mounted in the left-wing fuel tank was used to measure the aileron hinge moments.

The buffet data included herein were obtained by the wing-root—bending-moment gage technique described in reference 5. The wing gage location is shown in figure 1(a). The results presented in this report represent the average root-mean-square values of the fluctuating wing-root bending moments integrated over a 45-second sampling time.

Studies of the conditions in the boundary layer on the wing were made by the fluorescent-oil-film technique described in reference 6.

Measurements were made over an angle-of-attack range from -5° to 90° at Mach numbers varying from 0.50 to 0.80. The angle-of-attack range was extended to 19° at $M = 0.30$ to determine the maximum lift coefficient and stall characteristics at low speeds. Data were taken over an angle-of-attack range at angles of sideslip of 0° and -5° . Additional measurements were taken over an angle-of-sideslip range from -8° to 8° at a nominal angle of attack of 0° ; however, the corrected angle of attack for the data varied with Mach number from 0.30° to 2.40° because of sting and balance deflections under aerodynamic loads.

Corrections

The drag data have been adjusted to the condition of free-stream static pressure acting over the fuselage cavity and base areas.

Corrections have been made to the angle of attack for model support-sting and balance deflections, which occur as a result of aerodynamic loads on the model. Further corrections to the measured angle of attack have been made for tunnel airflow angularity and for the first-order boundary corrections calculated by the methods used in reference 7.

Accuracy

The accuracy of the individual measured quantities, based on calibrations and repeatability of the data, is estimated to be within the following limits:

C_L	±0.008
C_D	±0.0007
C_m	±0.0020
C_n	±0.0005
C_l	±0.0005
C_Y	±0.0050
α , deg	±0.07
β , deg	±0.07
M	±0.002
q , N/m ²	±70.0

PRESENTATION OF RESULTS

The results of this investigation are presented in the following figures:

Figure

Fluorescent-oil photographs	3, 4
Longitudinal aerodynamic characteristics:	
Effect of Reynolds number on longitudinal aerodynamic characteristics.	
$\delta_E = 0^\circ$; $i_h = 0^\circ$; $\delta_a = 0^\circ$; $\beta = 0^\circ$	5
Effect of elevator deflection on longitudinal aerodynamic characteristics.	
$i_h = 0^\circ$; $\delta_a = 0^\circ$; $\beta = 0^\circ$	6
Effect of horizontal-tail incidence on longitudinal aerodynamic characteristics. $\delta_E = 0^\circ$; $\delta_a = 0^\circ$; $\beta = 0^\circ$	7
Effect of wing trailing-edge modification on longitudinal aerodynamic characteristics. $\delta_E = 0^\circ$; $i_h = 0^\circ$; $\delta_a = 0^\circ$; $\beta = 0^\circ$	8

Figure

Variation of axial-force coefficient and wing-root bending moment with angle of attack. $\delta_e = 0^\circ$; $i_h = 0^\circ$; $\delta_a = 0^\circ$; $\beta = 0^\circ$	9
Effect of sealed aileron on longitudinal aerodynamic characteristics. $\delta_e = 0^\circ$; $i_h = 0^\circ$; $\delta_a = 0^\circ$; $\beta = 0^\circ$	10
Summary of longitudinal characteristics:	
Variation of C_D with Mach number	11
Variation of M_{DD} with C_L	12
Variation of C_{mCL} , $C_{m,0}$, and $C_{m\delta_e}$ with Mach number	13
Variation of $C_{L\alpha}$ with Mach number	14
Variation of $(L/D)_{max}$ and C_L at $(L/D)_{max}$ with Mach number	15
Variation of lift coefficient at buffet onset with Mach number	16
Lateral aerodynamic characteristics:	
Effect of angle of sideslip on lateral aerodynamic characteristics. $\delta_e = 0^\circ$; $i_h = 0^\circ$	17
Effect of angle of attack on lateral control characteristics. $\delta_e = 0^\circ$; $i_h = 0^\circ$; $\beta = 0^\circ$	18
Effect of angle of attack on lateral stability characteristics. $\delta_e = 0^\circ$; $i_h = 0^\circ$; $\delta_a = 0^\circ$	19
Effect of angle of attack on lateral stability characteristics. $\delta_e = 0^\circ$; $i_h = 0^\circ$; $\delta_a = 3^\circ$	20
Effect of angle of attack on lateral stability characteristics. $\delta_e = 0^\circ$; $i_h = 0^\circ$; $\delta_a = -3^\circ$	21
Effect of aileron hinge-line and end seals on lateral stability characteristics. $\delta_e = 0^\circ$; $i_h = 0^\circ$; $\delta_a = 0^\circ$; $\beta = 0^\circ$; configuration 2	22
Effect of sealed aileron on lateral stability characteristics. $\delta_e = 0^\circ$; $i_h = 0^\circ$; $\delta_a = 0^\circ$; $\beta = 0^\circ$	23
Summary of lateral characteristics:	
Variation of lateral stability derivatives with angle of attack. $\delta_e = 0^\circ$; $i_h = 0^\circ$; $\delta_a = 0^\circ$; $\beta = 0^\circ$	24
Variation of lateral stability and control derivatives with Mach number. $i_h = 0^\circ$; $\delta_a = 0^\circ$; $\beta = 0^\circ$; $\alpha = 1^\circ$	25
Aileron hinge-moment characteristics:	
Effect of angle of attack on aileron hinge-moment coefficients. $\delta_e = 0^\circ$; $i_h = 0^\circ$; $\beta = 0^\circ$	26
Effect of angle of attack on aileron hinge-moment coefficients. $\delta_e = 0^\circ$; $i_h = 0^\circ$; $\beta = -5^\circ$	27

Figure

DISCUSSION OF RESULTS

General Flow Characteristics

Fluorescent-oil photographs of the wing upper and lower surfaces are shown in figures 3 and 4, respectively. In the first oblique photograph of the upper surface at $M = 0.70$ (fig. 3(a)), the surface is free of shock waves; however, a small amount of separation exists near the trailing edge. As the lift is increased, the extent of separation is reduced somewhat, and a weak shock wave can be observed aft of the transition trip at $C_L = 0.759$. As the Mach number is increased to 0.73 (fig. 3(b)), similar conditions exist except that the shock wave is well established for lift coefficients of 0.690 and 0.706, and there is slightly less separation indicated at the trailing edge than is evident at the lower Mach number. As the Mach number is further increased to 0.76 (fig. 3(c)), the shock wave is well established at all lift coefficients, the shock waves are apparently stronger, and larger areas of separation near the trailing edge appear as the lift coefficient is increased.

Fluorescent-oil photographs of the lower surface (fig. 4) were obtained with the camera normal to the lower surface. A few turbulent boundary-layer wedges are evident forward of the transition trip, otherwise the flow over this area of the wing is laminar. For a configuration with an unswept wing, the flow over the lower surface of the wing would be expected to be nearly parallel to free-stream flow, especially near the mid-semispan where the flow should be less influenced by the fuselage or wing-tip fuel tank. However, there is a strong inboard spanwise flow on the lower surface originating at the entry of the cusp on the inboard 70 percent of the wing. Unpublished pressure distributions indicate that this inboard flow is the result of a pressure gradient toward the fuselage at the entry of the cusp and is caused primarily by the forward sweep of the cusp entry line. At the higher Mach numbers this spanwise flow is also influenced to some extent by the separation bubble formed at the wing-fuselage juncture. (See figs. 4(b) and 4(c).)

Reynolds Number Effects

The Reynolds number results (fig. 5) generally indicate the usual decrease in drag coefficient as the Reynolds number is increased from 2.00 to 3.00×10^6 . These drag increments are of an order of magnitude to be expected from this Reynolds number variation.

~~CONFIDENTIAL~~

At the higher Mach numbers ($M \geq 0.75$), however, unusual effects are noted in that increases in lift-curve slope, significant decreases in drag at the higher lift coefficients, and delays in an abrupt pitching-moment break are associated with a reduction in Reynolds number to 2.00×10^6 . Reasons for these variations are not apparent; however, since the transition strip was sized for the highest Reynolds number of the investigation, it is probable that the trips were not fully effective at the lowest Reynolds number. Examination of unpublished pressure-distribution results for these conditions tends to bear out this conjecture in that the upper surface shock wave is located somewhat rearward for the lower Reynolds number, a result which would be expected if the trip was not effective in causing transition at the desired location. (See, for example, ref. 4.) As a result, caution should be exercised in the use of results obtained for the lowest Reynolds number.

Longitudinal Aerodynamic Characteristics

The basic longitudinal characteristics are presented in figures 6 to 10 and are summarized in figures 11 to 16. The dashed curves in figures 11(a), 13, 14, and 15 were obtained from the low Reynolds number data ($R_C = 2.00 \times 10^6$) and are included in order to provide results for the lower Mach numbers. The solid curves, however, were taken from the highest Reynolds number obtained (generally, $R_C = 3.86 \times 10^6$) at the specific Mach numbers of the investigation.

Drag characteristics. - The variation of the drag coefficient as a function of Mach number at various lift coefficients is shown in figure 11(a). It can be noted that there is an increase in the value of the drag coefficient with increasing Mach number (drag creep) in the Mach number range from 0.60 to 0.70. A similar drag creep was also observed in the flight data. However, the drag-divergence Mach number M_{DD} ($\frac{\partial C_D}{\partial M} = 0.1$) occurs above 0.70 for all the lift coefficients presented and has a measured value of 0.72 for the design lift coefficient of 0.50.

The trimmed wind-tunnel drag data in figure 11(b) are shown compared with flight data taken from reference 8 for both the supercritical wing (abbreviated S.C.) and the conventional wing with a modified NACA 64₁A212 airfoil section. Although the drag level was somewhat higher at subsonic Mach numbers for the wind-tunnel data, the correlation of the drag creep and drag-divergence Mach number for the supercritical airfoil was good. The drag-divergence Mach number as a function of lift coefficient (fig. 12) was higher for the supercritical airfoil at lift coefficients greater than 0.30.

Stability and control characteristics. - The basic longitudinal stability and control data presented in figure 6 indicate that the model was longitudinally stable with adequate control effectiveness at all Mach numbers of the investigation. There was an abrupt increase in the stability level at the higher lift coefficients, and this stable break occurred at lower lift coefficients as the Mach number was increased. The model with the tail on

and elevators undeflected trimmed out at lift coefficients near those for cruise throughout the Mach number range of the investigation. This result combined with good control effectiveness allows the model to be trimmed over a wide range of lift coefficients with only small elevator deflections.

The longitudinal stability and control derivatives C_{mC_L} and $C_{m\delta_e}$ presented in figure 13 were taken over a lift-coefficient range from 0.3 to 0.4. The variation of the longitudinal stability derivative is only approximately 7 percent of the reference length over the Mach number range of interest (0.30 to 0.76). It is observed that the large rearward shift in aerodynamic center that occurs in the Mach number range from 0.75 to 0.80 is compensated for by the positive shift in $C_{m,0}$ in this same Mach number range. This characteristic has been observed on other supercritical-wing configurations and is desirable since it reduces the trim drag in this part of the flight envelope. This configuration, however, would not be expected to operate in this range, since it is above the drag-divergence Mach number and extensive separation on the wing is evident at Mach numbers near 0.80. The lift-curve slope $C_{L\alpha}$ presented as a function of Mach number in figure 14 was taken over a lift-coefficient range from 0.3 to 0.5. Unpublished pressure-distribution data indicate that the increase in $C_{L\alpha}$ in the Mach number range from 0.60 to 0.74 is associated with the development of a region of supersonic flow over the upper surface of the wing. As the Mach number is increased to $M \geq 0.75$, supersonic flow is also developed on the lower surface and the strength of the shock wave is sufficient to separate the flow over much of the airfoil. As a result, there is a substantial decrease in $C_{L\alpha}$ in the Mach number range from 0.75 to 0.80.

Wing trailing-edge modifications. - Most of the investigation was conducted with the step (fig. 1(b)) in the trailing edge of the wing from the inboard end of the aileron to the fuselage. This trailing-edge shape was designated configuration 1. The step was filled to form a $0.0075c$ -thick (blunt) trailing edge for configuration 2. Data for these two trailing-edge configurations (fig. 8) indicate a small performance improvement and a negative pitching-moment-coefficient increment for configuration 2. Additional wind-tunnel data on the effects of trailing-edge geometry on a NASA supercritical airfoil section can be found in reference 9. It is interesting to observe the low Mach number data ($M = 0.30$, fig. 8(a)) where the angle-of-attack range was increased to include $C_{L,\max}$. Beyond $C_{L,\max}$ an abrupt stall occurred; however, the value of $C_{L,\max}$ achieved was about 1.45 or 26 percent higher than that for the basic NACA 64₁A212 wing based on unpublished data. The increase in $C_{L,\max}$ at landing speed ($M = 0.15$) was approximately 50 percent based on a comparison with the flight data presented in reference 8.

Buffet characteristics. - Buffet characteristics for both wing trailing-edge configurations are presented in the form of axial-force coefficients and fluctuating wing-root-bending-moment data as functions of angle of attack in figure 9. The divergence of the

~~CONFIDENTIAL~~

axial-force coefficient and that of the wing-root bending moment (each has been used as an indication of buffet onset) generally occur at the same angle of attack. It appears that buffet onset at $M = 0.30$ occurs at $C_{L,\max}$ or very near stall (compare α_{stall} in fig. 8(a) with α_{buffet} in fig. 9(a)), whereas at the higher Mach numbers the lift coefficient continues to increase at angles of attack beyond those for buffet onset (compare fig. 6(e) with fig. 9(g) at $M = 0.75$). A noticeable break in the lift curve does occur, however, at the angle of attack for buffet onset, as would be expected. The lift coefficient at buffet onset is presented as a function of Mach number in figure 16 and is compared with flight data for the conventional wing and the supercritical wing. The correlation of wind-tunnel buffet-onset data with the flight data for the supercritical wing was good through the Mach number range. In addition, the supercritical wing had an increase in lift coefficient at buffet onset of approximately 48 percent at $M = 0.30$ and 16 percent at $M = 0.70$ compared with that of the conventional wing. This increase in buffet-free lift coefficient would be expected, since the supercritical airfoil has a large leading-edge radius and higher thickness ratio, two features that are favorable for higher buffet-free lift coefficients at low subsonic Mach numbers. (See, for example, ref. 10.)

Aileron-seal effects.- During the investigation, the aileron hinge line and end gaps were sealed to improve the flow characteristics over the wing. Longitudinal data for the sealed and unsealed ailerons are presented in figure 10. There is a small improvement in the drag coefficient and lift coefficient at $M = 0.75$. Although the increments are small, it is noted that they are for only one aileron and would be larger if both ailerons were considered. The more important effects of the aileron seals on the lateral characteristics are discussed in a subsequent section.

Lateral Stability and Control

The basic lateral stability and control data at constant values of angle of attack are presented in figure 17 and generally indicate linear variations to sideslip angles of $\pm 8^\circ$. Aileron control effectiveness was positive. A larger range of aileron deflection angles is presented as a function of angle of attack at $\beta = 0^\circ$ in figure 18. With increasing angle of attack, the aileron effectiveness decreases at the lowest Mach number and increases at the high Mach numbers. There is a substantial negative rolling-moment coefficient with the aileron undeflected that becomes larger at the higher Mach numbers. Basic lateral stability data as a function of angle of attack at constant sideslip angles are presented in figures 19, 20, and 21 at aileron deflection angles of 0° , $+3^\circ$, and -3° , respectively. The negative rolling-moment coefficients are also observed in these figures; the lateral control deflections, however, appear to have little effect on the lateral stability. The lateral stability derivatives as a function of angle of attack, as shown in figure 24, indicate that the model was laterally stable at all conditions presented. The variation of the lateral stability and control derivatives with Mach number is presented in figure 25

~~CONFIDENTIAL~~

for an angle of attack of approximately 1° . Small variations of the lateral stability derivatives are noted at the high Mach numbers. There is a substantial increase in the aileron effectiveness for negative deflection compared with positive deflection (positive is trailing edge down). It should be noted that only the left aileron is considered, and $C_{l\delta_a,L}$ is positive for positive control effectiveness; however, if the conventional equation for differential roll control ($\delta_a = \delta_{a,R} - \delta_{a,L}$) was applied, the value of $C_{l\delta_a}$ would be negative and positive roll-control effectiveness would be indicated.

Aileron modifications. - As previously discussed, the model had a substantial negative rolling-moment coefficient at $\beta = 0^{\circ}$ with the aileron undeflected, and it was conjectured that this result was associated with a loss in lift on the wing caused by airflow through the hinge line of the aileron. As a result, fluorescent-oil-flow studies of the aileron and the wing were made with the aileron unsealed, with the hinge line sealed, and with the hinge-line and end gaps of the aileron sealed. The lateral data for configuration 2 (fig. 22) show progressive improvements associated with sealing the aileron hinge-line and end gaps. The fluorescent-oil photographs (fig. 22(d)) show the improvement in the flow characteristics over the aileron for the sealed condition. The photographs for the aileron unsealed are on the left side of the figure and indicate more apparent spanwise flow and more separation near the trailing edge of the aileron relative to the case of the aileron sealed (shown on the right side of the figure). Data for this last sealed condition were obtained through a large angle-of-attack range, and these data are compared with the data for configuration 1 in figure 23.

Aileron hinge-moment coefficients. - The aileron hinge-moment data (figs. 26, 27, and 28) indicate relatively large negative hinge-moment coefficients for the undeflected aileron, which are associated with the characteristic aft loading of this airfoil section. The derivatives $C_{h\alpha}$ and $C_{h\delta_a}$ are shown as a function of Mach number in figure 29 for near-cruise lift conditions. It is noted that $C_{h\delta_a}$ is relatively constant with Mach number and $C_{h\alpha}$ has a relatively large negative variation in the Mach number range from 0.60 to 0.76 and exceeds the value of $C_{h\delta_a}$ at the highest test Mach number.

CONCLUSIONS

Results of a wind-tunnel investigation to determine the aerodynamic characteristics of a model of an airplane with a 17-percent-thick supercritical wing indicate the following conclusions:

1. The drag-divergence Mach number (M_{DD} as defined by $\frac{\partial C_D}{\partial M} = 0.1$, where C_D is the drag coefficient and M is the free-stream Mach number) was 0.72 at the design lift coefficient of 0.50. On the basis of a comparison with flight data from North American Rockwell Corp. publication NR71H-150 for the configuration with a 12-percent-thick con-

~~CONFIDENTIAL~~

ventional airfoil section, M_{DD} was slightly increased by the 42-percent increase in thickness to the 17-percent-thick supercritical airfoil of the present investigation.

2. Compared with flight data from North American Rockwell Corp. publication NR71H-150 for the conventional wing, the lift coefficient at buffet onset for the present configuration is increased by 48 percent at a Mach number of 0.30 and 16 percent at a Mach number of 0.70.

3. The correlation between wind-tunnel and flight data to determine drag-divergence Mach number and buffet-free lift coefficient for the supercritical wing was good.

4. A maximum lift coefficient of 1.45 was achieved at a Mach number of 0.30 for the supercritical-wing configuration. This value is approximately 26 percent higher than that obtained with the conventional wing.

5. The model was longitudinally and laterally stable with adequate control.

6. Substantial improvement in the flow over the aileron was obtained by sealing the end gaps and hinge line of the aileron.

Langley Research Center,
National Aeronautics and Space Administration,
Hampton, Va., March 30, 1972.

~~CONFIDENTIAL~~
REFERENCES

1. Bartlett, Dennis W.; and Re, Richard J.: Wind-Tunnel Investigation of Basic Aerodynamic Characteristics of a Supercritical-Wing Research Airplane Configuration. NASA TM X-2470, 1972.
2. Harris, Charles D.: Wind-Tunnel Measurements of Aerodynamic Load Distribution on an NASA Supercritical-Wing Research Airplane Configuration. NASA TM X-2469, 1972.
3. Loving, Donald L.: Wind-Tunnel—Flight Correlation of Shock-Induced Separated Flow. NASA TN D-3580, 1966.
4. Blackwell, James A., Jr.: Preliminary Study of Effects of Reynolds Number and Boundary-Layer Transition Location on Shock-Induced Separation. NASA TN D-5003, 1969.
5. Ray, Edward J.: Techniques for Determining Buffet Onset. NASA TM X-2103, 1970.
6. Loving, Donald L.; and Katzoff, S.: The Fluorescent-Oil Film Method and Other Techniques for Boundary-Layer Flow Visualization. NASA MEMO 3-17-59L, 1959.
7. Wright, Ray H.; and Barger, Raymond L.: Wind-Tunnel Lift Interference on Swept-back Wings in Rectangular Test Sections With Slotted Top and Bottom Walls. NASA TR R-241, 1966.
8. Palmer, W. E.; Elliott, D. W.; and White, J. E.: Flight and Wind Tunnel Evaluation of a 17% Thick Supercritical Airfoil on a T-2C Airplane. NR71H-150 (Navy Contract N00019-70-C-0474), North American Rockwell Corp., July 31, 1971.
Vol. I – Basic Report.
Vol. II – Flight Measured Wing Wake Profiles and Surface Pressures.
9. Harris, Charles D.: Wind-Tunnel Investigation of Effects of Trailing-Edge Geometry on a NASA Supercritical Airfoil Section. NASA TM X-2336, 1971.
10. Ray, Edward J.; and Taylor, Robert T.: Buffet and Static Aerodynamic Characteristics of a Systematic Series of Wings Determined From a Subsonic Wind-Tunnel Study. NASA TN D-5805, 1970.

~~CONFIDENTIAL~~

TABLE I.- MODEL GEOMETRIC CHARACTERISTICS

Wing:

Total area, m ²	0.192
Aileron area (one aileron), m ²	0.007
Span (theoretical), cm	98.618
Aspect ratio	5.07
Taper ratio	0.496
Dihedral angle, deg	3.323
Incidence at root, deg	2.5
Incidence at tip, deg	1
Airfoil at root and tip	See table II
Mean aerodynamic chord, cm	20.318
Horizontal distance to center line of airplane, cm	21.735
Vertical distance to fuselage reference line at 25 percent chord, cm	1.084
Incidence, deg	2

Horizontal tail:

Total area, m ²	0.054
Elevator area (total aft of hinge line), m ²	0.016
Span, cm	49.131
Aspect ratio	4.47
Taper ratio	0.508
Dihedral angle, deg	0
Airfoil at root and tip	NACA 65 ₁ A012
Mean aerodynamic chord, cm	11.533
Horizontal distance to center of airplane, cm	10.923
Vertical distance to fuselage reference line at 25 percent chord, cm	13.076

Vertical tail:

Total area (exposed), m ²	0.027
Rudder area, m ²	0.007
Span (theoretical) (exposed), cm	22.055
Aspect ratio (exposed)	1.800
Taper ratio (exposed)	0.375
Airfoil at root and tip, cm	NACA 63 ₁ A012
Mean aerodynamic chord, cm	13.385
Vertical distance to fuselage reference line, cm	16.848

~~CONFIDENTIAL~~

TABLE II.- WING AIRFOIL COORDINATES ALONG STREAMWISE CHORDS

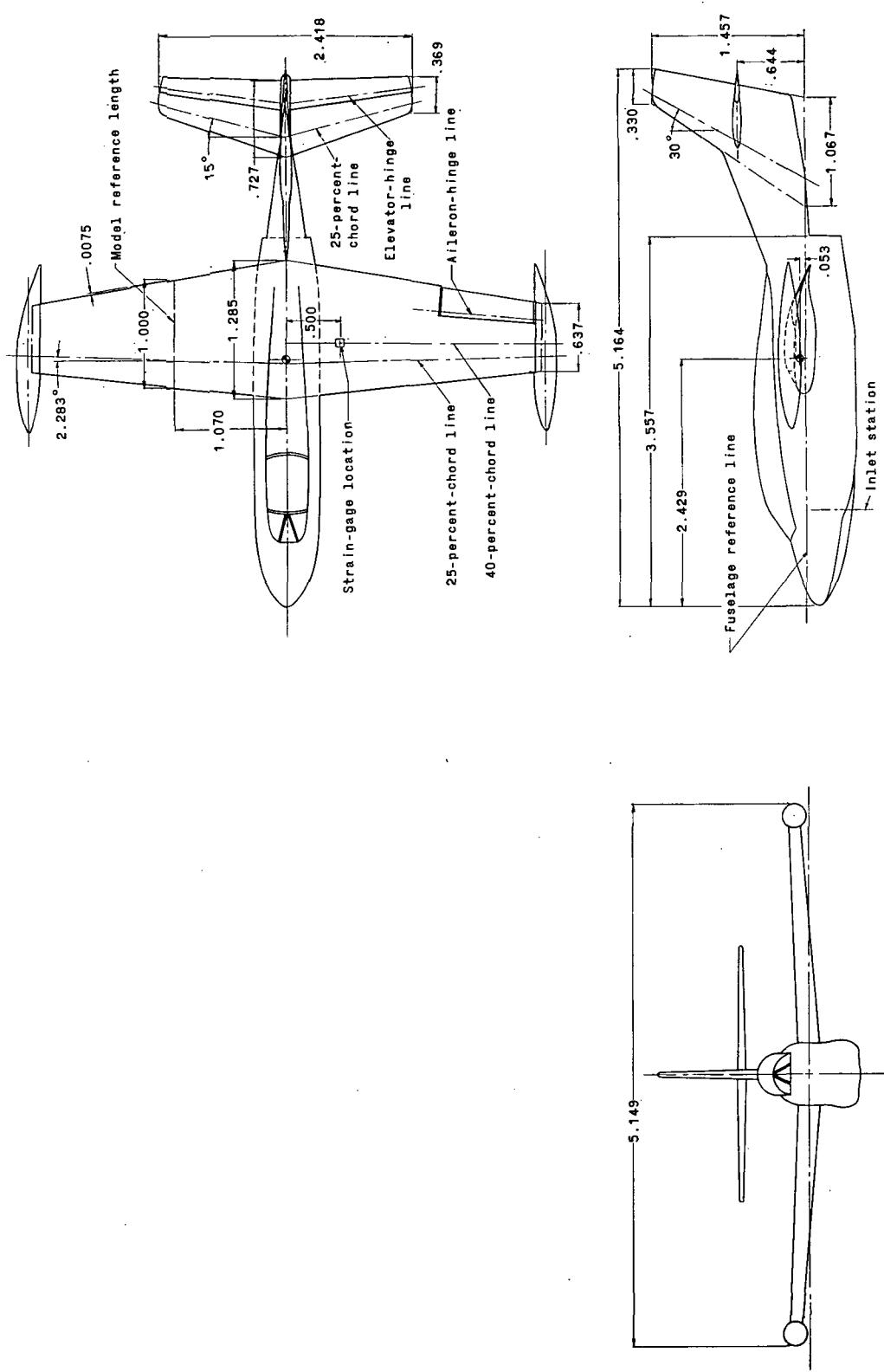
[Leading-edge radius/c = 0.0428; $(x/c)_{LER} = 0.0428$; $(y/c)_{LER} = 0.00$]

x/c	y/c		x/c	y/c	
	Upper	Lower		Upper	Lower
0.0	0.000	0.000	0.575	0.08423	-0.0652
.0125	.0304	-.030	.600	.08248	-.0607
.0250	.0401	-.0408	.625	.08043	-.0554
.0375	.0469	-.048	.650	.07811	-.0495
.0500	.0519	-.0533	.675	.07541	-.0431
.075	.0593	-.0611	.700	.07233	-.0366
.100	.0652	-.0664	.725	.06881	-.0301
.125	.06963	-.0704	.750	.06476	-.0240
.150	.07325	-.0735	.775	.0595	-.0184
.175	.07625	-.0760	.800	.0553	-.0134
.200	.07890	-.0779	.825	.0499	-.0093
.250	.0832	-.0807	.850	.0440	-.0060
.300	.0863	-.0819	.875	.0376	-.0036
.350	.08825	-.0820	.900	.0308	-.0021
.400	.0891	-.0810	.925	.0236	-.0017
.450	.08893	-.0786	.950	.0160	-.0025
.500	.08783	-.0748	.975	.0081	-.0044
.550	.08568	-.0690	1.000	.00	-.0080

~~CONFIDENTIAL~~

~~CONFIDENTIAL~~
TABLE III.- WIND-TUNNEL OPERATING CONDITIONS

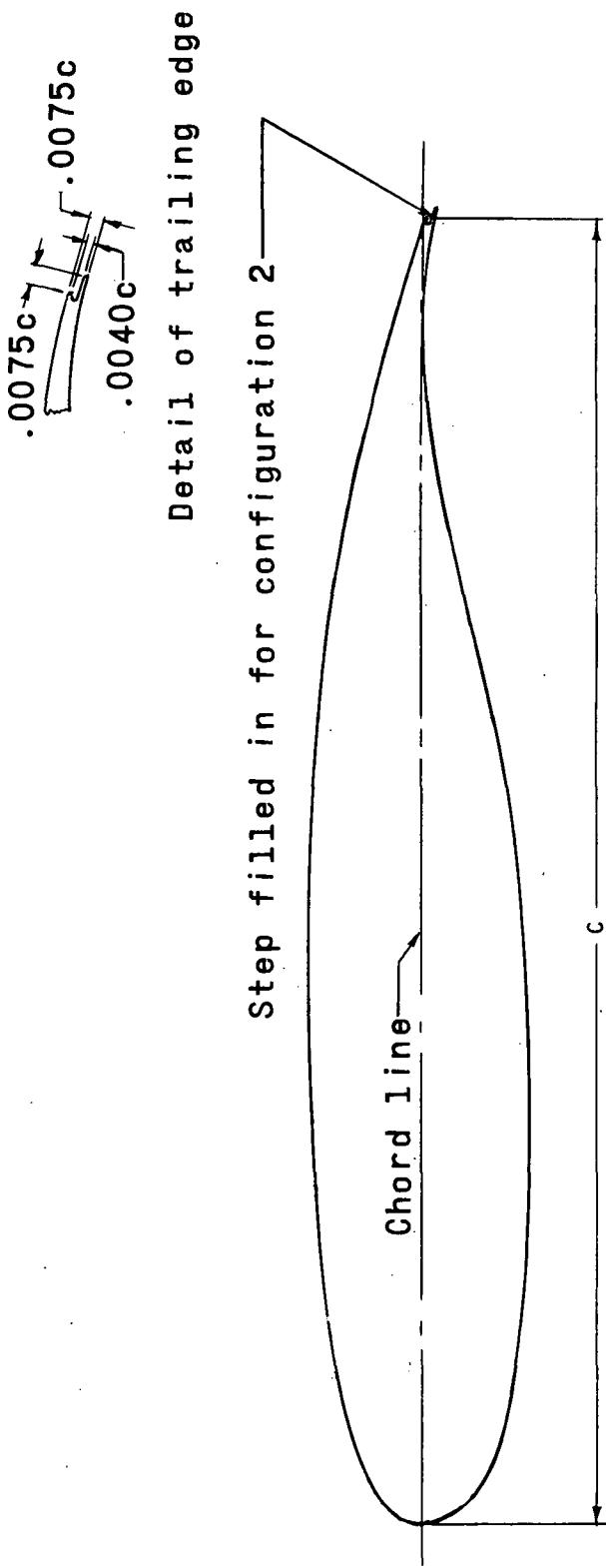
Mach number	p_t , N/m ²	q , N/m ²	$R_{\bar{c}}$
.30	171 699	10 103	2.00×10^6
.50	109 885	16 184	2.00
	146 609	21 690	2.67
.60	95 856	18 913	2.00
	143 880	28 393	3.00
	159 872	31 649	3.33
.65	151 541	33 756	3.33
.70	86 711	21 498	2.00
	130 091	32 176	3.00
	167 820	41 464	3.86
.73	85 083	22 312	2.00
	126 978	33 277	3.00
	163 655	42 853	3.86
.75	83 360	20 445	2.00
	125 111	33 947	3.00
	161 165	43 619	3.86
.76	82 737	22 839	2.00
	124 201	34 282	3.00
	159 920	44 098	3.86
.80	155 850	45 774	3.86



(a) General arrangement of model.

Figure 1.- Drawings and photographs of wind-tunnel model. All dimensions are in terms of model reference length (20.318 cm).

~~CONFIDENTIAL~~

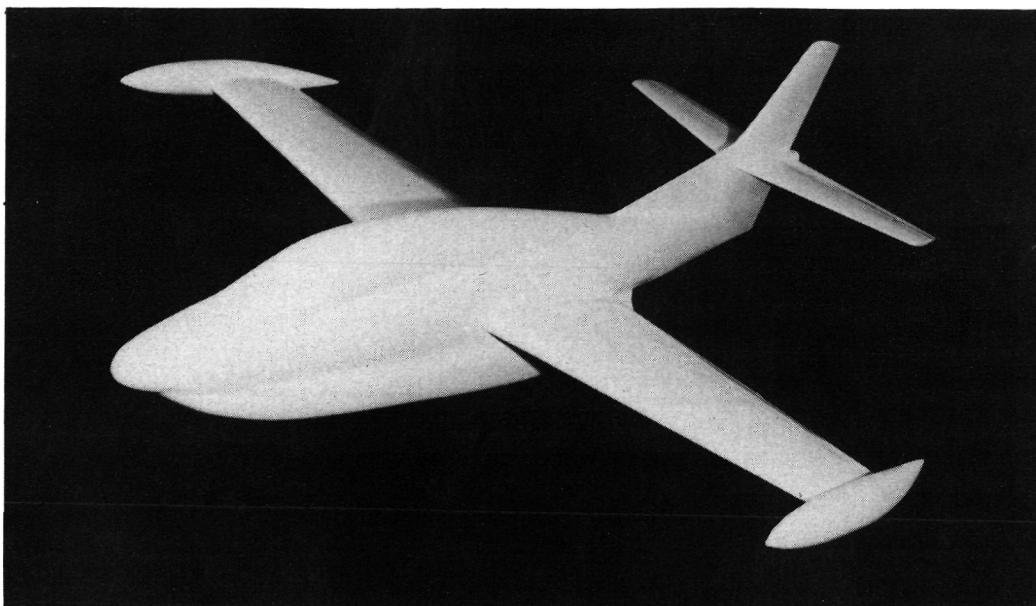


(b) 17-percent-thick supercritical airfoil.

Figure 1.- Concluded.

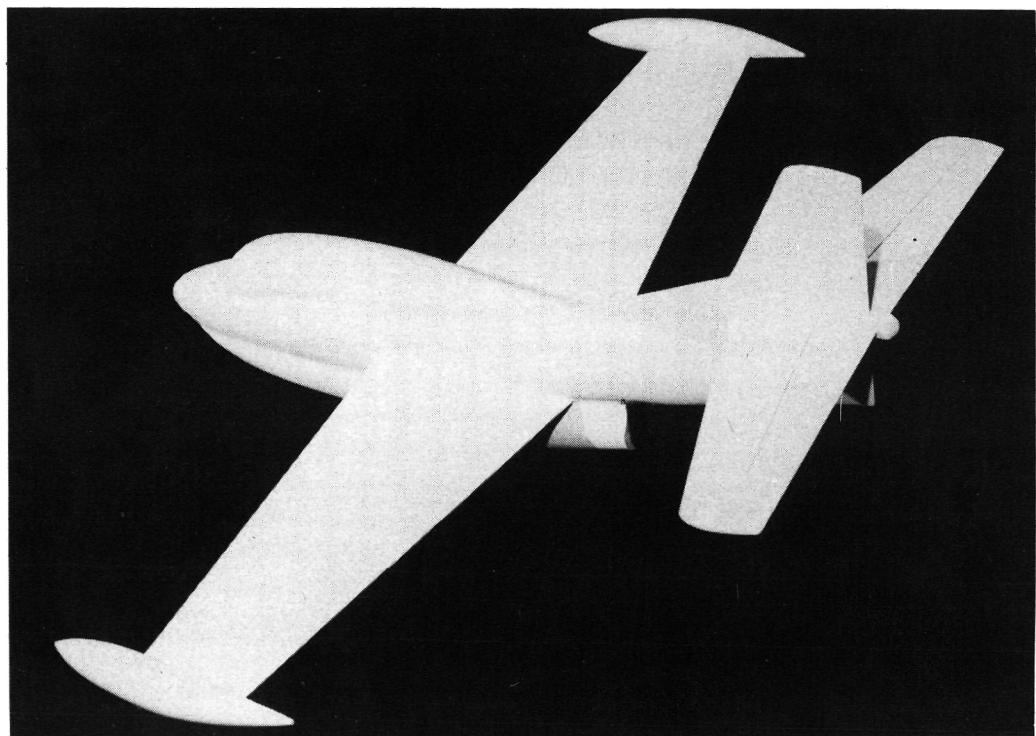
~~CONFIDENTIAL~~

~~CONFIDENTIAL~~



Three-quarter front

L-70-6044



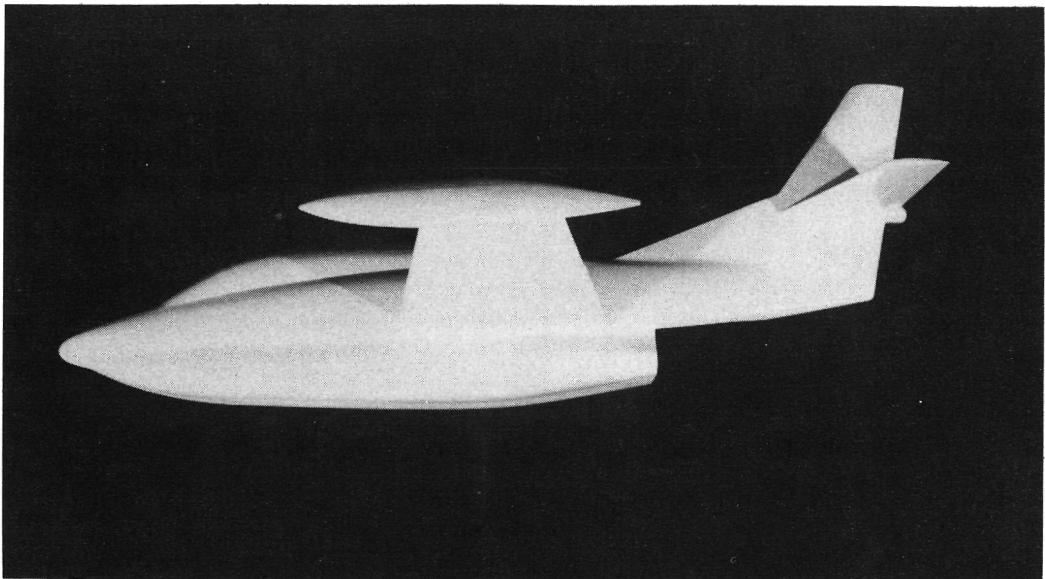
Three-quarter rear

L-70-6042

Figure 2.- Photographs of wind-tunnel model.

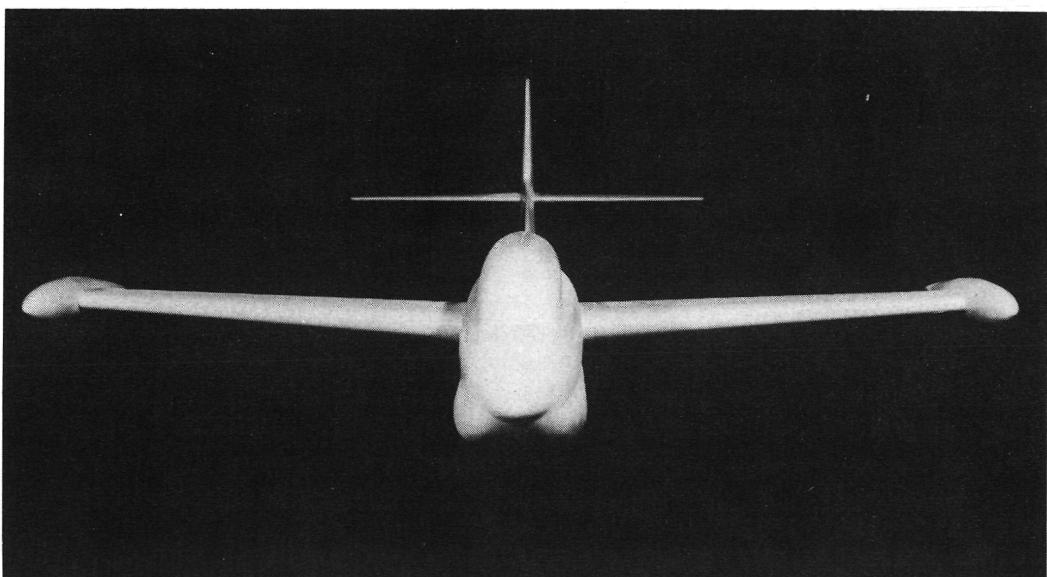
~~CONFIDENTIAL~~

~~CONFIDENTIAL~~



Lower side view

L-70-6041

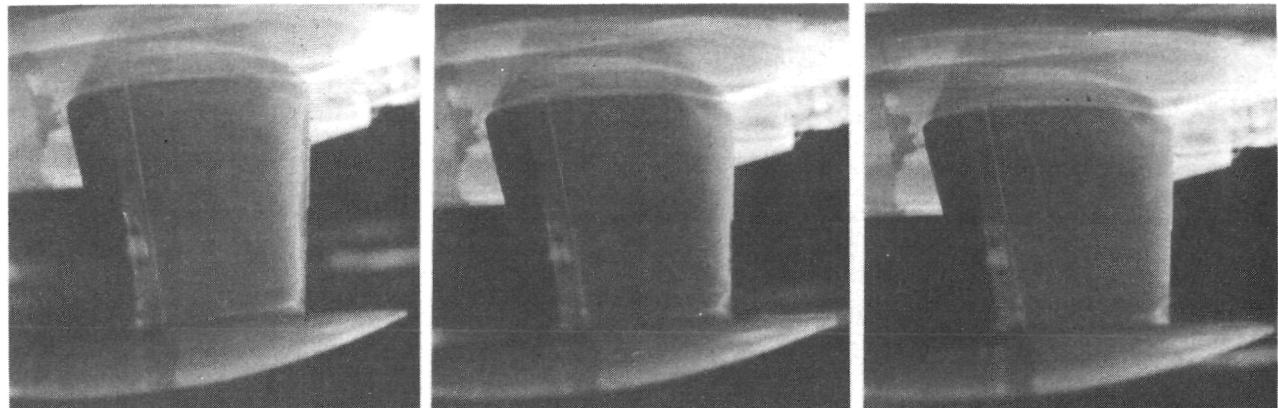


Front view

L-70-6040

Figure 2.- Concluded.

~~CONFIDENTIAL~~



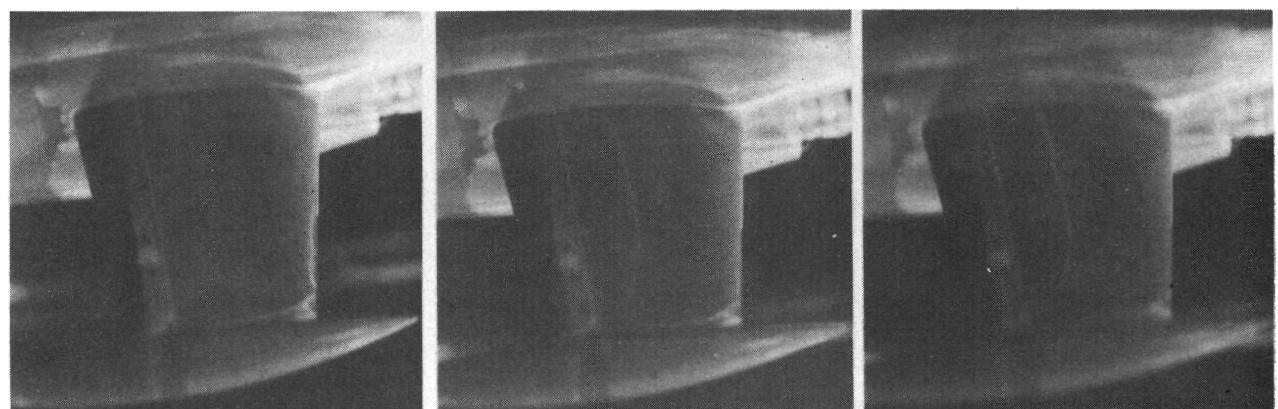
$C_L = 0.401$

$C_L = 0.649$

$C_L = 0.759$

(a) $M = 0.70.$

L-72-2404



$C_L = 0.464$

$C_L = 0.690$

$C_L = 0.706$

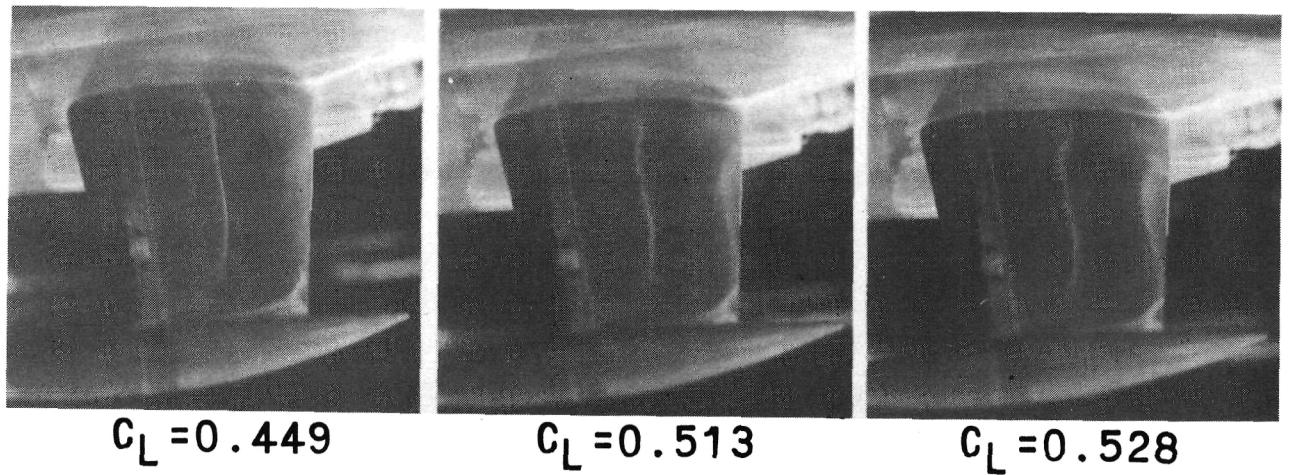
(b) $M = 0.73.$

L-72-2405

Figure 3.- Fluorescent-oil photographs of wing upper surface.

~~CONFIDENTIAL~~

~~CONFIDENTIAL~~

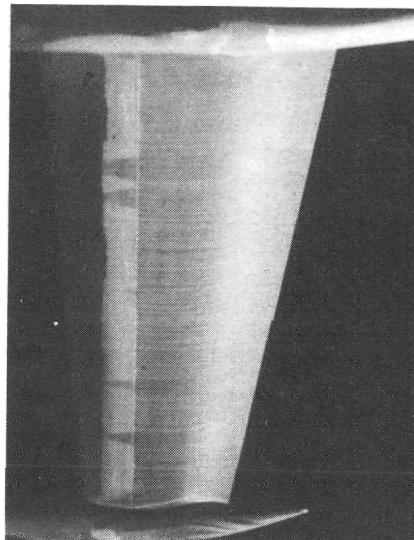


(c) $M = 0.76$.

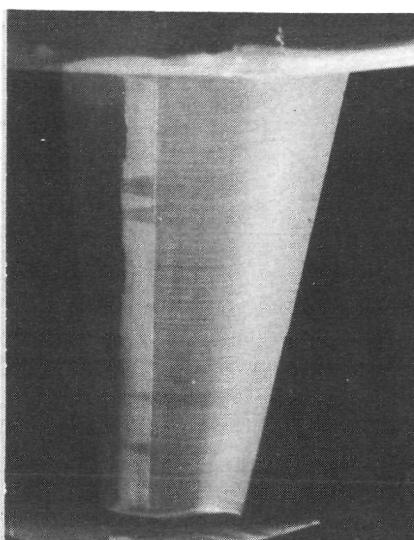
L-72-2406

Figure 3.- Concluded.

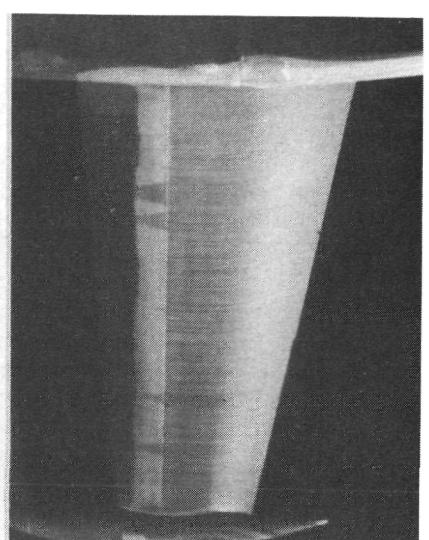
~~CONFIDENTIAL~~



$C_L = 0.264$



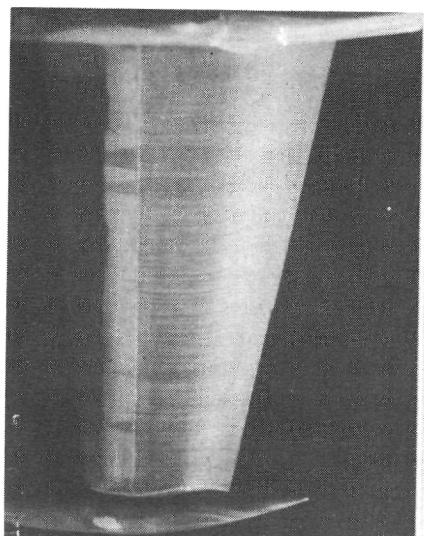
$C_L = 0.449$



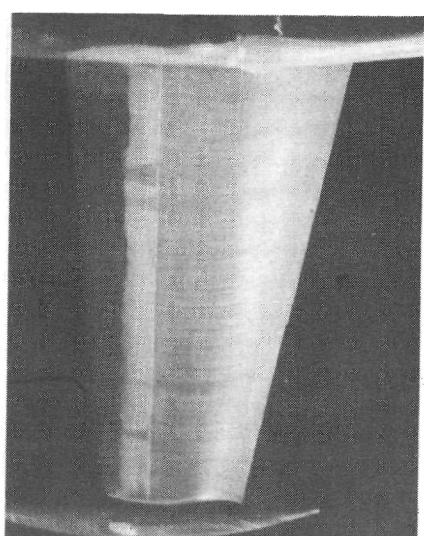
$C_L = 0.625$

(a) $M = 0.70.$

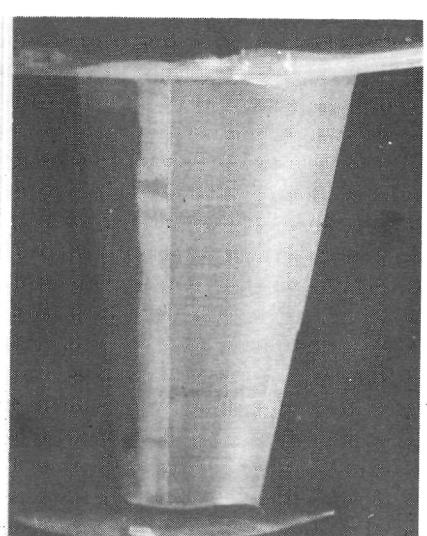
L-72-2407



$C_L = 0.314$



$C_L = 0.516$



$C_L = 0.648$

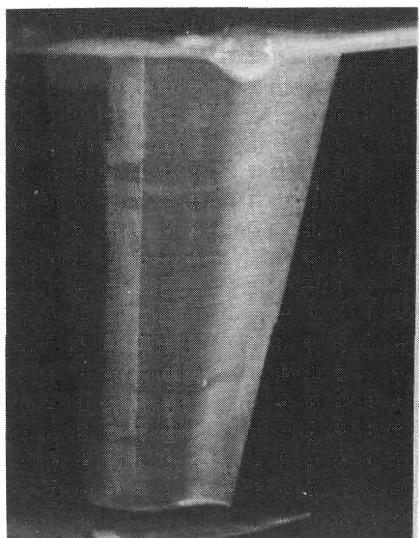
(b) $M = 0.73.$

L-72-2408

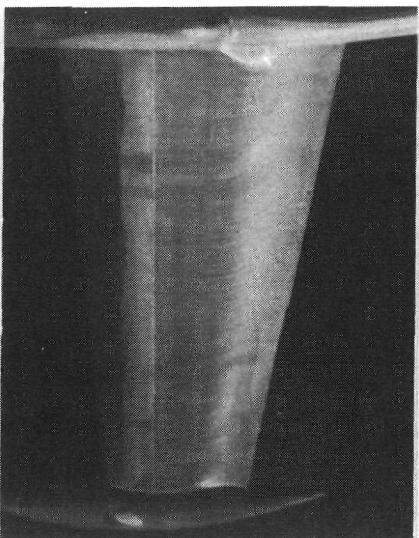
Figure 4.- Fluorescent-oil photographs of wing lower surface.

~~CONFIDENTIAL~~

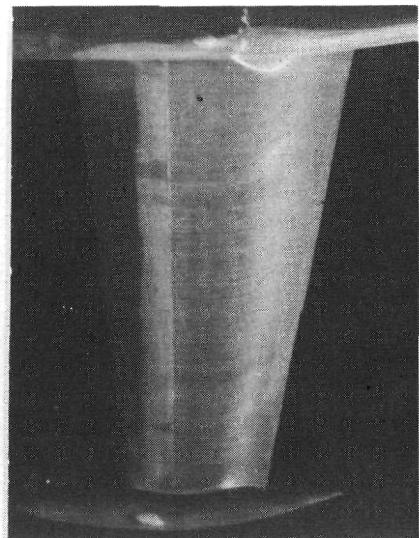
~~CONFIDENTIAL~~



$C_L = 0.326$



$C_L = 0.425$

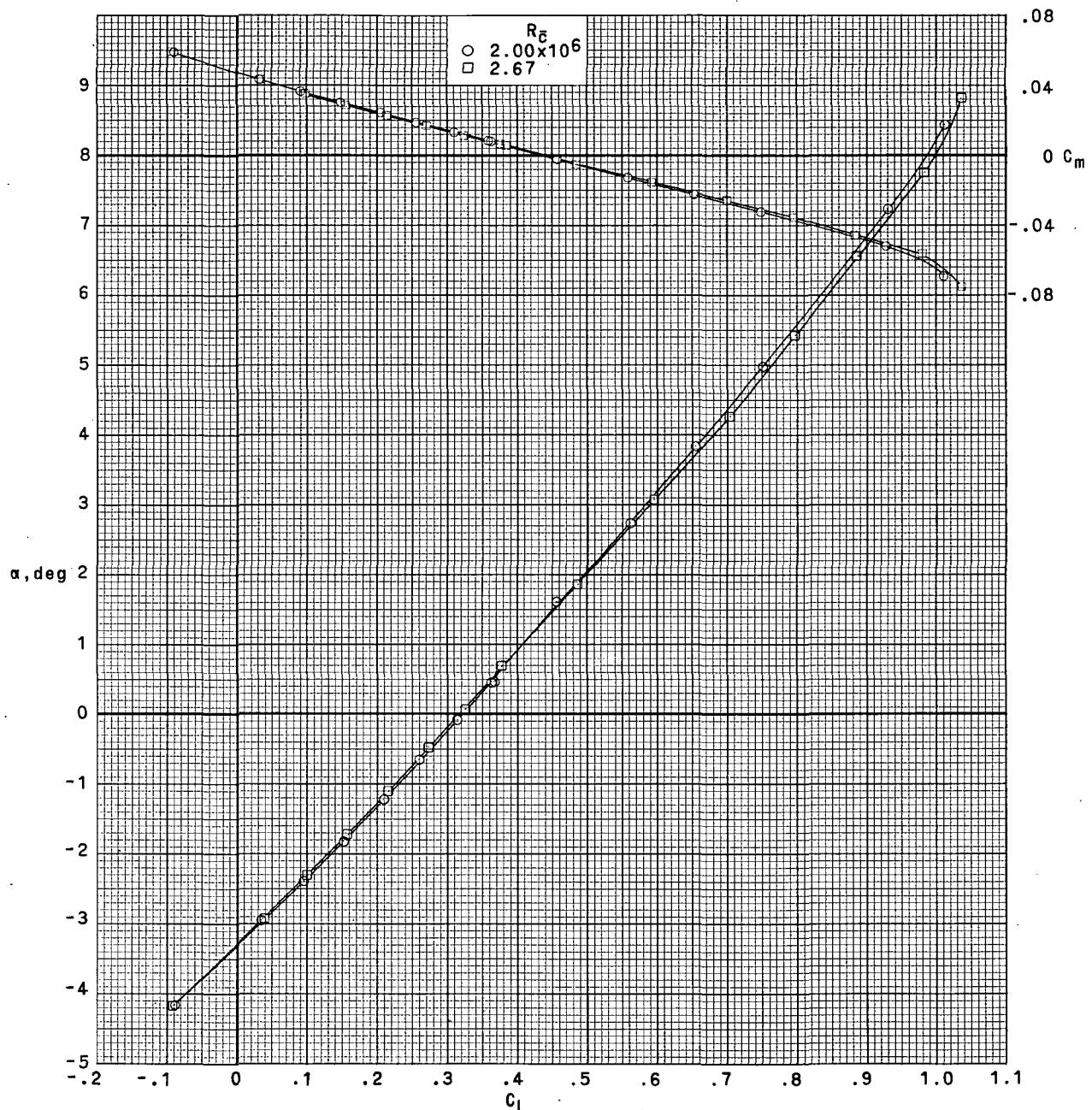


$C_L = 0.486$

(c) $M = 0.76$

L-72-2409

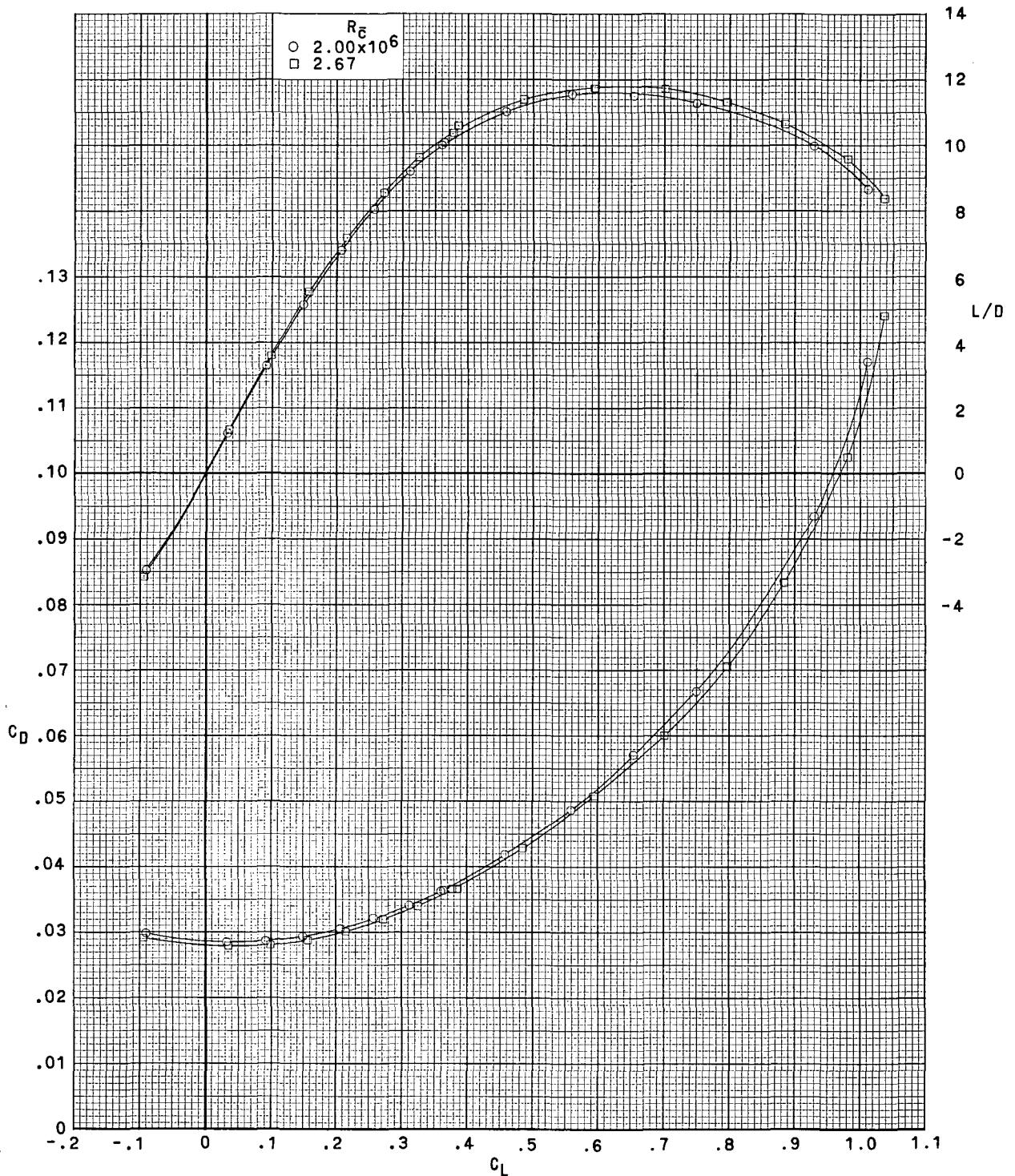
Figure 4.- Concluded.



(a) $M = 0.50$.

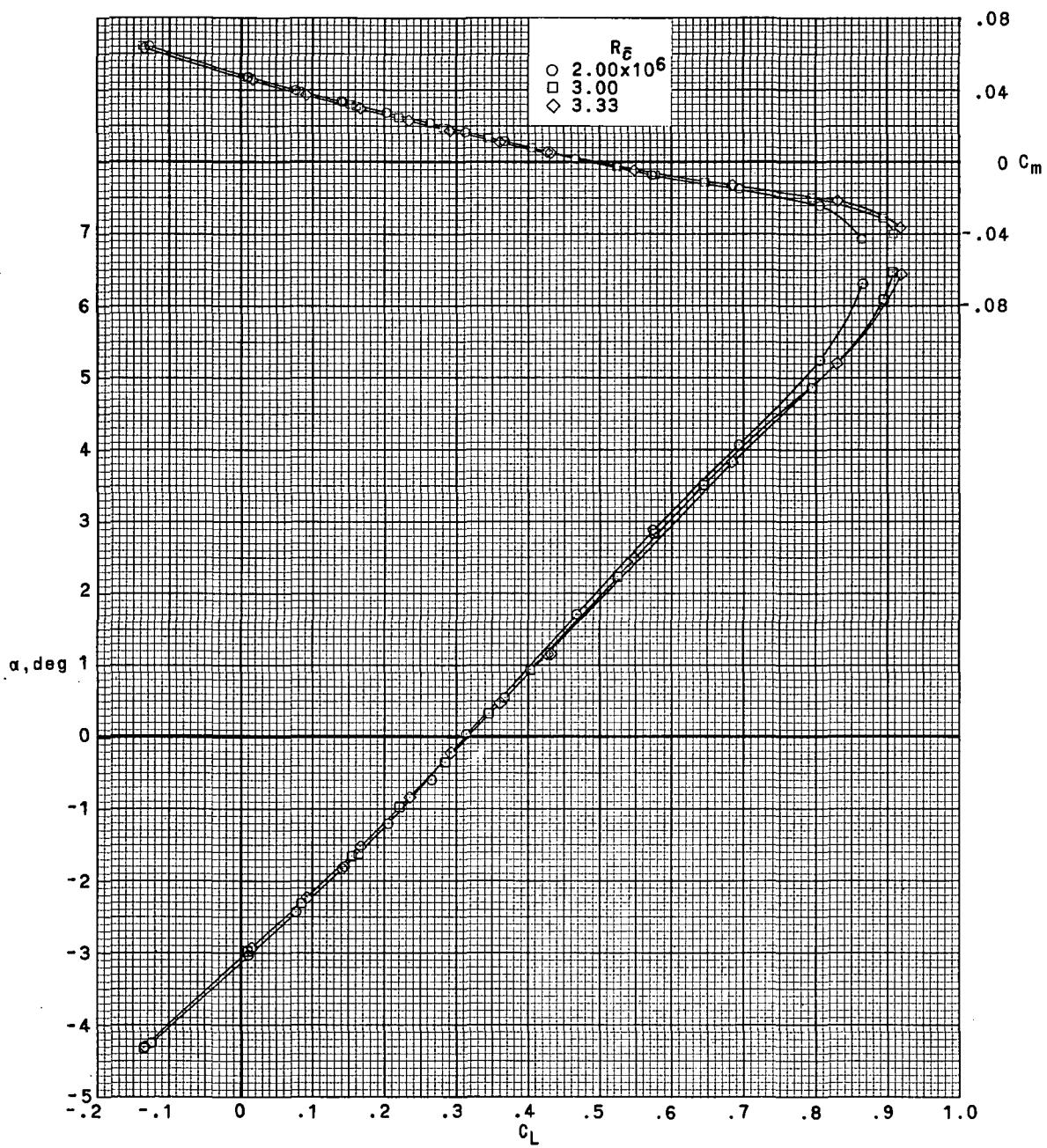
Figure 5.- Effect of Reynolds number on longitudinal aerodynamic characteristics.

$$\delta_e = 0^\circ; i_h = 0^\circ; \delta_a = 0^\circ; \beta = 0^\circ.$$



(a) $M = 0.50$. Concluded.

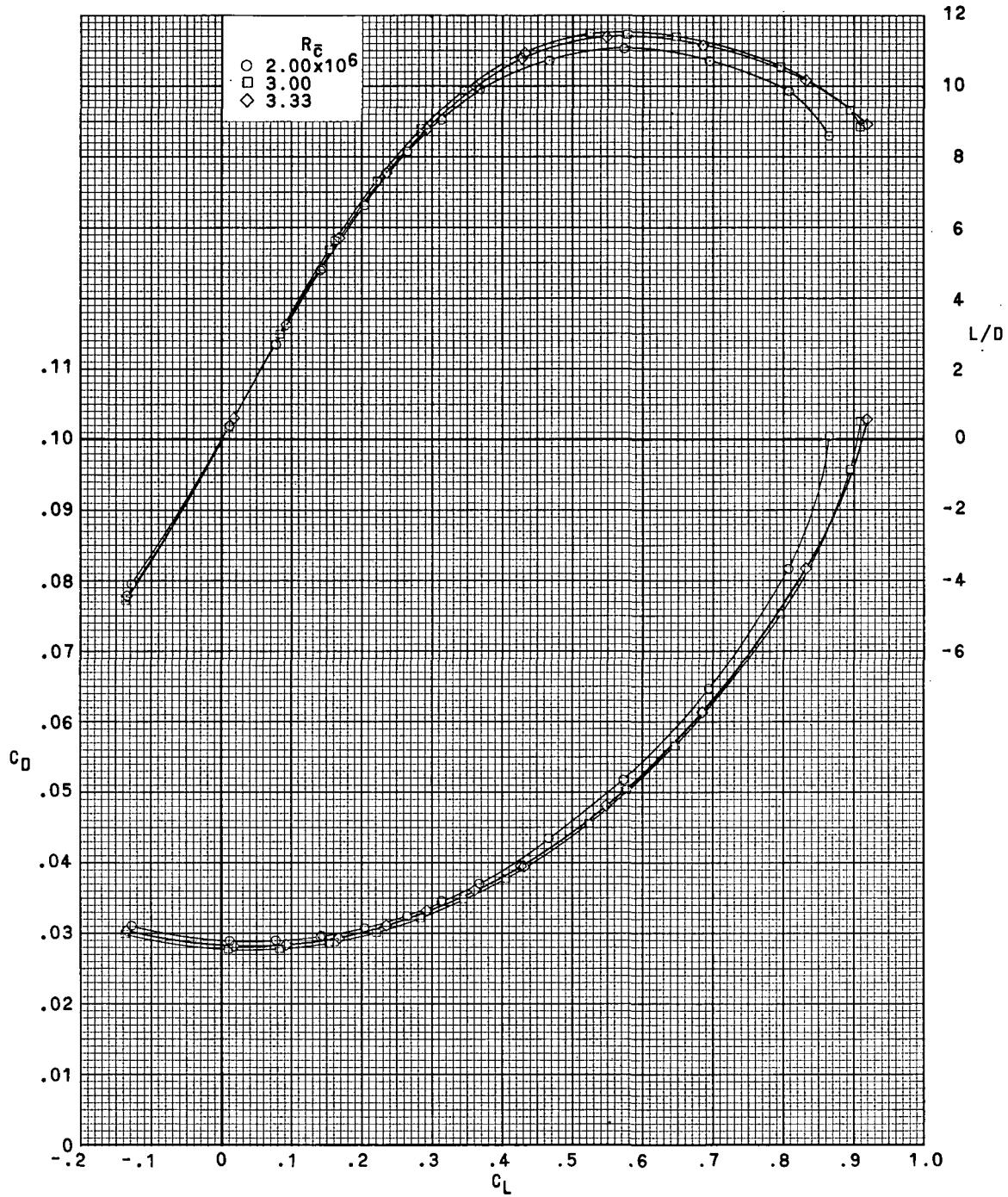
Figure 5.- Continued.



(b) $M = 0.60.$

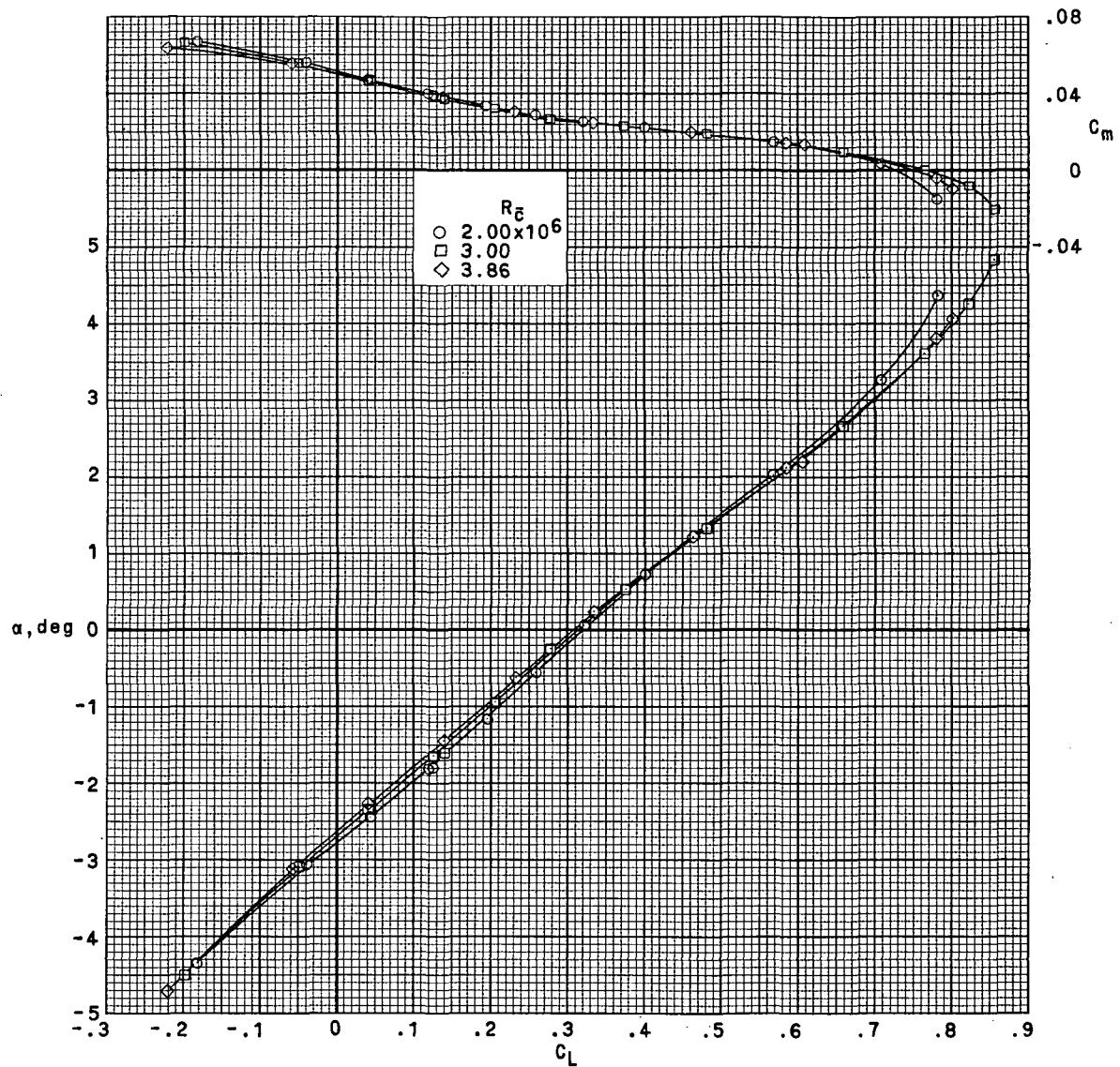
Figure 5.- Continued.

~~CONFIDENTIAL~~



(b) $M = 0.60$. Concluded.

Figure 5.- Continued.

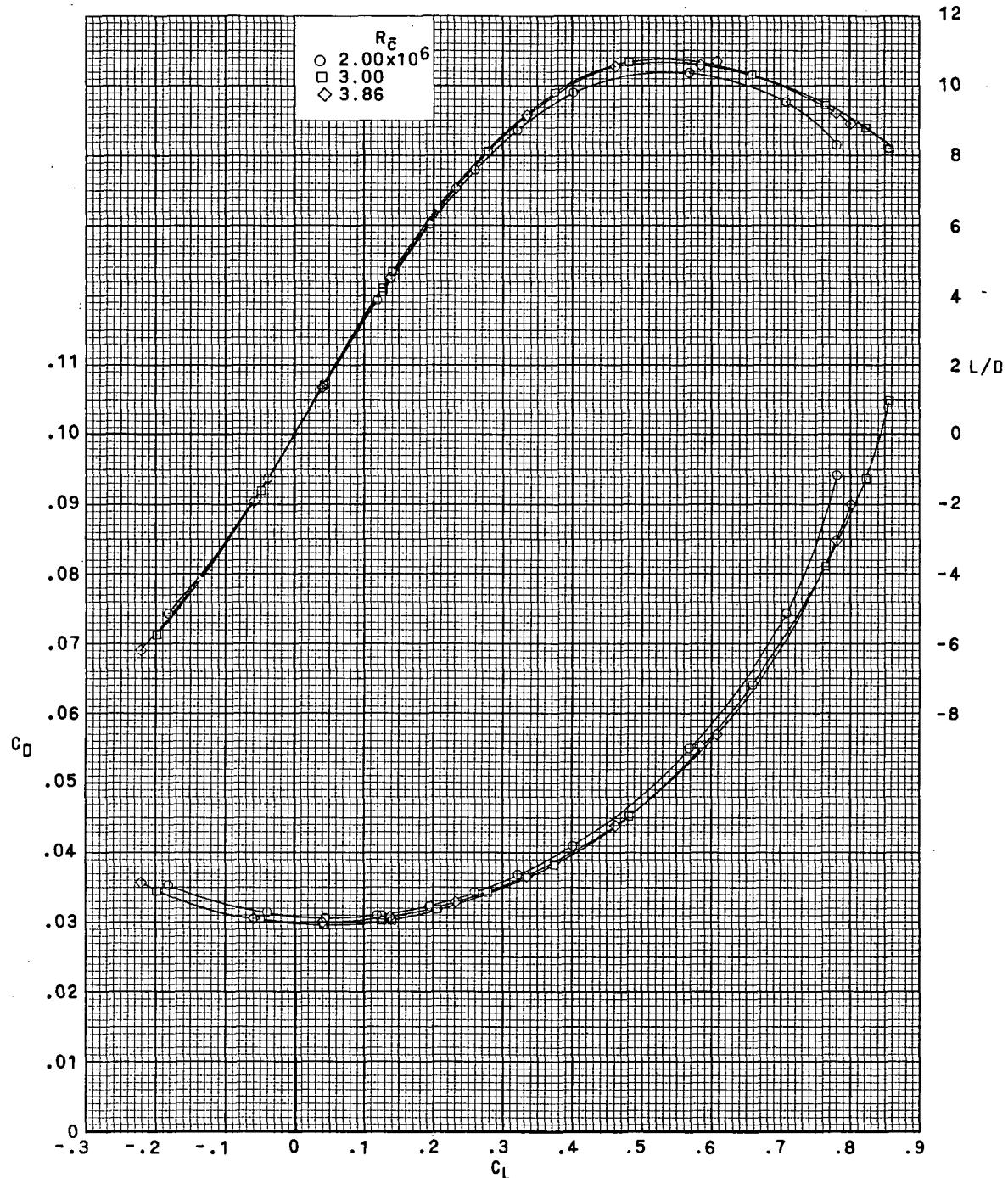


(c) $M = 0.70$.

Figure 5.- Continued.

~~CONFIDENTIAL~~

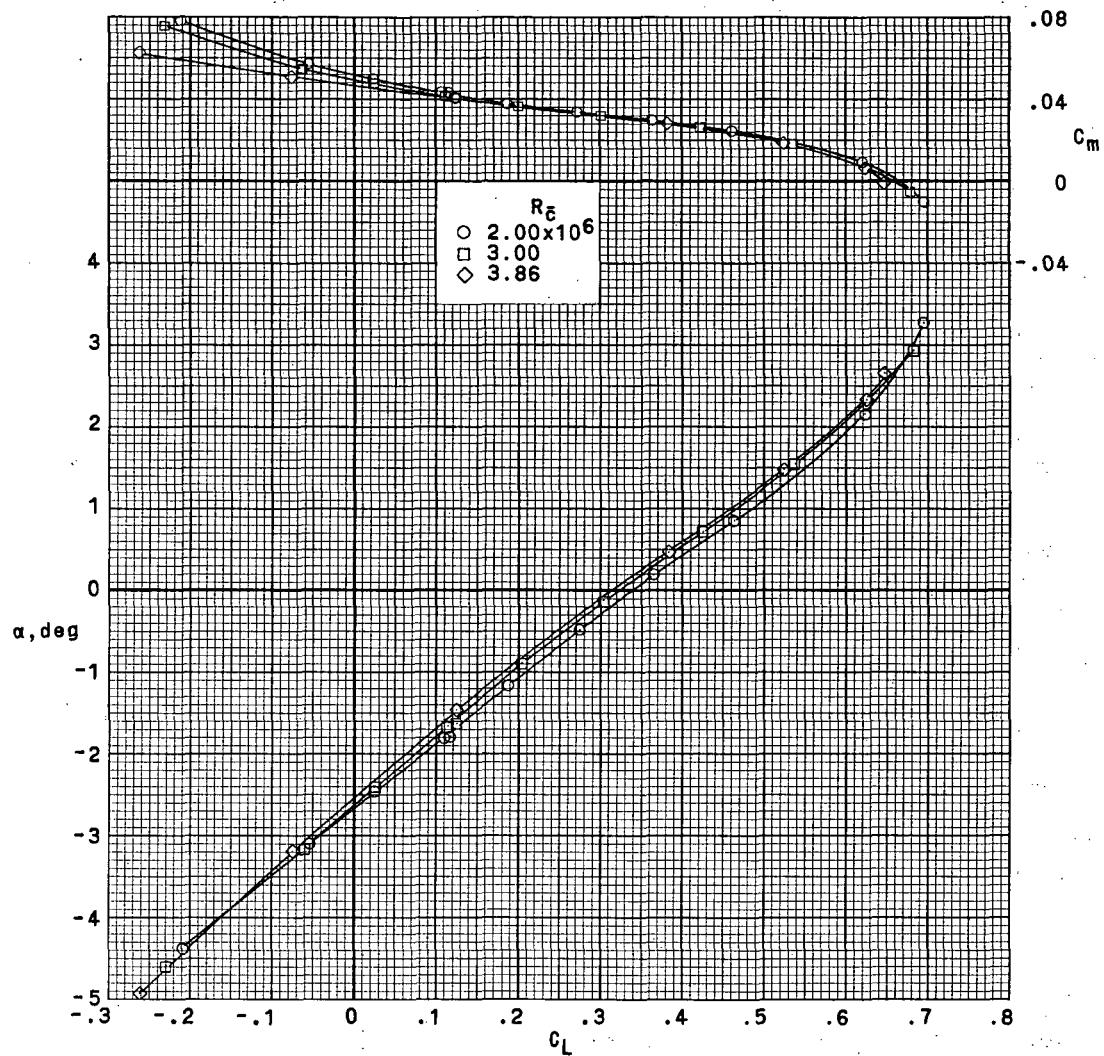
~~CONFIDENTIAL~~



(c) $M = 0.70$. Concluded.

Figure 5.- Continued.

~~CONFIDENTIAL~~

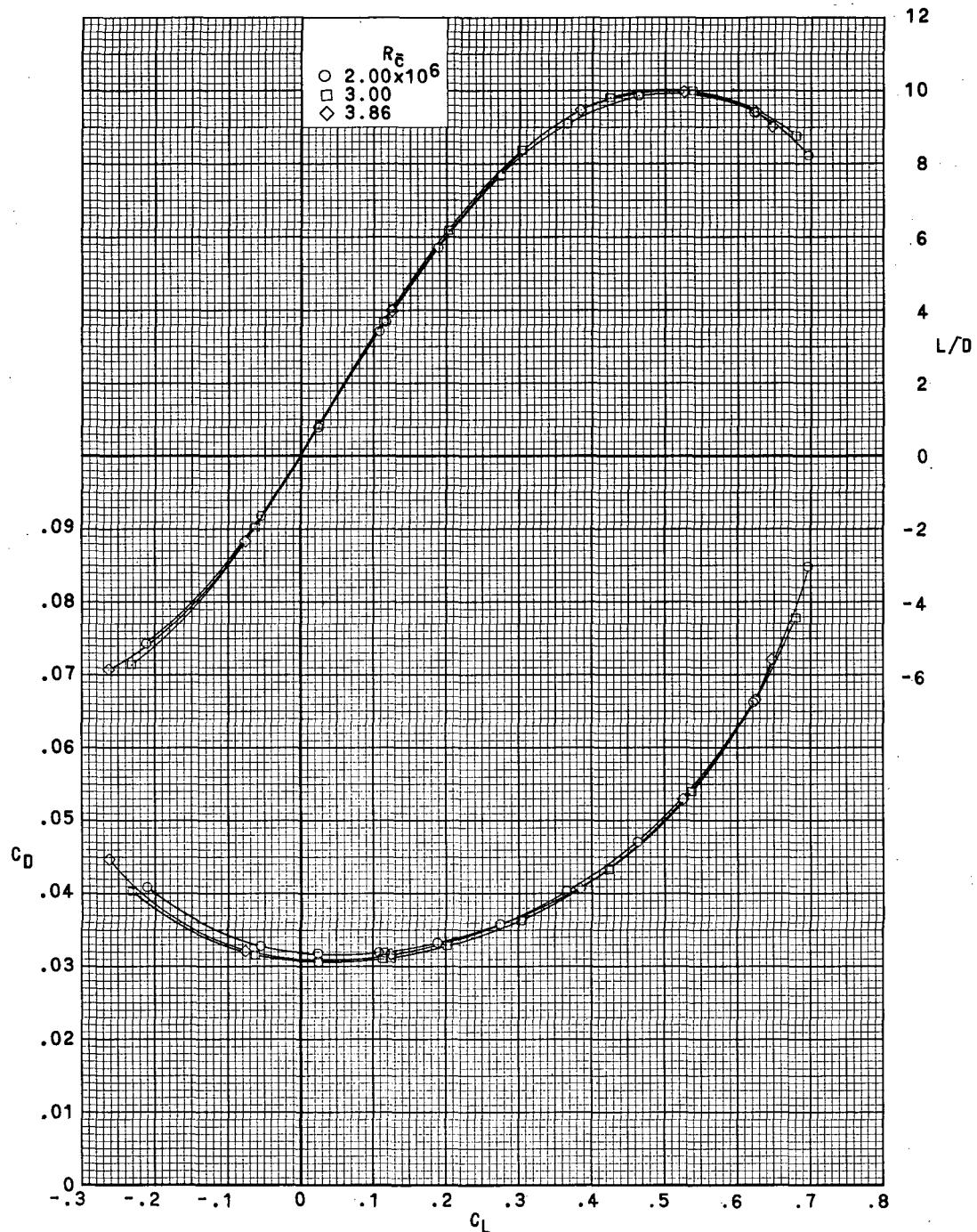


(d) $M = 0.73$.

Figure 5.- Continued.

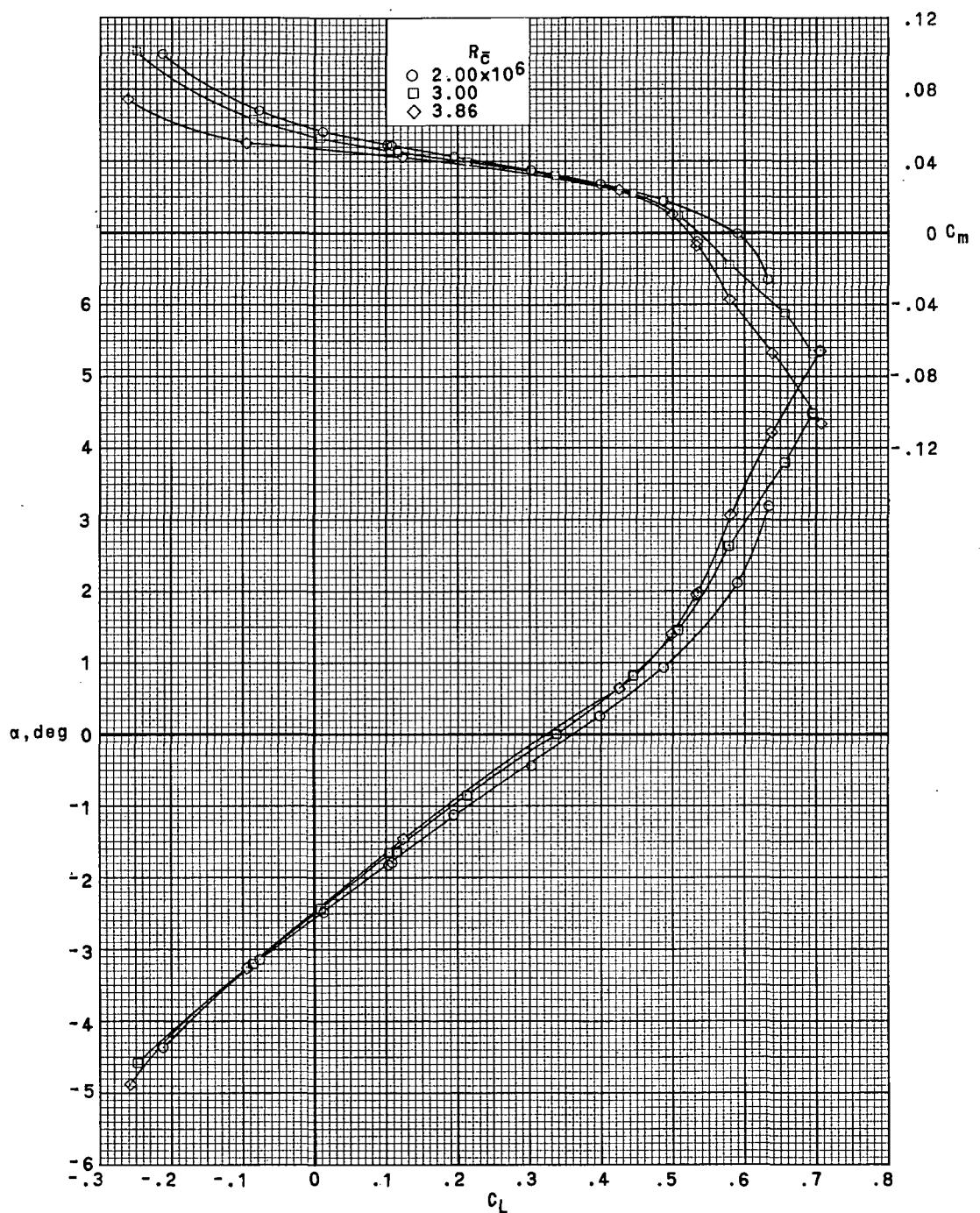
~~CONFIDENTIAL~~

~~CONFIDENTIAL~~



(d) $M = 0.73$. Concluded.

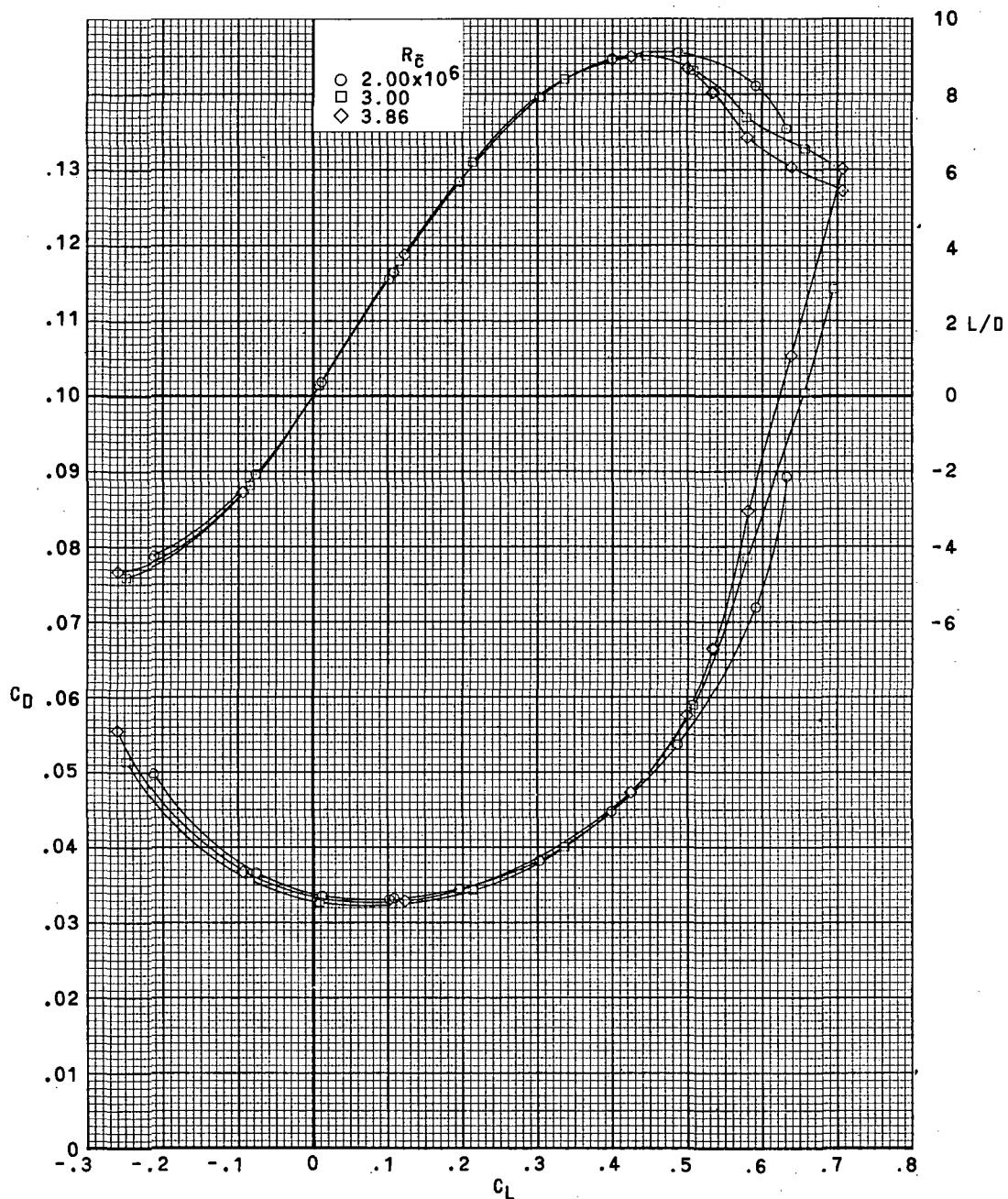
Figure 5.- Continued.



(e) $M = 0.75$.

Figure 5.- Continued.

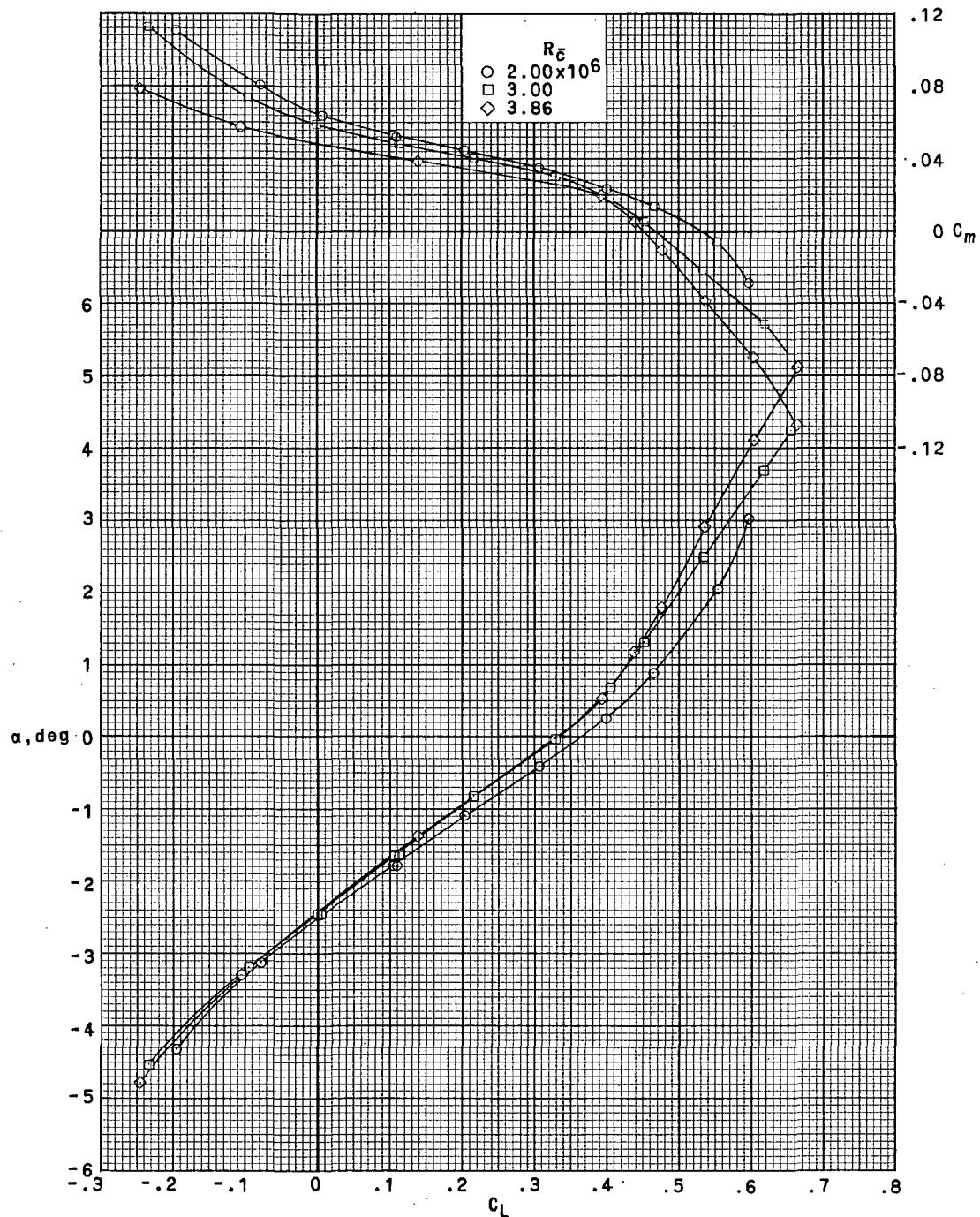
~~CONFIDENTIAL~~



(e) $M = 0.75$. Concluded.

Figure 5.- Continued.

~~CONFIDENTIAL~~

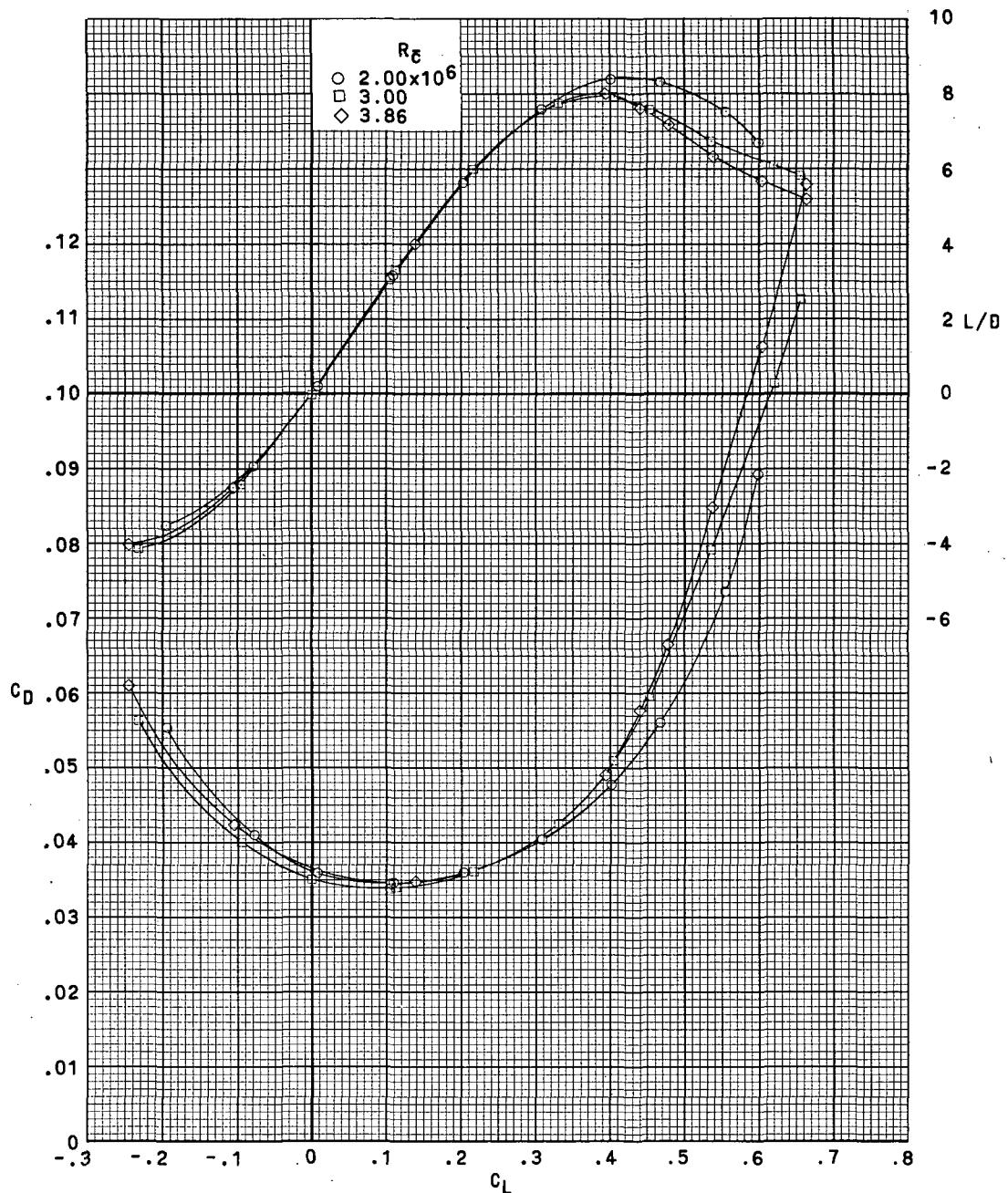


(f) $M = 0.76$.

Figure 5.- Continued.

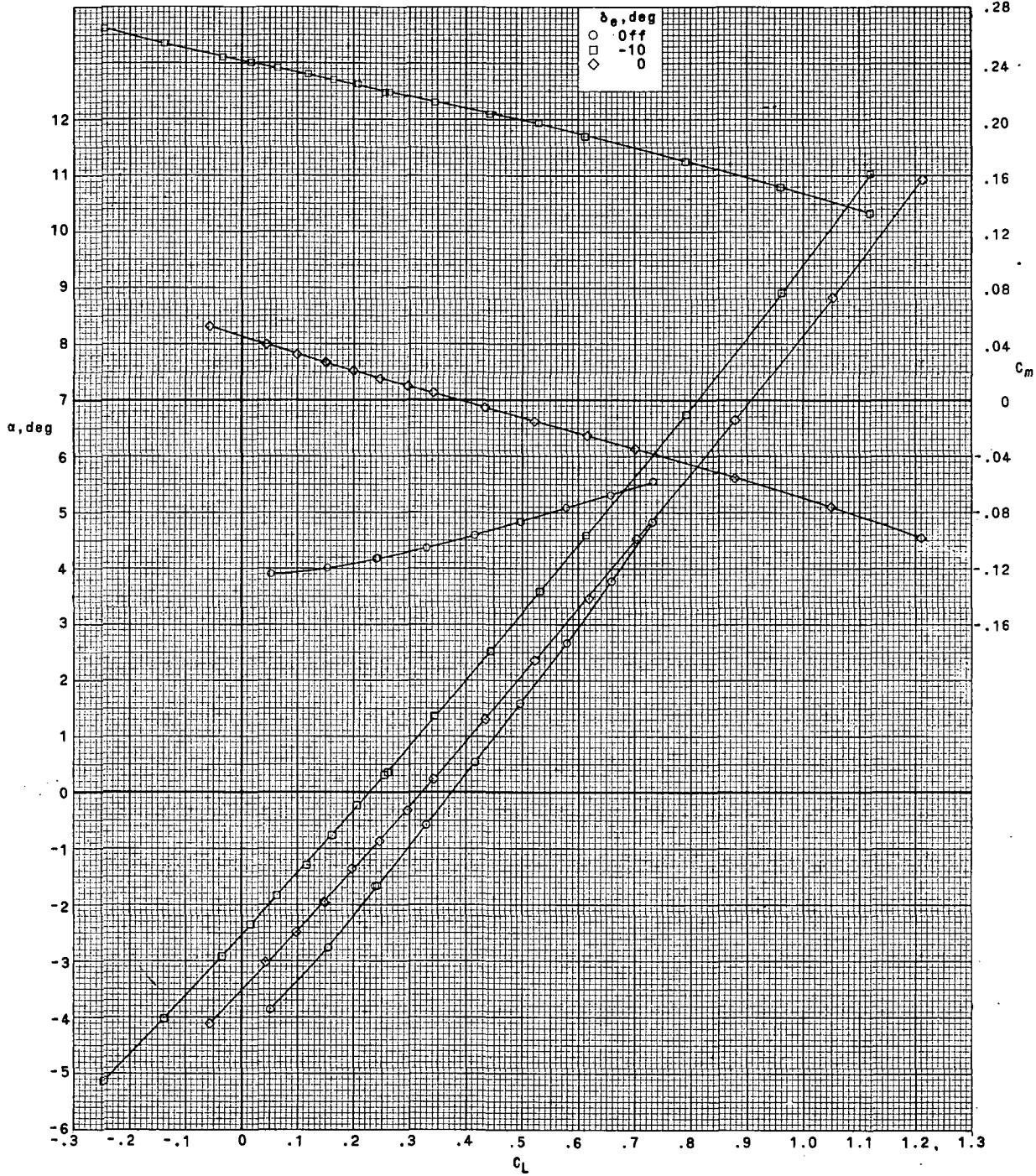
~~CONFIDENTIAL~~

~~CONFIDENTIAL~~



(f) $M = 0.76$. Concluded.

Figure 5.- Concluded.

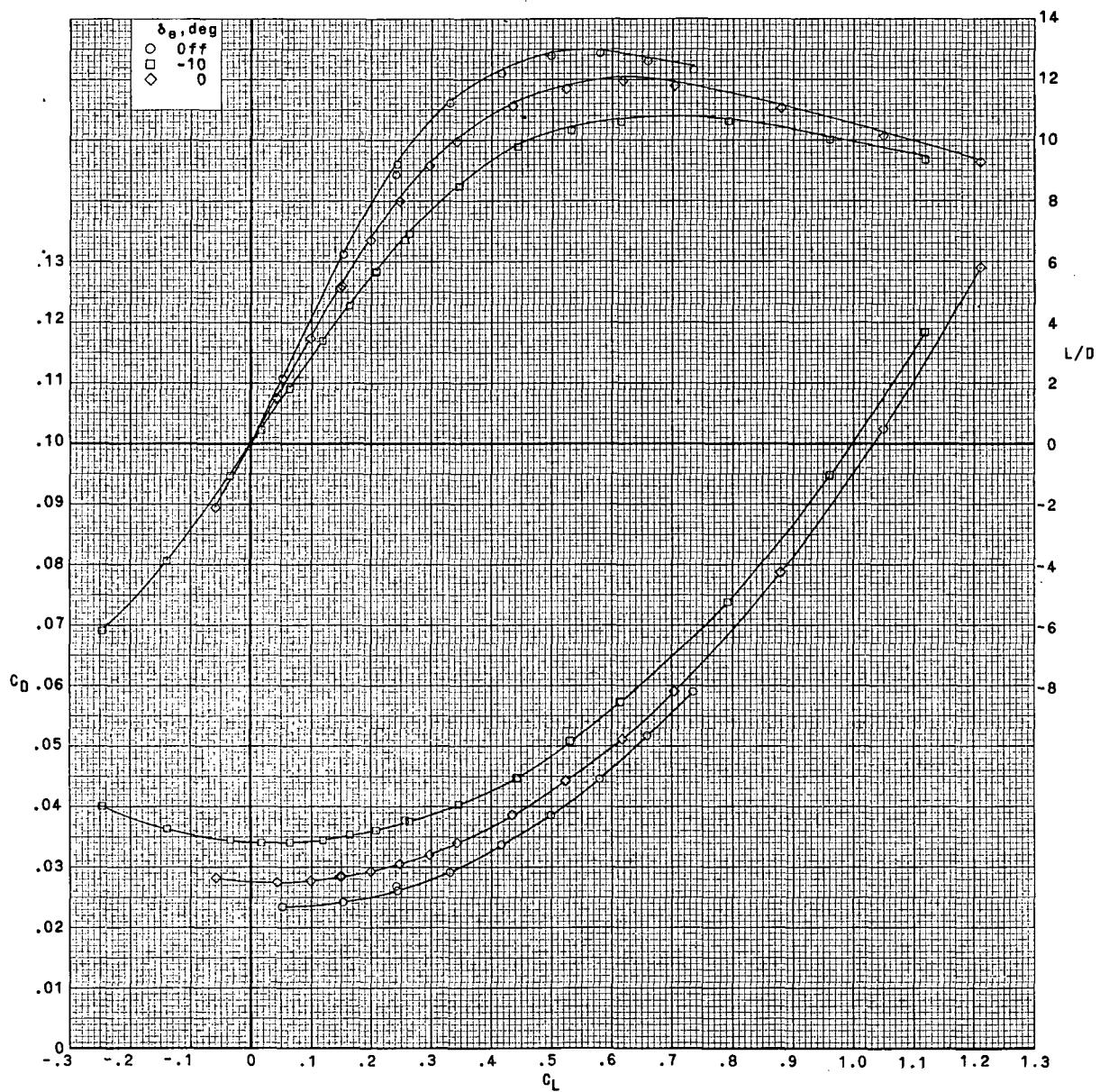


(a) $M = 0.30; R_C = 2.00 \times 10^6$.

Figure 6.- Effect of elevator deflection on longitudinal aerodynamic characteristics.
 $i_h = 0^\circ; \delta_a = 0^\circ; \beta = 0^\circ$.

~~CONFIDENTIAL~~

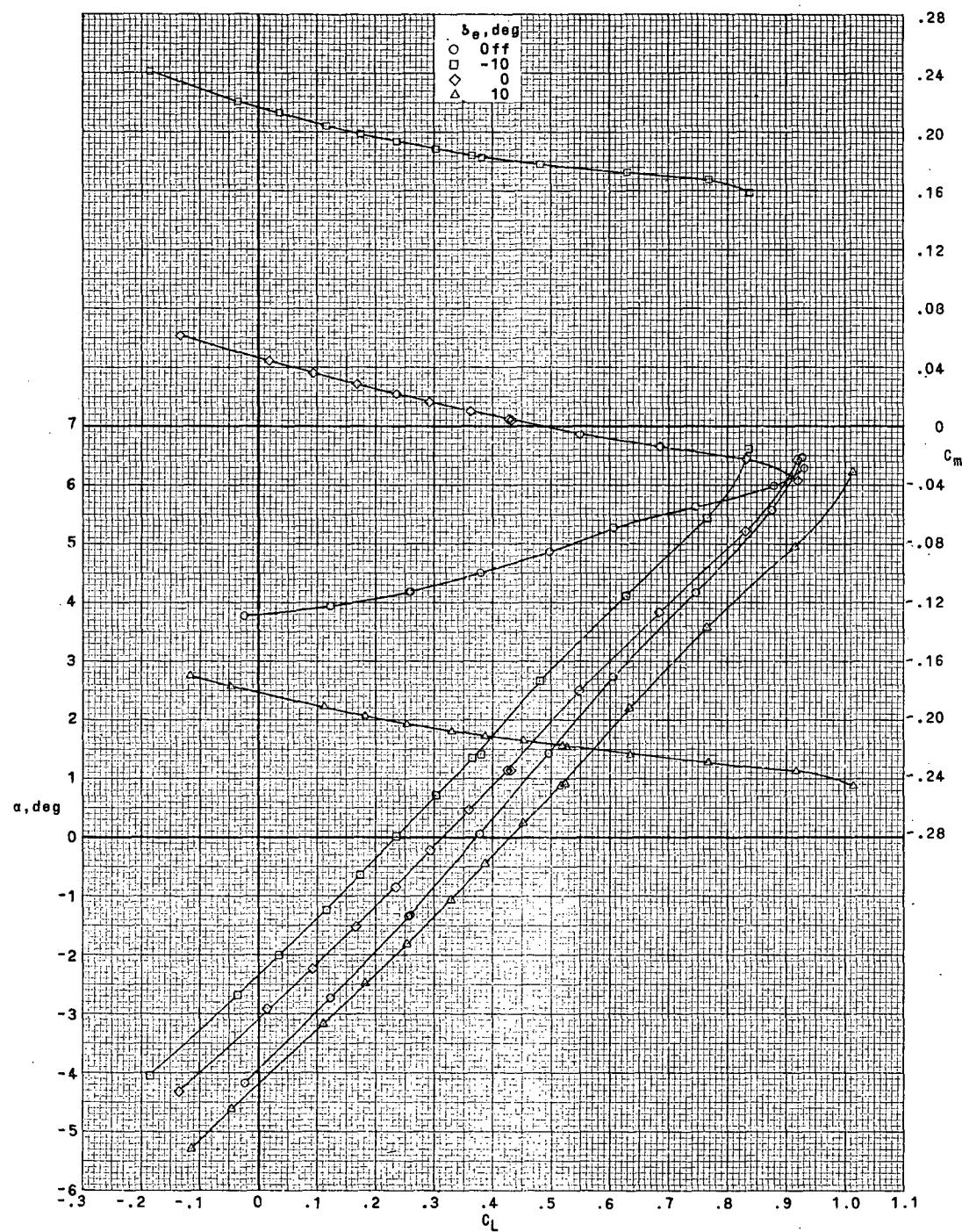
~~CONFIDENTIAL~~



(a) $M = 0.30; R_{\bar{C}} = 2.00 \times 10^6$. Concluded.

Figure 6.- Continued.

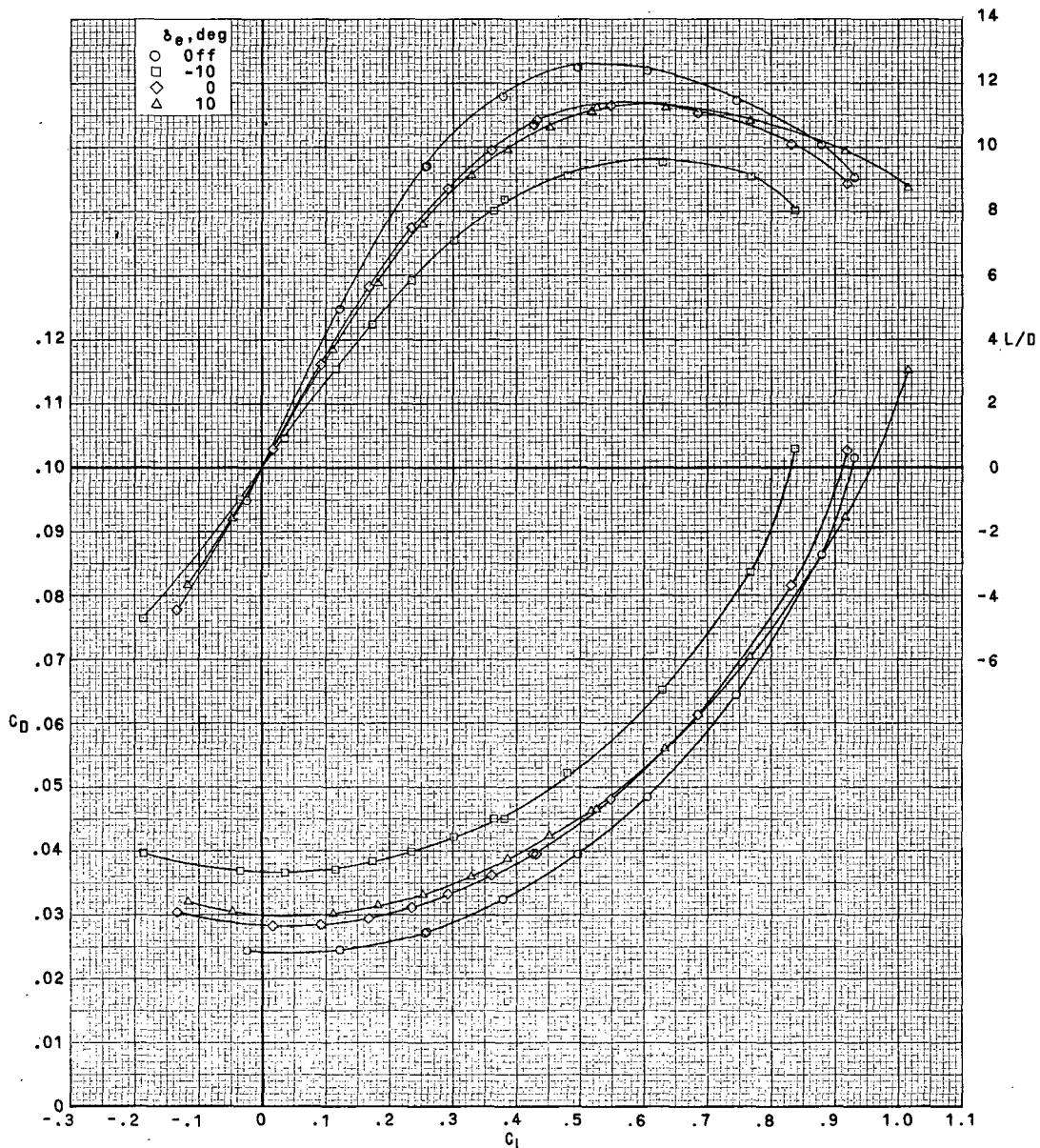
~~CONFIDENTIAL~~



(b) $M = 0.60; R_C = 3.33 \times 10^6$.

Figure 6.- Continued.

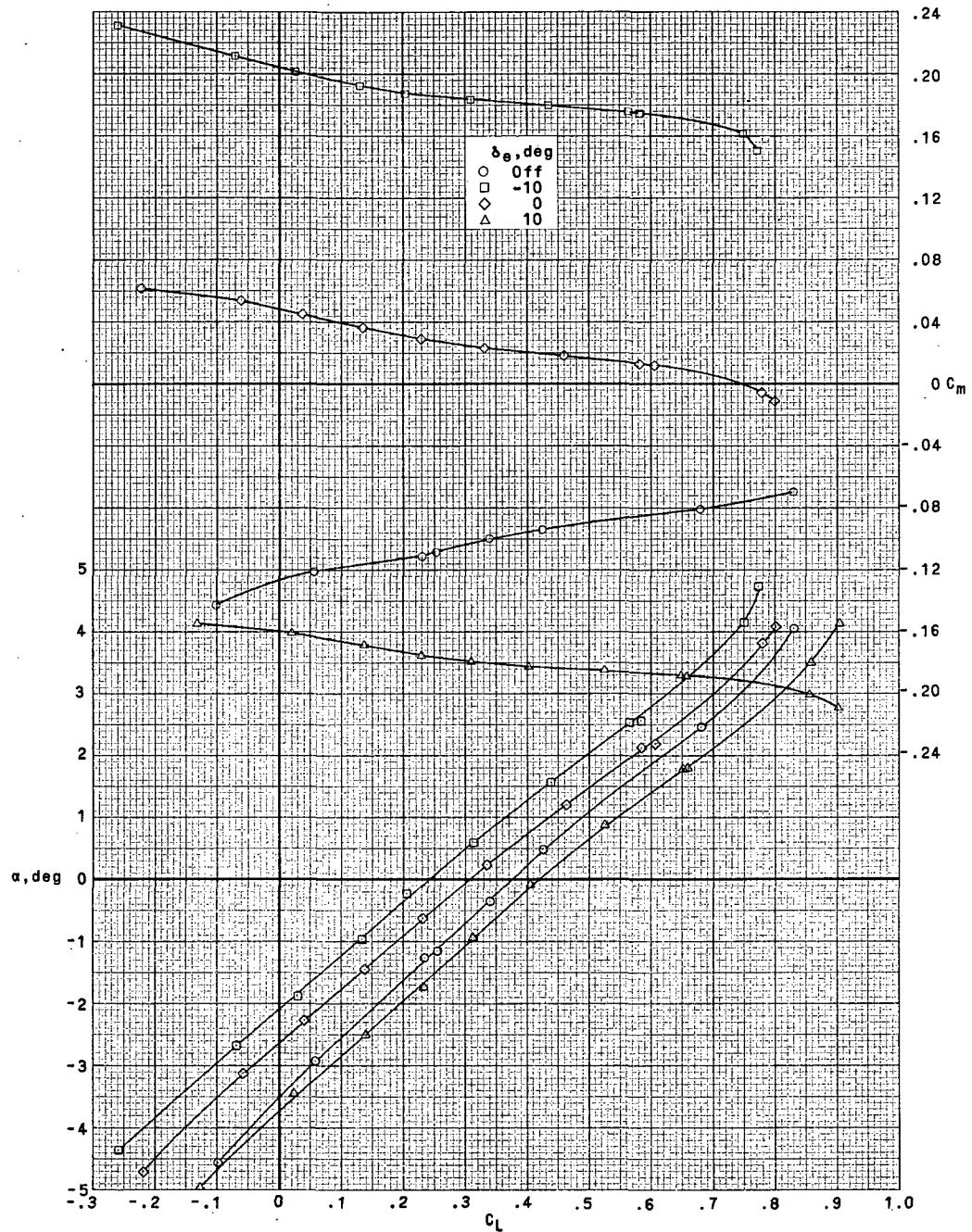
~~CONFIDENTIAL~~



(b) $M = 0.60$; $R_C = 3.33 \times 10^6$. Concluded.

Figure 6.- Continued.

~~CONFIDENTIAL~~

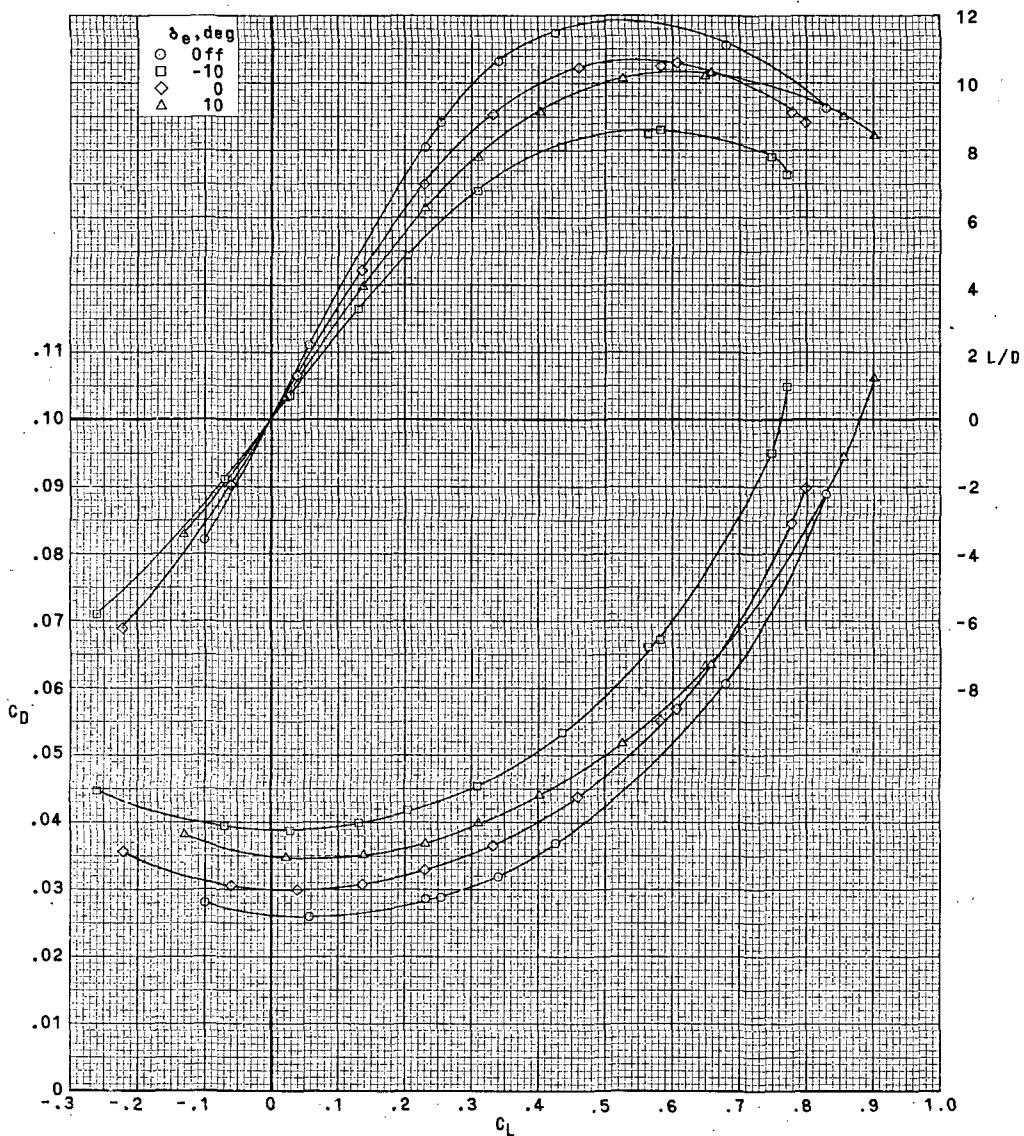


(c) $M = 0.70; R_{\bar{C}} = 3.86 \times 10^6$.

Figure 6.- Continued.

~~CONFIDENTIAL~~

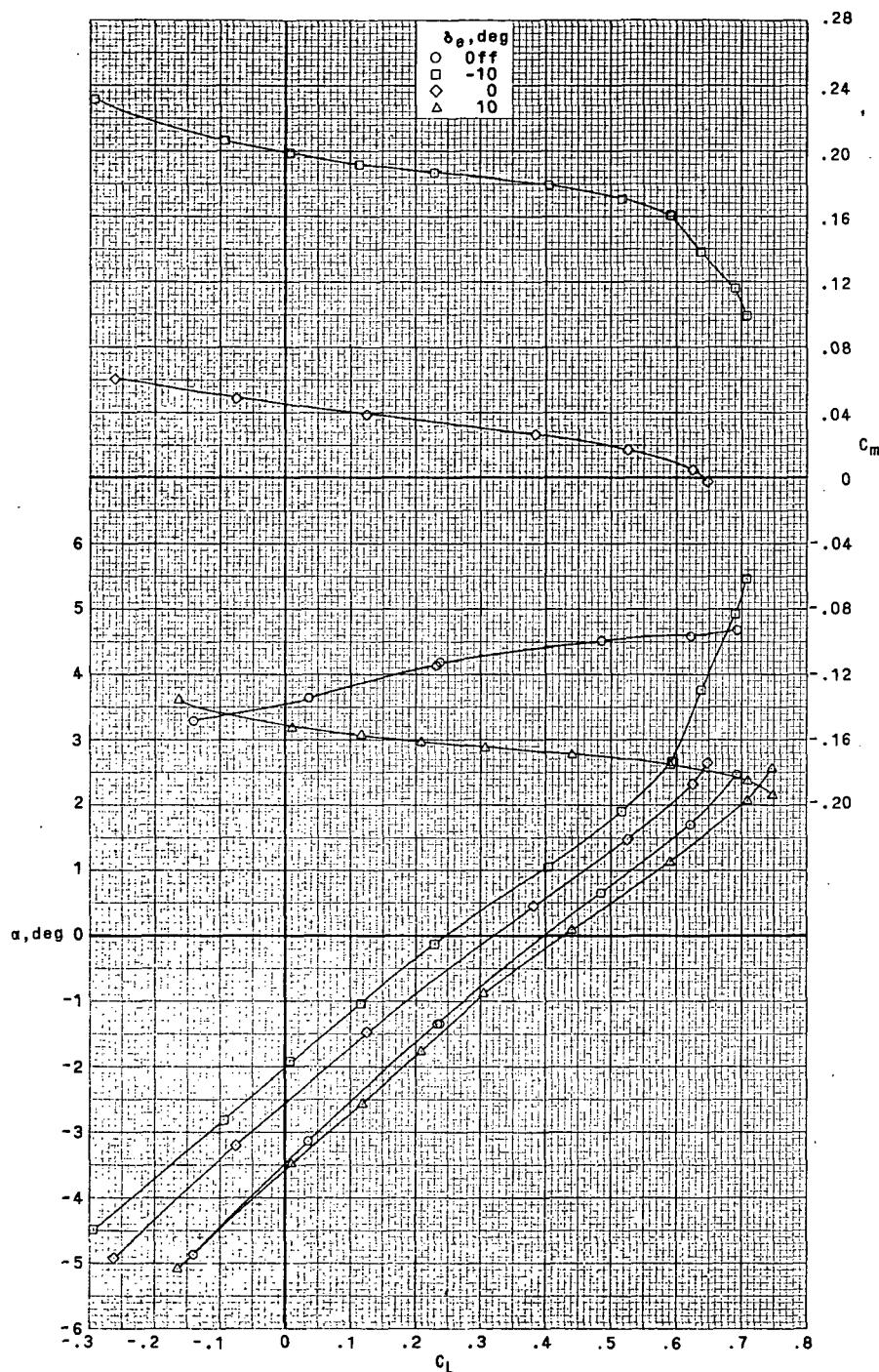
~~CONFIDENTIAL~~



(c) $M = 0.70$; $R_C = 3.86 \times 10^6$. Concluded.

Figure 6.- Continued.

~~CONFIDENTIAL~~

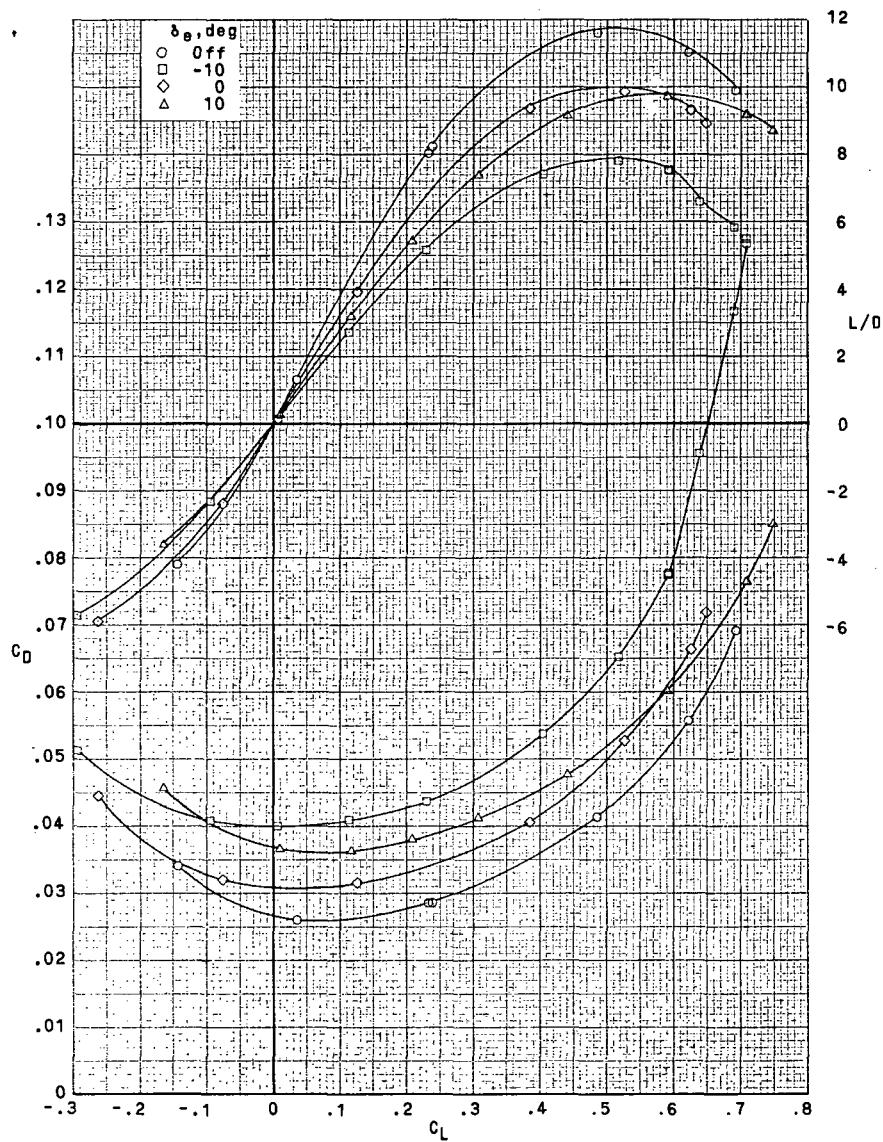


(d) $M = 0.73; R_C = 3.86 \times 10^6.$

Figure 6.- Continued.

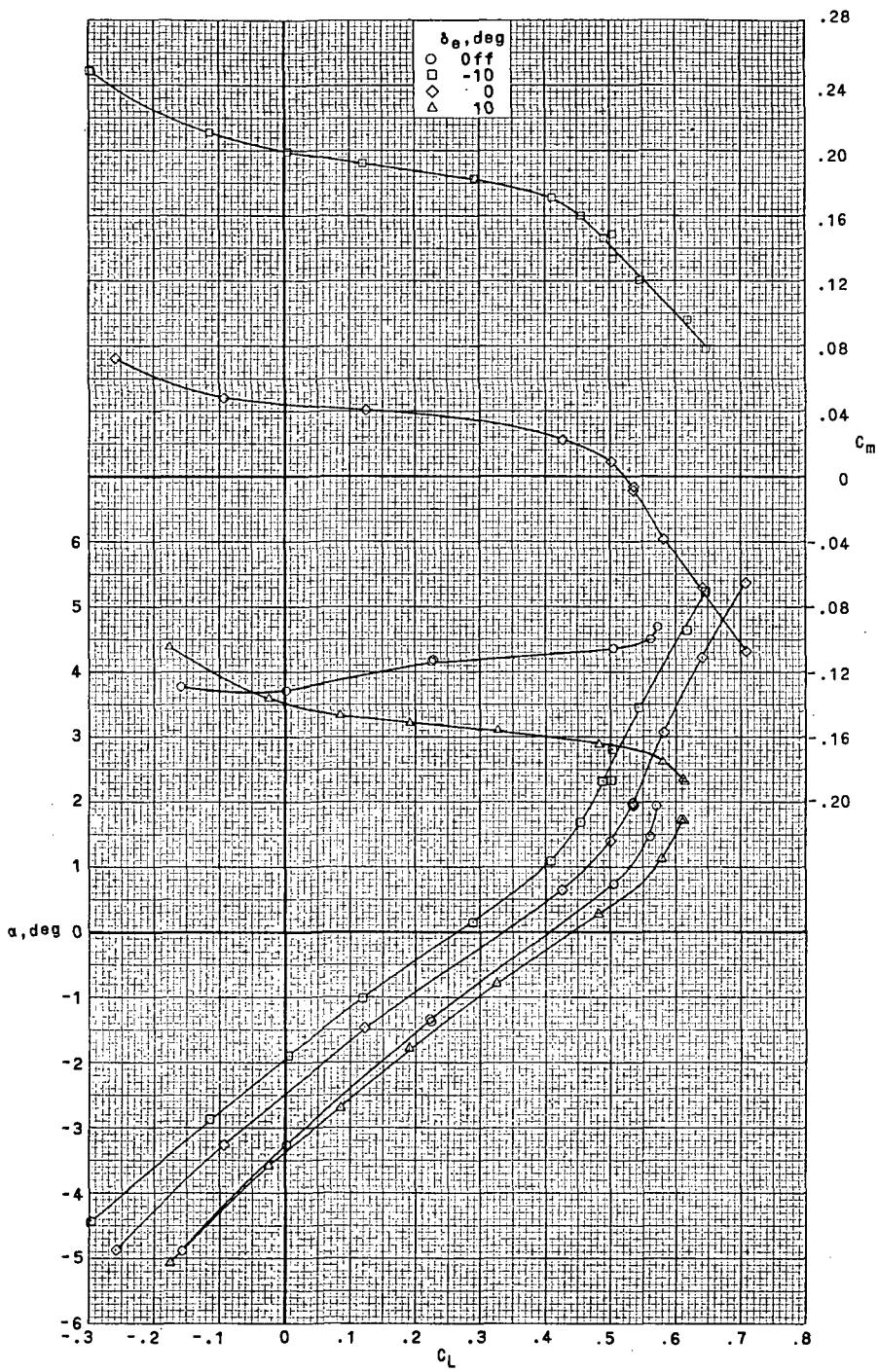
~~CONFIDENTIAL~~

~~CONFIDENTIAL~~



(d) $M = 0.73; R_{\bar{C}} = 3.86 \times 10^6$. Concluded.

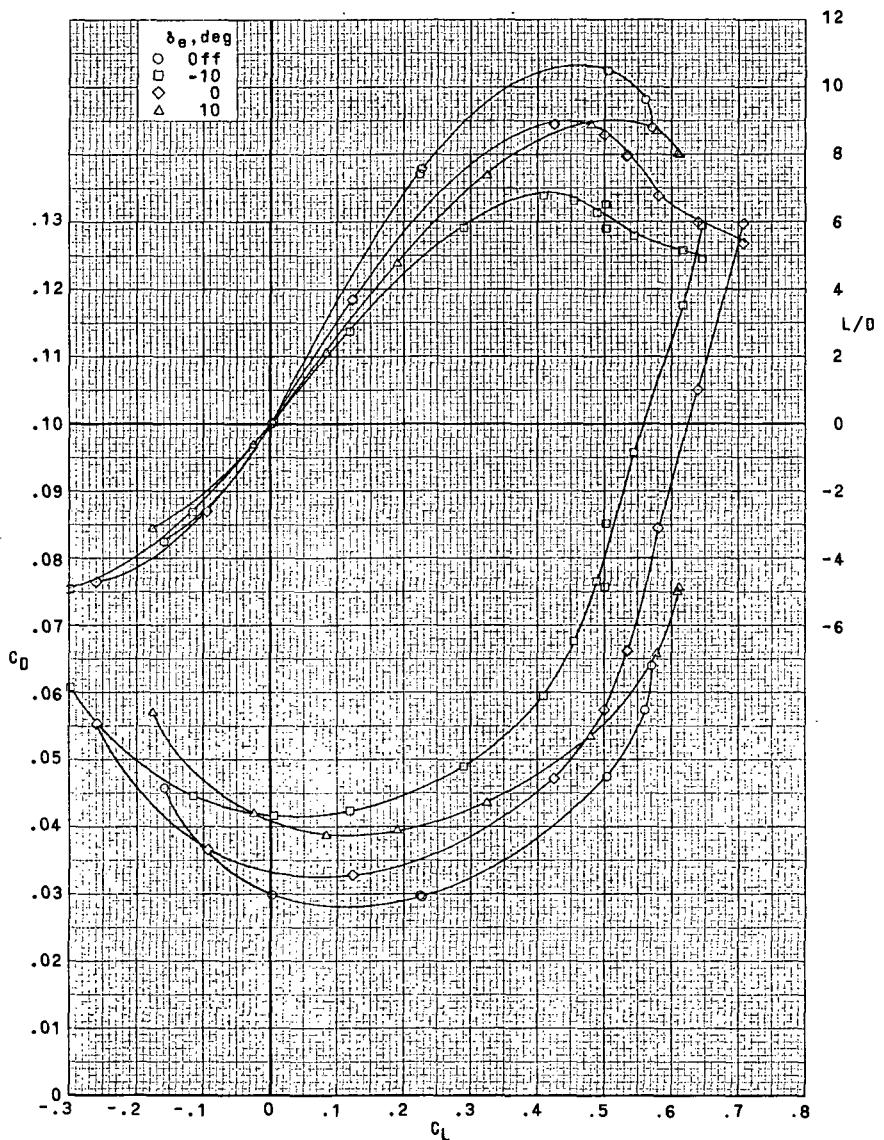
Figure 6.- Continued.



(e) $M = 0.75; R_C^- = 3.86 \times 10^6$.

Figure 6.- Continued.

~~CONFIDENTIAL~~

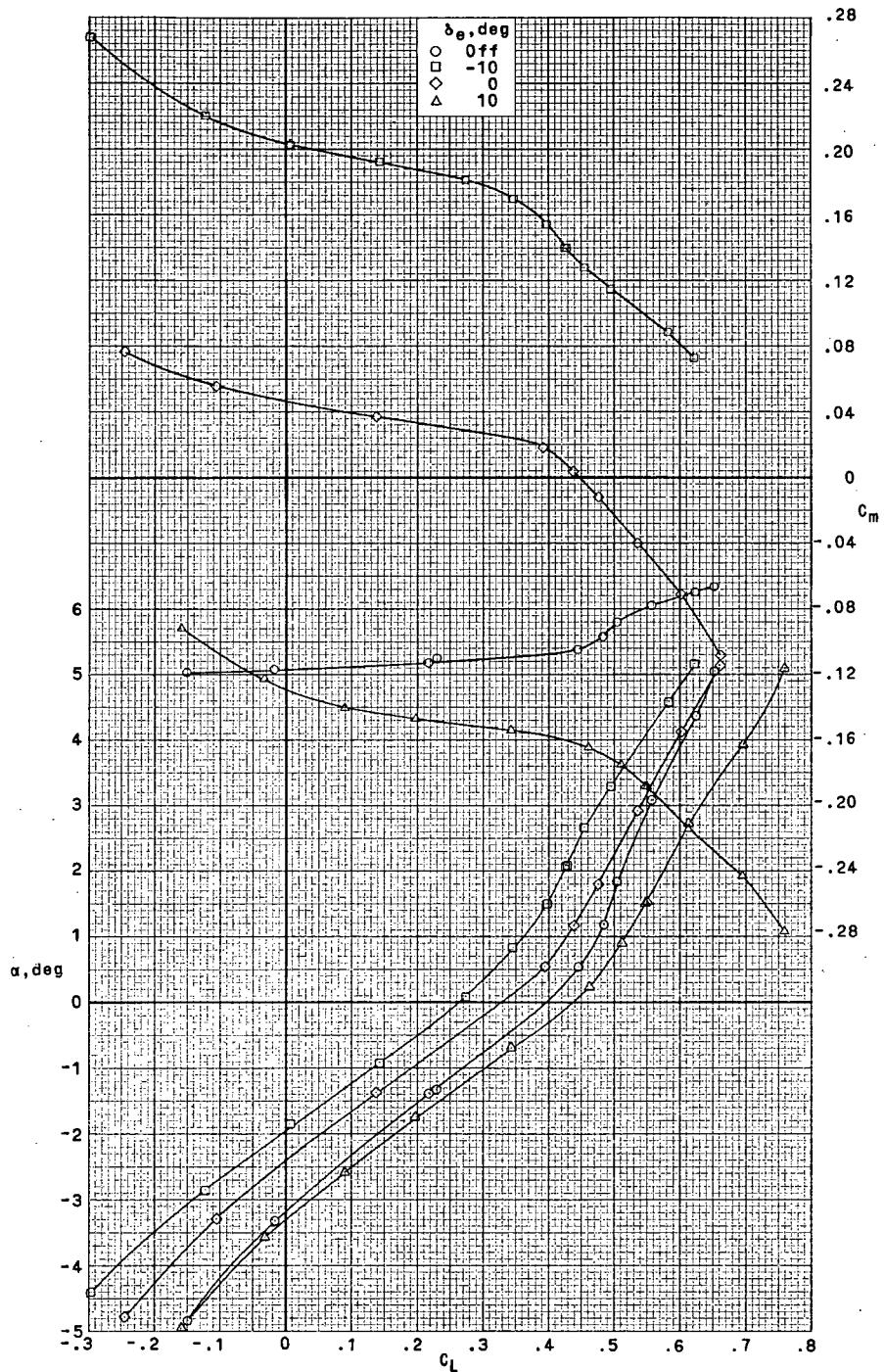


(e) $M = 0.75$; $R_{\bar{C}} = 3.86 \times 10^6$. Concluded.

Figure 6.- Continued.

~~CONFIDENTIAL~~

~~CONFIDENTIAL~~

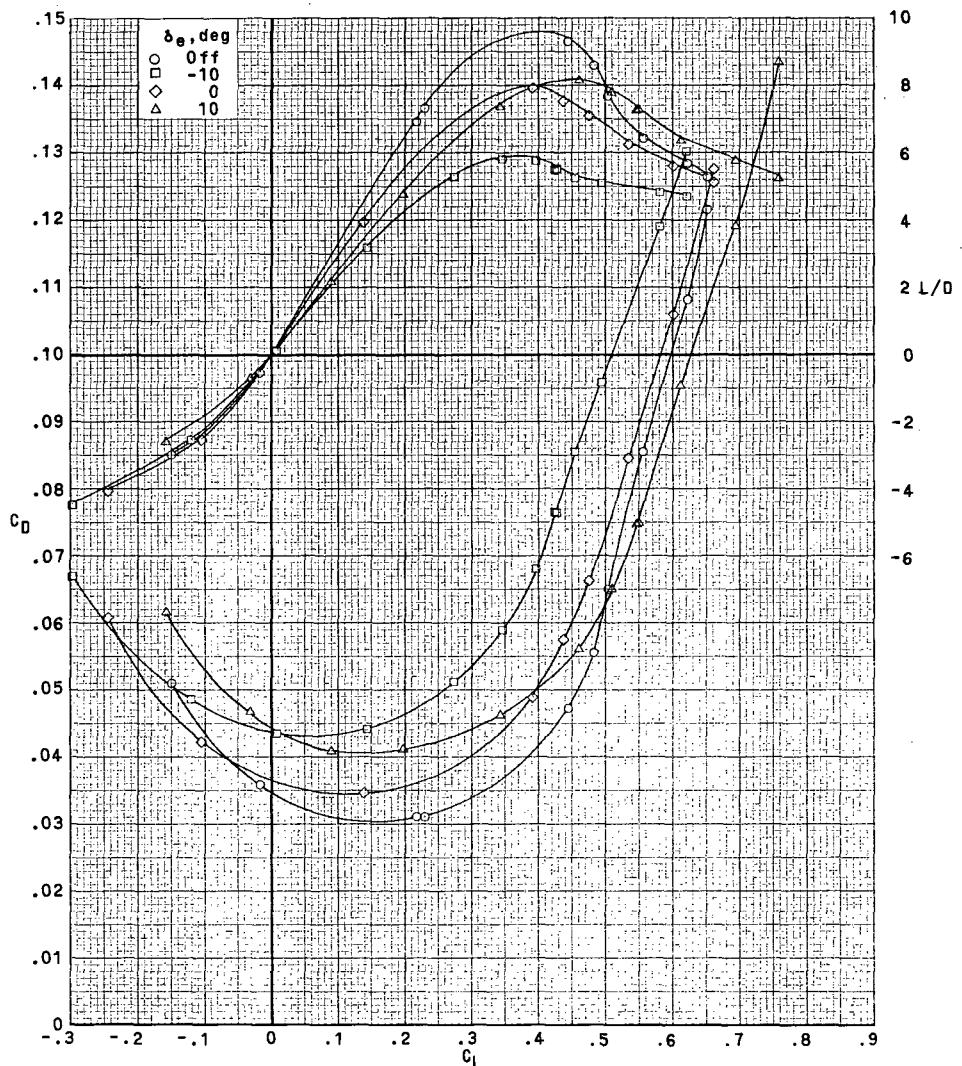


(f) $M = 0.76; R_{\bar{C}} = 3.86 \times 10^6$.

Figure 6.- Continued.

~~CONFIDENTIAL~~

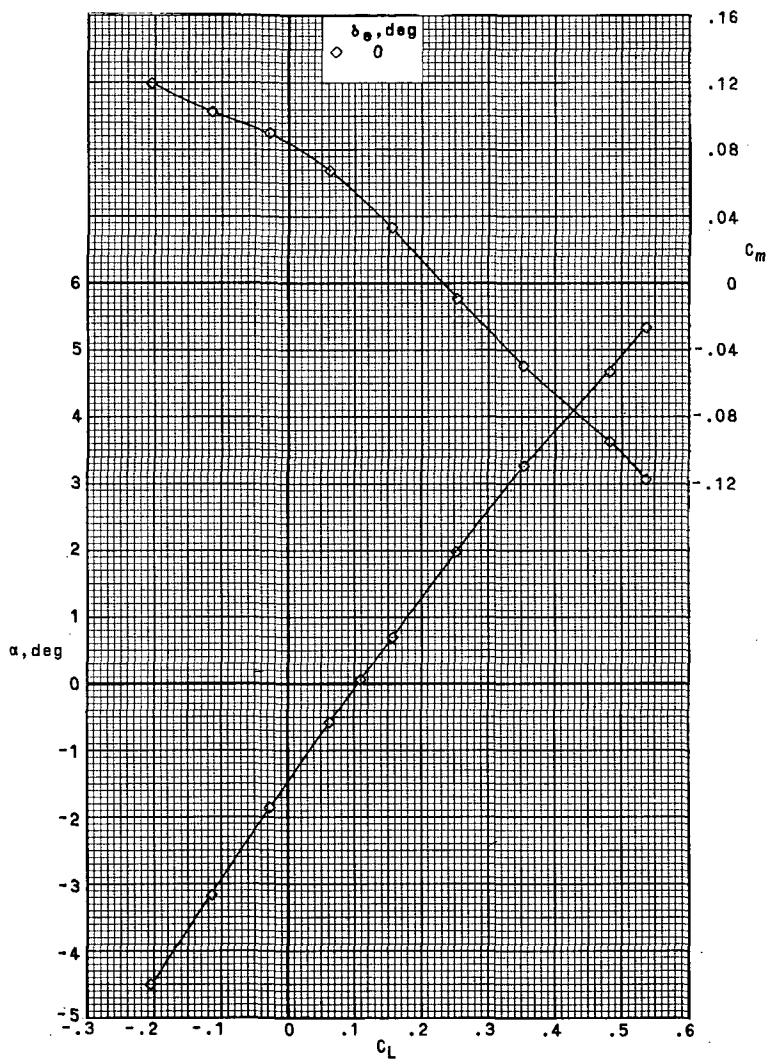
~~CONFIDENTIAL~~



(f) $M = 0.76; R_C = 3.86 \times 10^6$. Concluded.

Figure 6.- Continued.

~~CONFIDENTIAL~~

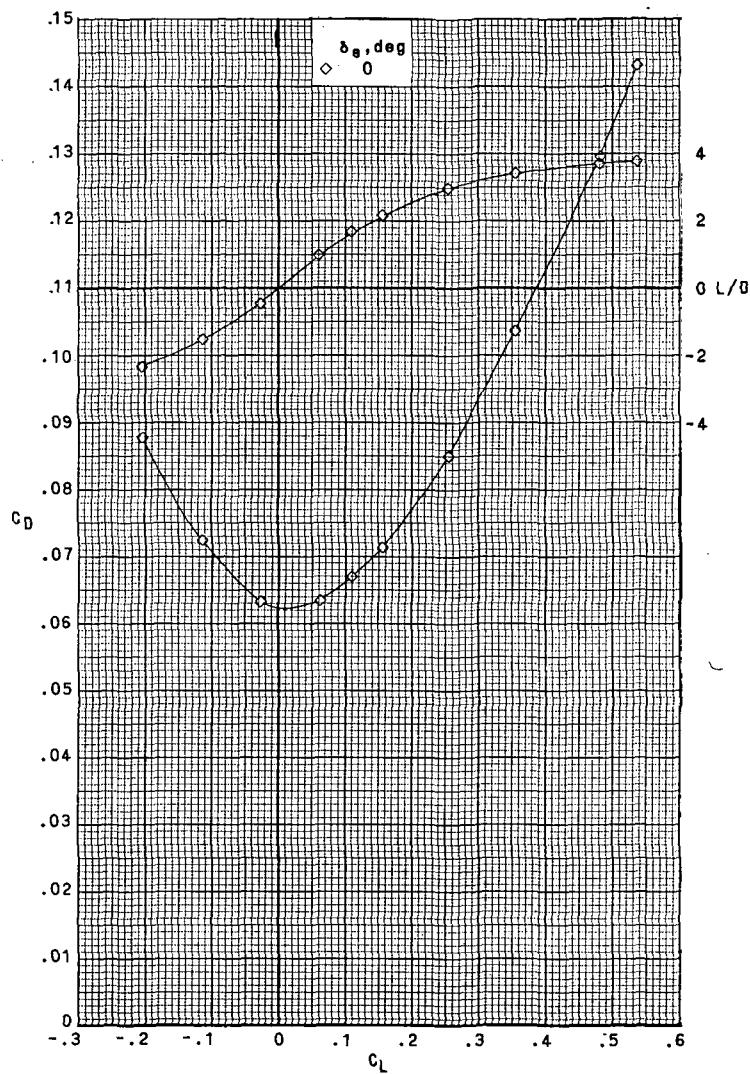


(g) $M = 0.80$; $R_C = 3.86 \times 10^6$.

Figure 6.- Continued.

~~CONFIDENTIAL~~

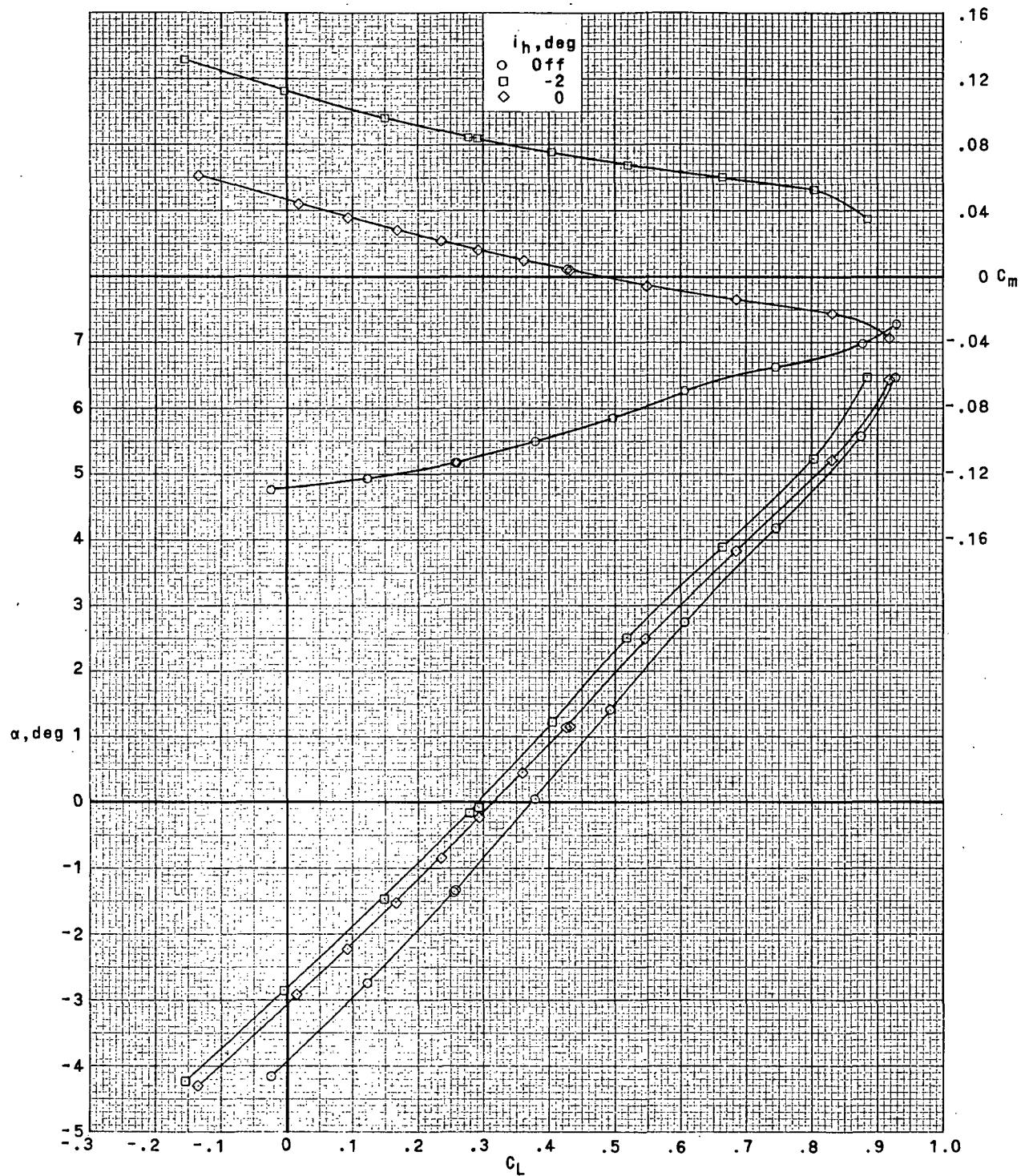
~~CONFIDENTIAL~~



(g) $M = 0.80$; $R_C = 3.86 \times 10^6$. Concluded.

Figure 6.- Concluded.

~~CONFIDENTIAL~~



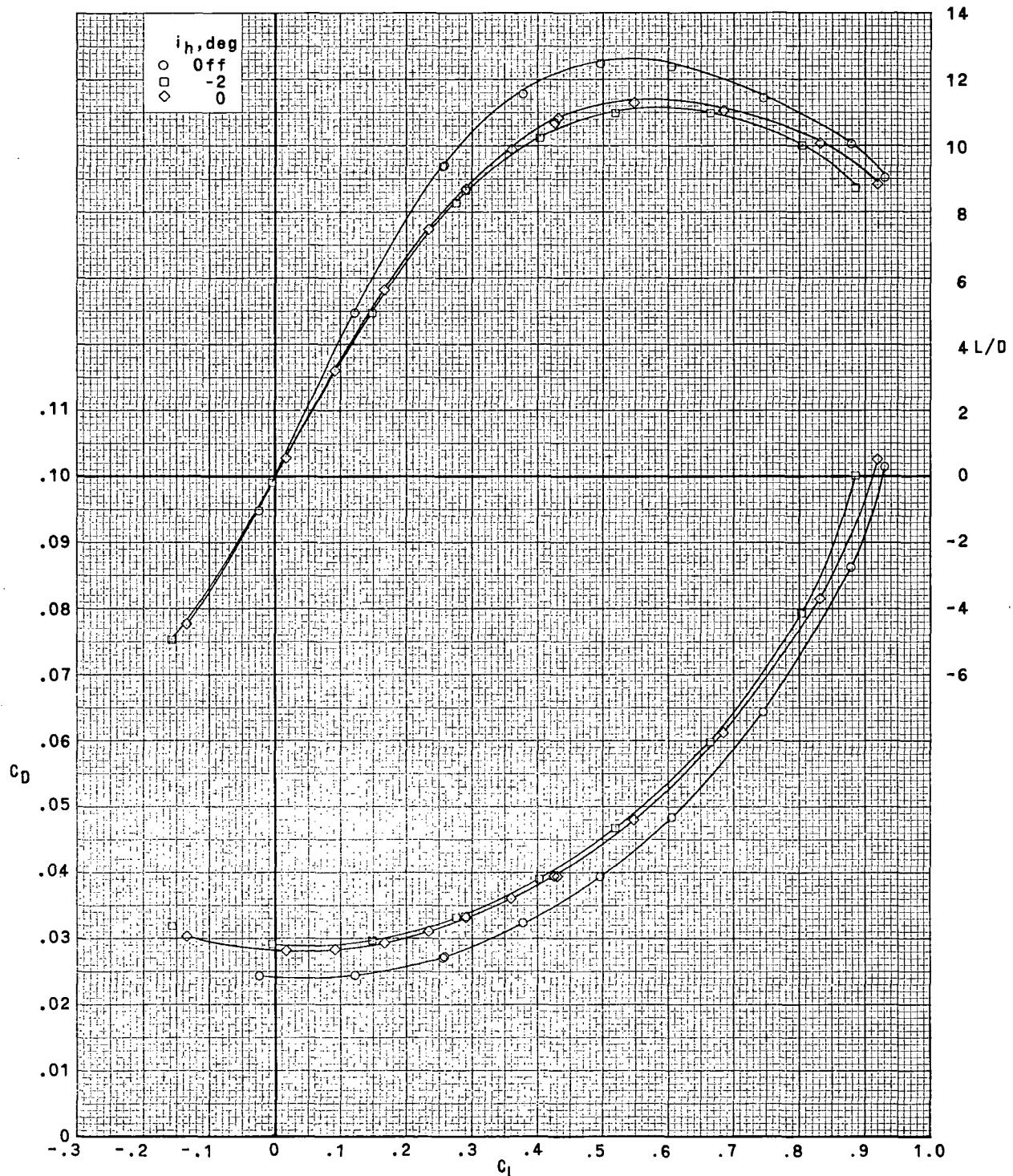
(a) $M = 0.60; R_{\bar{C}} = 3.33 \times 10^6$.

Figure 7.- Effect of horizontal-tail incidence on longitudinal aerodynamic characteristics.

$$\delta_e = 0^\circ; \delta_a = 0^\circ; \beta = 0^\circ.$$

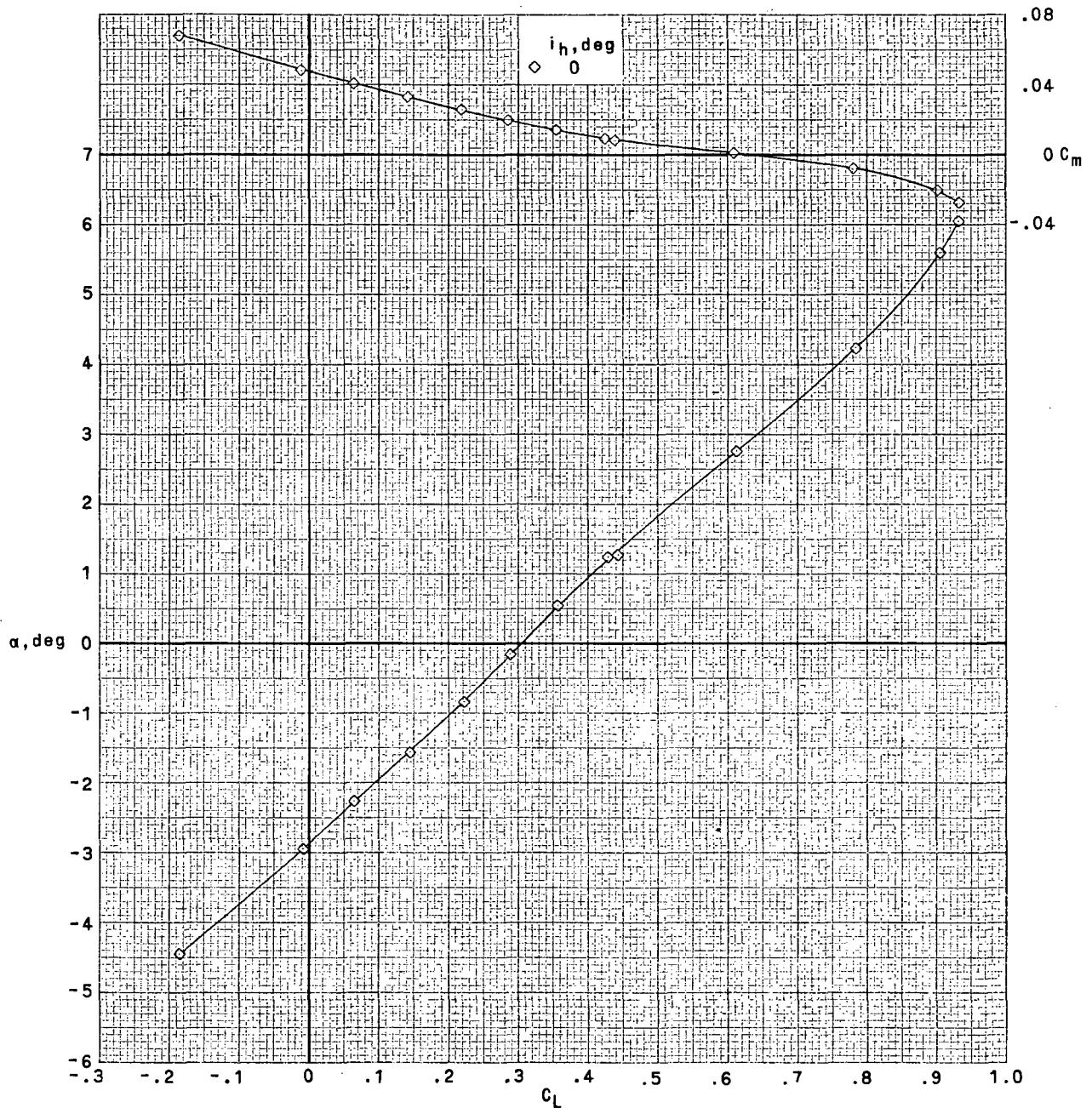
~~CONFIDENTIAL~~

~~CONFIDENTIAL~~



(a) $M = 0.60$; $R_C = 3.33 \times 10^6$. Concluded.

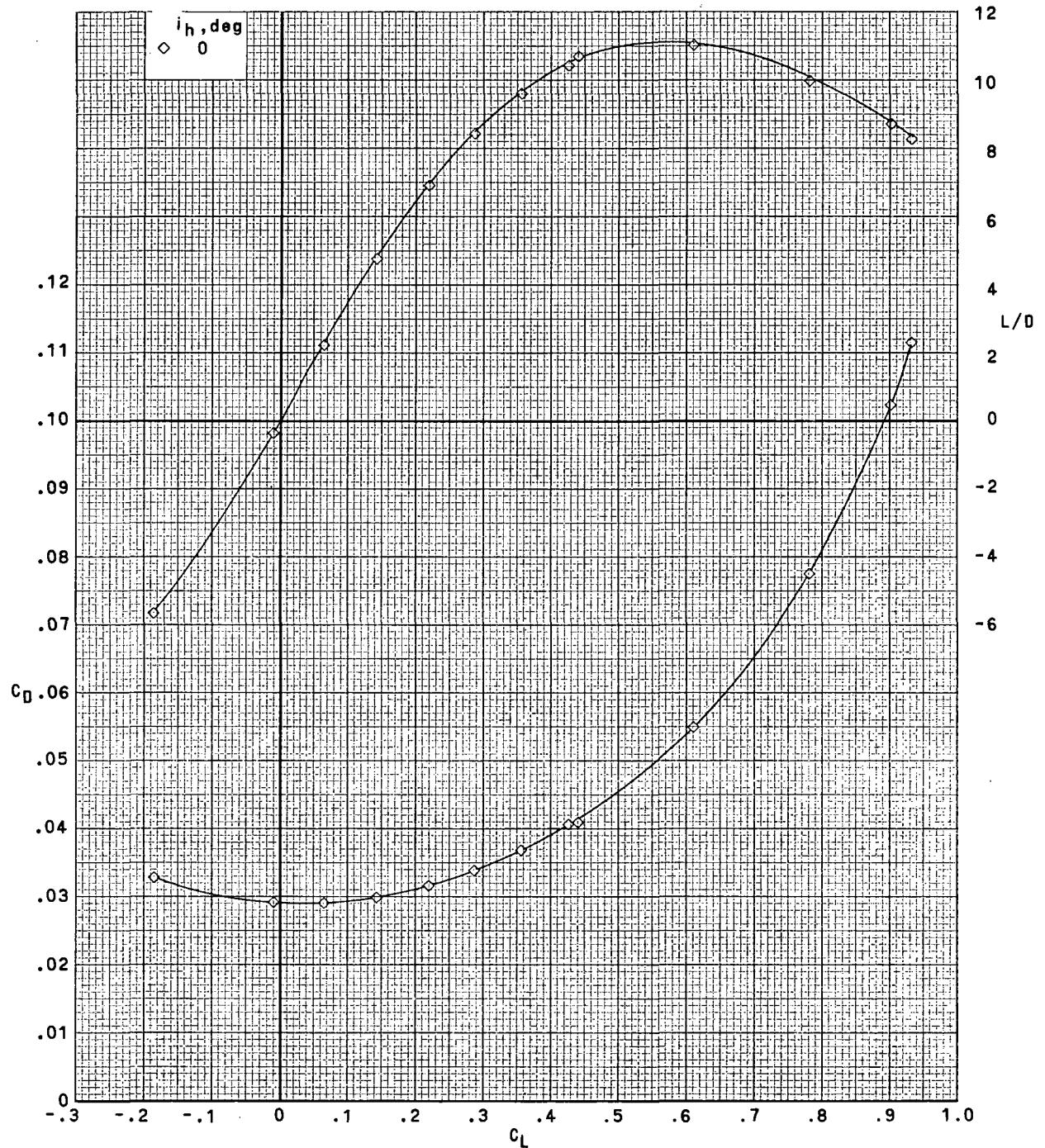
Figure 7.- Continued.



(b) $M = 0.65; R_{\bar{C}} = 3.33 \times 10^6$.

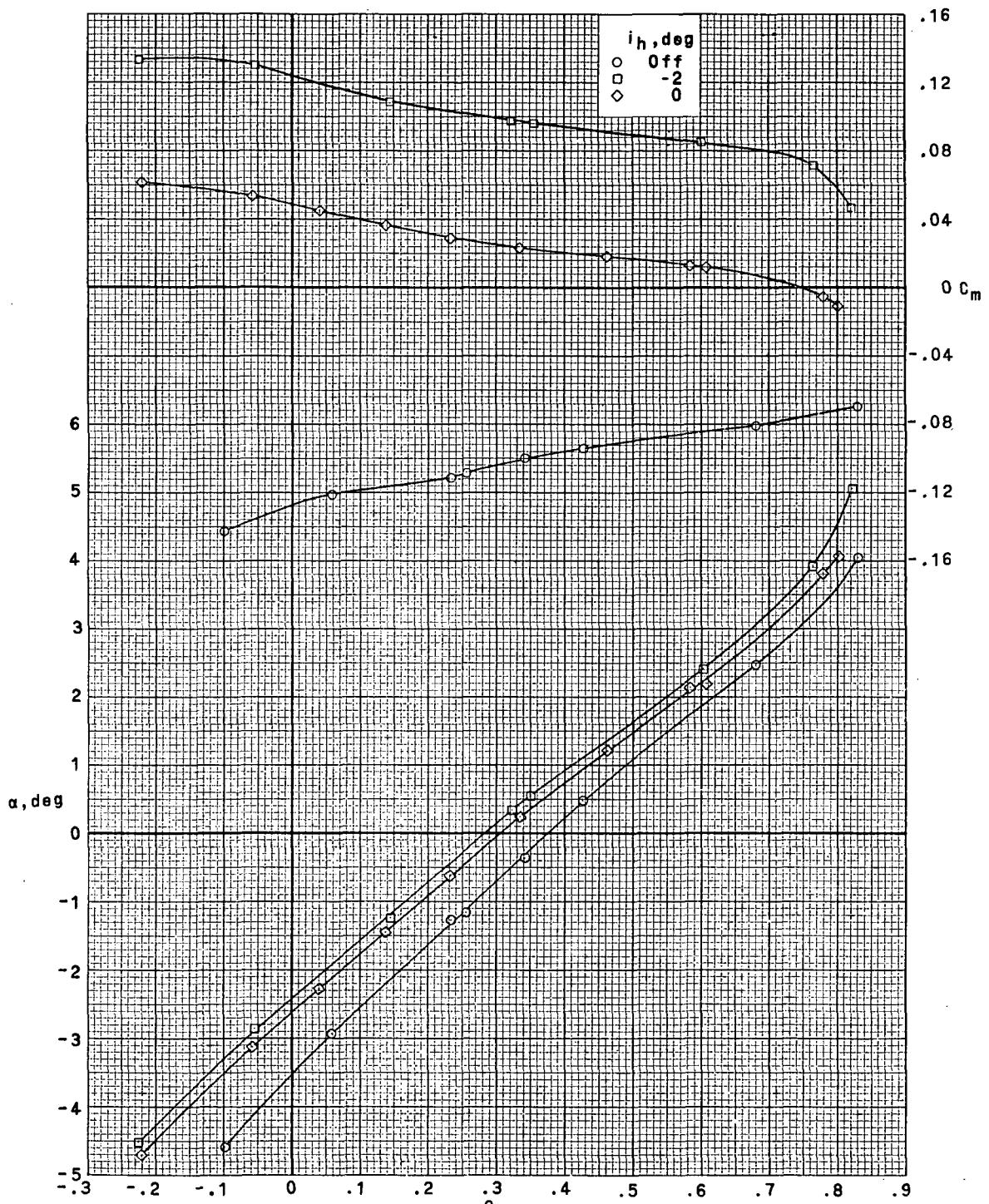
Figure 7.- Continued.

~~CONFIDENTIAL~~



(b) $M = 0.65; R_{\bar{C}} = 3.33 \times 10^6$. Concluded.

Figure 7.- Continued.

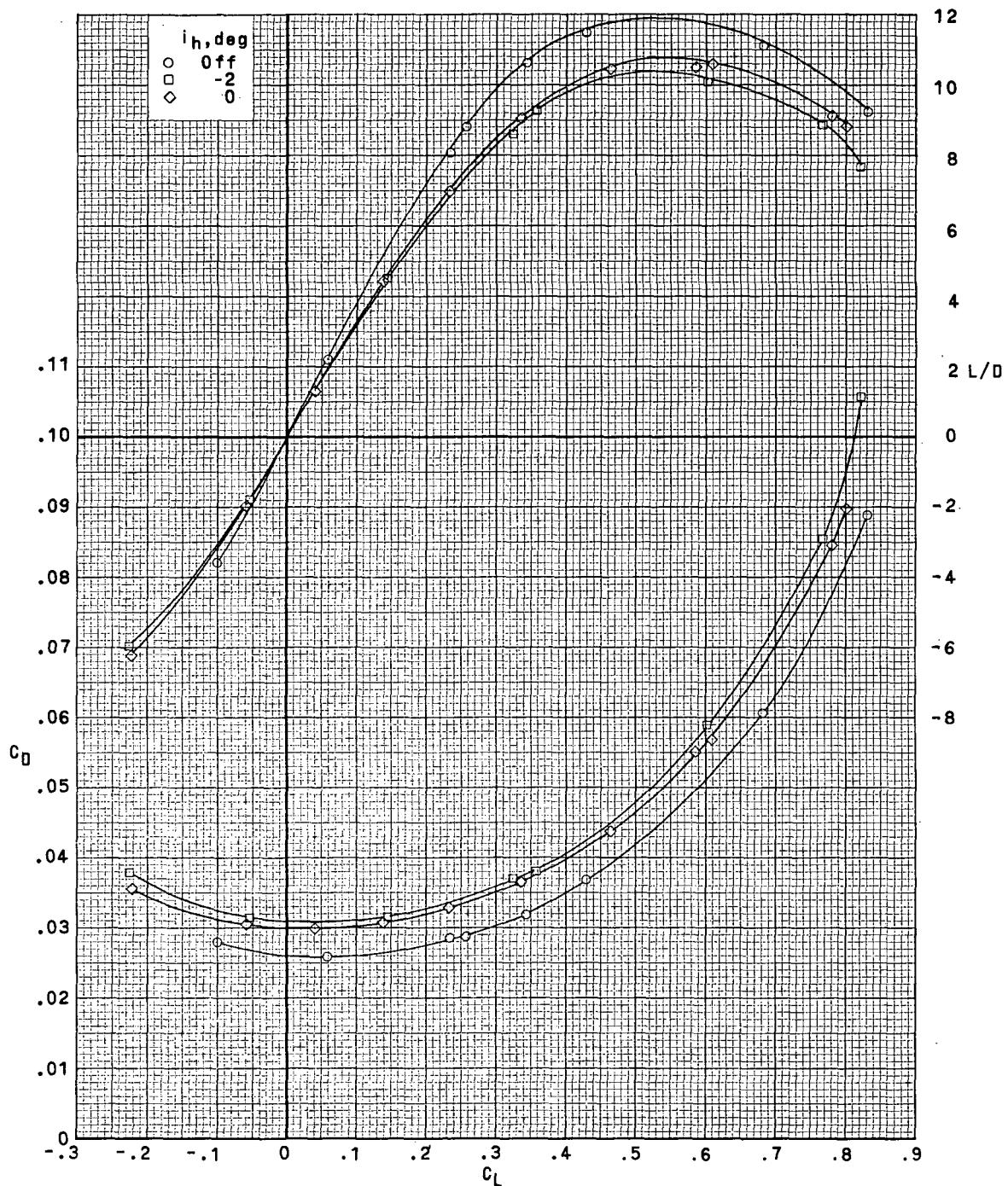


(c) $M = 0.70; R_{\bar{C}} = 3.86 \times 10^6$.

Figure 7.- Continued.

CONFIDENTIAL

~~CONFIDENTIAL~~

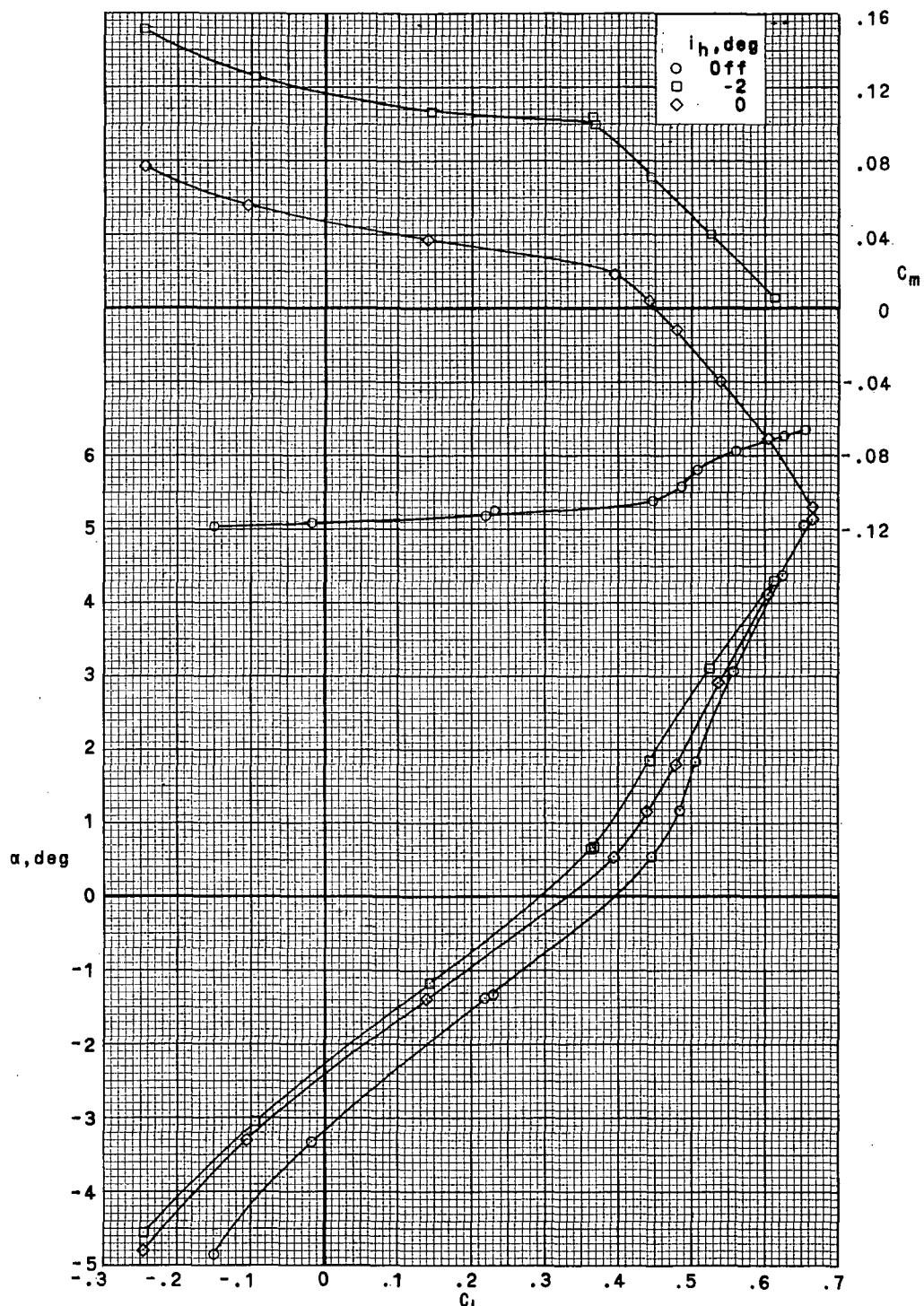


(c) $M = 0.70; R_{\bar{C}} = 3.86 \times 10^6$. Concluded.

Figure 7.- Continued.

~~CONFIDENTIAL~~

~~CONFIDENTIAL~~

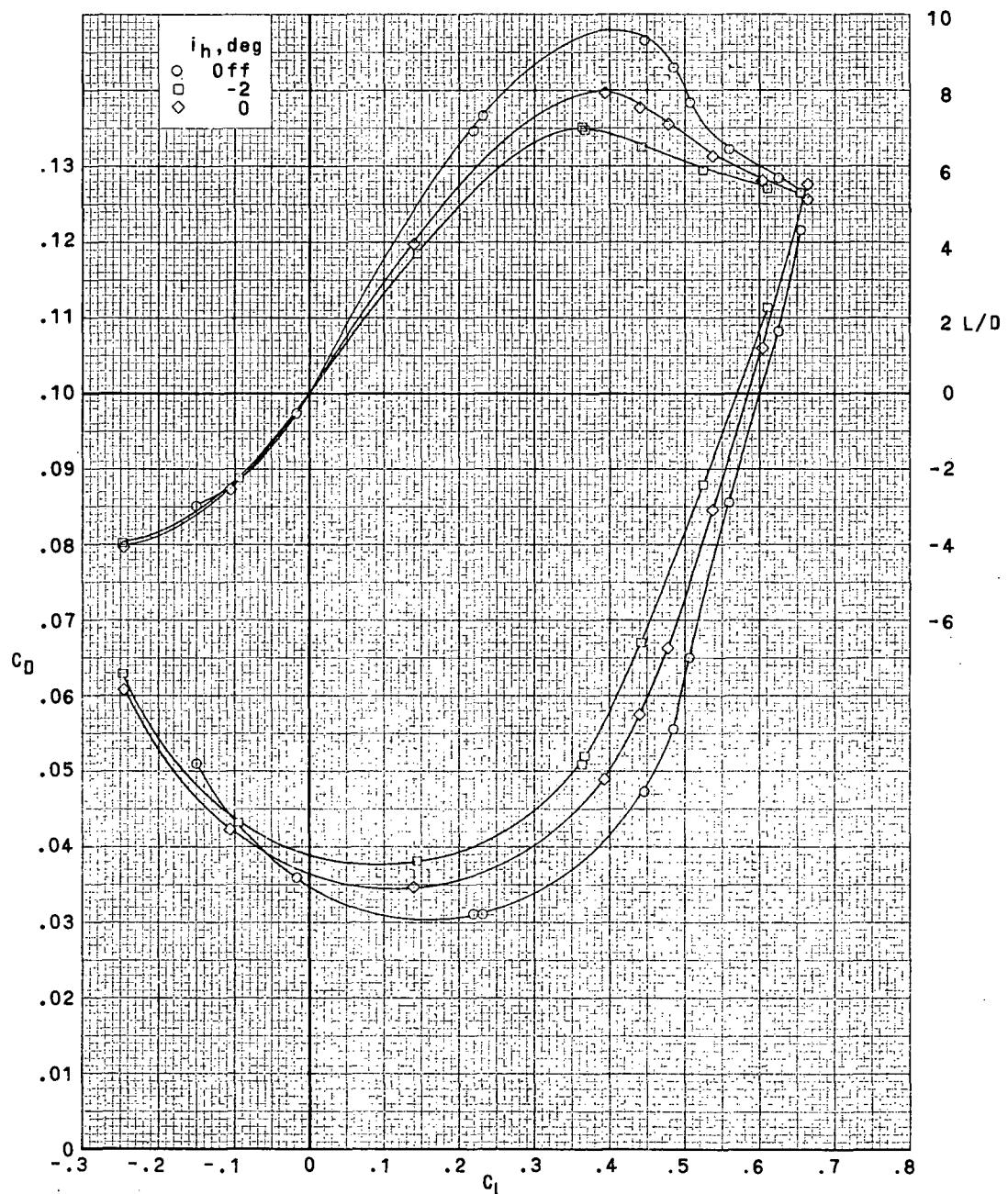


(d) $M = 0.76; R_C = 3.86 \times 10^6$.

Figure 7.- Continued.

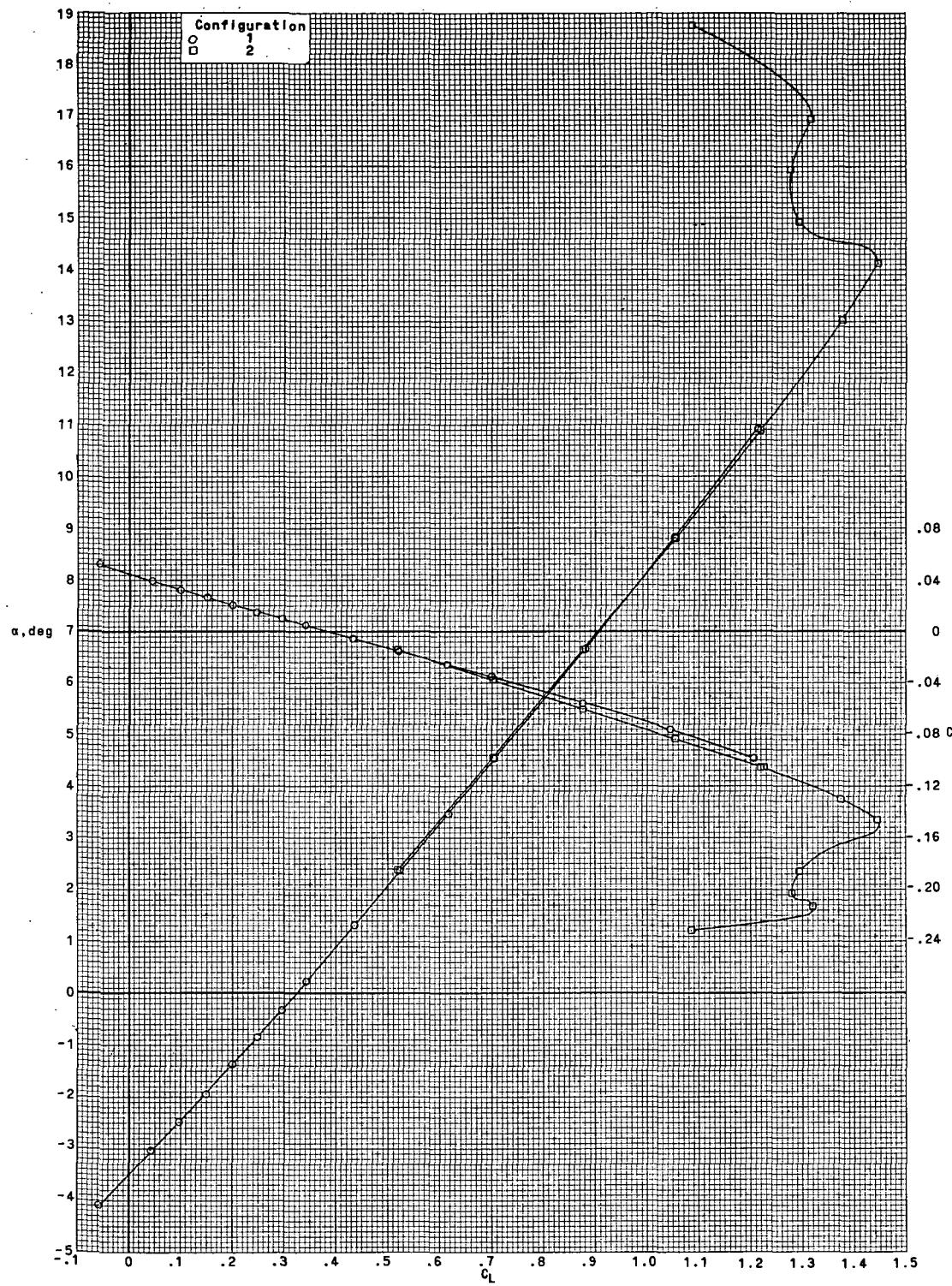
~~CONFIDENTIAL~~

~~CONFIDENTIAL~~



(d) $M = 0.76$; $R_C = 3.86 \times 10^6$. Concluded.

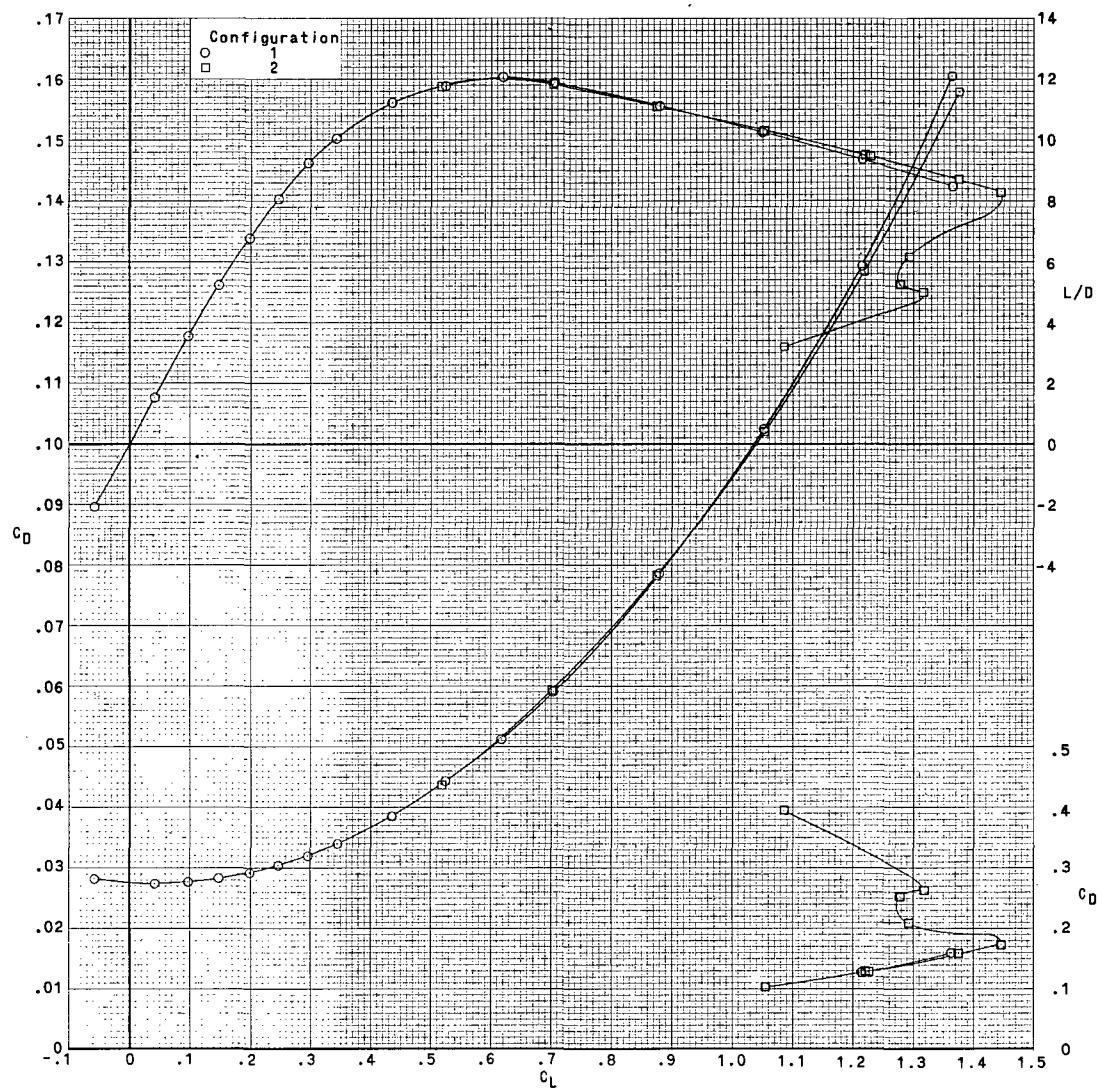
Figure 7.- Concluded.



(a) $M = 0.30; R_{\bar{C}} = 2.00 \times 10^6$.

Figure 8.- Effect of wing trailing-edge modification on longitudinal aerodynamic characteristics. $\delta_e = 0^\circ$; $i_h = 0^\circ$; $\delta_a = 0^\circ$; $\beta = 0^\circ$.

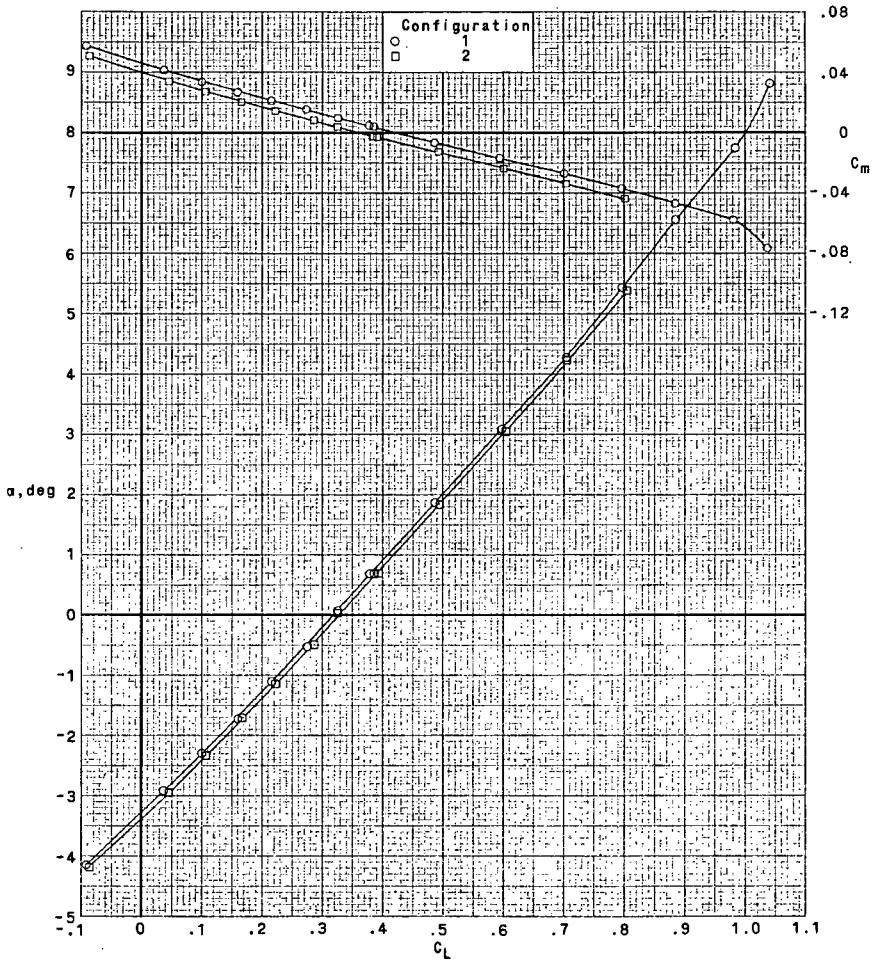
~~CONFIDENTIAL~~



(a) $M = 0.30$; $R_{\bar{C}} = 2.00 \times 10^6$. Concluded.

Figure 8.- Continued.

~~CONFIDENTIAL~~

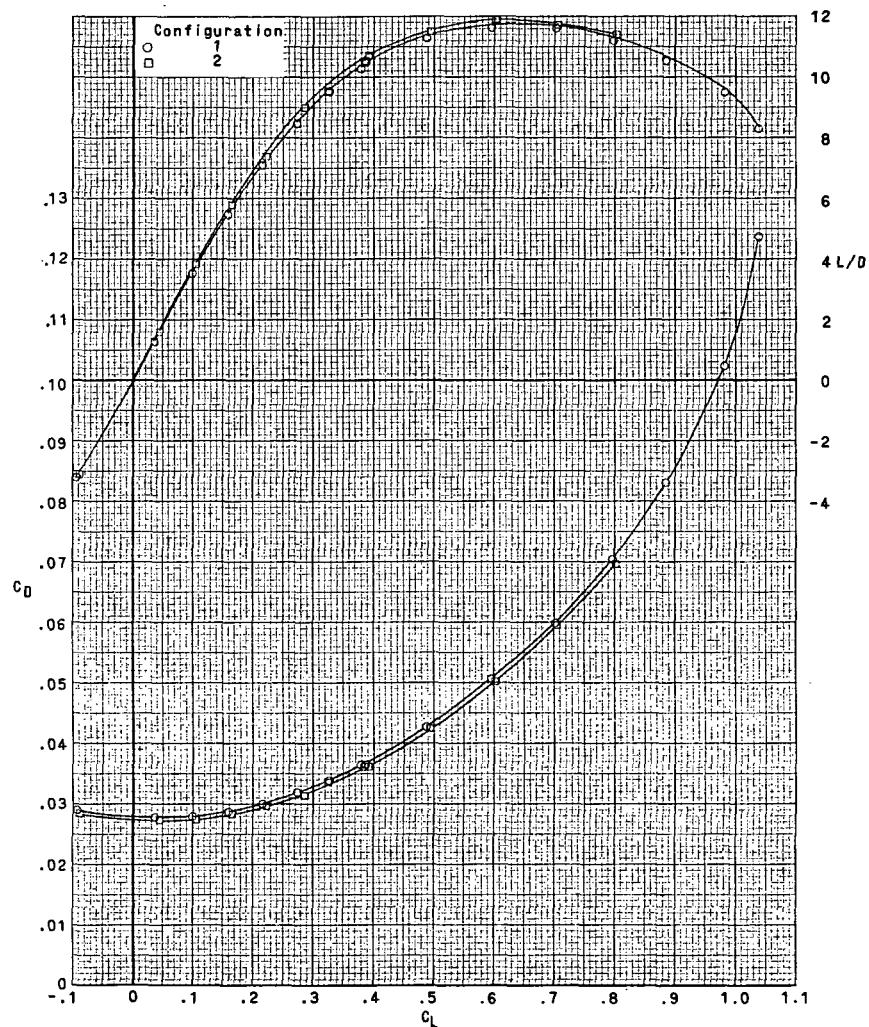


(b) $M = 0.50$; $R_C = 2.67 \times 10^6$.

Figure 8.- Continued.

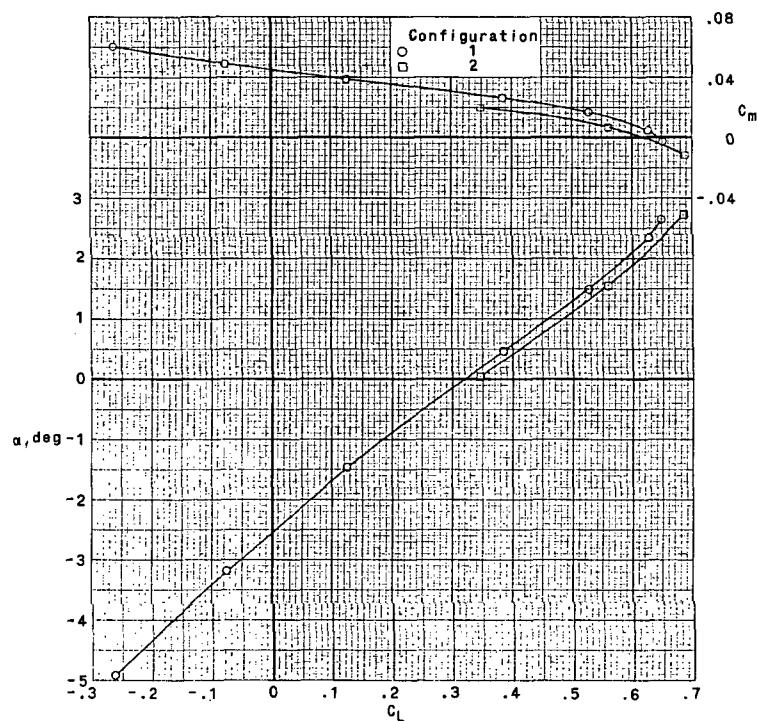
~~CONFIDENTIAL~~

~~CONFIDENTIAL~~



(b) $M = 0.50$; $R_{\bar{C}} = 2.67 \times 10^6$. Concluded.

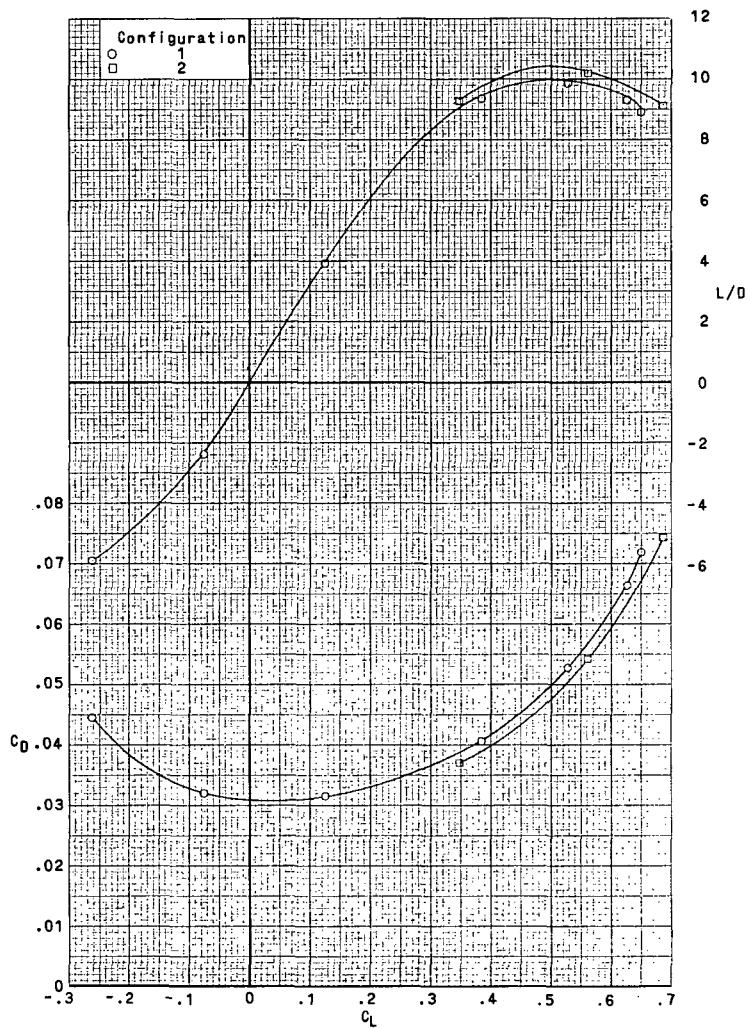
Figure 8.- Continued.



(c) $M = 0.73; R_{\bar{C}} = 3.86 \times 10^6$.

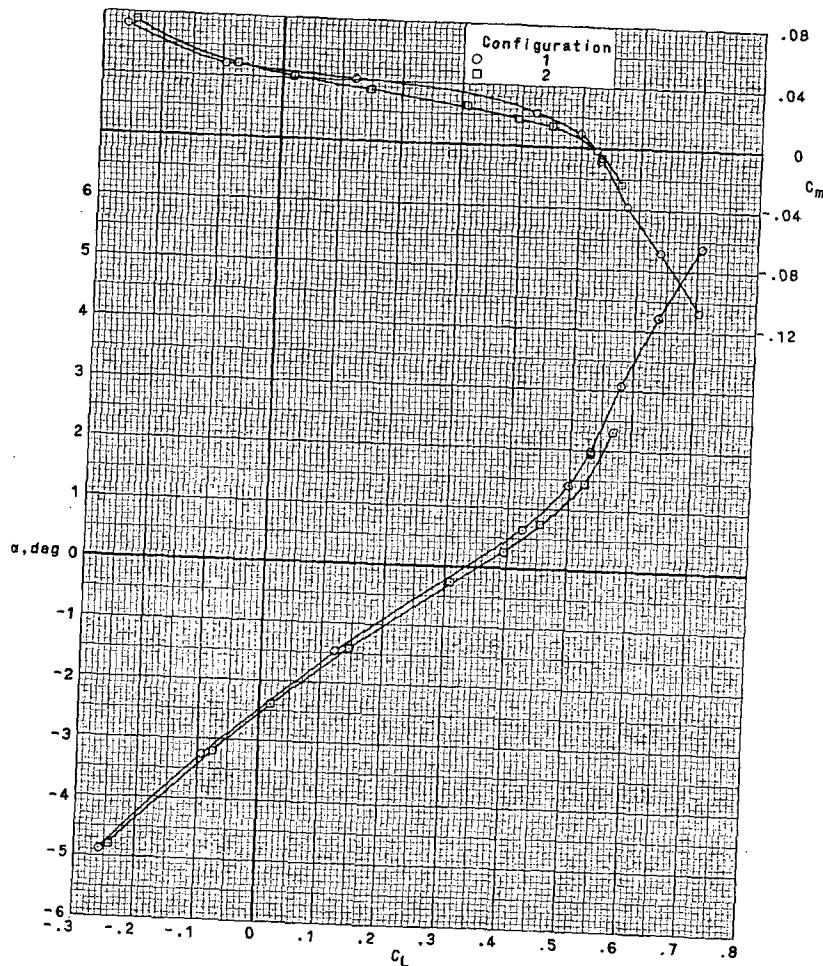
Figure 8.- Continued.

~~CONFIDENTIAL~~



(c) $M = 0.73; R_C = 3.86 \times 10^6$. Concluded.

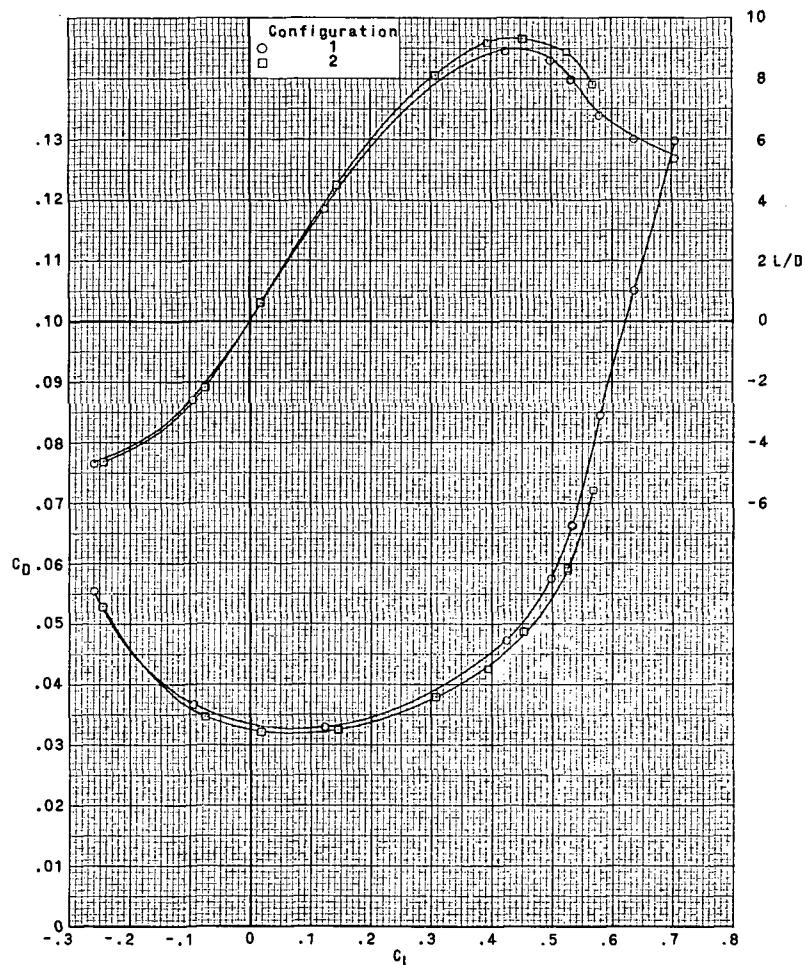
Figure 8.- Continued.



(d) $M = 0.75; R_{\bar{C}} = 3.86 \times 10^6$.

Figure 8.- Continued.

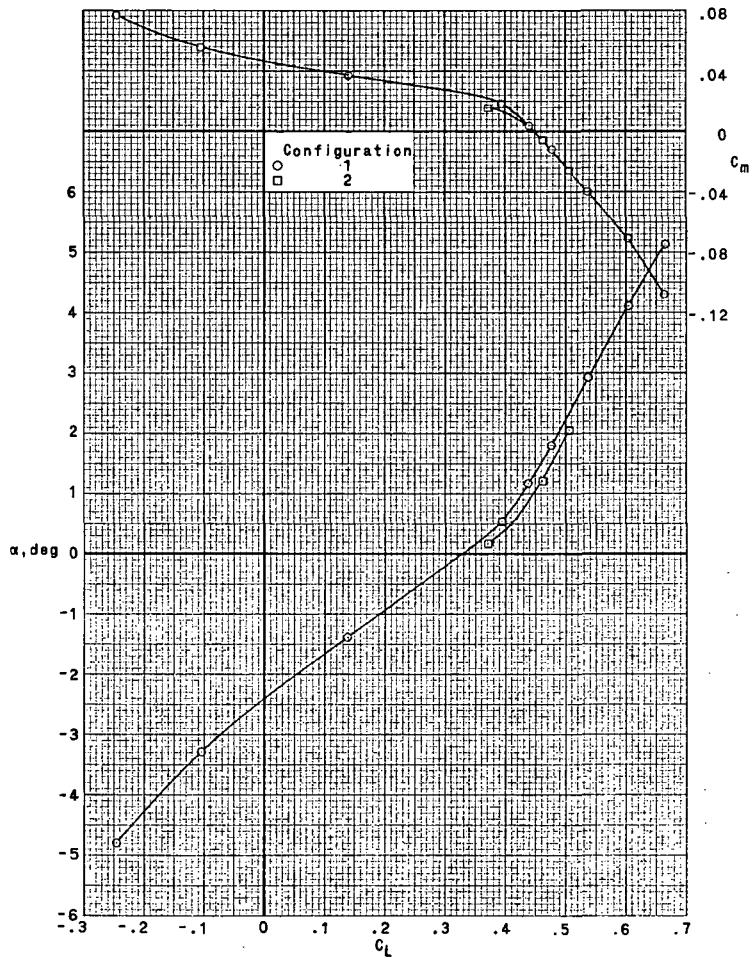
~~CONFIDENTIAL~~



(d) $M = 0.75$; $R_C = 3.86 \times 10^6$. Concluded.

Figure 8.- Continued.

~~CONFIDENTIAL~~

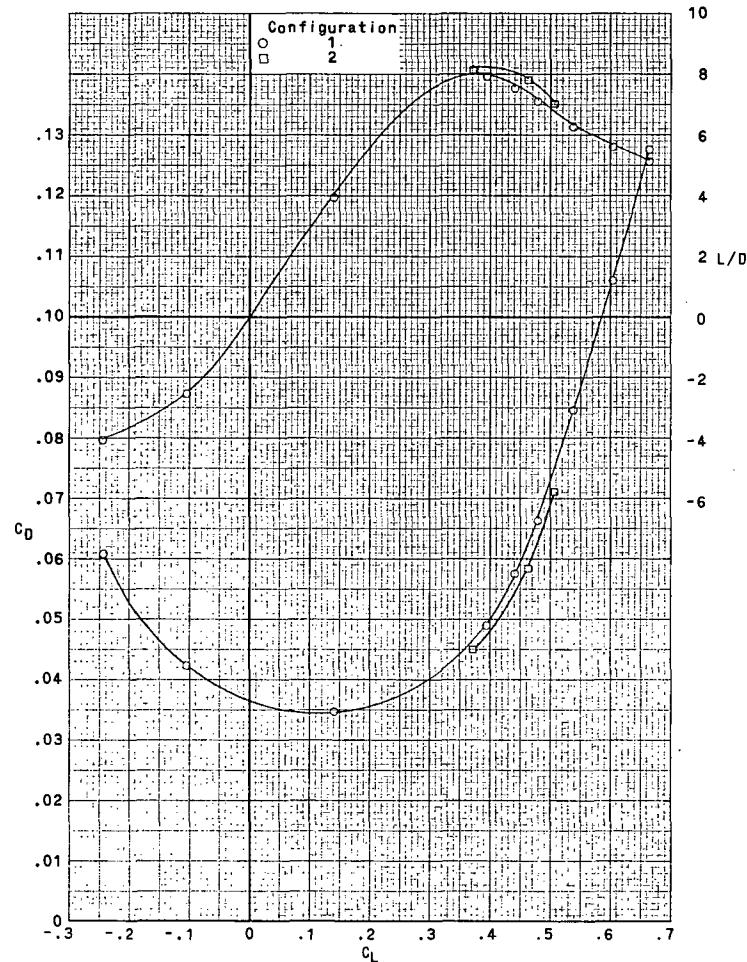


(e) $M = 0.76$; $R_C = 3.86 \times 10^6$.

Figure 8.- Continued.

~~CONFIDENTIAL~~

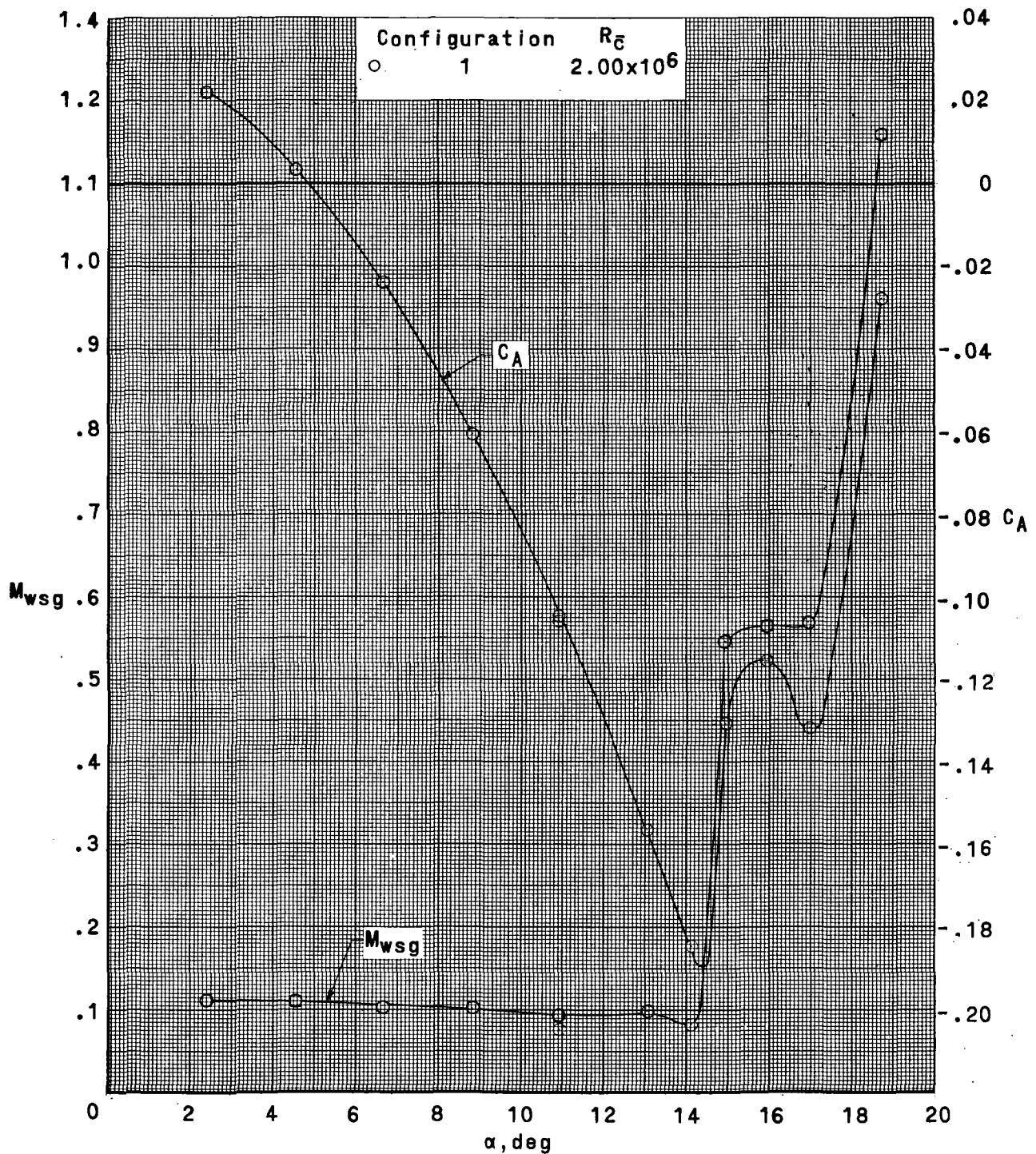
~~CONFIDENTIAL~~



(e) $M = 0.76$; $R\bar{c} = 3.86 \times 10^6$. Concluded.

Figure 8.- Concluded.

~~CONFIDENTIAL~~



(a) $M = 0.30$.

Figure 9.- Variation of axial-force coefficient and wing-root bending moment with angle of attack. $\delta_e = 0^{\circ}$; $i_h = 0^{\circ}$; $\delta_a = 0^{\circ}$; $\beta = 0^{\circ}$.

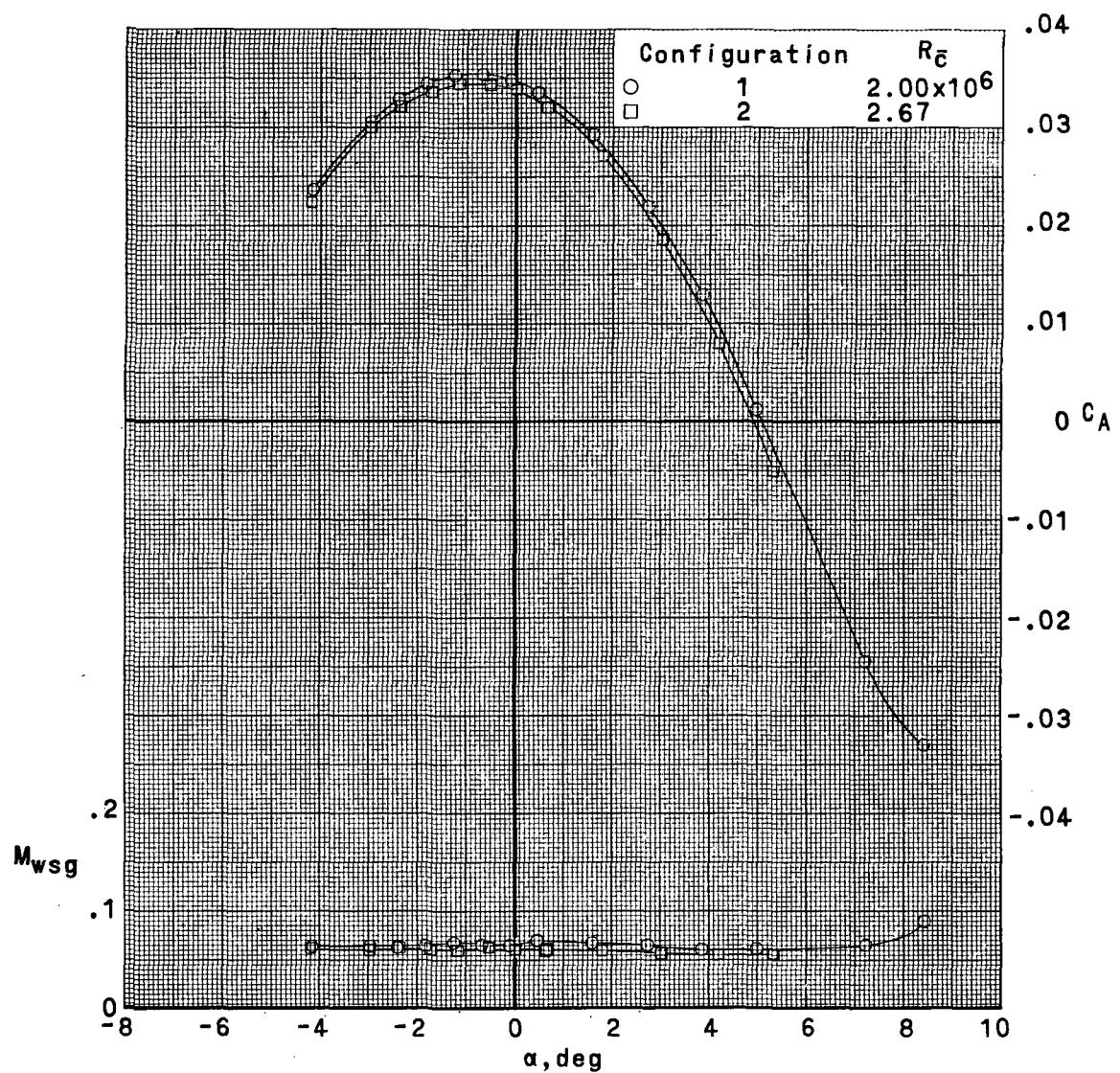
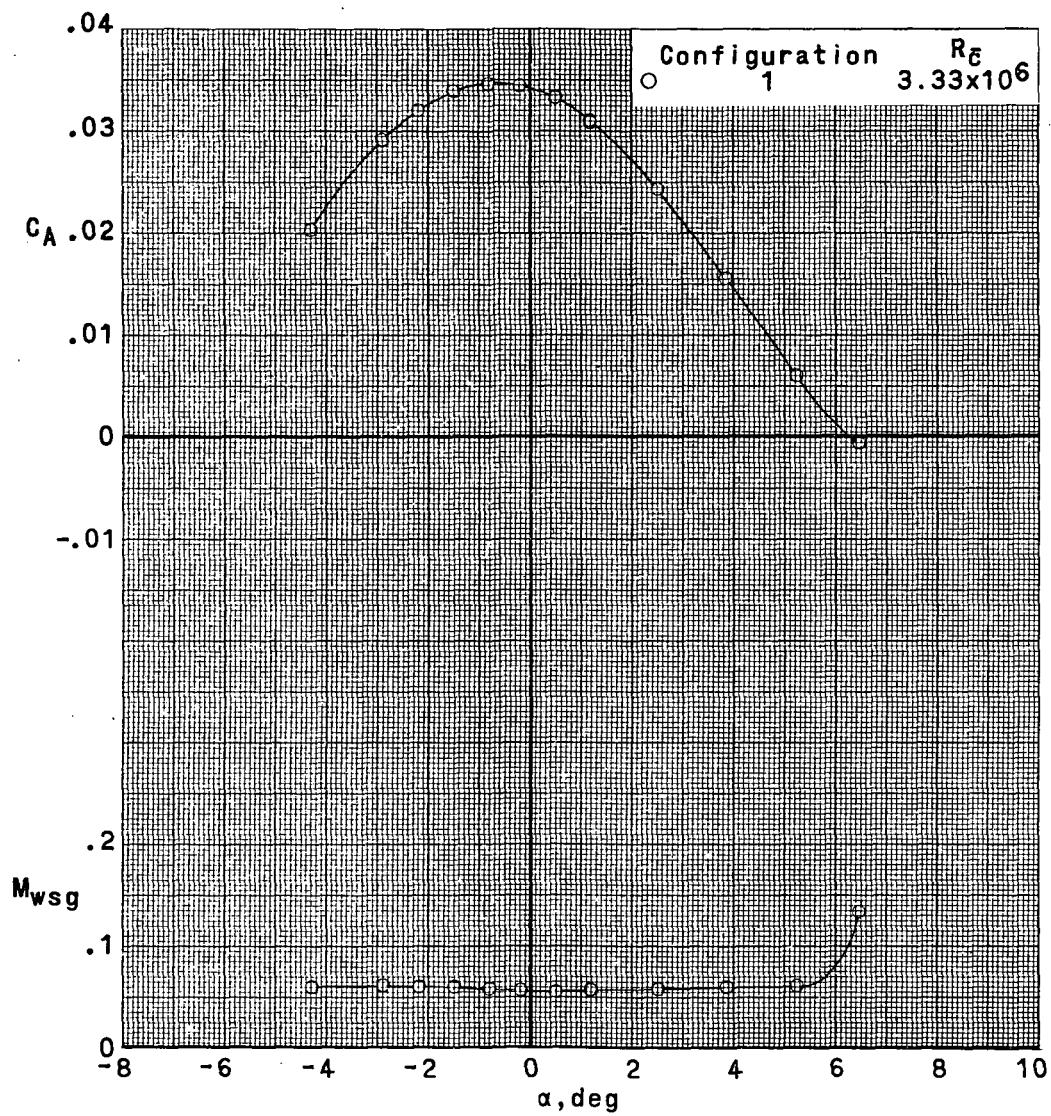


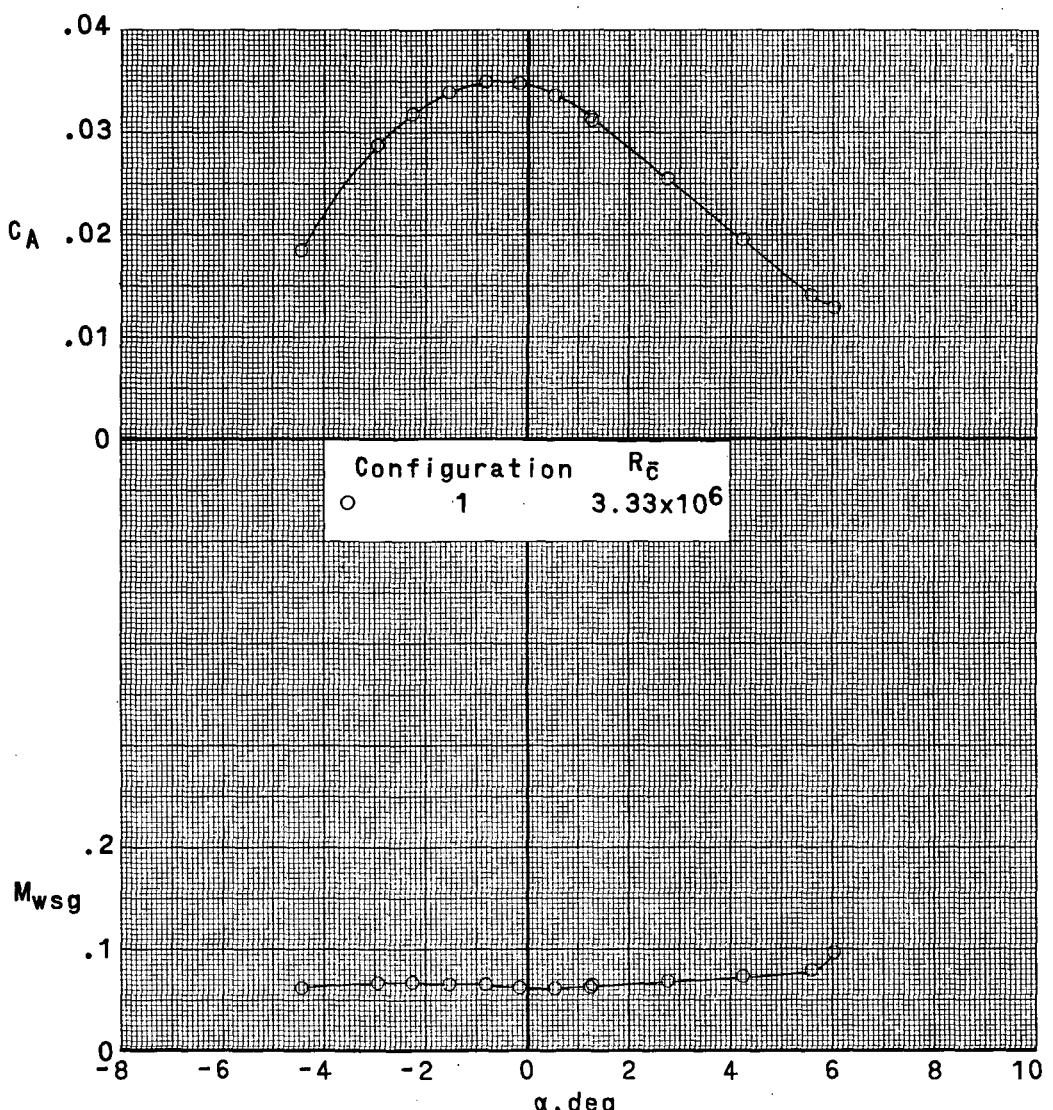
Figure 9.- Continued.



(c) $M = 0.60.$

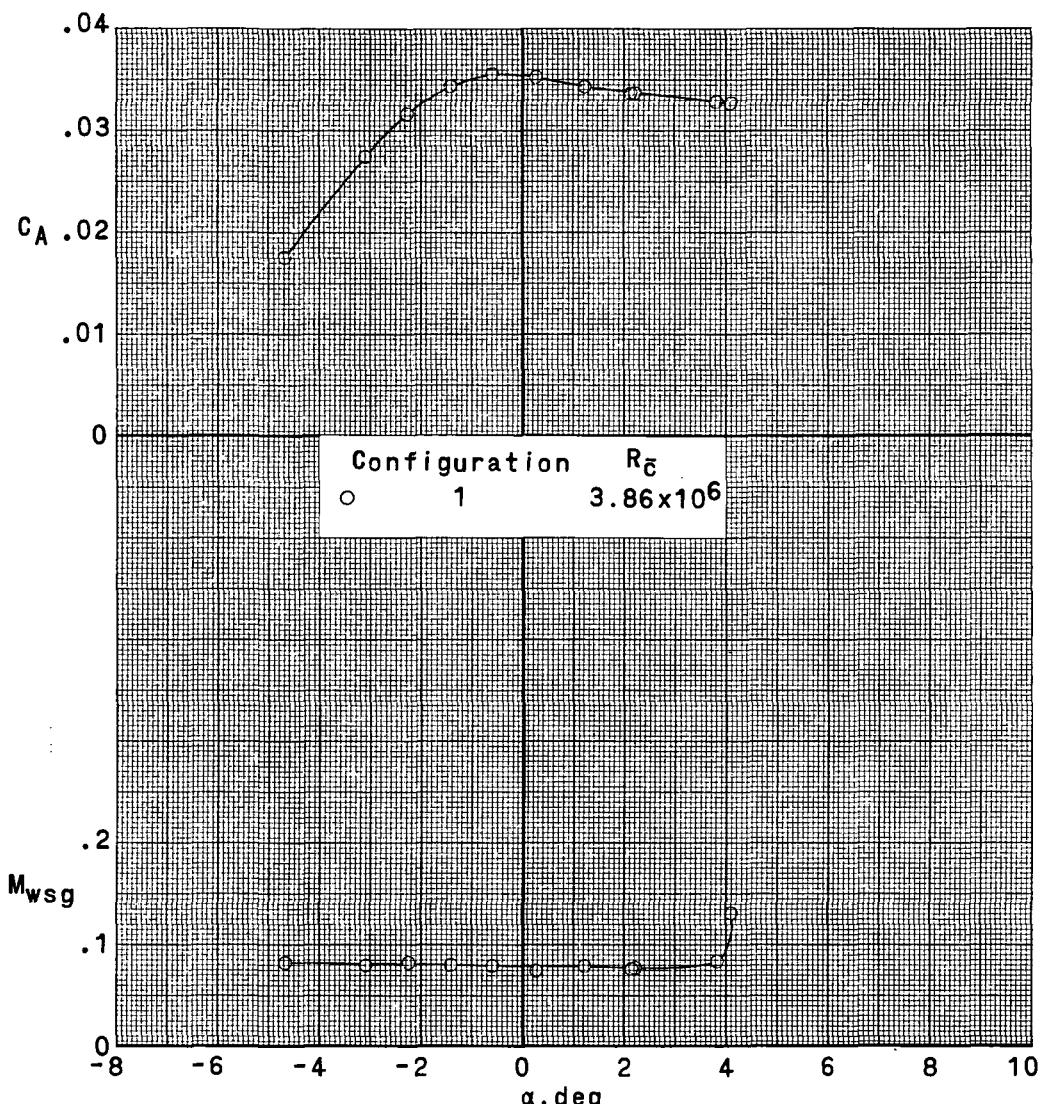
Figure 9.- Continued.

~~CONFIDENTIAL~~



(d) $M = 0.65$.

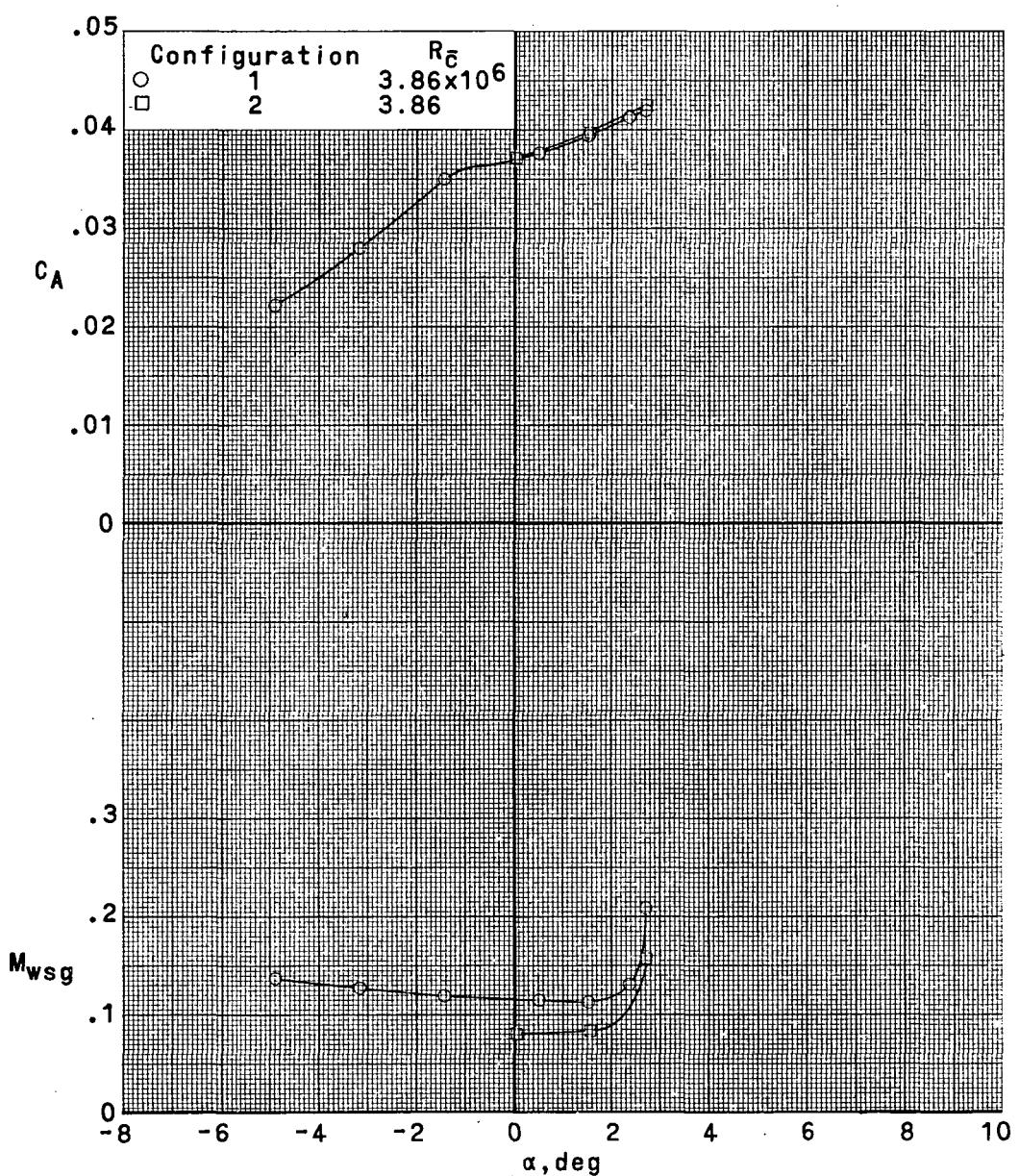
Figure 9.- Continued.



(e) $M = 0.70.$

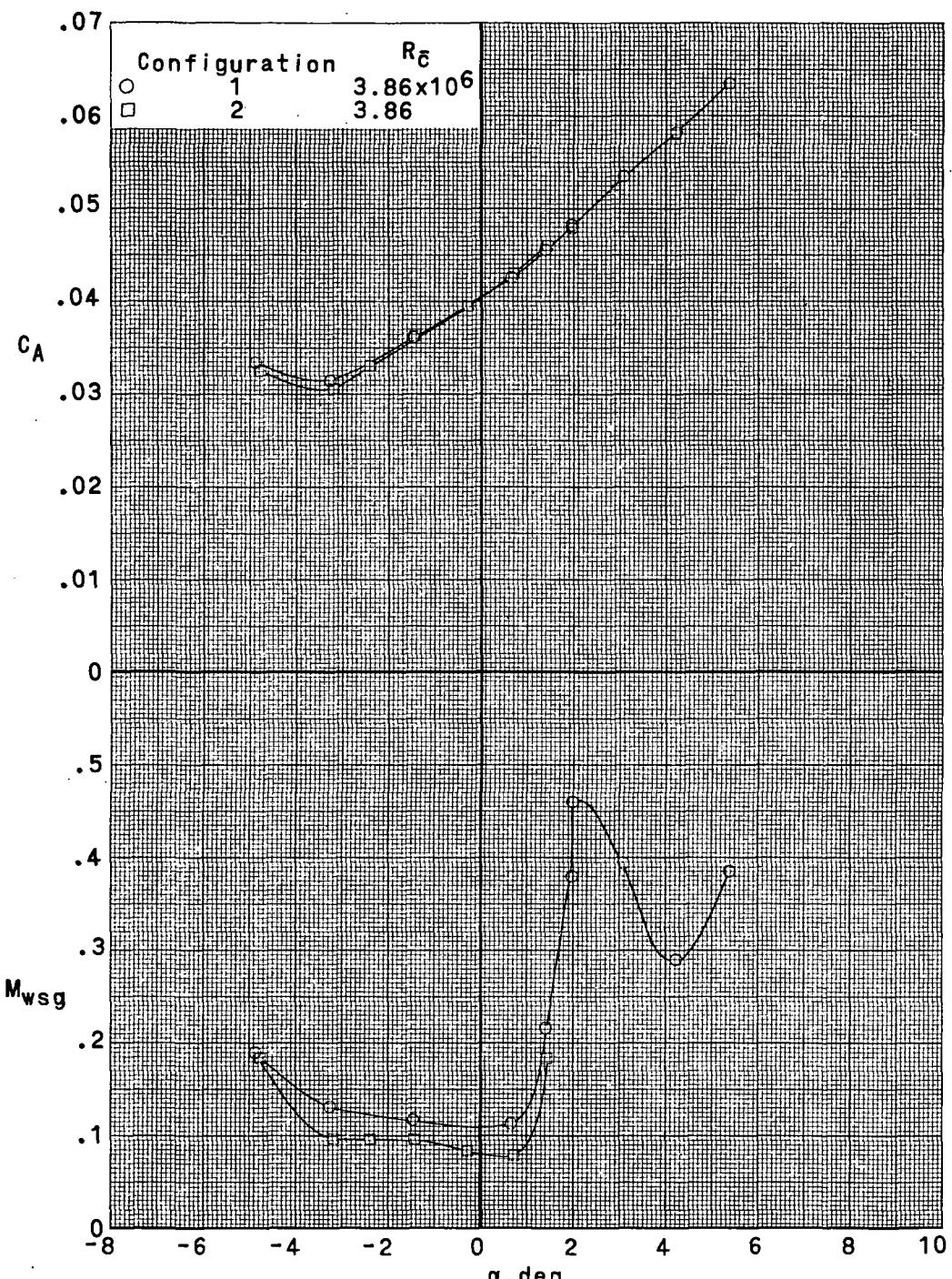
Figure 9.- Continued.

~~CONFIDENTIAL~~



(f) $M = 0.73.$

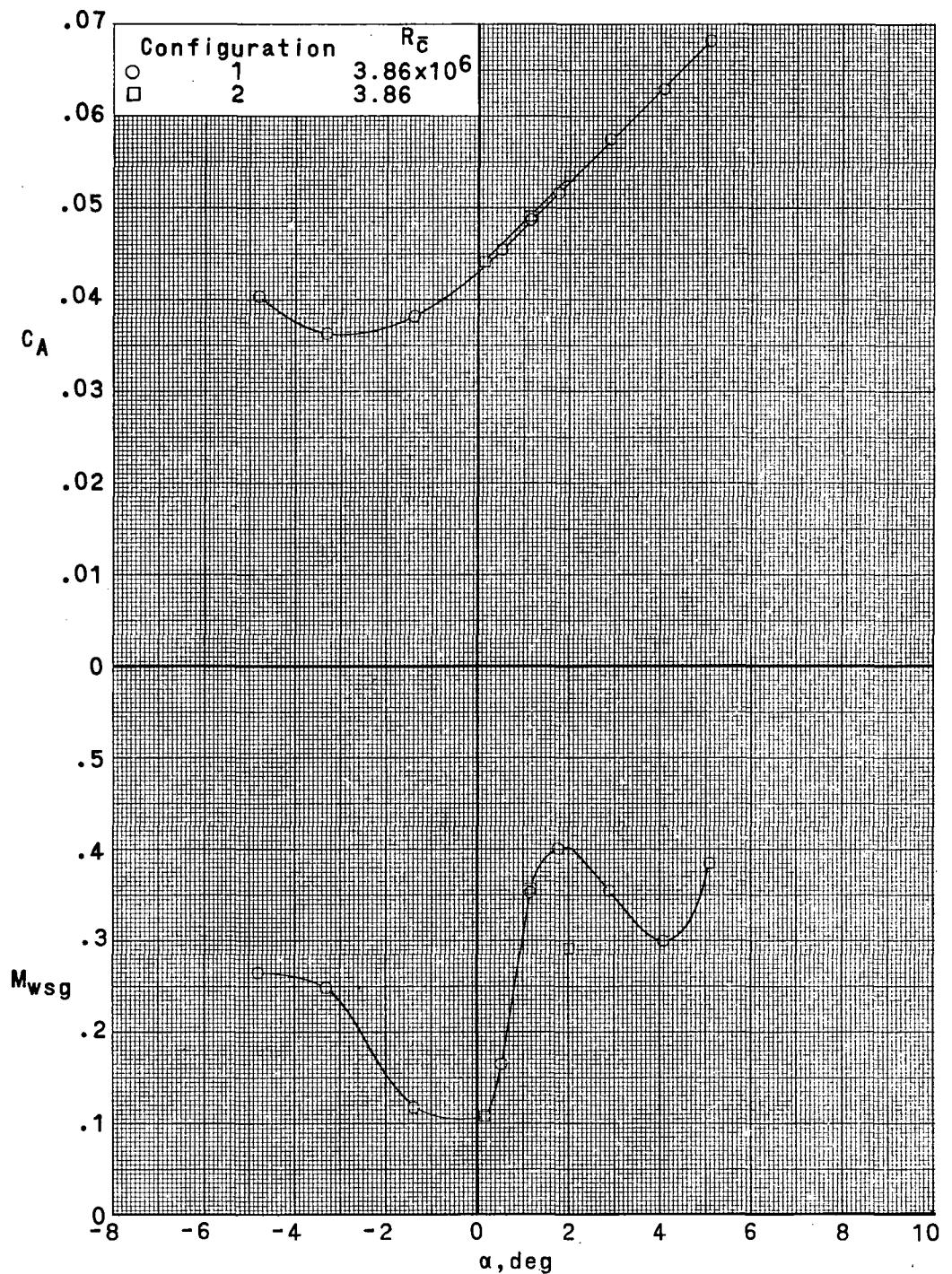
Figure 9.- Continued.



(g) $M = 0.75.$

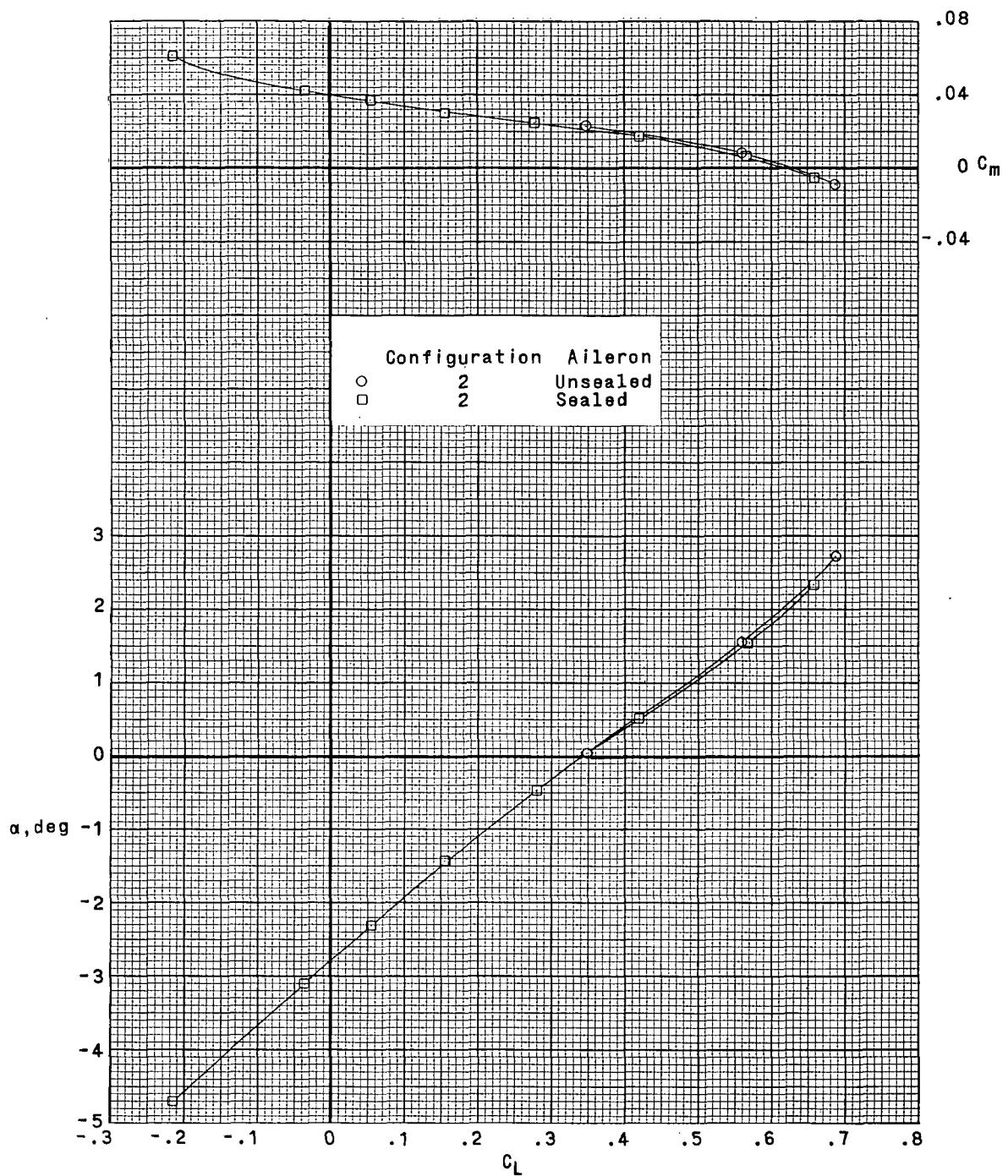
Figure 9.- Continued.

~~CONFIDENTIAL~~



(h) $M = 0.76.$

Figure 9.- Concluded.

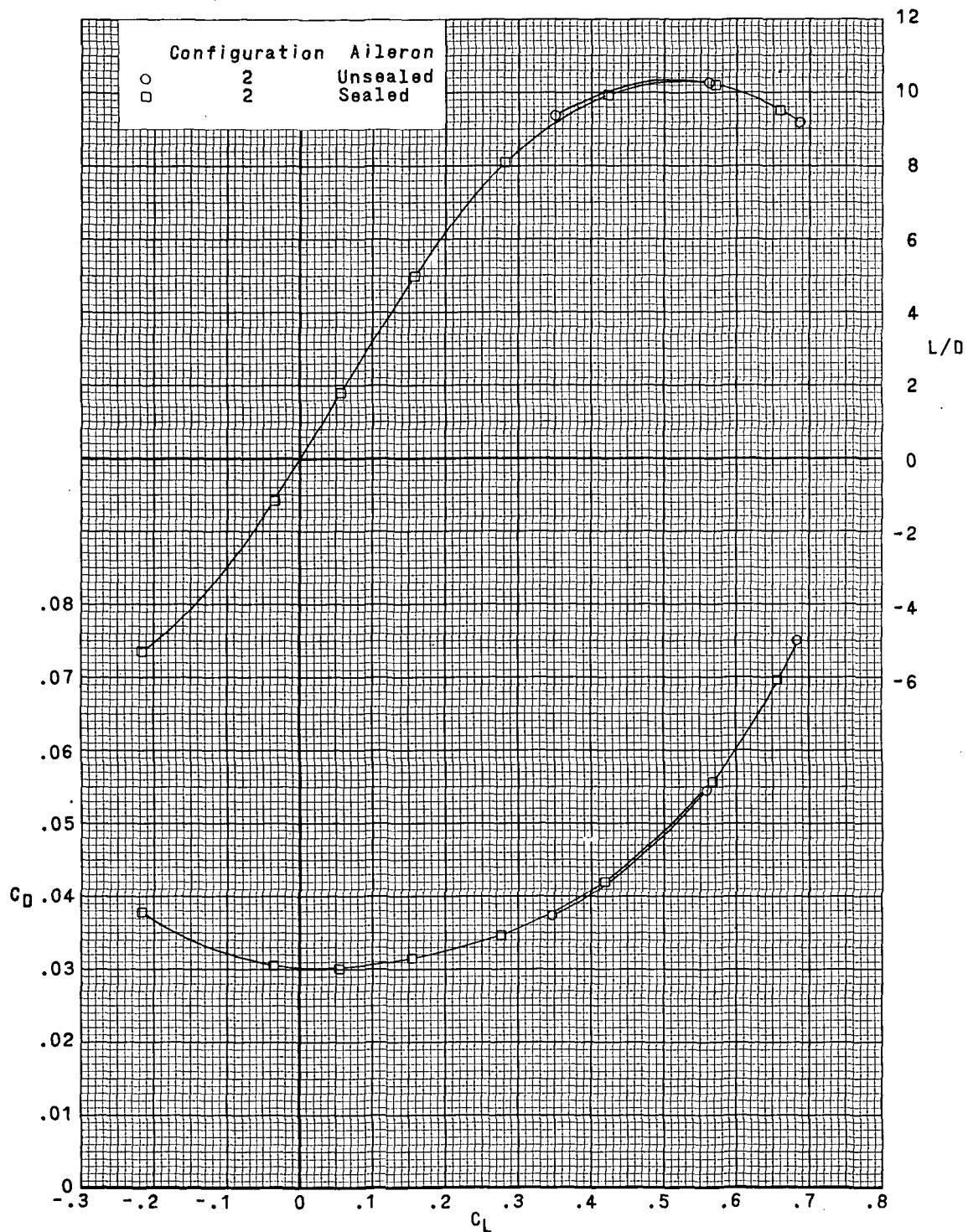


(a) $M = 0.73; R_C^- = 3.86 \times 10^6$.

Figure 10.- Effect of sealed aileron on longitudinal aerodynamic characteristics.
 $\delta_e = 0^\circ; i_h = 0^\circ; \delta_a = 0^\circ; \beta = 0^\circ$.

~~CONFIDENTIAL~~

~~CONFIDENTIAL~~

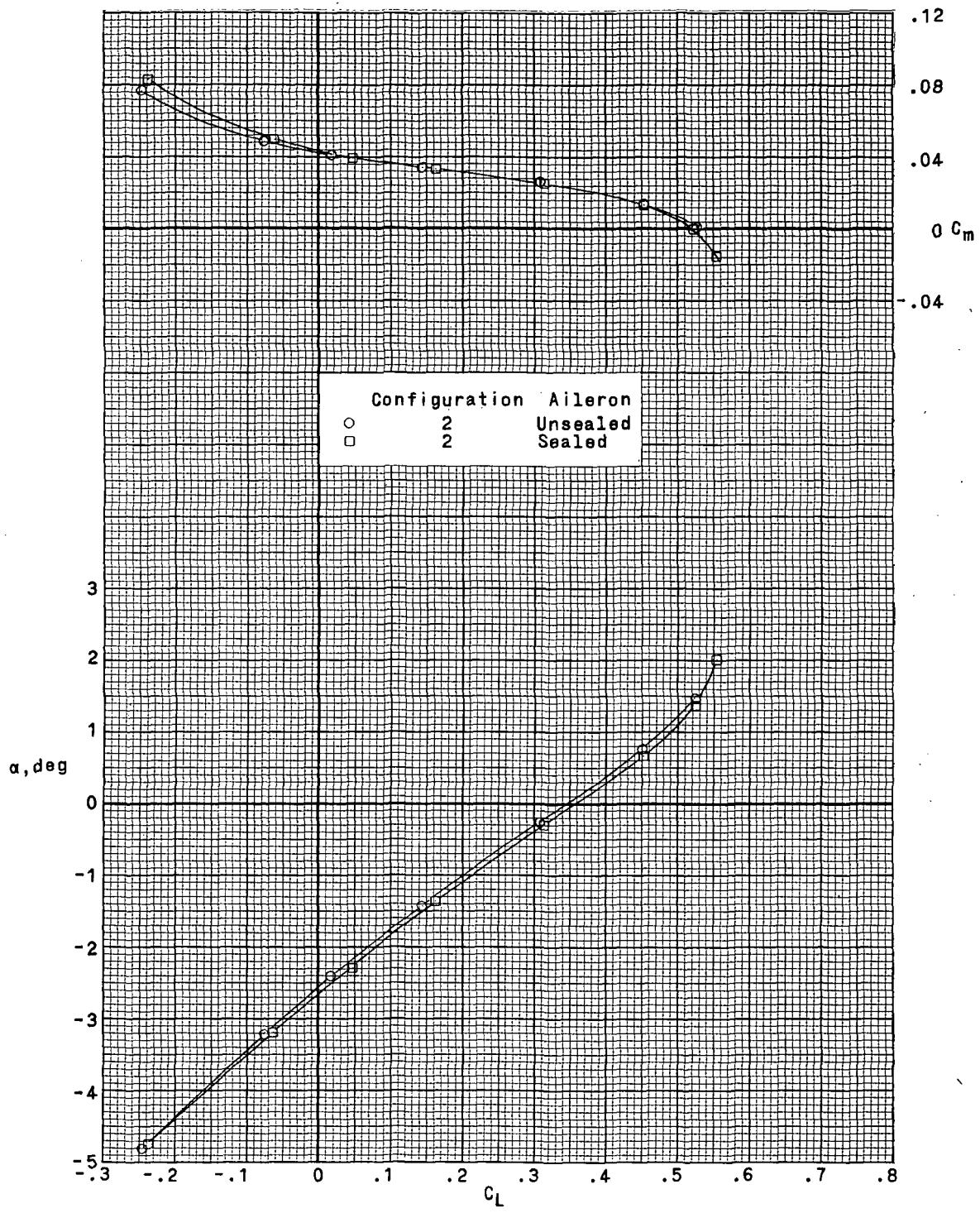


(a) $M = 0.73; R_{\bar{C}} = 3.86 \times 10^6$. Concluded.

Figure 10.- Continued.

~~CONFIDENTIAL~~

~~CONFIDENTIAL~~

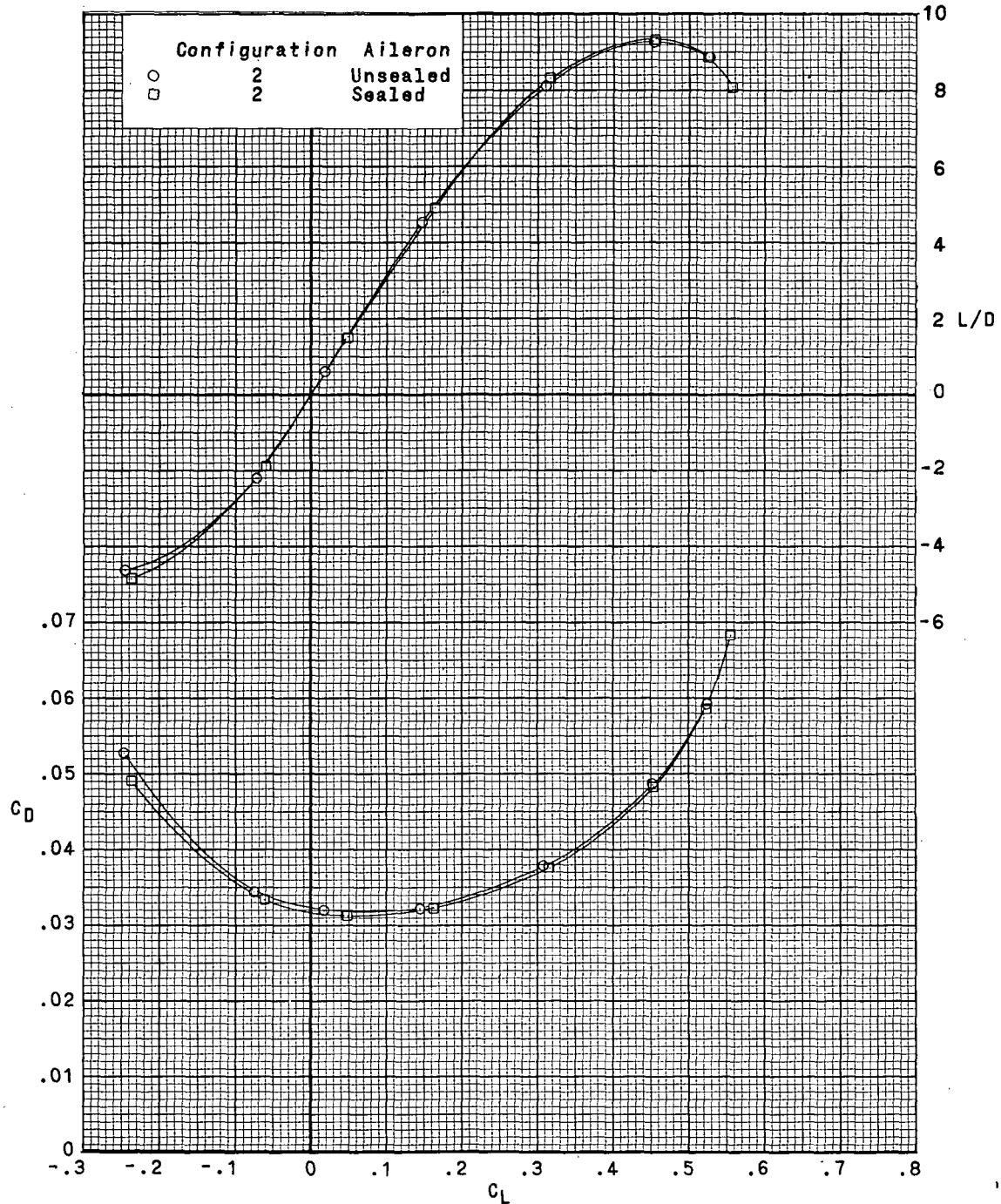


(b) $M = 0.75; R_C = 3.86 \times 10^6$.

Figure 10.- Continued.

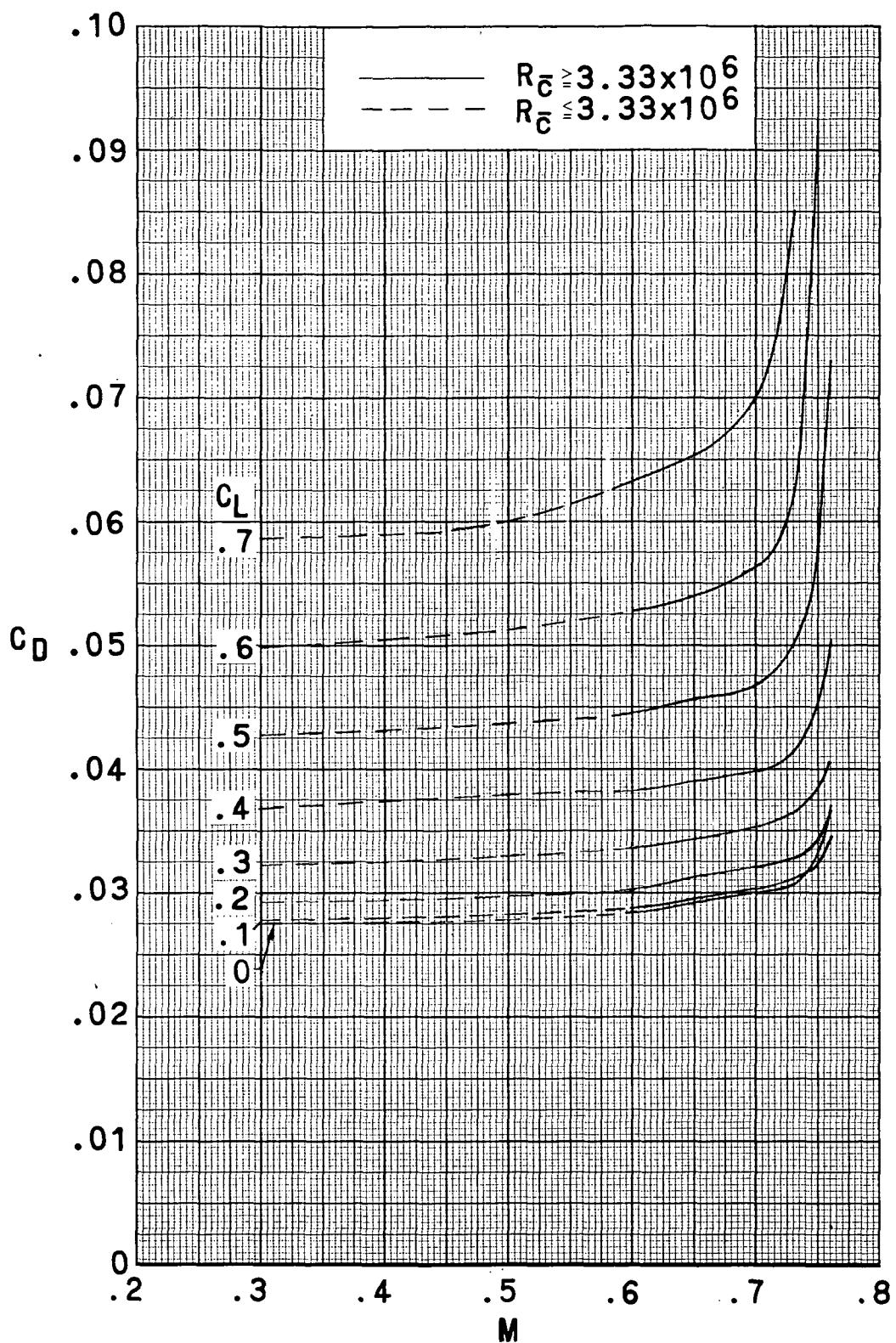
~~CONFIDENTIAL~~

~~CONFIDENTIAL~~



(b) $M = 0.75; R_{\bar{C}} = 3.86 \times 10^6$. Concluded.

Figure 10.- Concluded.



(a) Wind-tunnel model with supercritical wing. $i_h = 0^\circ$; $\delta_a = 0^\circ$; $\beta = 0^\circ$.

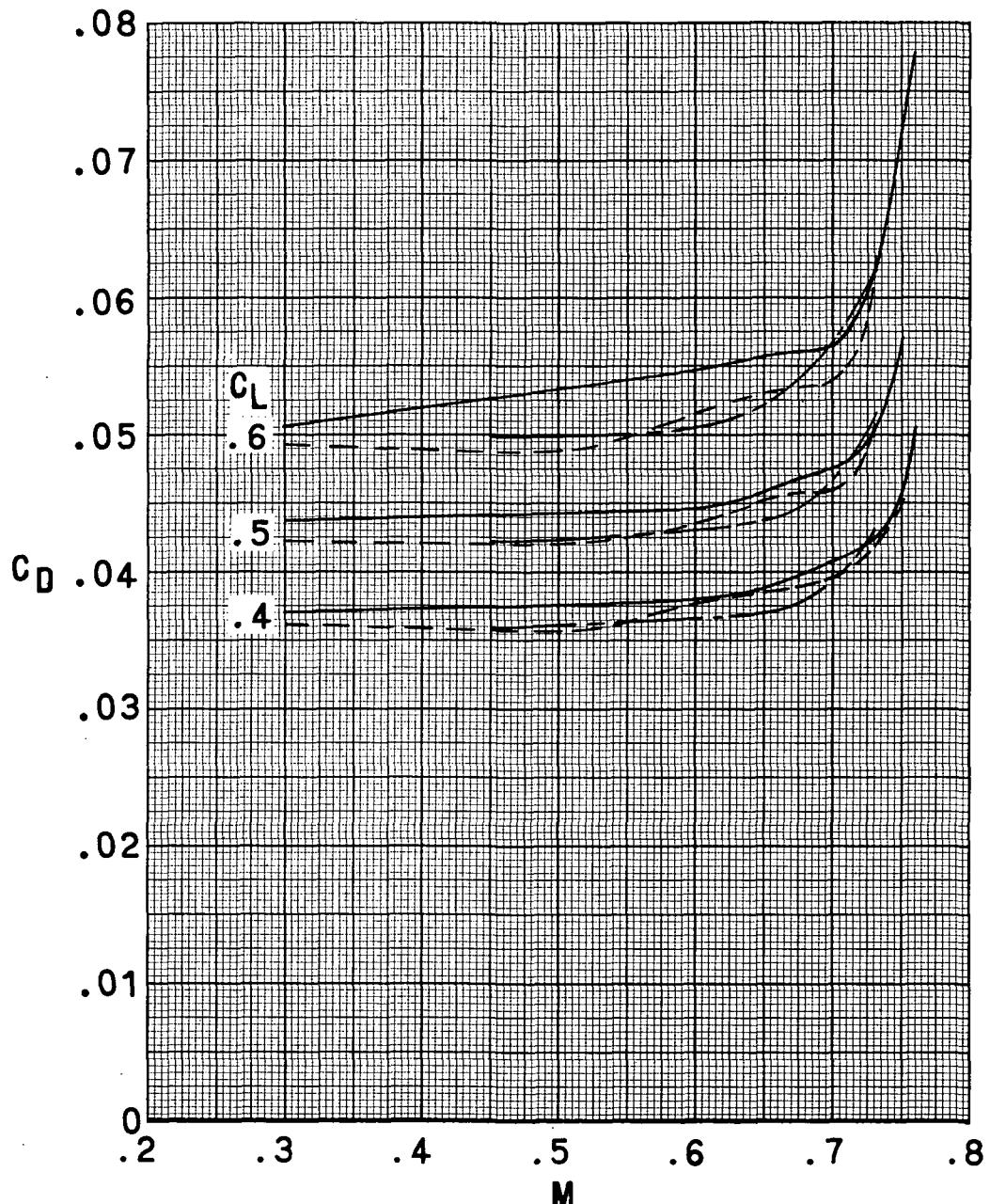
Figure 11.- Variation of drag coefficient with Mach number.

~~CONFIDENTIAL~~

~~CONFIDENTIAL~~

Airfoil section Data source

—	17-percent S.C.	Wind tunnel
- - -	17-percent S.C.	Flight (ref.8)
- - -	NACA 64 ₁ A212	Flight (ref.8)



(b) Comparison of wind-tunnel and flight data.

Figure 11.- Concluded.

~~CONFIDENTIAL~~

~~CONFIDENTIAL~~

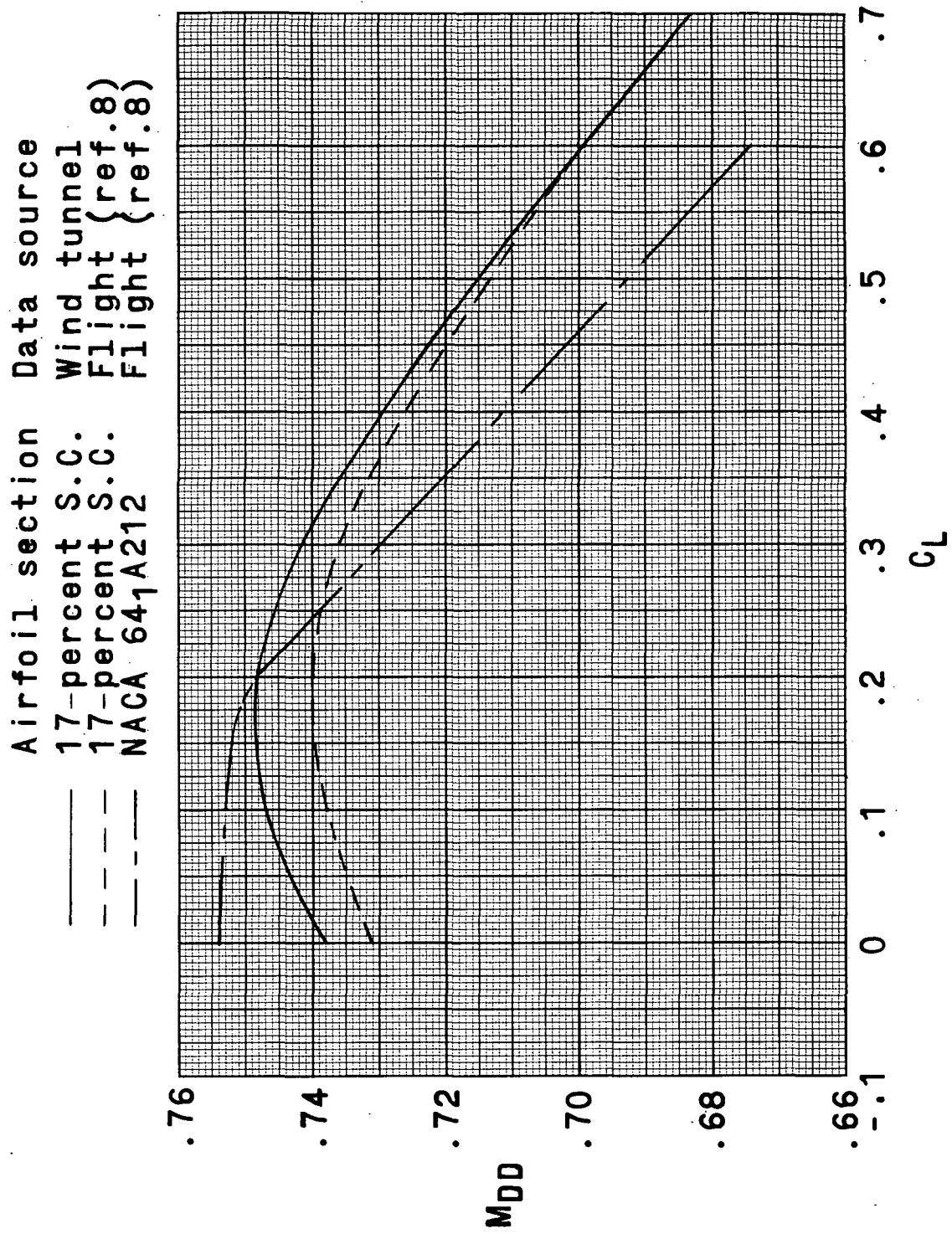


Figure 12.- Variation of drag-divergence Mach number with lift coefficient. $i_h = 0^\circ$; $\delta_a = 0^\circ$; $\beta = 0^\circ$.

~~CONFIDENTIAL~~

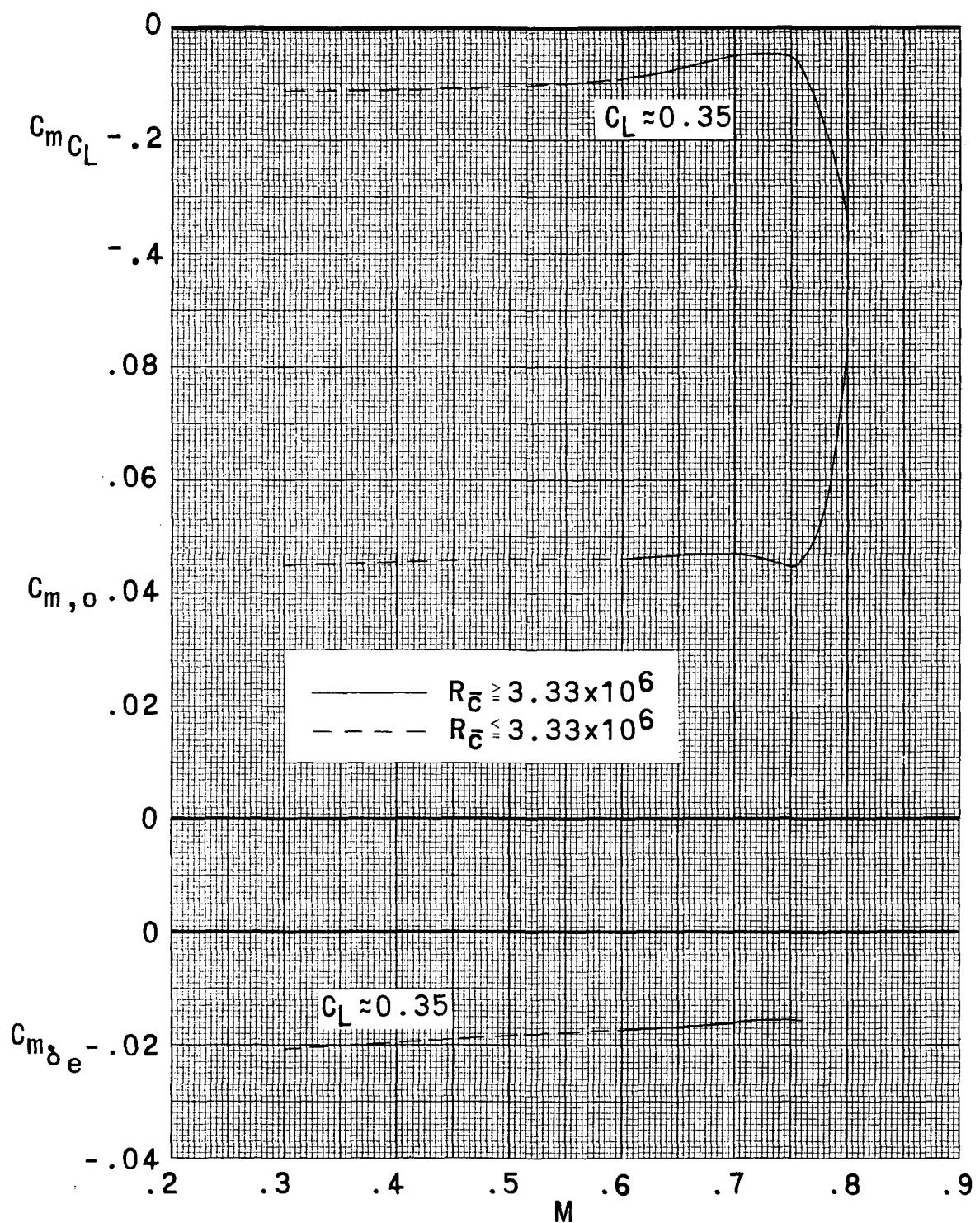


Figure 13.- Variation of longitudinal stability derivative, zero-lift pitching moment, and longitudinal control derivative with Mach number. $i_h = 0^\circ$; $\delta_a = 0^\circ$; $\beta = 0^\circ$.

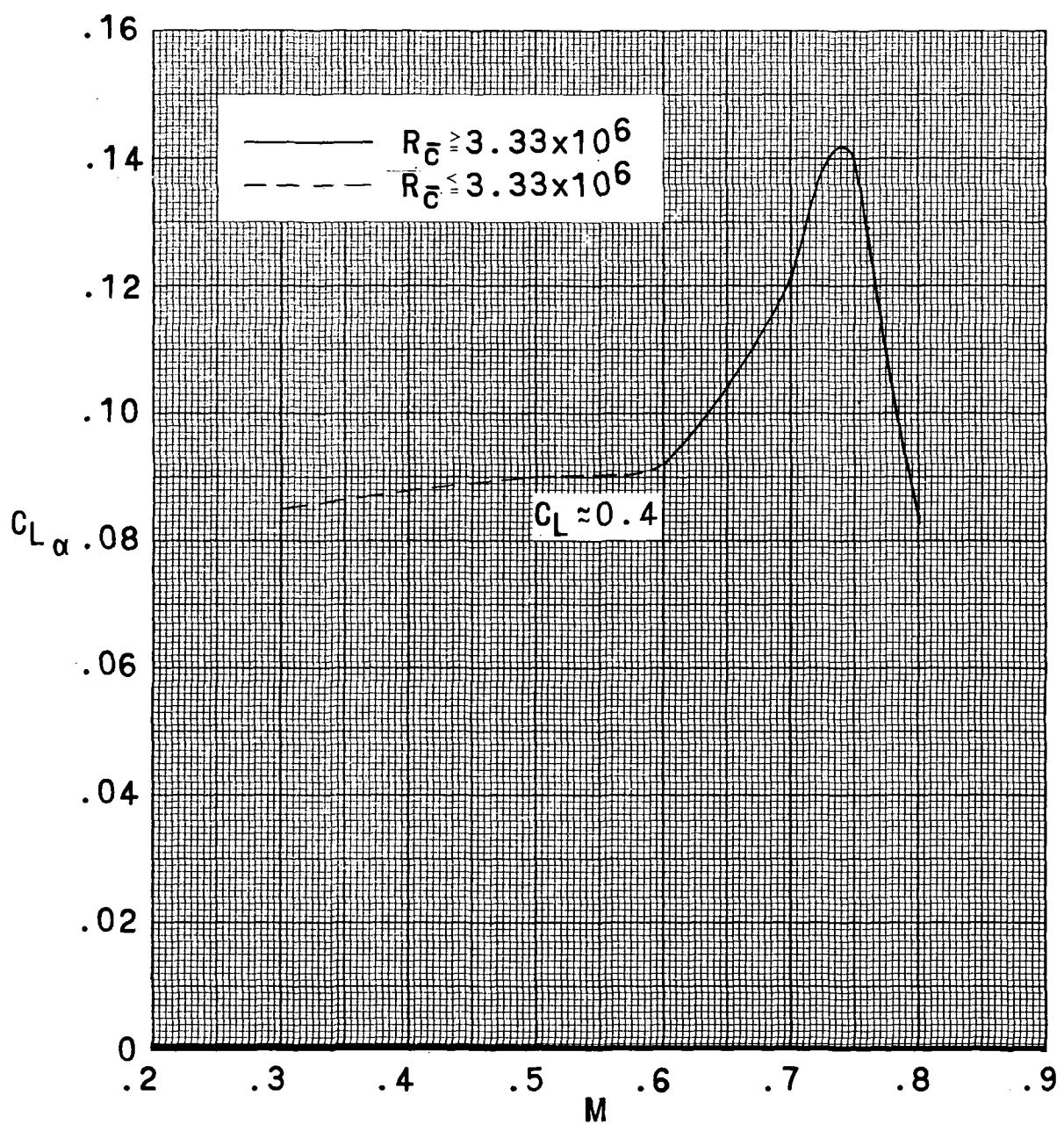


Figure 14.- Variation of lift-curve slope with Mach number. $\delta_e = 0^\circ$; $i_h = 0^\circ$; $\delta_a = 0^\circ$; $\beta = 0^\circ$.

~~CONFIDENTIAL~~

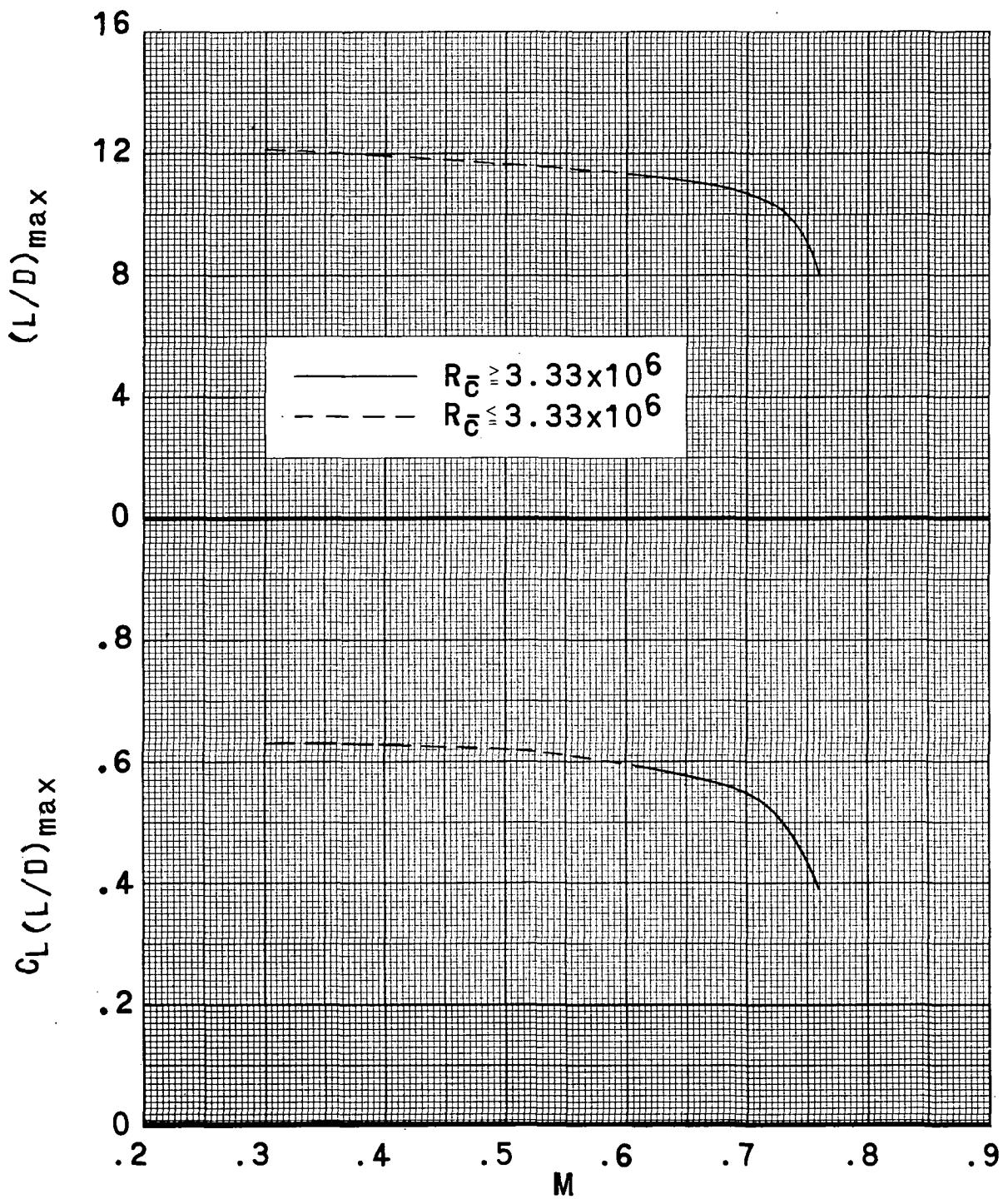


Figure 15.- Variation of untrimmed maximum lift-drag ratio and lift coefficient at $(L/D)_{\max}$ with Mach number. $\delta_e = 0^\circ$; $i_h = 0^\circ$; $\delta_a = 0^\circ$; $\beta = 0^\circ$.

~~CONFIDENTIAL~~

~~CONFIDENTIAL~~

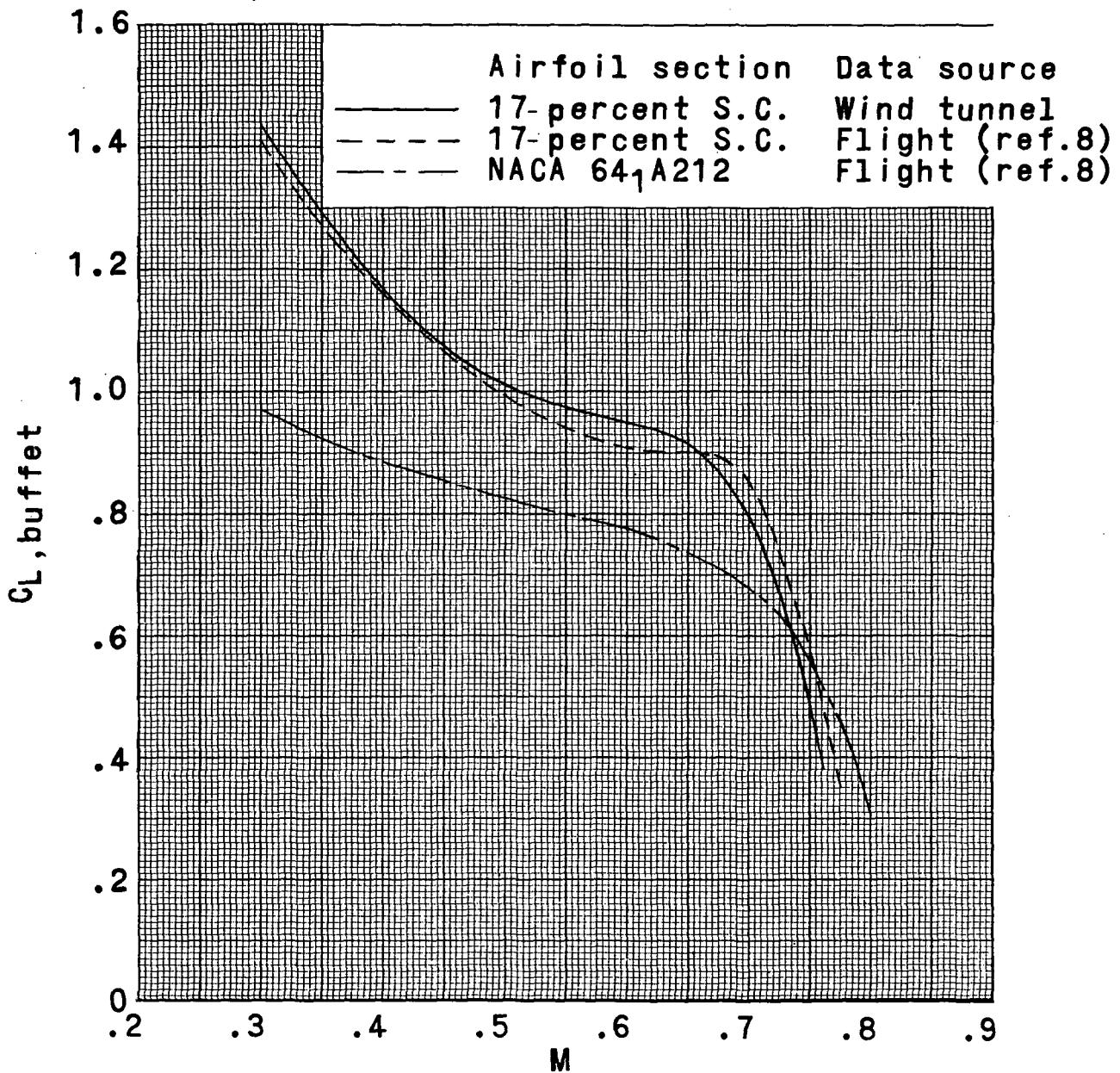
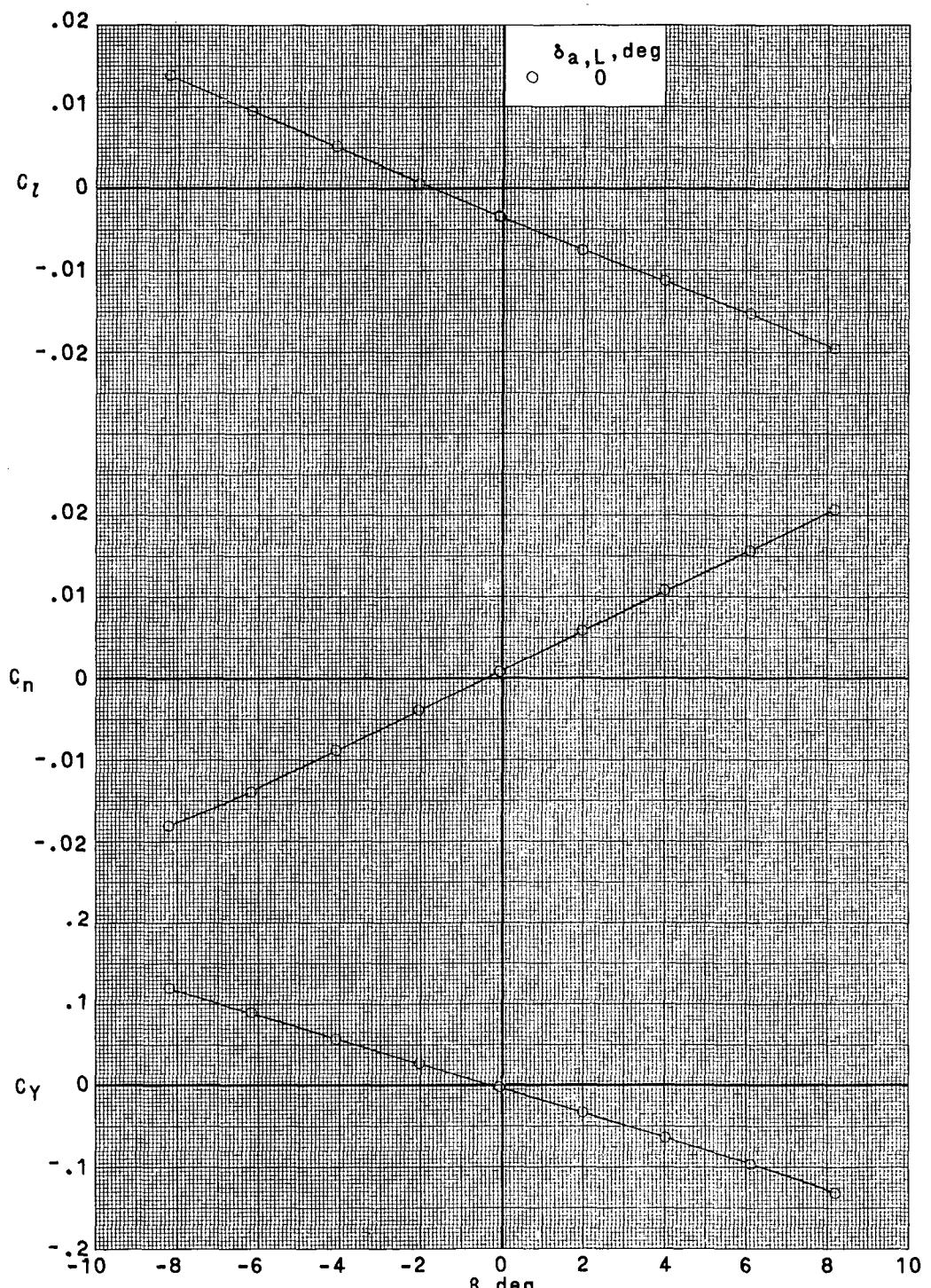


Figure 16.- Variation of lift coefficient at buffet onset with Mach number.

$$\delta_e = 0^\circ; i_h = 0^\circ; \delta_a = 0^\circ; \beta = 0^\circ.$$

~~CONFIDENTIAL~~

~~CONFIDENTIAL~~



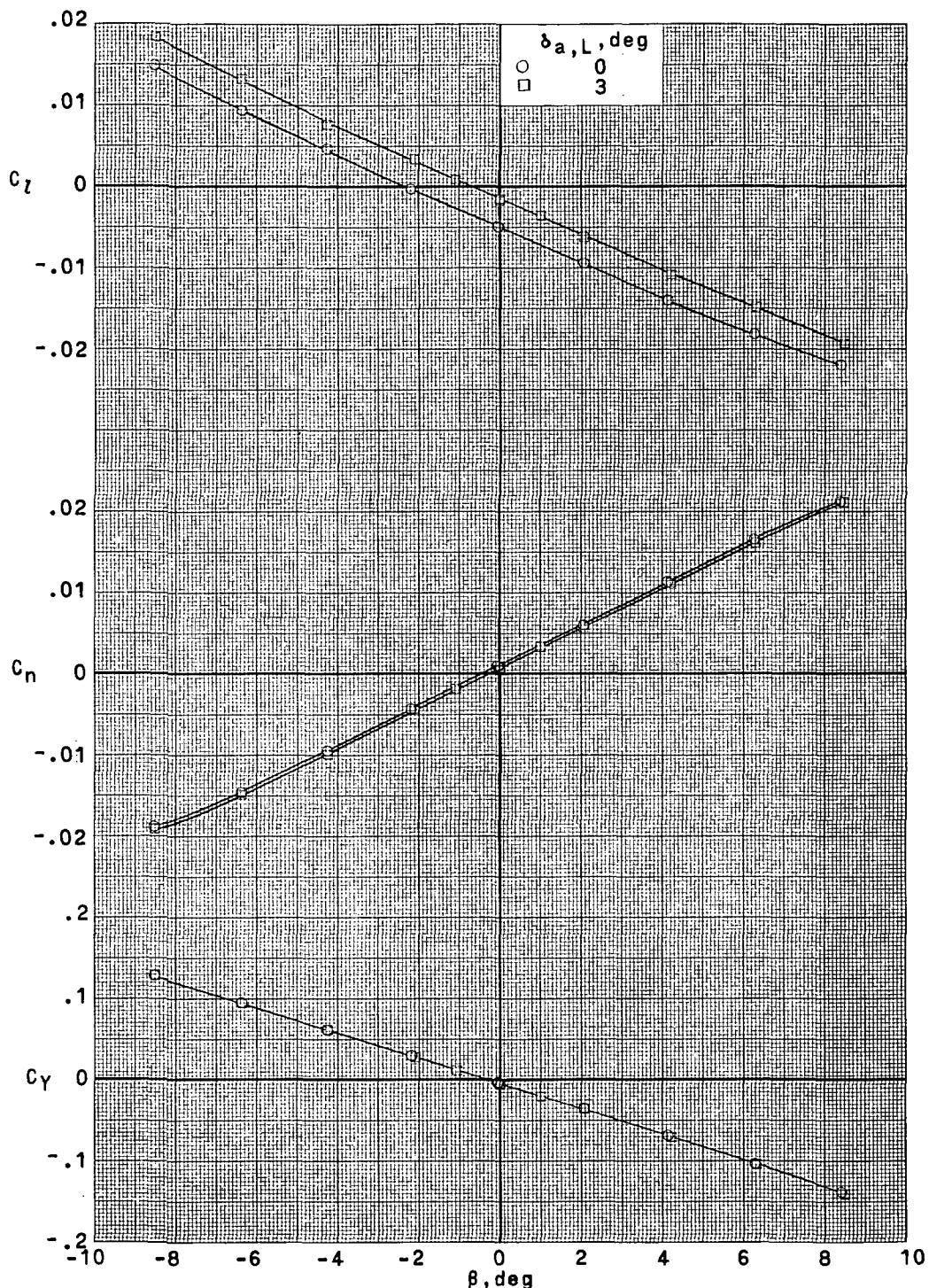
(a) $M = 0.30; \alpha = 0.3^\circ; R_C = 2.00 \times 10^6$.

Figure 17.- Effect of angle of sideslip on lateral aerodynamic characteristics.

$$\delta_e = 0^\circ; i_h = 0^\circ.$$

~~CONFIDENTIAL~~

~~CONFIDENTIAL~~

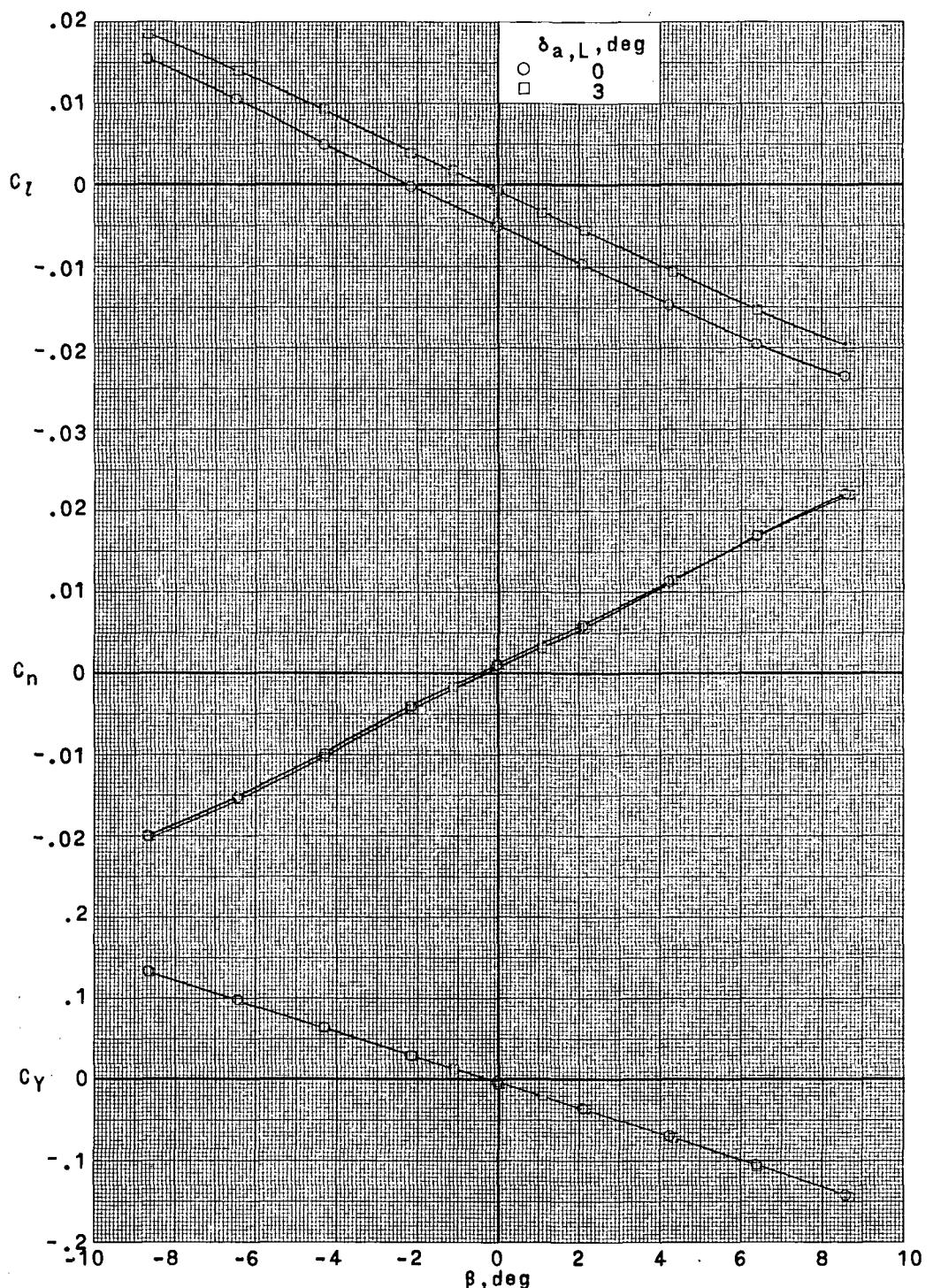


(b) $M = 0.60; \alpha = 1.3^\circ; R_{\bar{C}} = 3.33 \times 10^6$.

Figure 17. - Continued.

~~CONFIDENTIAL~~

~~CONFIDENTIAL~~

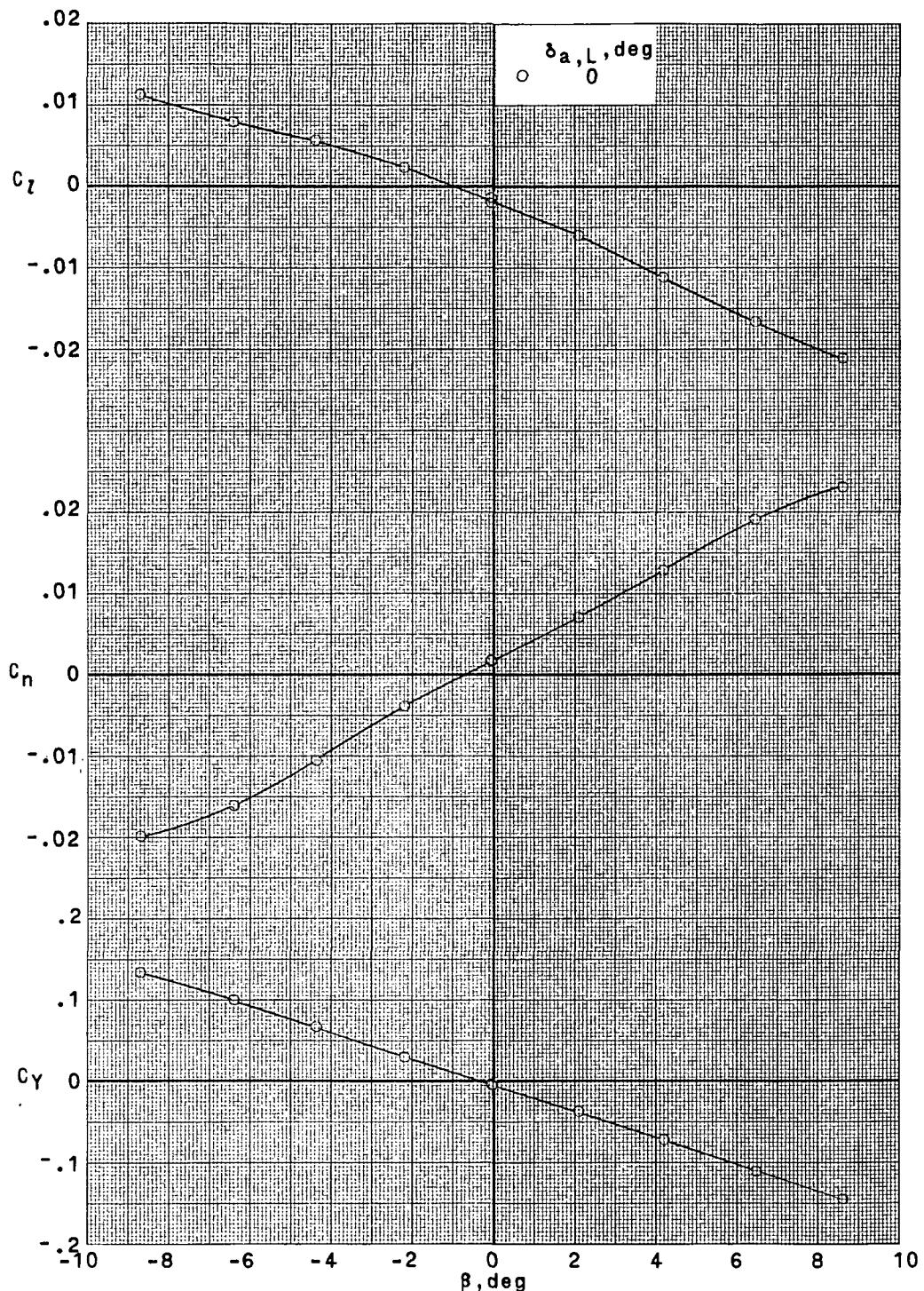


(c) $M = 0.70$; $\alpha = 2.4^\circ$; $R_c = 3.86 \times 10^6$.

Figure 17.- Continued.

~~CONFIDENTIAL~~

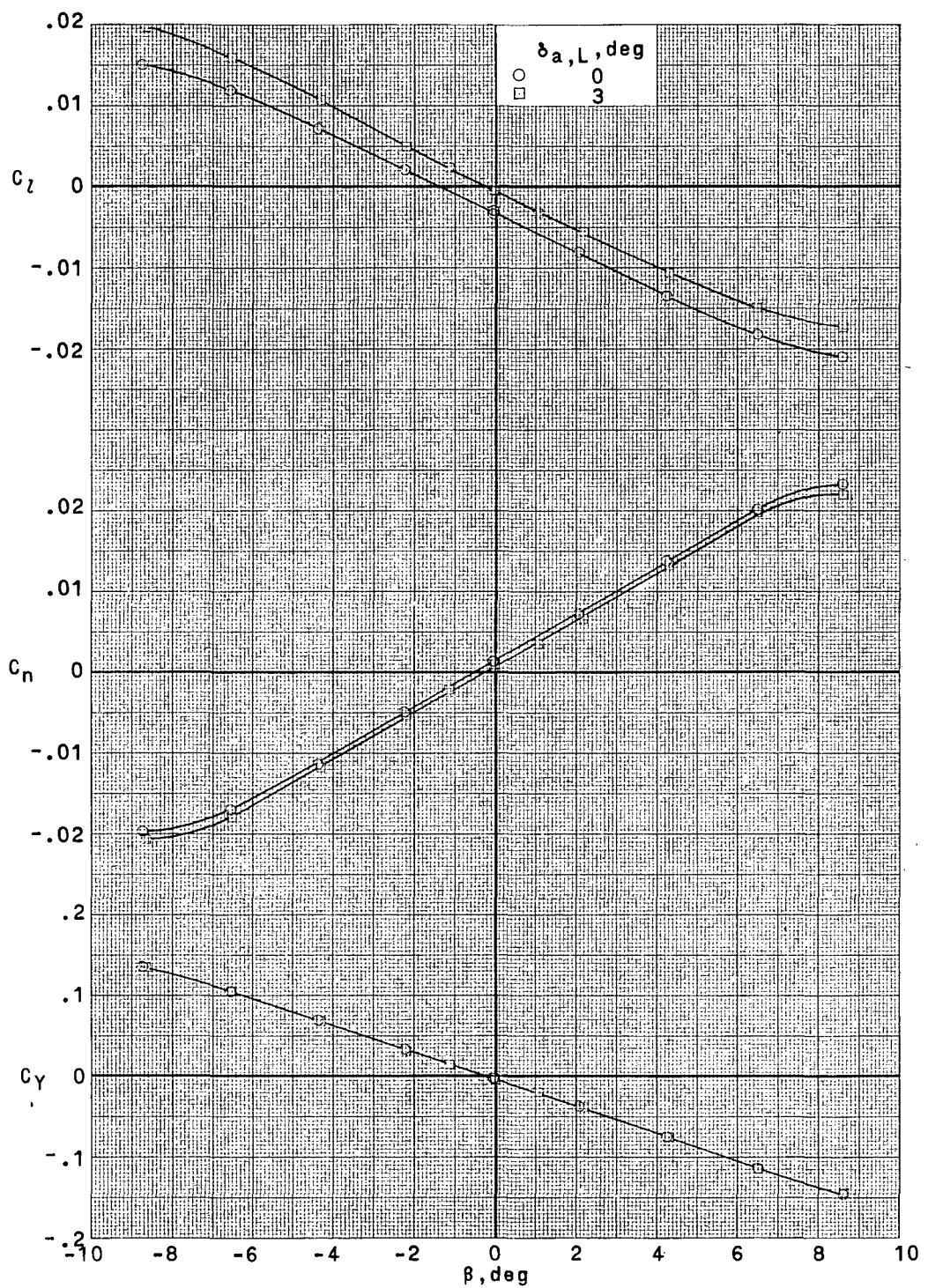
~~CONFIDENTIAL~~



(d) $M = 0.73; \alpha = 2.4^\circ; R_{\bar{C}} = 3.86 \times 10^6.$

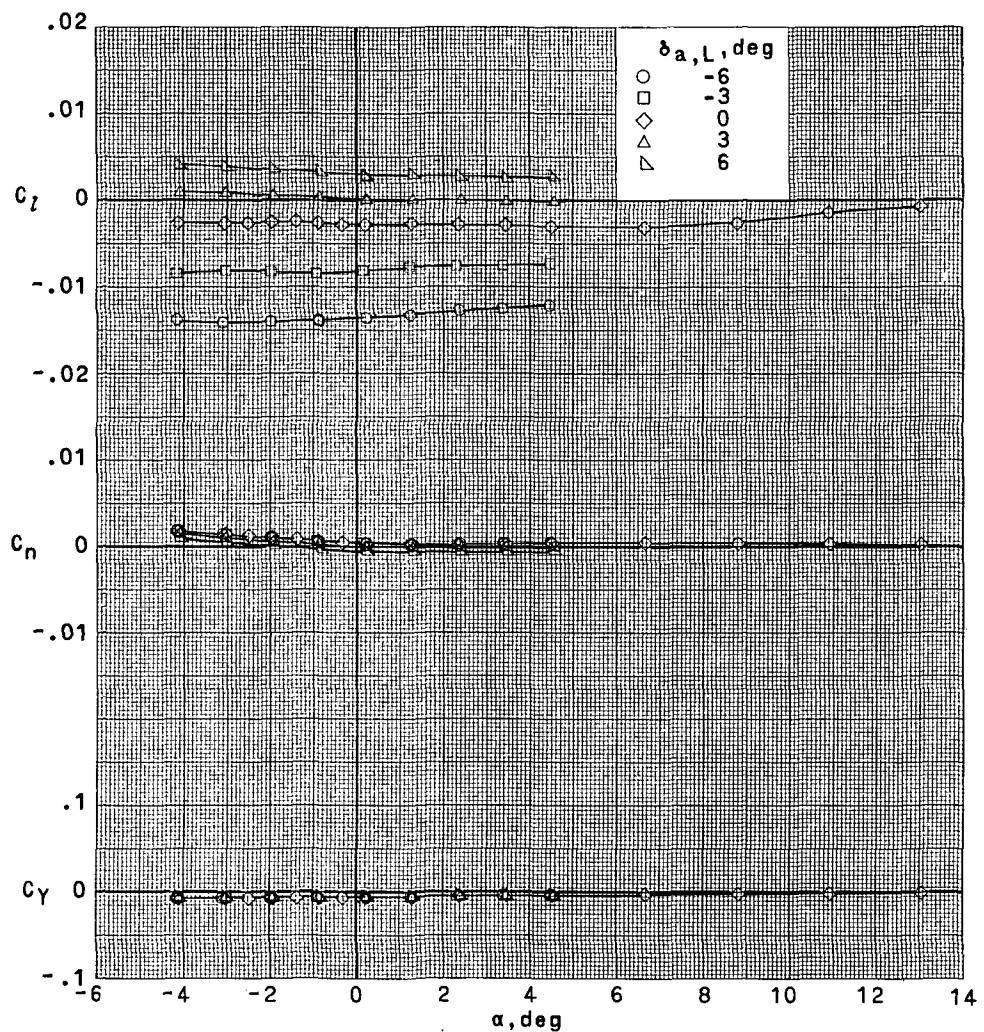
Figure 17.- Continued.

~~CONFIDENTIAL~~



(e) $M = 0.76; \alpha = 2.0^\circ; R_C = 3.86 \times 10^6$.

Figure 17.- Concluded.

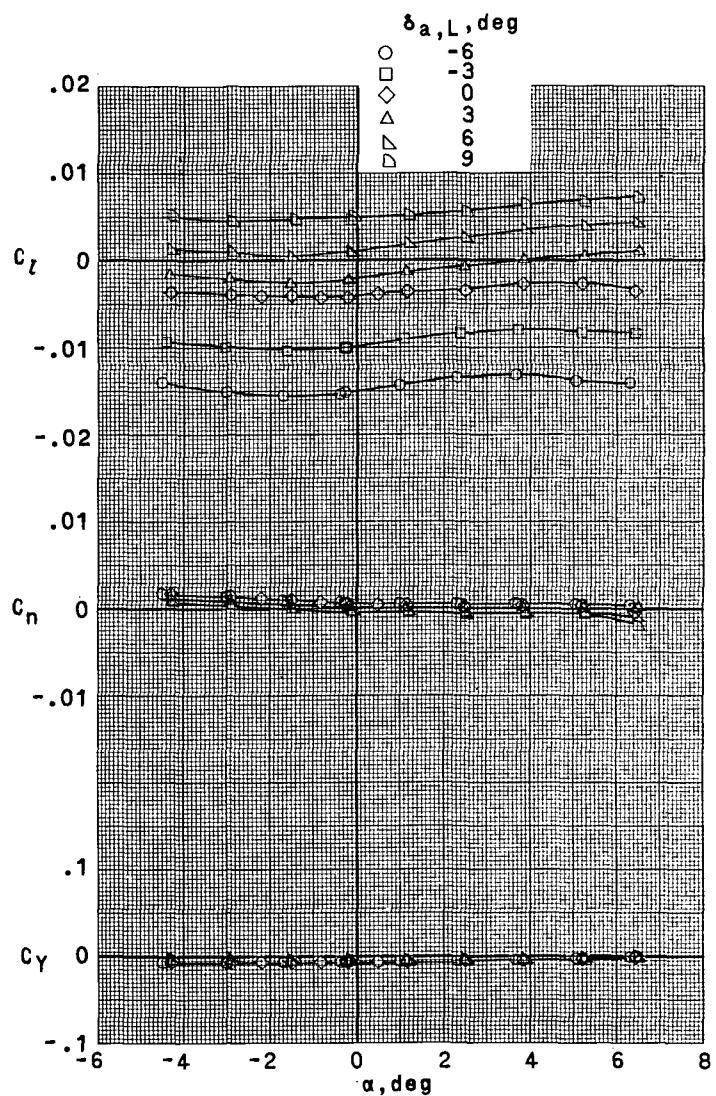


(a) $M = 0.30$; $R_C = 2.00 \times 10^6$.

Figure 18.- Effect of angle of attack on lateral control characteristics.

$\delta_e = 0^\circ$; $i_h = 0^\circ$; $\beta = 0^\circ$.

~~CONFIDENTIAL~~

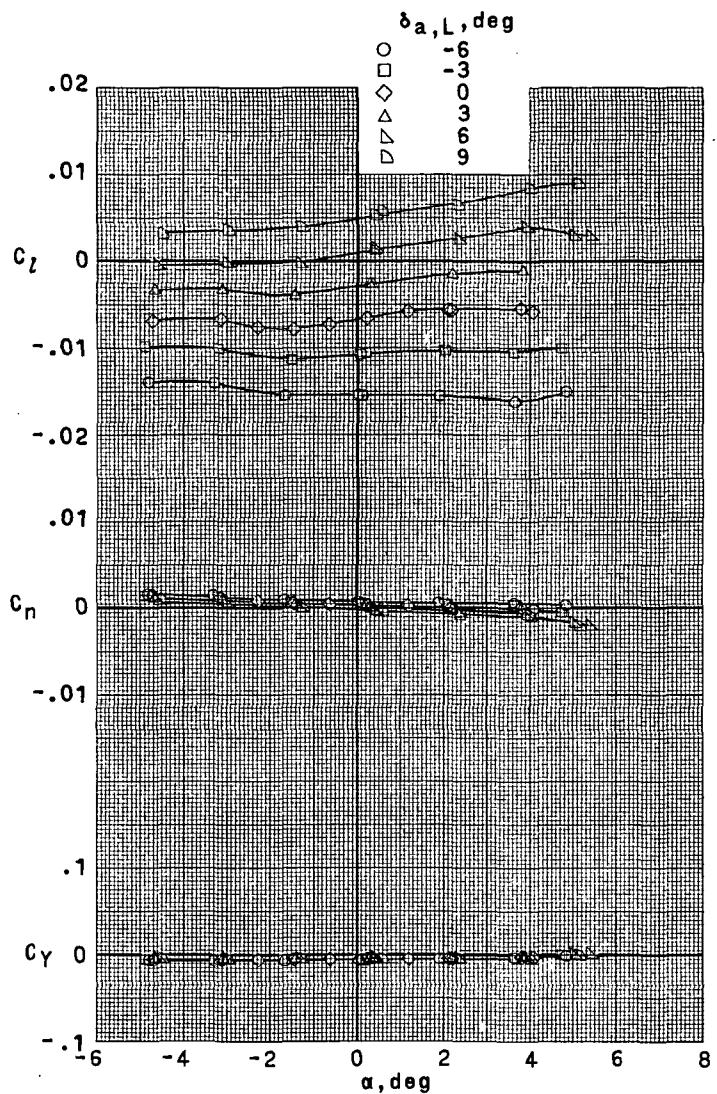


(b) $M = 0.60; R_{\bar{C}} = 3.33 \times 10^6$.

Figure 18.- Continued.

~~CONFIDENTIAL~~

~~CONFIDENTIAL~~

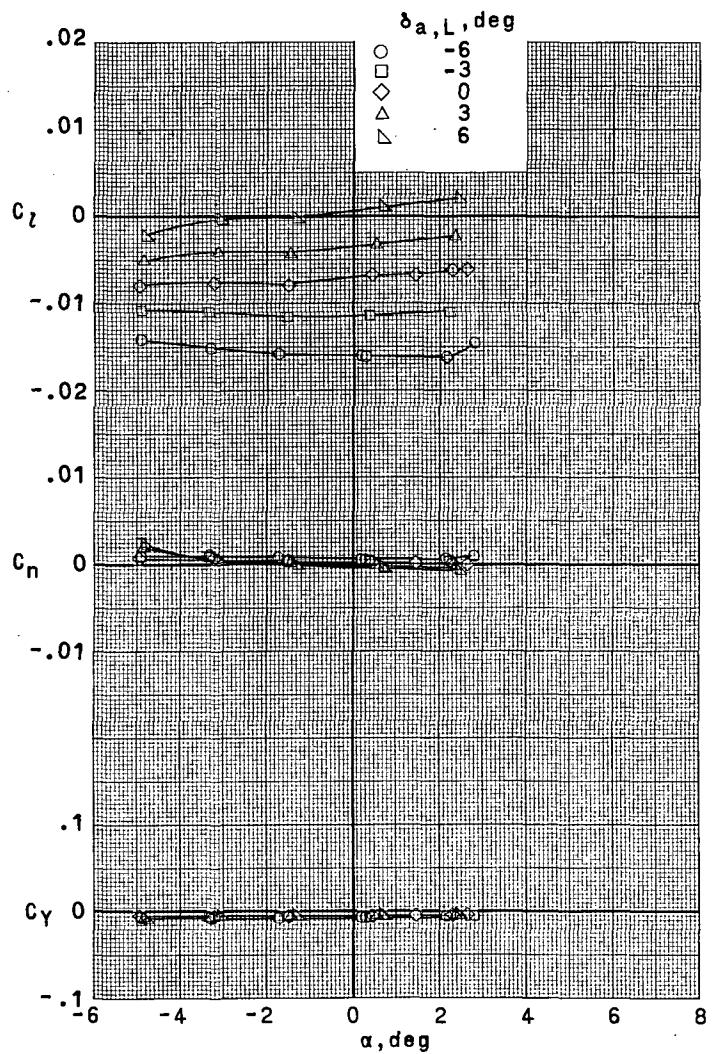


(c) $M = 0.70$; $R_C^- = 3.86 \times 10^6$.

Figure 18.- Continued.

~~CONFIDENTIAL~~

~~CONFIDENTIAL~~

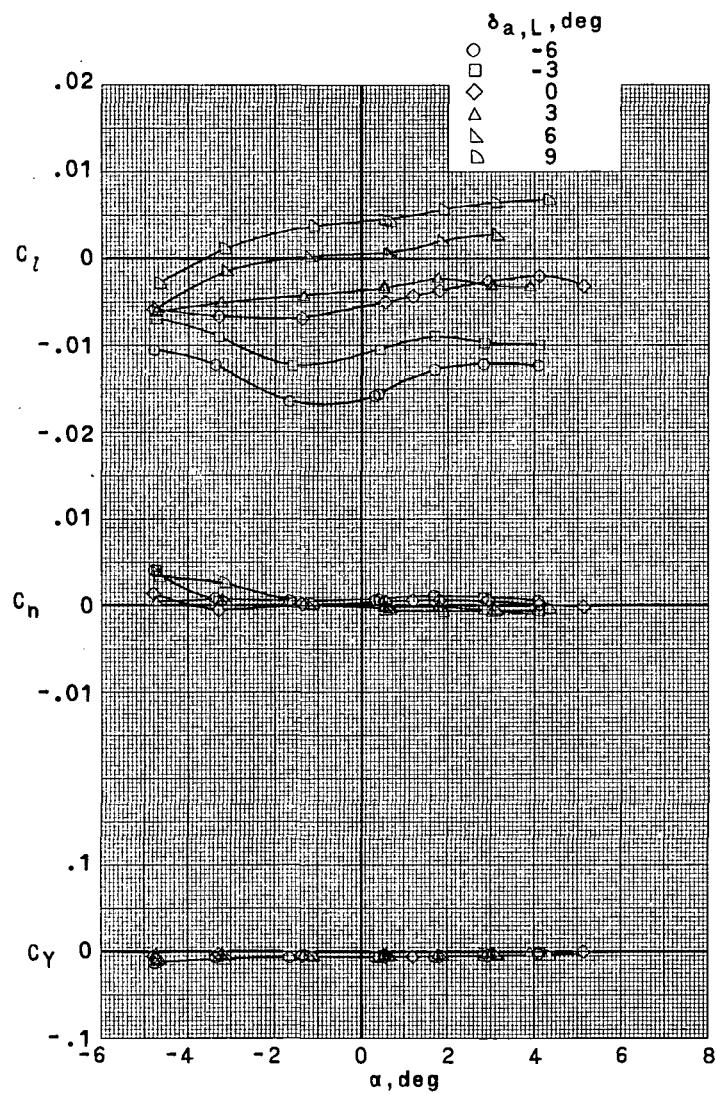


(d) $M = 0.73; R_{\bar{C}} = 3.86 \times 10^6$.

Figure 18.- Continued.

~~CONFIDENTIAL~~

~~CONFIDENTIAL~~

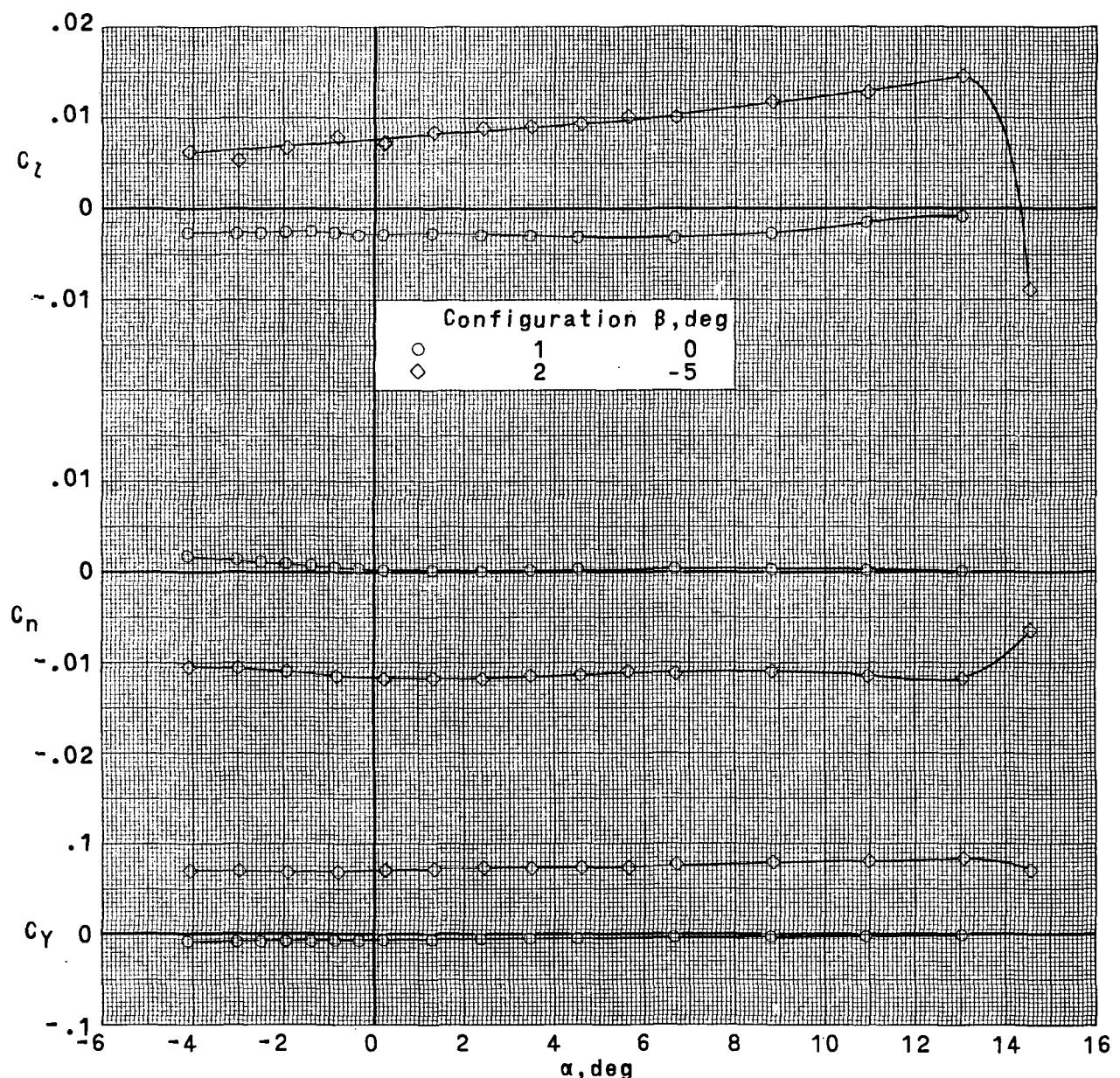


(e) $M = 0.76$; $R_{\bar{C}} = 3.86 \times 10^6$.

Figure 18.- Concluded.

~~CONFIDENTIAL~~

~~CONFIDENTIAL~~

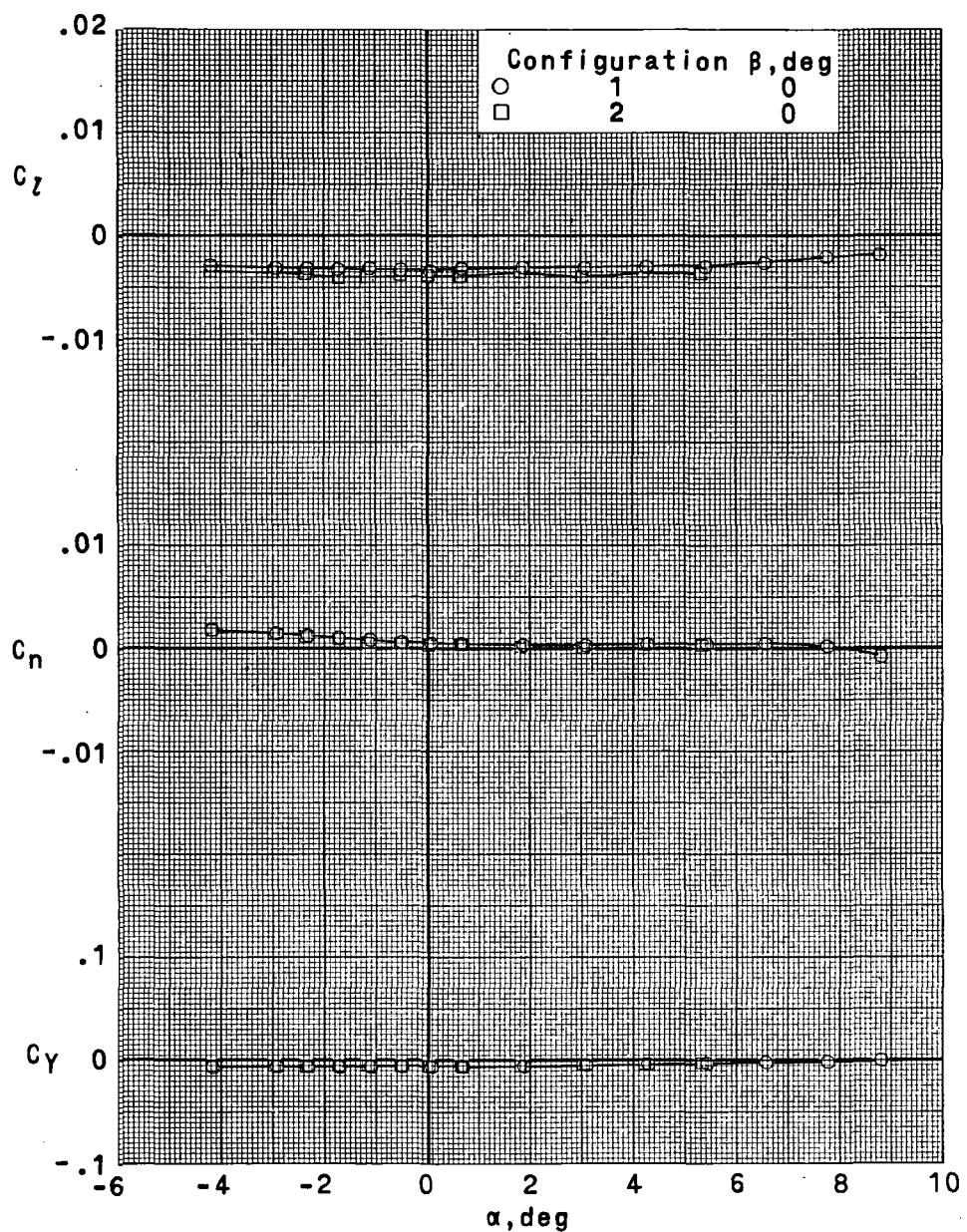


(a) $M = 0.30; R_C^- = 2.00 \times 10^6$.

Figure 19.- Effect of angle of attack on lateral stability characteristics.

$\delta_e = 0^\circ; i_h = 0^\circ; \delta_a = 0^\circ$.

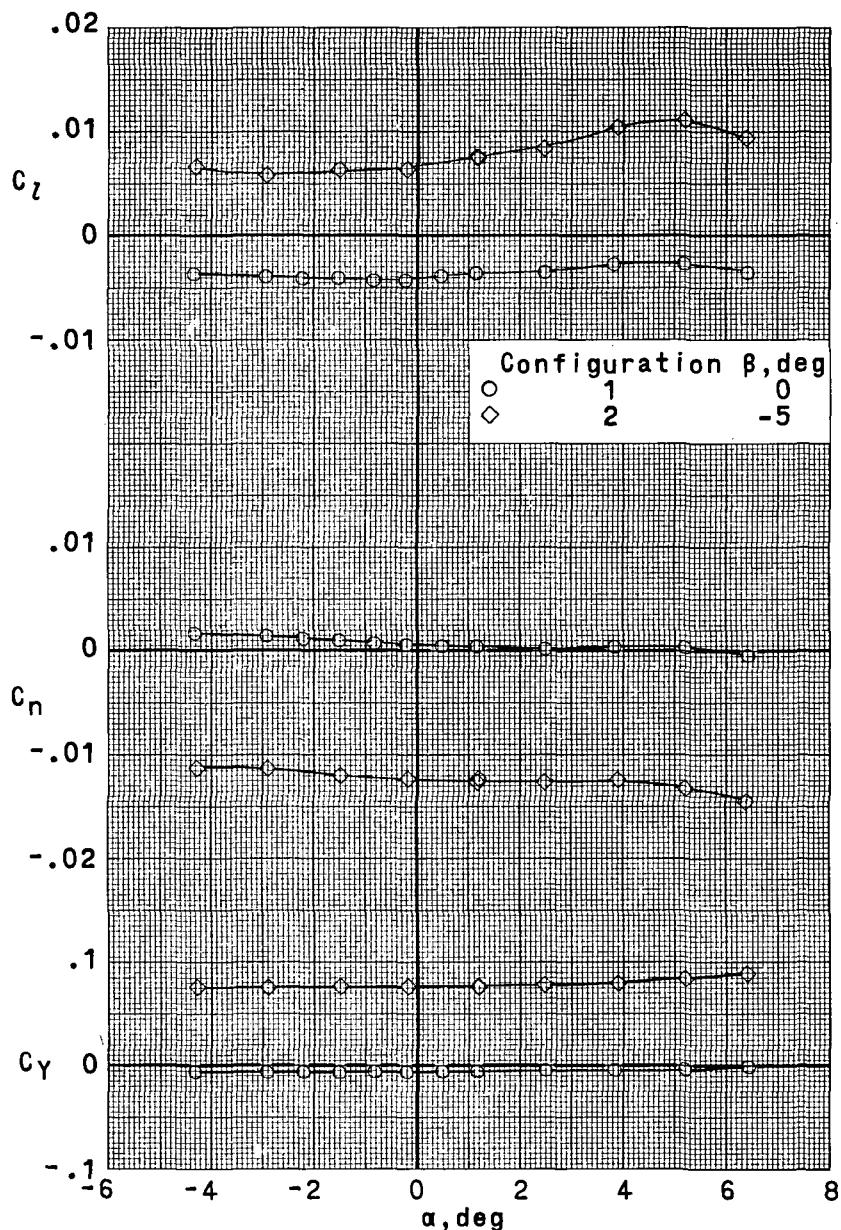
~~CONFIDENTIAL~~



(b) $M = 0.50; R_{\bar{C}} = 2.67 \times 10^6$.

Figure 19.- Continued.

~~CONFIDENTIAL~~

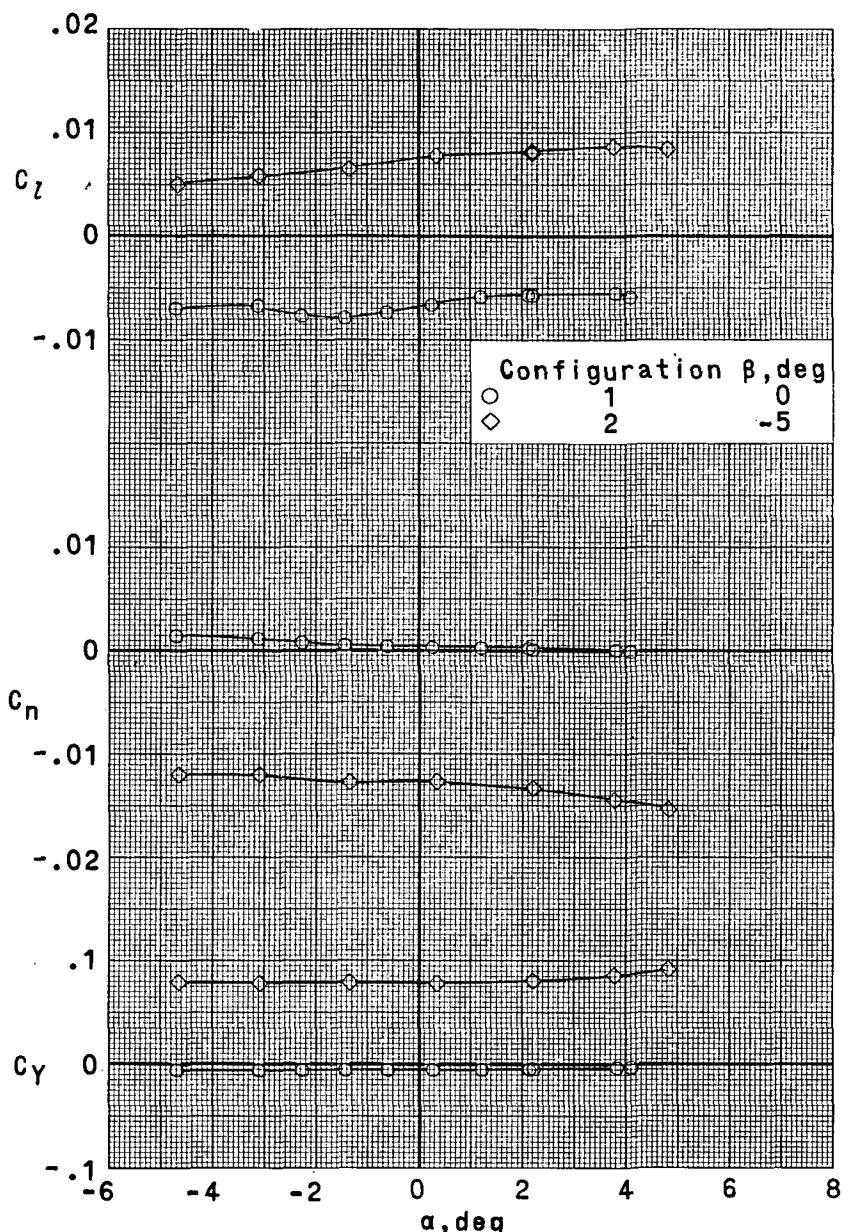


(c) $M = 0.60; R_C = 2.67 \times 10^6$.

Figure 19.- Continued.

~~CONFIDENTIAL~~

~~CONFIDENTIAL~~

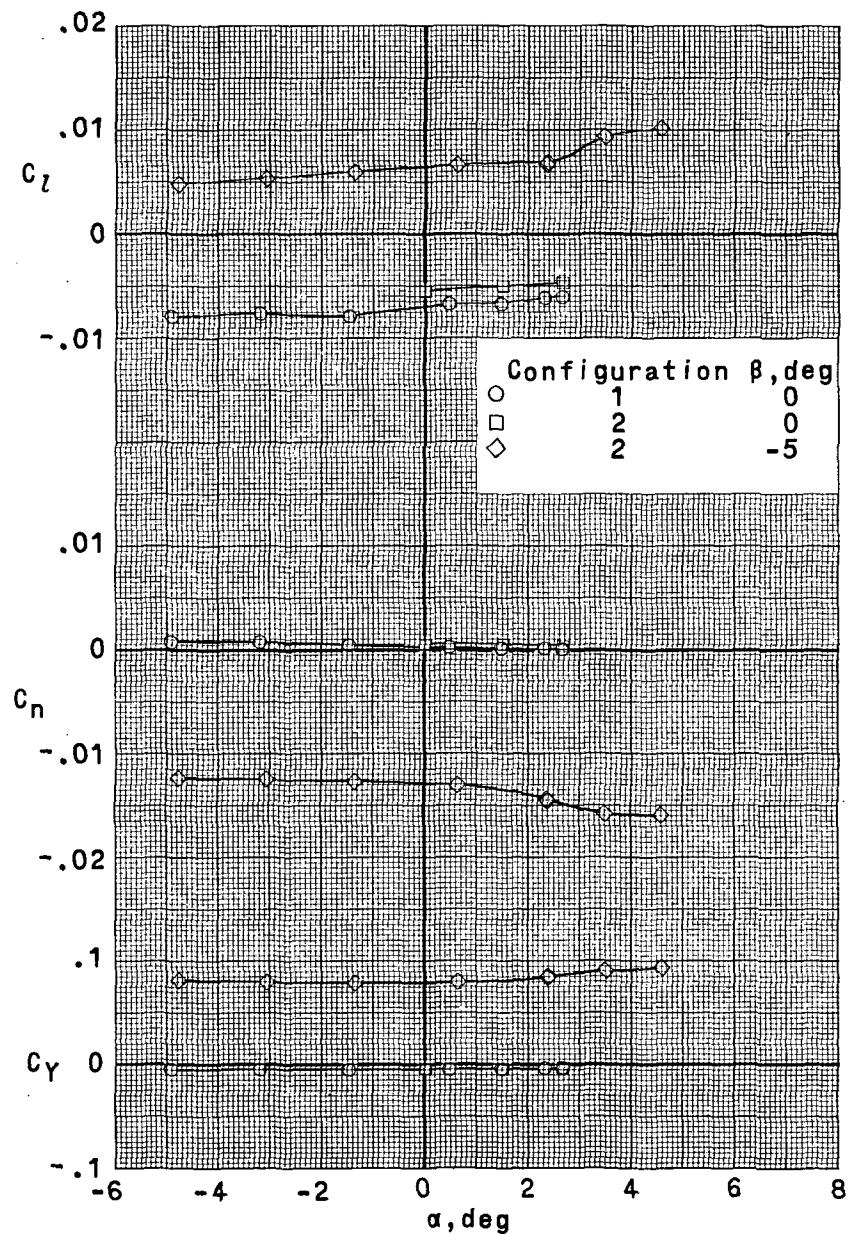


(d) $M = 0.70; R_C^- = 3.86 \times 10^6$.

Figure 19.- Continued.

~~CONFIDENTIAL~~

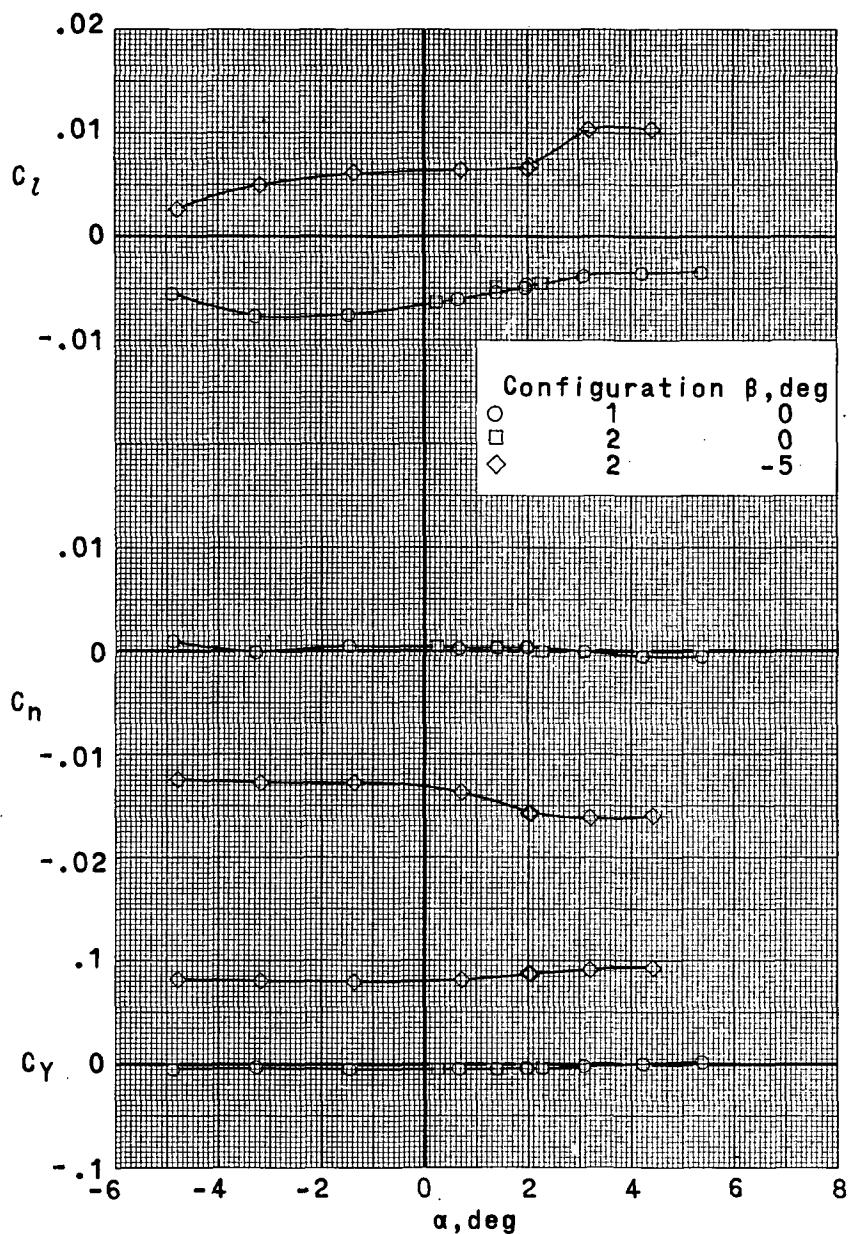
~~CONFIDENTIAL~~



(e) $M = 0.73; R_C = 3.86 \times 10^6$.

Figure 19.- Continued.

~~CONFIDENTIAL~~

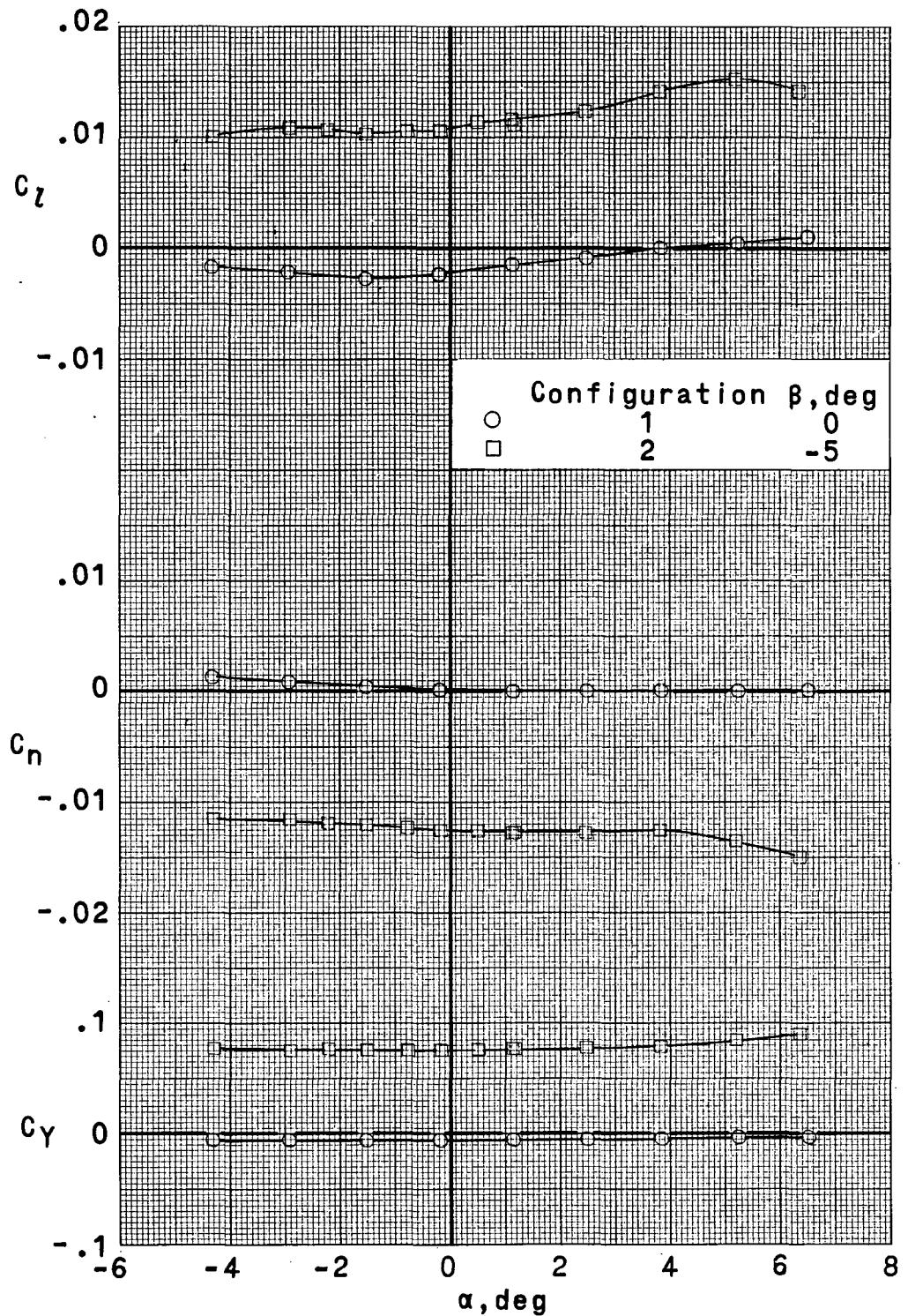


(f) $M = 0.75$; $R_{\bar{C}} = 3.86 \times 10^6$.

Figure 19.- Concluded.

~~CONFIDENTIAL~~

~~CONFIDENTIAL~~



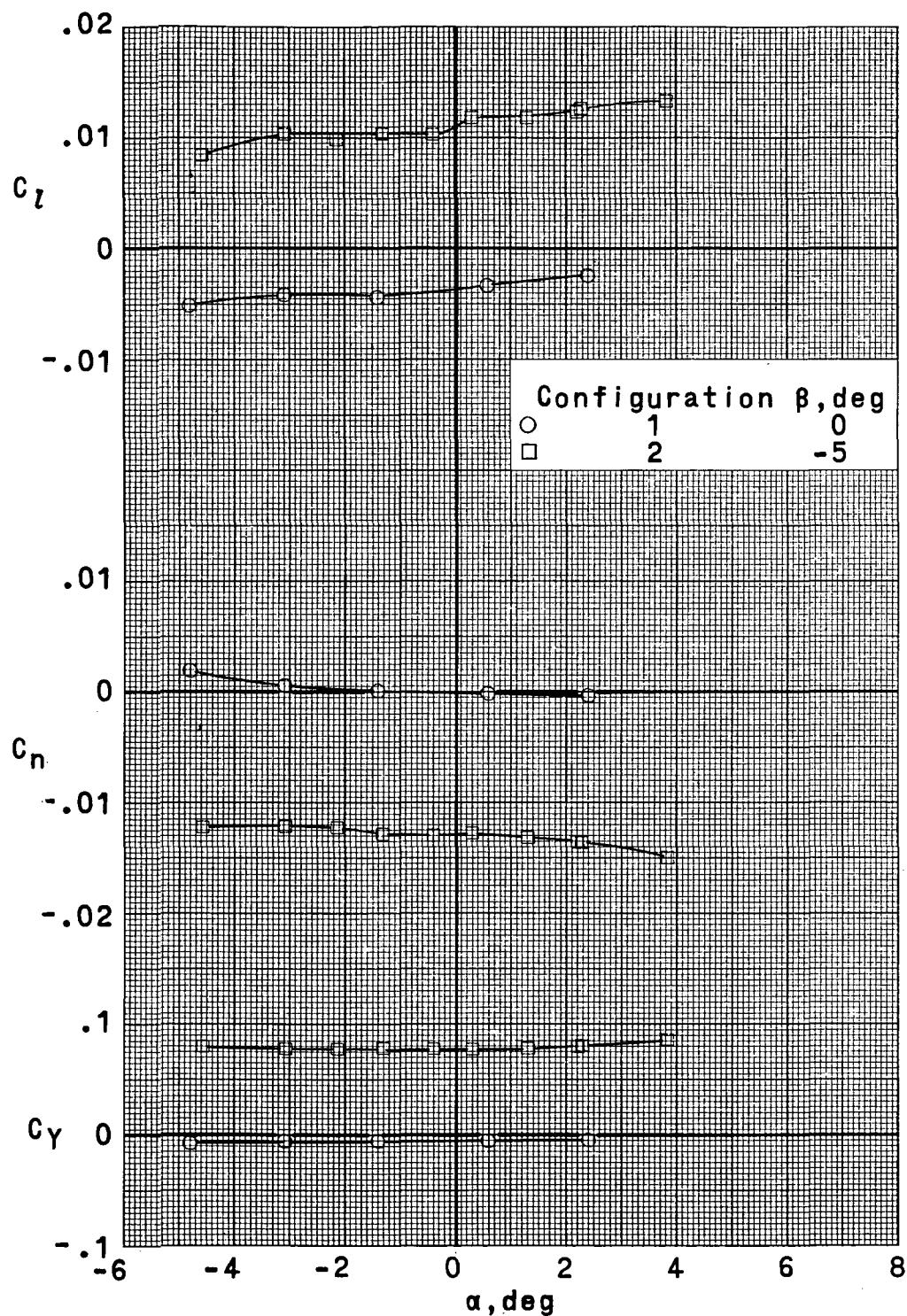
(a) $M = 0.60; R_C = 3.33 \times 10^6$.

Figure 20.- Effect of angle of attack on lateral stability characteristics.

$\delta_e = 0^\circ; i_h = 0^\circ; \delta_a = 3^\circ$.

~~CONFIDENTIAL~~

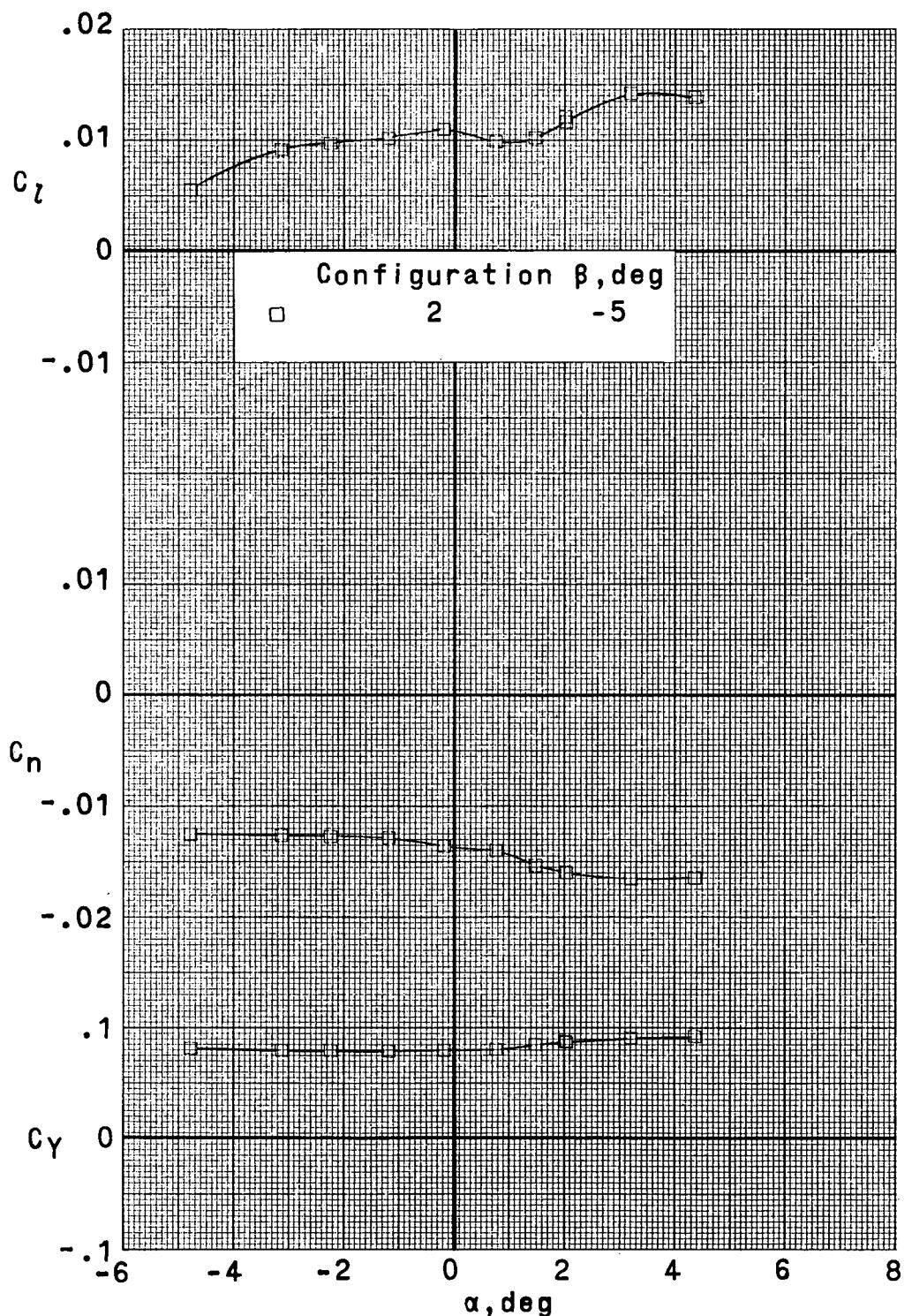
~~CONFIDENTIAL~~



(b) $M = 0.70; R_{\bar{C}} = 3.86 \times 10^6$.

Figure 20.- Continued.

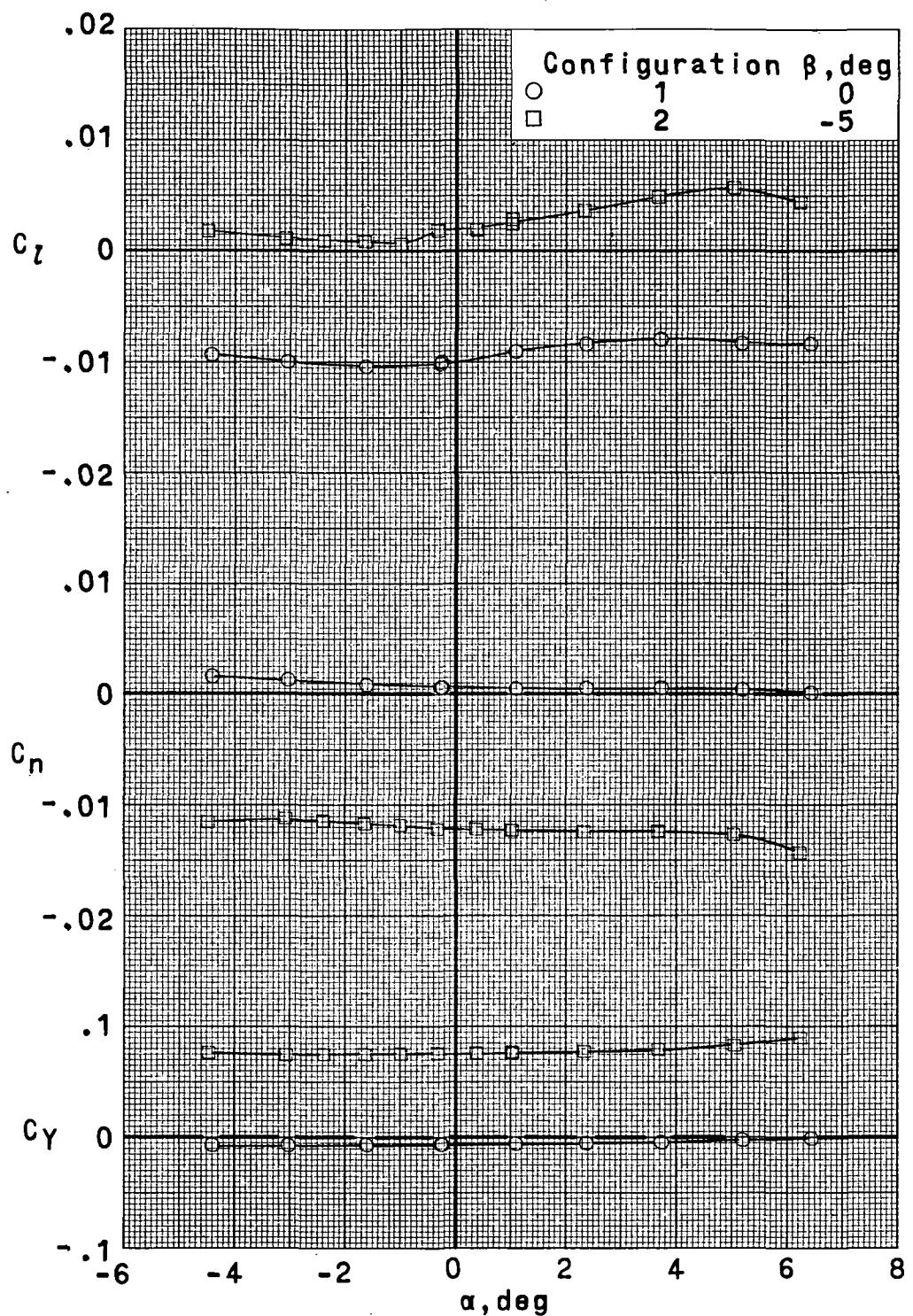
~~CONFIDENTIAL~~



(c) $M = 0.75; R_{\bar{C}} = 3.86 \times 10^6$.

Figure 20.- Concluded.

~~CONFIDENTIAL~~



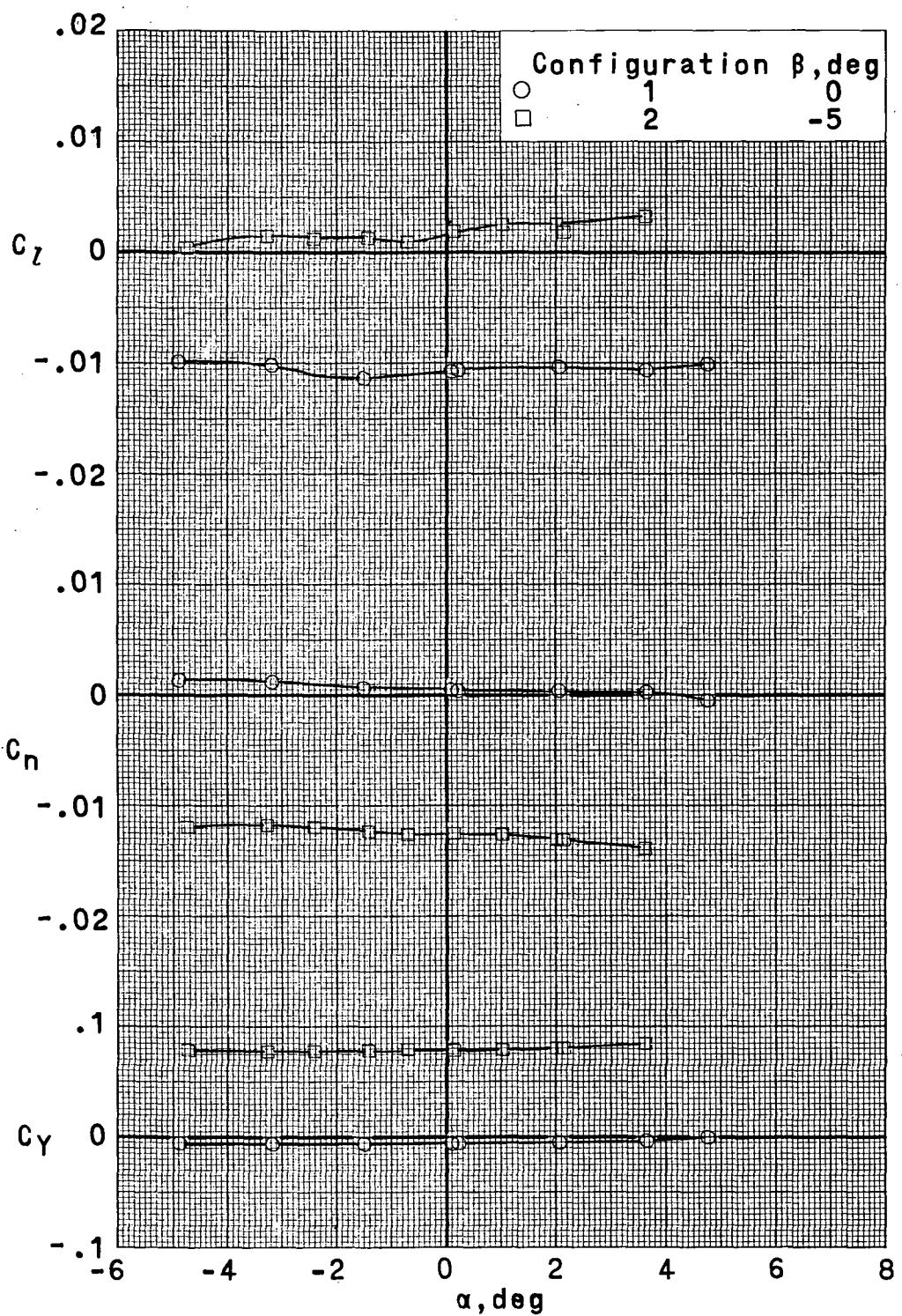
(a) $M = 0.60$; $R_{\bar{C}} = 3.86 \times 10^6$.

Figure 21.- Effect of angle of attack on lateral stability characteristics.

$\delta_e = 0^\circ$; $i_h = 0^\circ$; $\delta_a = -3^\circ$.

~~CONFIDENTIAL~~

~~CONFIDENTIAL~~

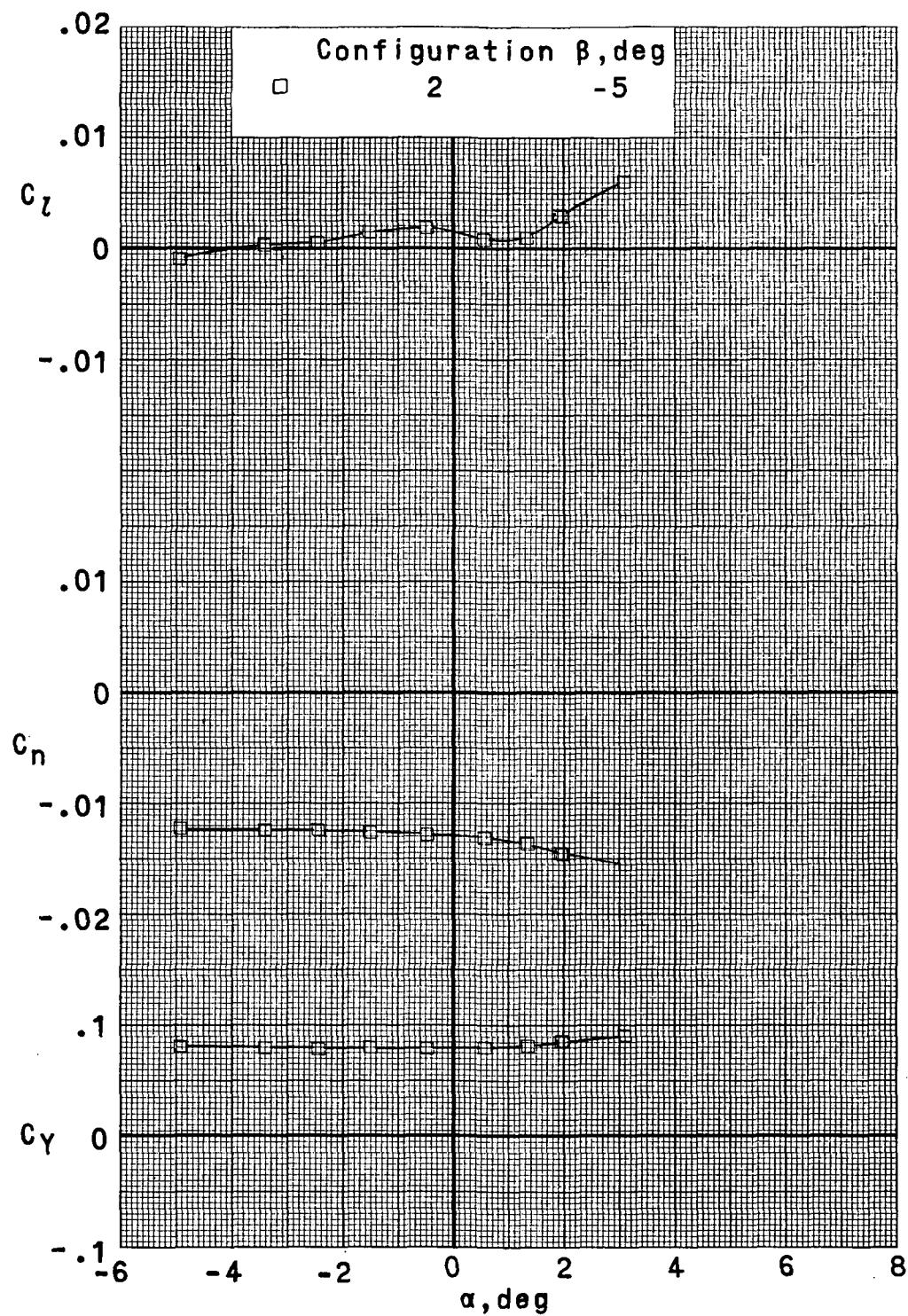


(b) $M = 0.70; R_C = 3.86 \times 10^6$.

Figure 21.- Continued.

~~CONFIDENTIAL~~

~~CONFIDENTIAL~~

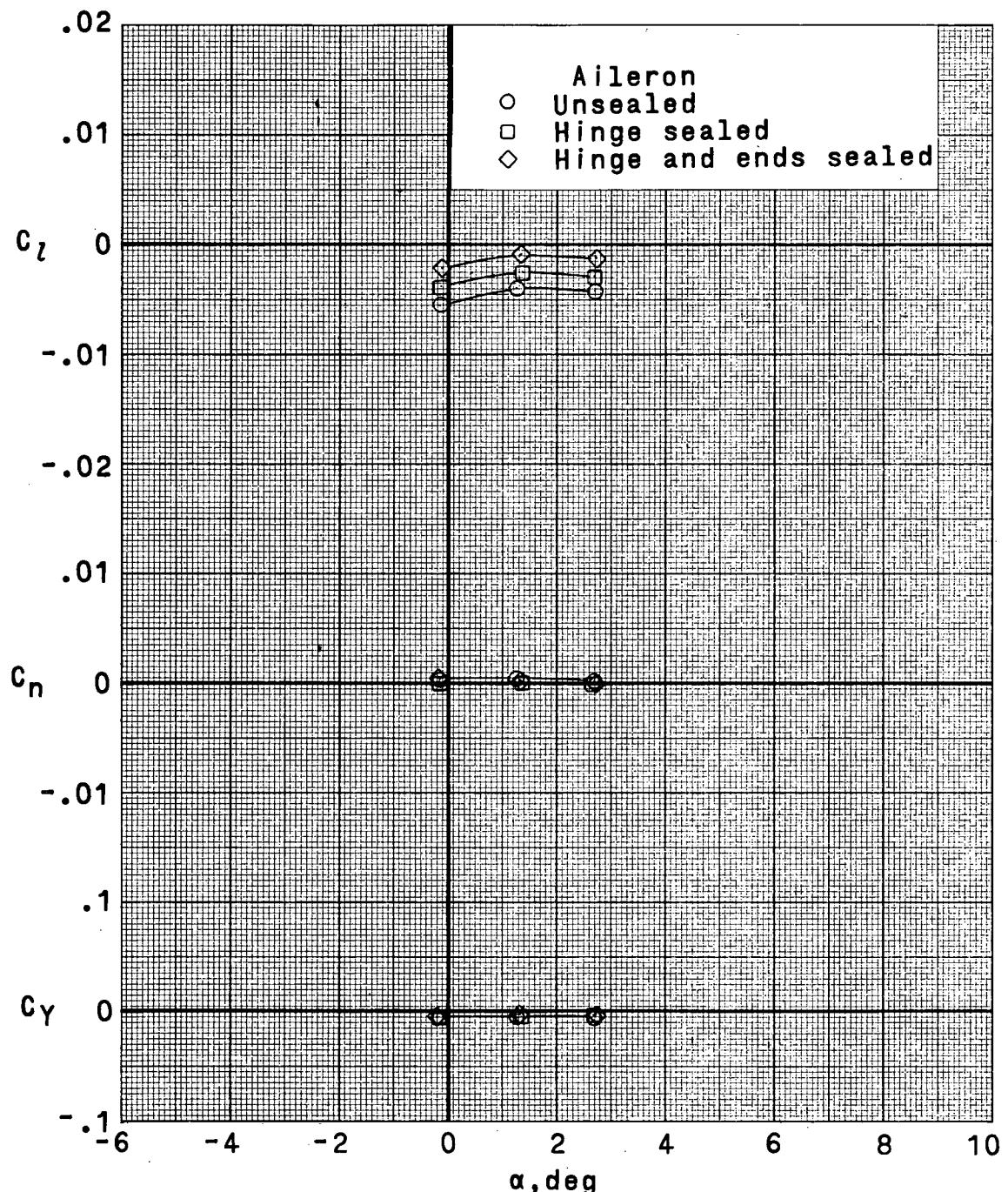


(c) $M = 0.75; R_{\bar{C}} = 3.86 \times 10^6$.

Figure 21.- Concluded.

~~CONFIDENTIAL~~

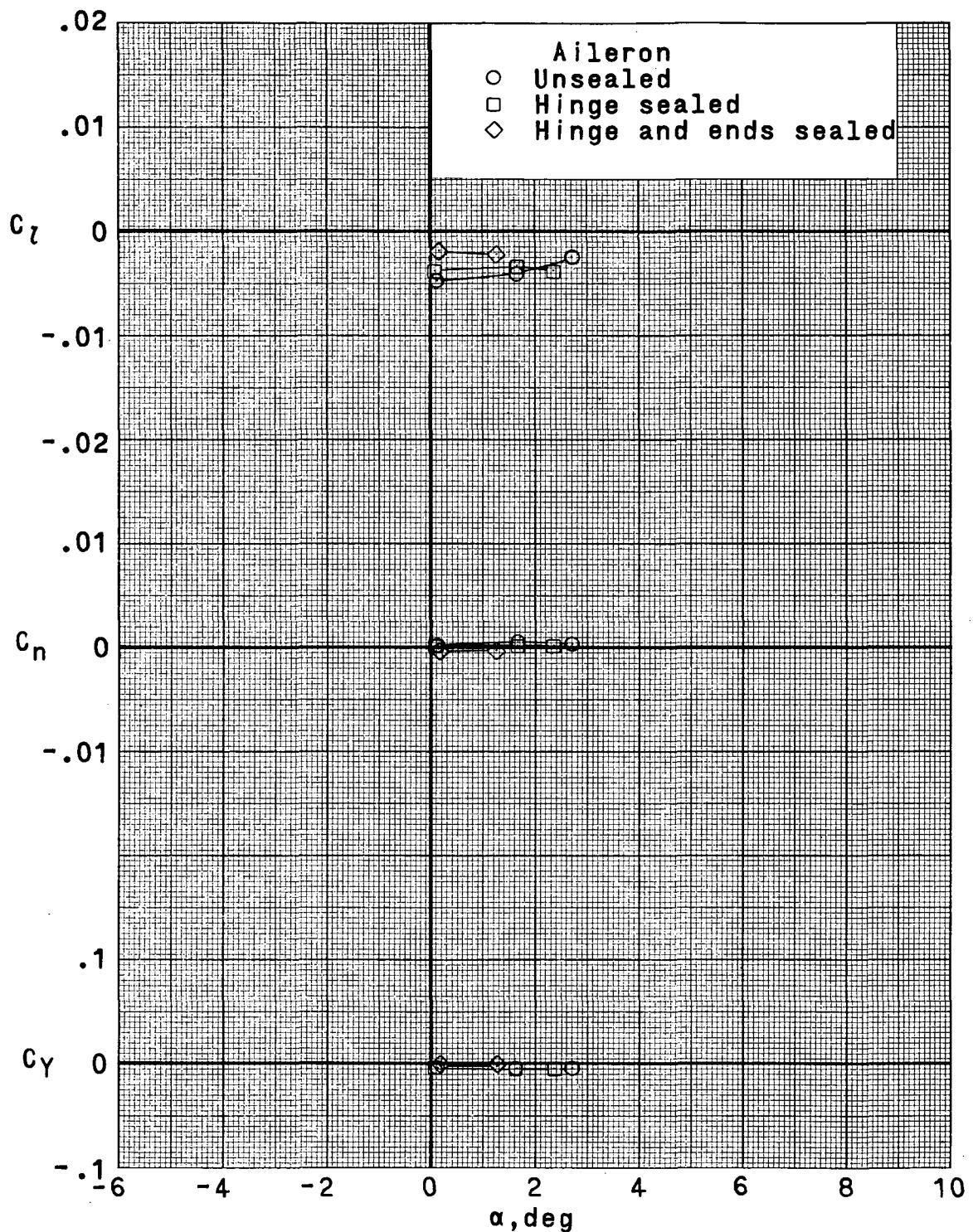
~~CONFIDENTIAL~~



(a) $M = 0.70$; $R_{\bar{C}} = 3.86 \times 10^6$.

Figure 22. - Effect of aileron hinge-line and end seals on lateral stability characteristics.
 $\delta_e = 0^\circ$; $i_h = 0^\circ$; $\delta_a = 0^\circ$; $\beta = 0^\circ$; configuration 2.

~~CONFIDENTIAL~~

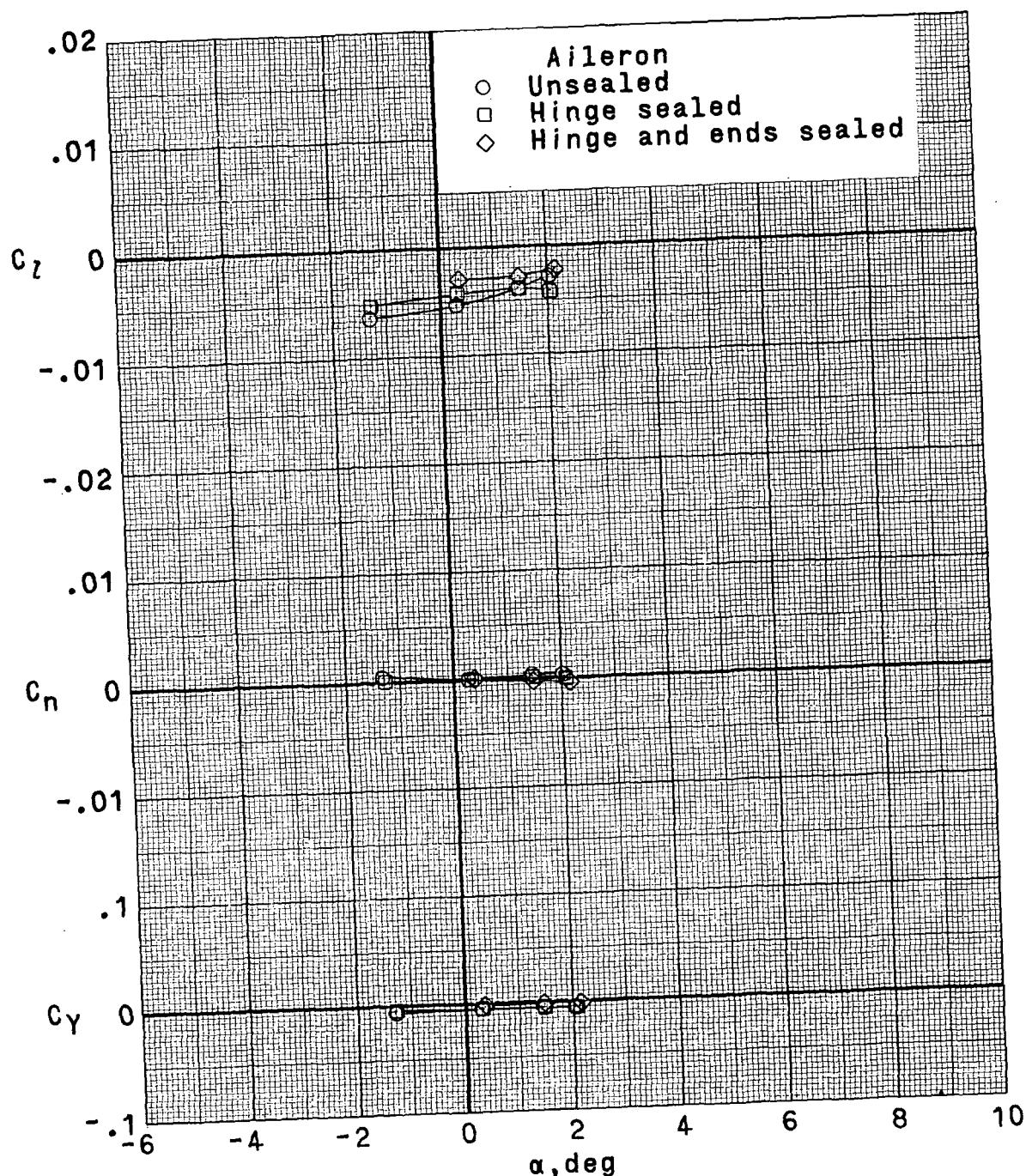


(b) $M = 0.73$; $R_{\bar{C}} = 3.86 \times 10^6$.

Figure 22.- Continued.

~~CONFIDENTIAL~~

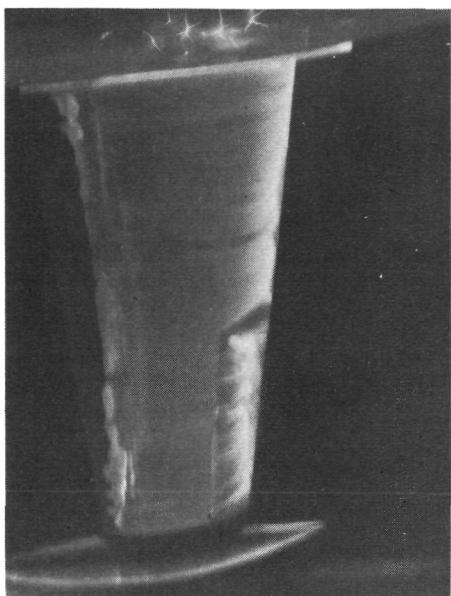
~~CONFIDENTIAL~~



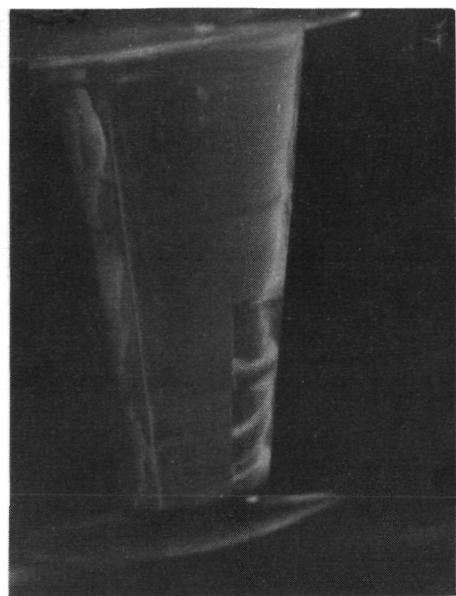
(c) $M = 0.75; R_{\bar{C}} = 3.86 \times 10^6$.

Figure 22.- Continued.

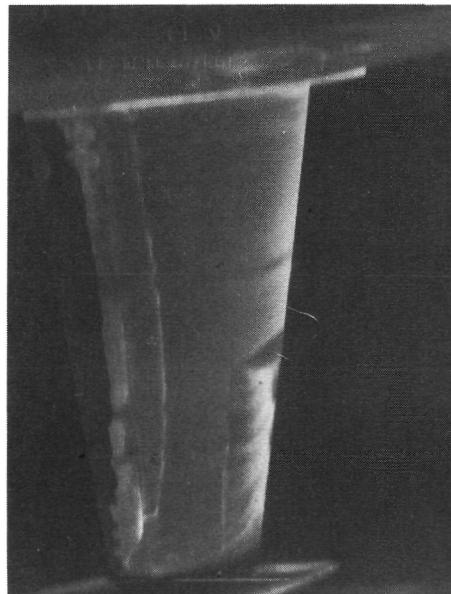
~~CONFIDENTIAL~~



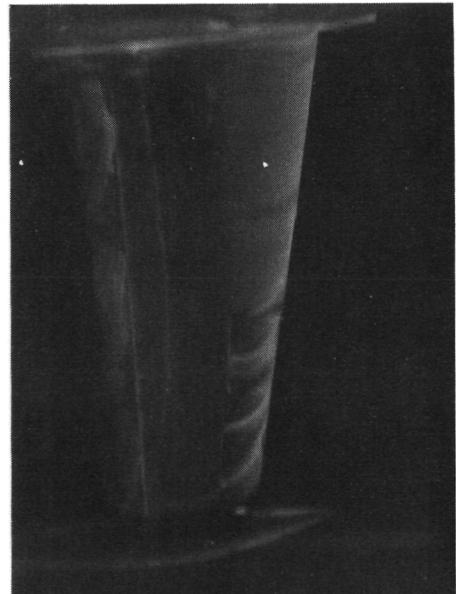
$$C_L = 0.494$$



$$C_L = 0.507$$



$$C_L = 0.682$$



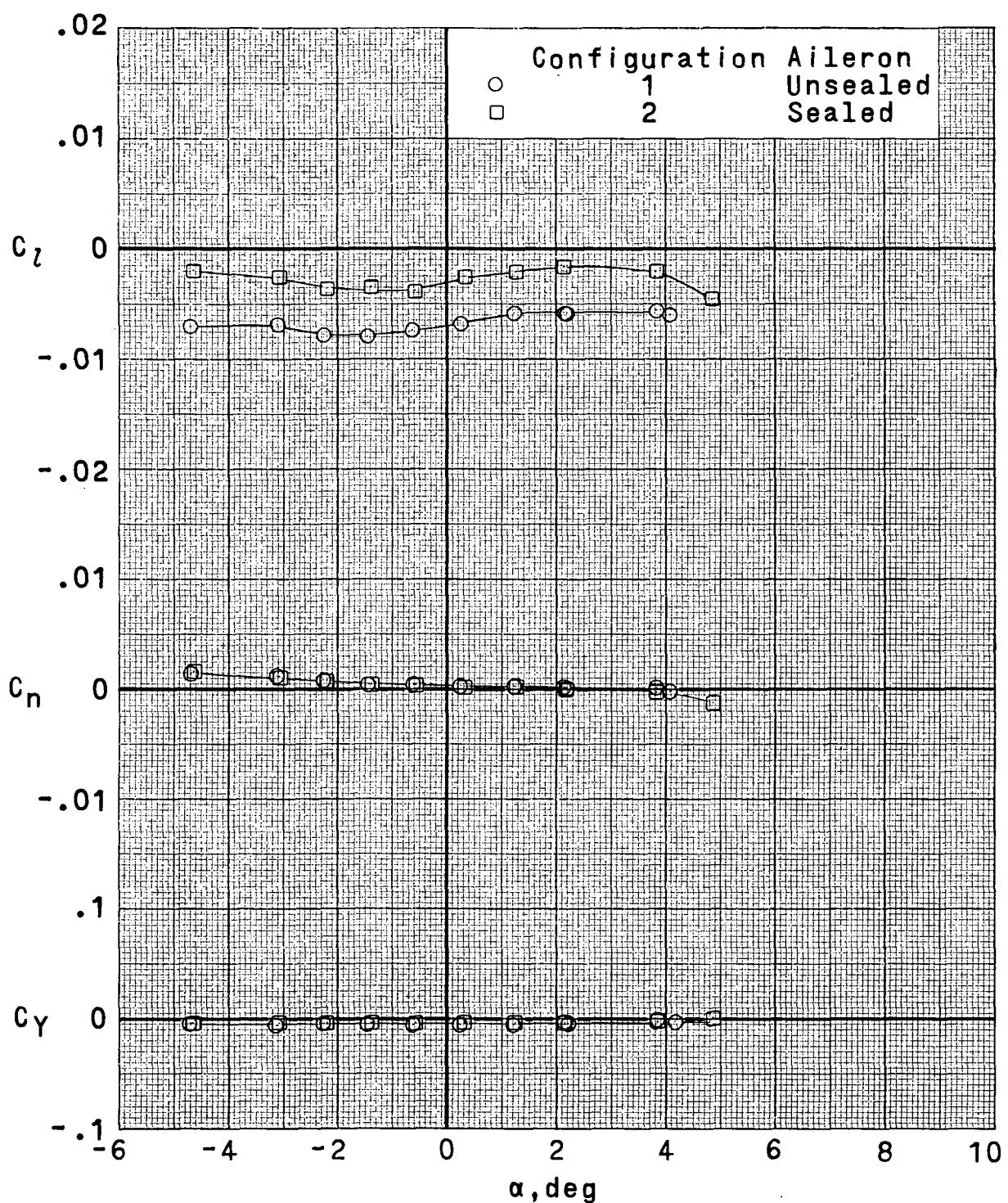
$$C_L = 0.696$$

(d) Upper surface aileron; $M = 0.70.$ L-72-2410

Figure 22.- Concluded.

~~CONFIDENTIAL~~

~~CONFIDENTIAL~~

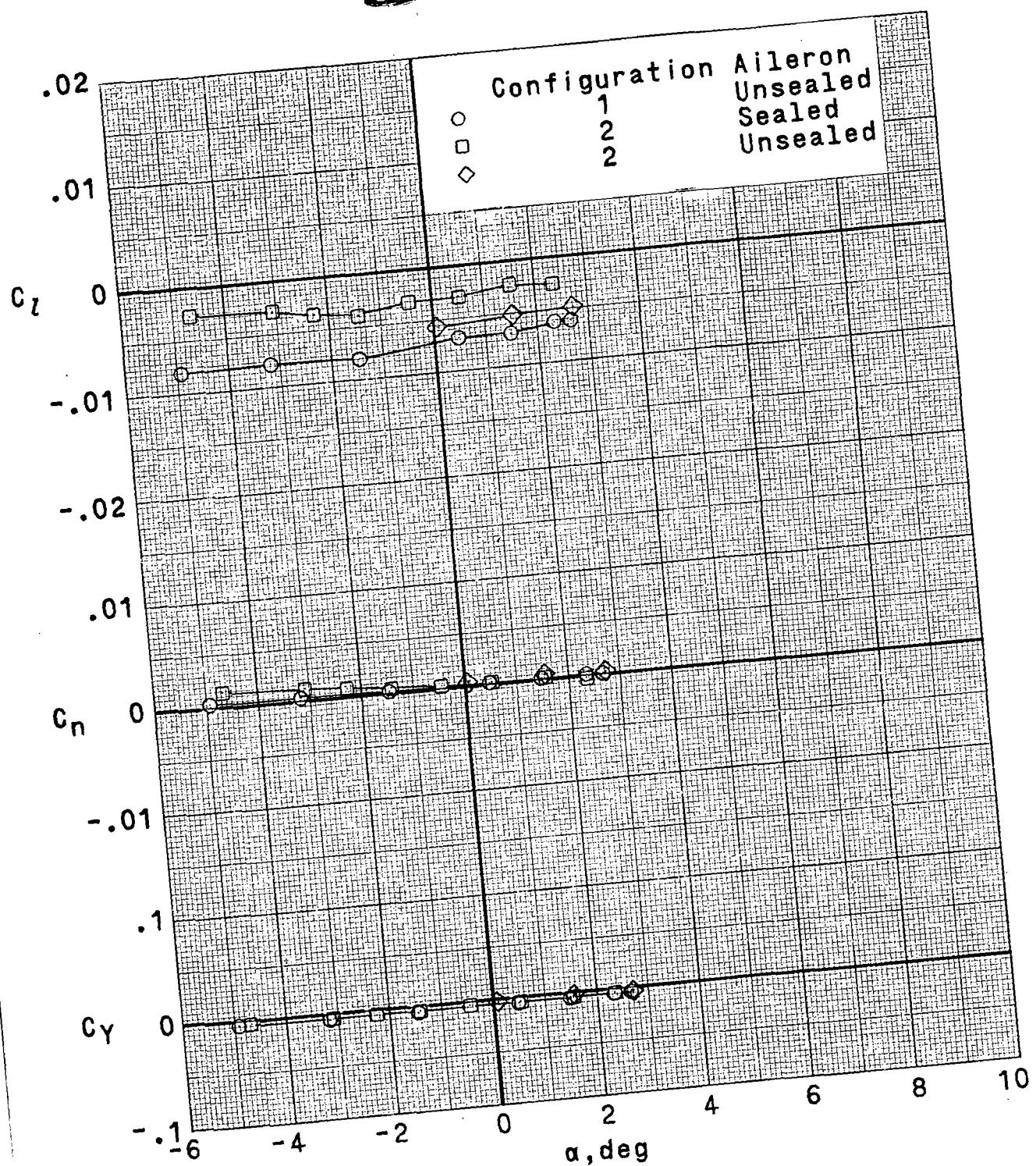


(a) $M = 0.70$; $R_{\bar{C}} = 3.86 \times 10^6$.

Figure 23.- Effect of sealed aileron on lateral stability characteristics.

$\delta_e = 0^\circ$; $i_h = 0^\circ$; $\delta_a = 0^\circ$; $\beta = 0^\circ$.

~~CONFIDENTIAL~~

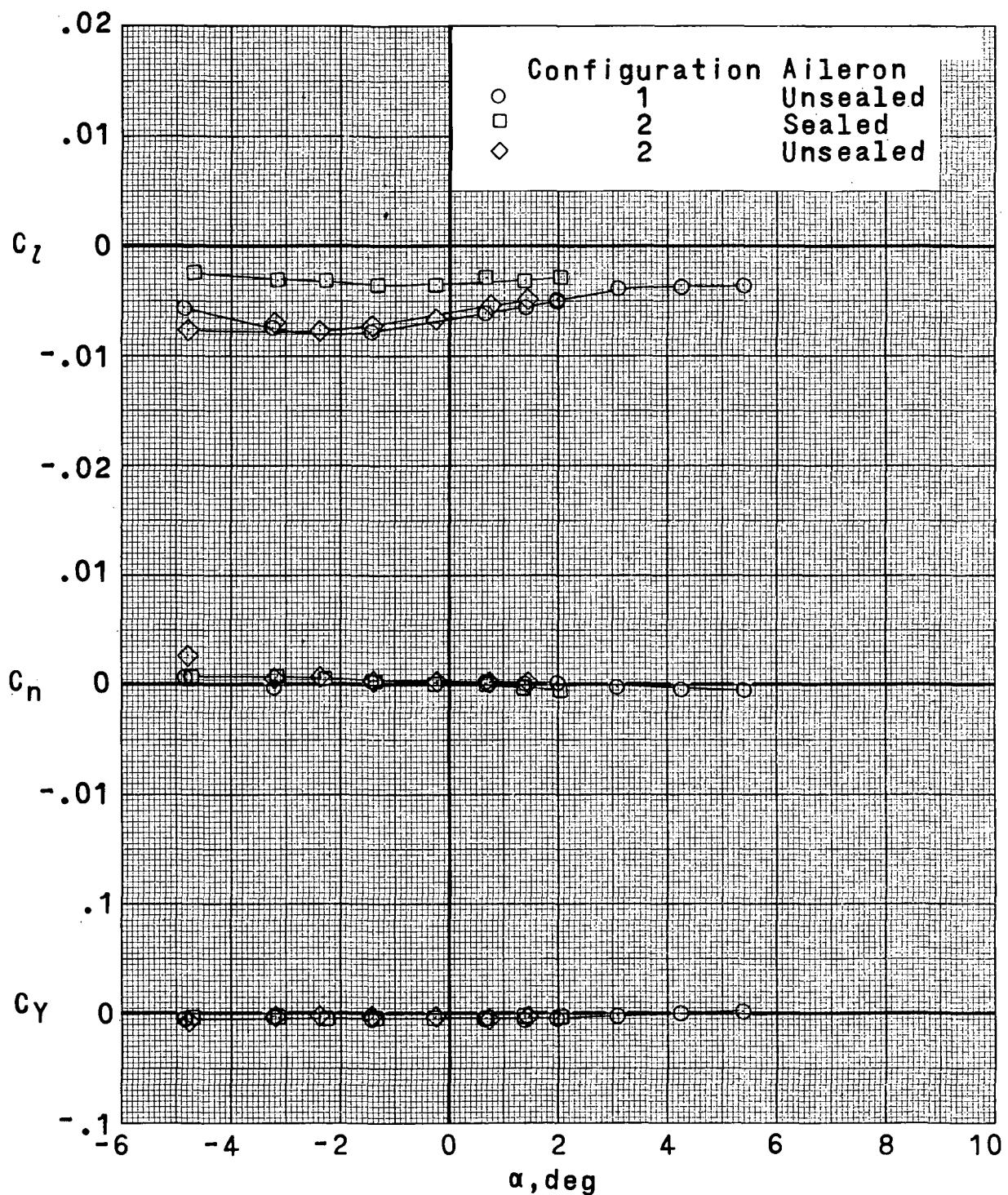


(b) $M = 0.73; R_{\bar{C}} = 3.86 \times 10^6$.

Figure 23.- Continued.

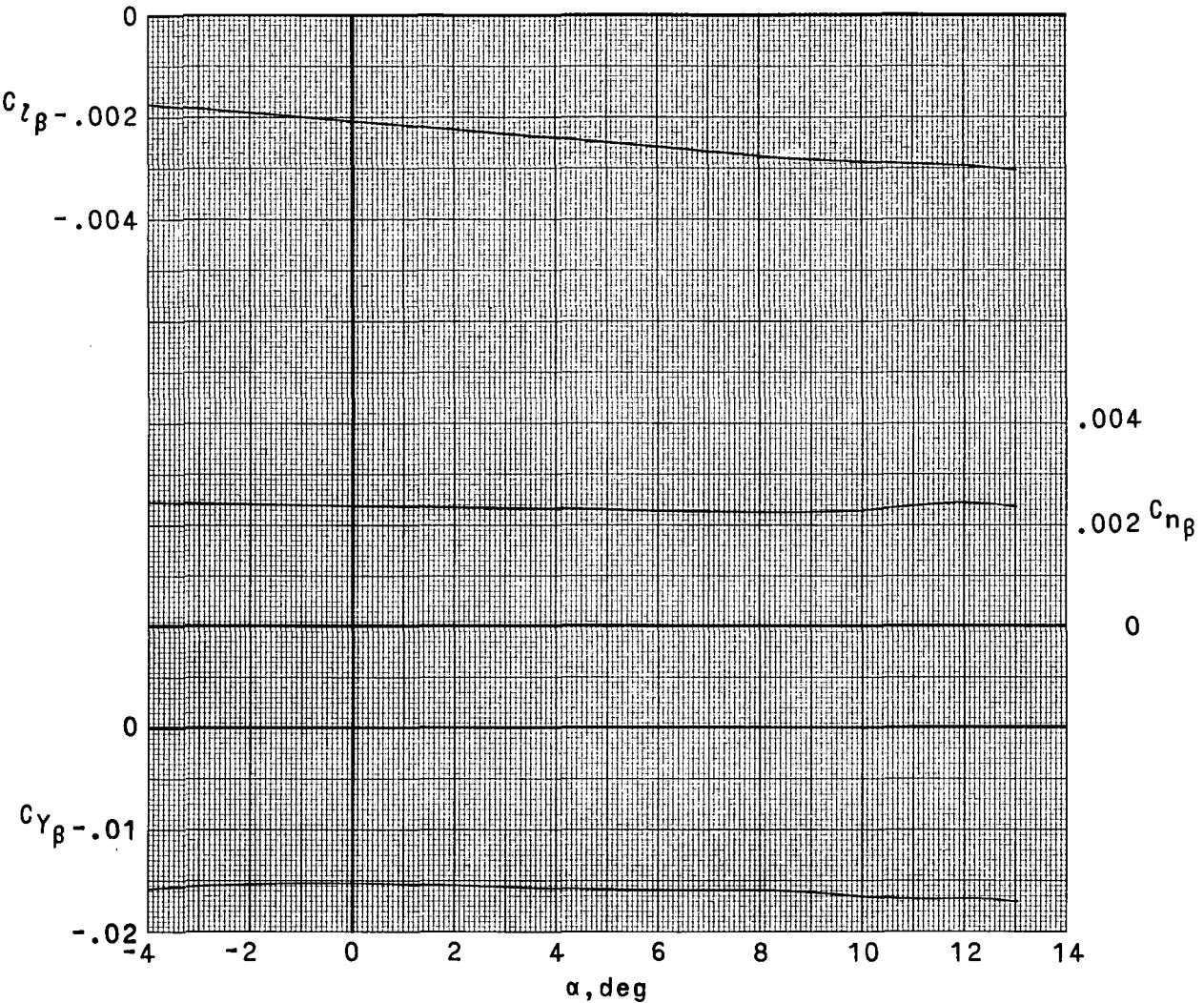
~~CONFIDENTIAL~~

~~CONFIDENTIAL~~



(c) $M = 0.75$; $R_{\bar{C}} = 3.86 \times 10^6$.

Figure 23.- Concluded.

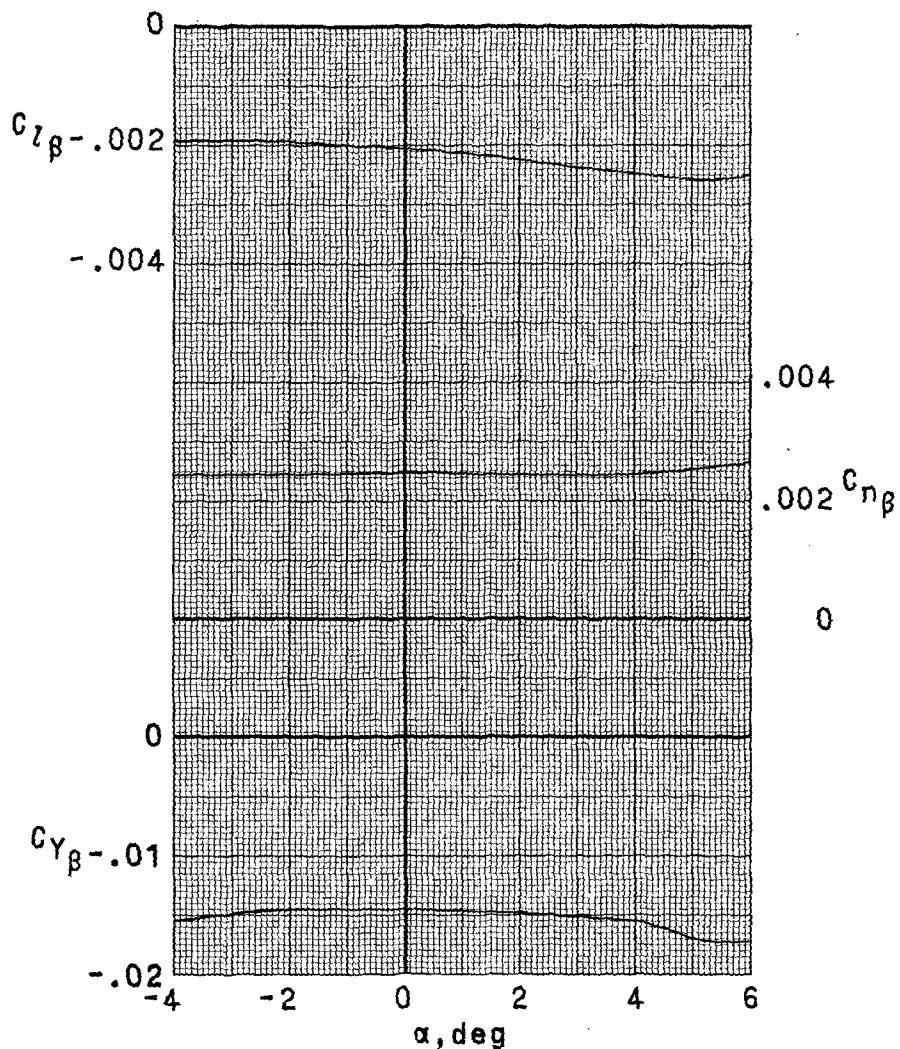


(a) $M = 0.30; R_C = 2.00 \times 10^6$.

Figure 24.- Variation of lateral stability derivatives with angle of attack.

$\delta_e = 0^\circ; i_h = 0^\circ; \delta_a = 0^\circ; \beta = 0^\circ$.

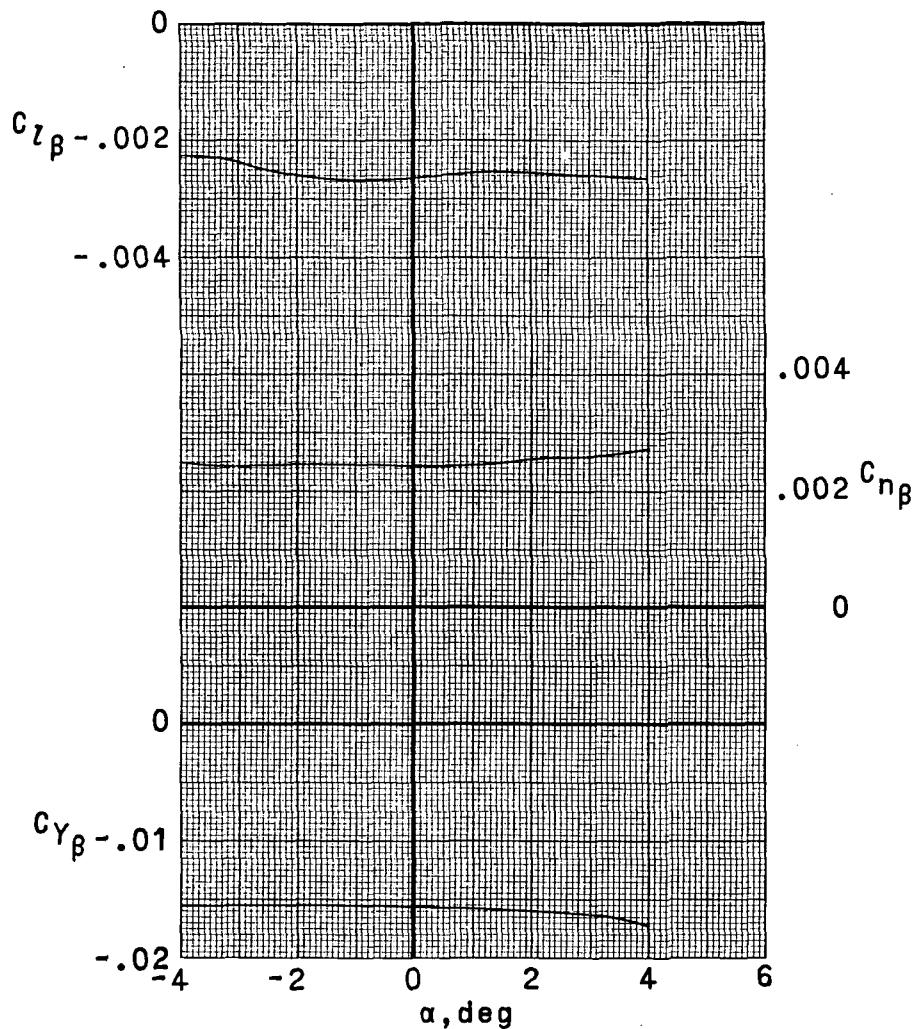
~~CONFIDENTIAL~~



(b) $M = 0.60; R_{\bar{C}} = 3.33 \times 10^6$.

Figure 24.- Continued.

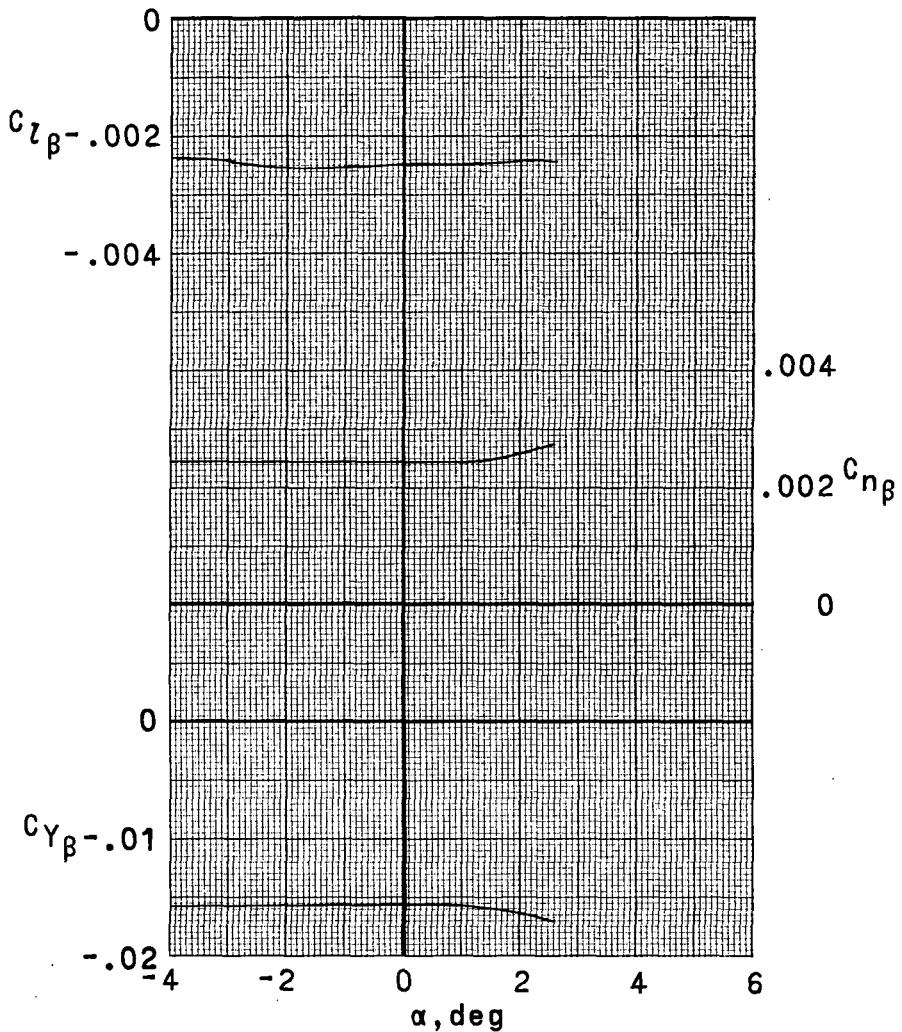
~~CONFIDENTIAL~~



(c) $M = 0.70; R_C = 3.86 \times 10^6.$

Figure 24.- Continued.

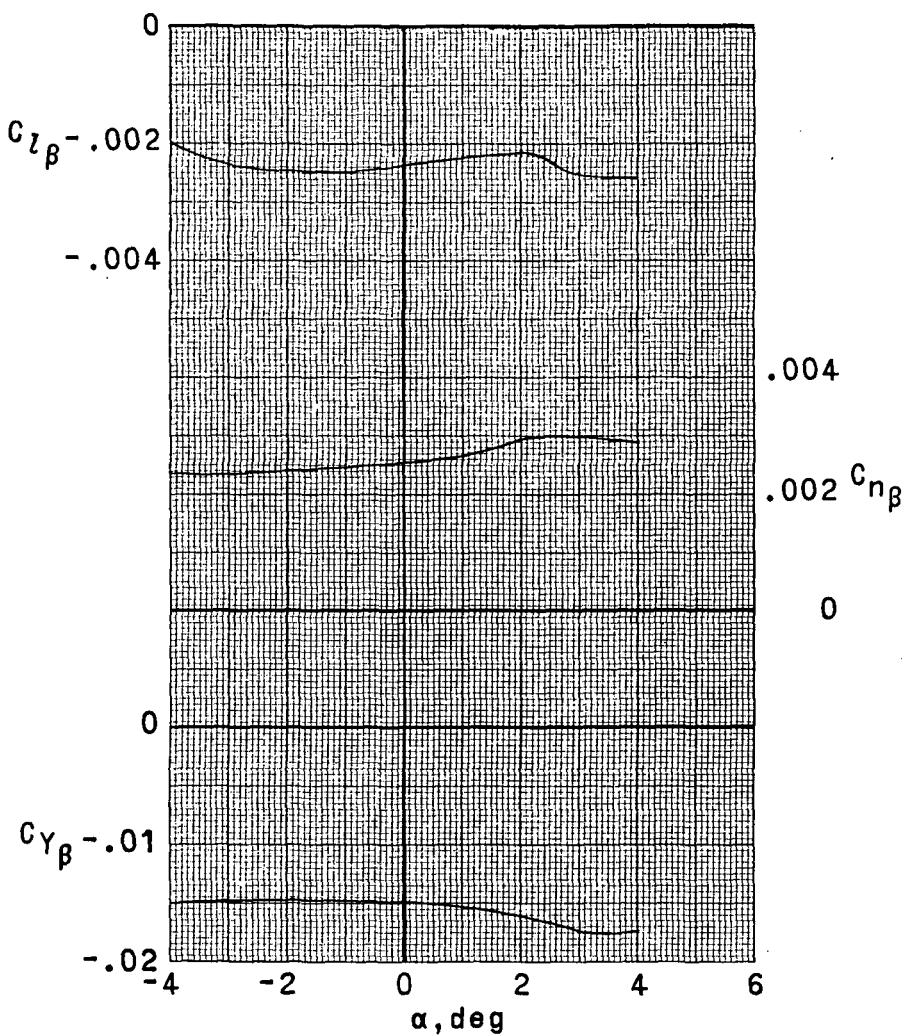
~~CONFIDENTIAL~~



(d) $M = 0.73; R_{\bar{C}} = 3.86 \times 10^6$.

Figure 24.- Continued.

~~CONFIDENTIAL~~



(e) $M = 0.75; R_{\bar{C}} = 3.86 \times 10^6$.

Figure 24.- Concluded.

~~CONFIDENTIAL~~

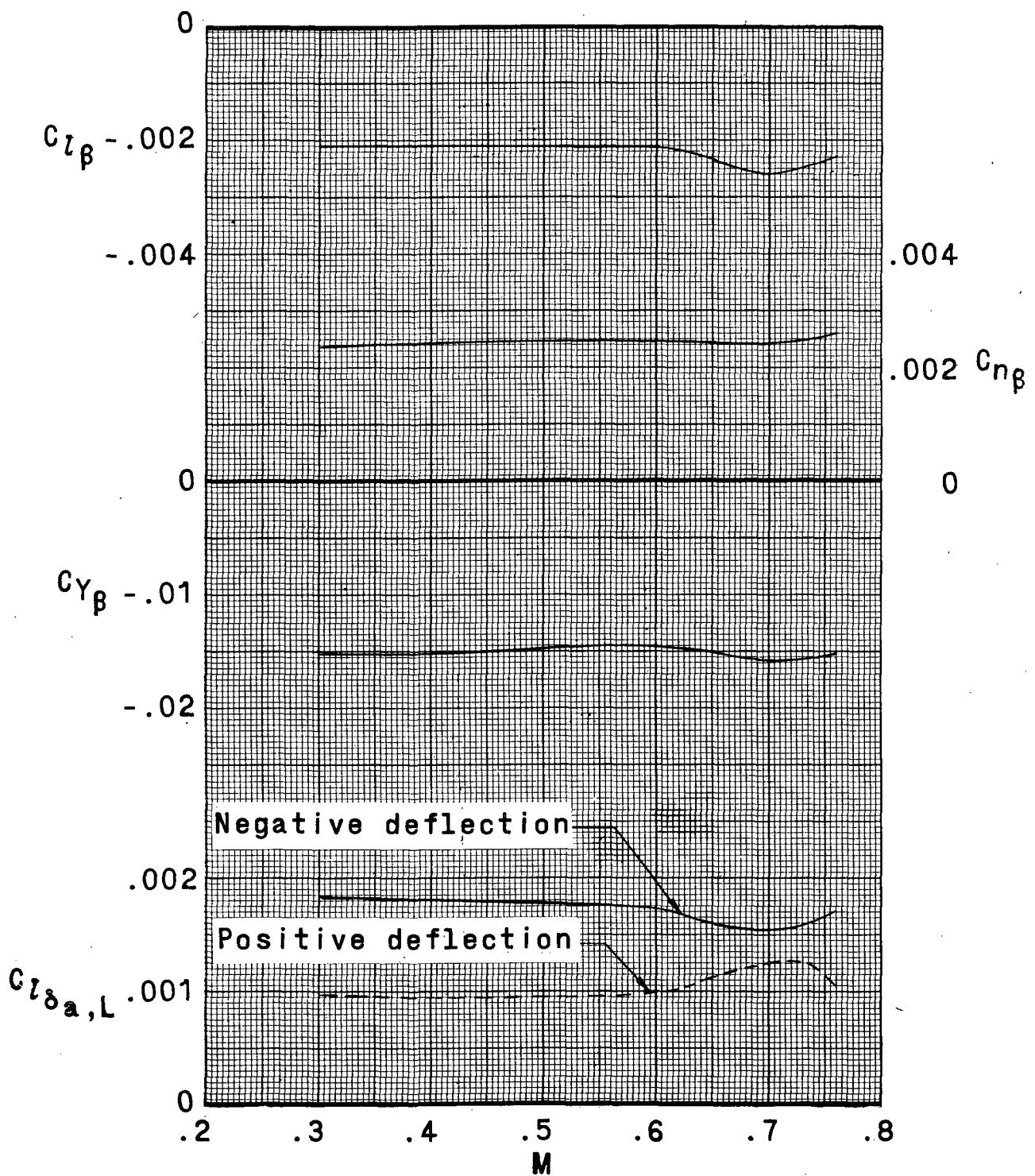
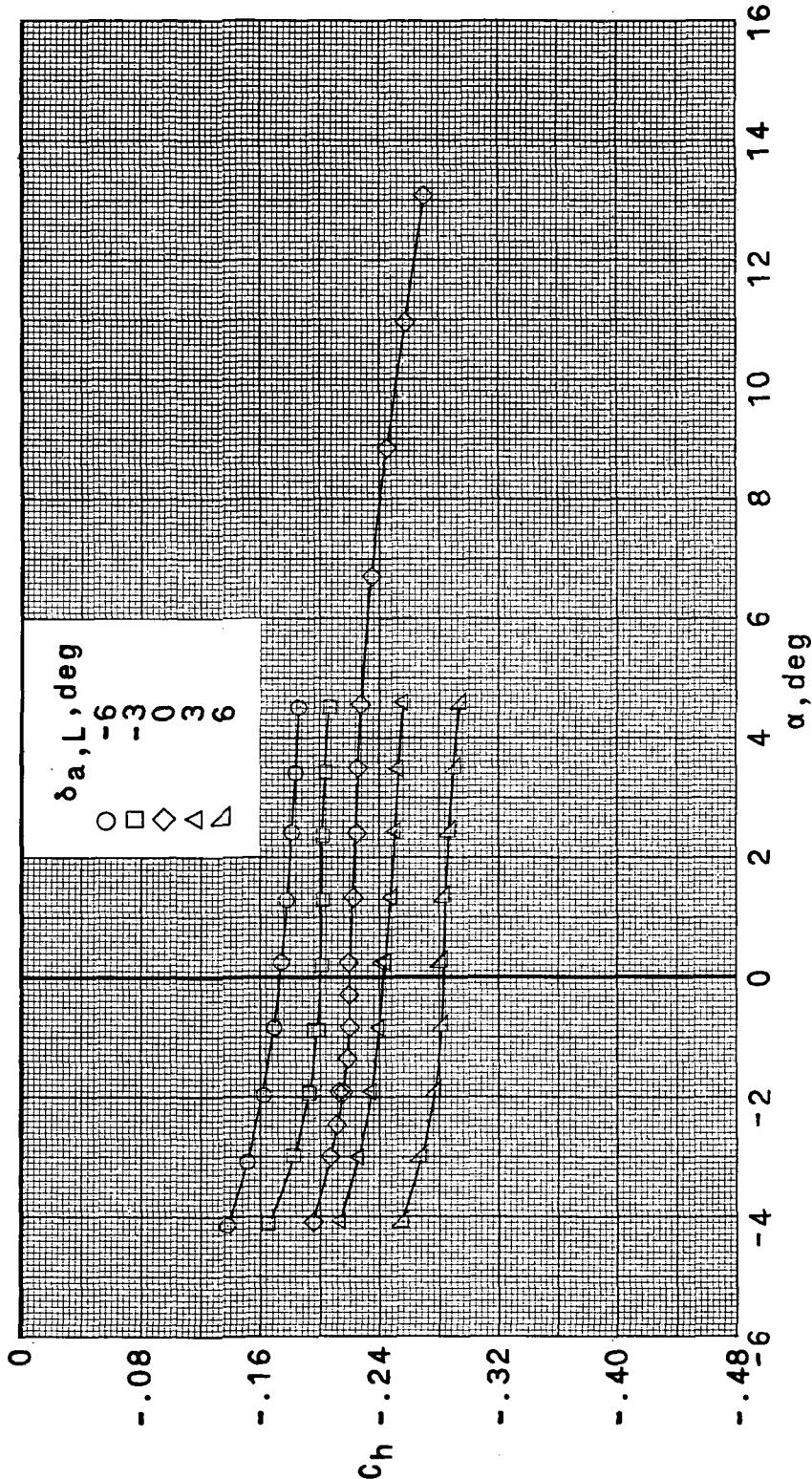


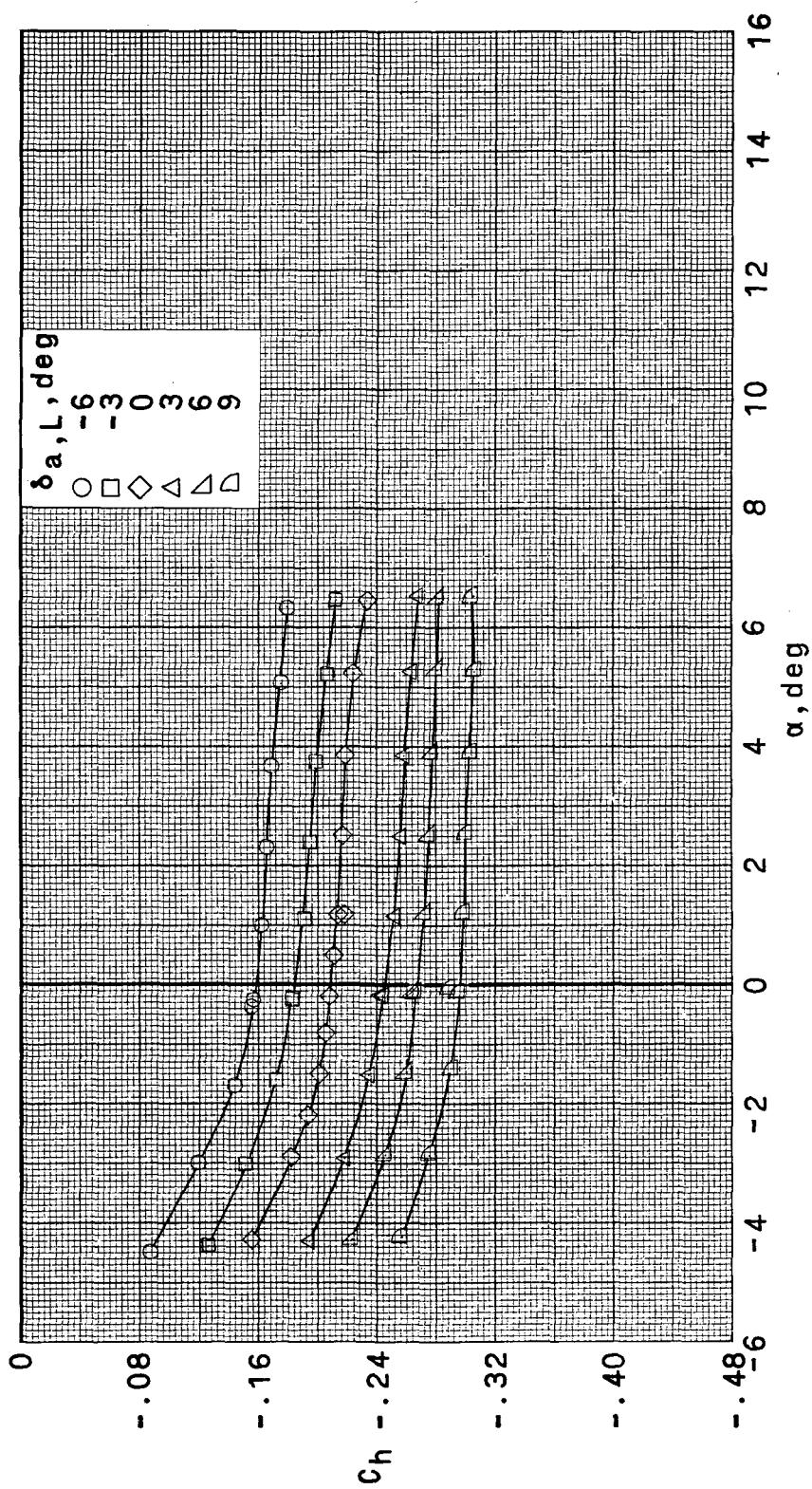
Figure 25.- Variation of lateral stability and control derivatives with Mach number.

$$\delta_a = 0^\circ; \quad i_h = 0^\circ; \quad \beta = 0^\circ; \quad \alpha \approx 1^\circ.$$



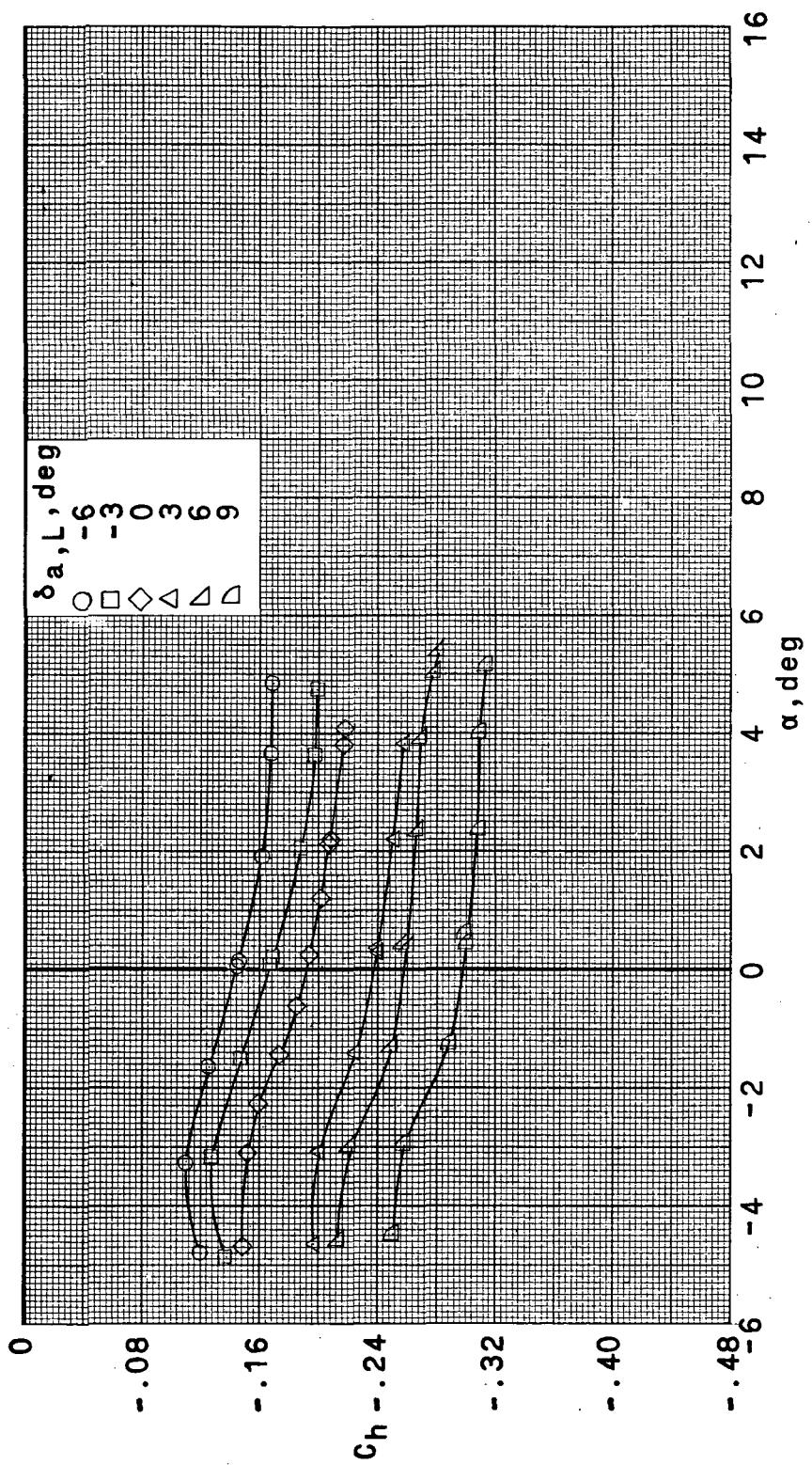
(a) $M = 0.30; R_C = 2.00 \times 10^6$.

Figure 26.- Effect of angle of attack on aileron hinge-moment coefficients. $\delta_e = 0^\circ$; $i_h = 0^\circ$; $\beta = 0^\circ$.



(b) $M = 0.60$; $R_C = 3.33 \times 10^6$.

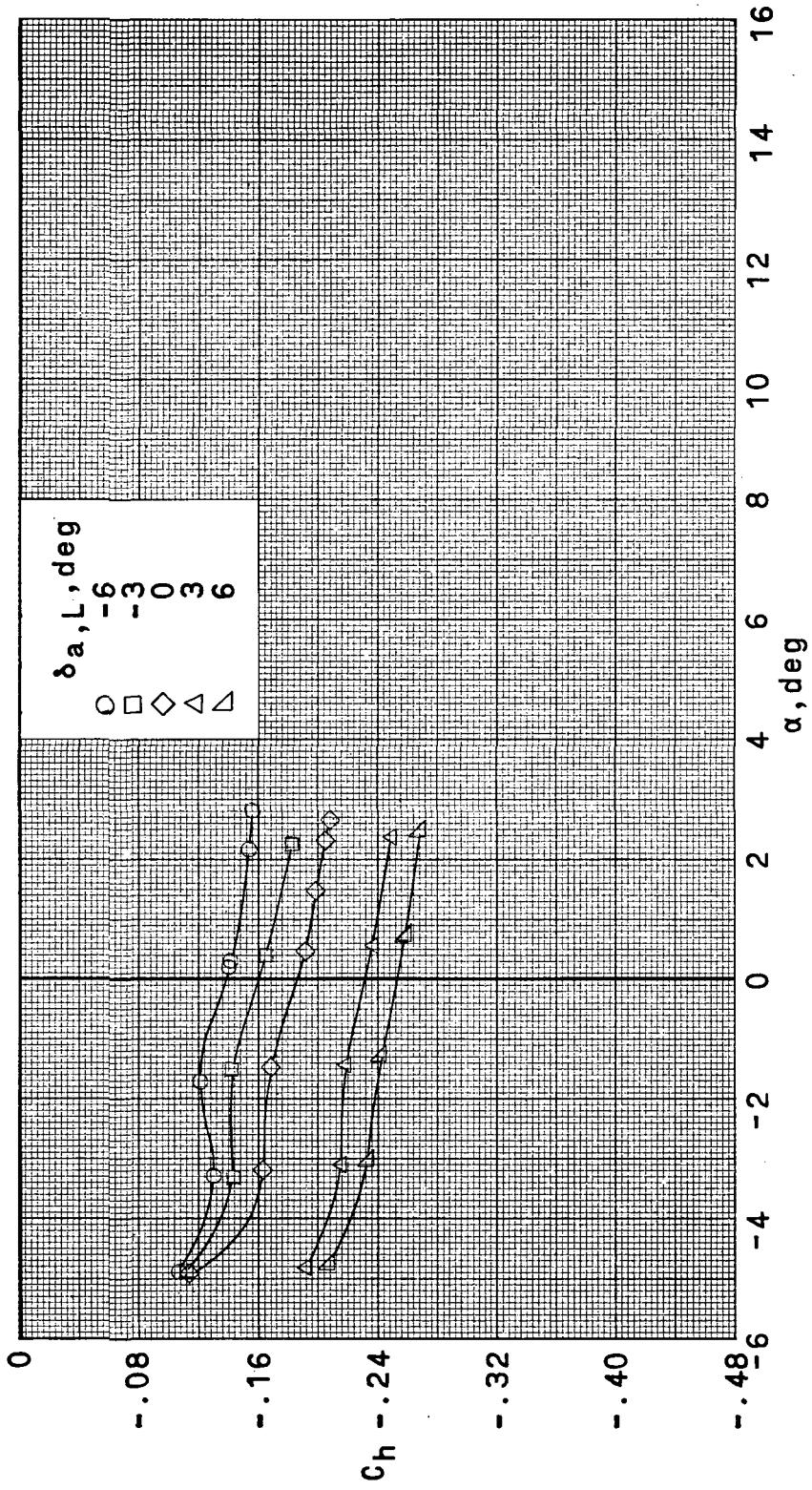
Figure 26.- Continued.



(c) $M = 0.70; R\bar{C} = 3.86 \times 10^6$.

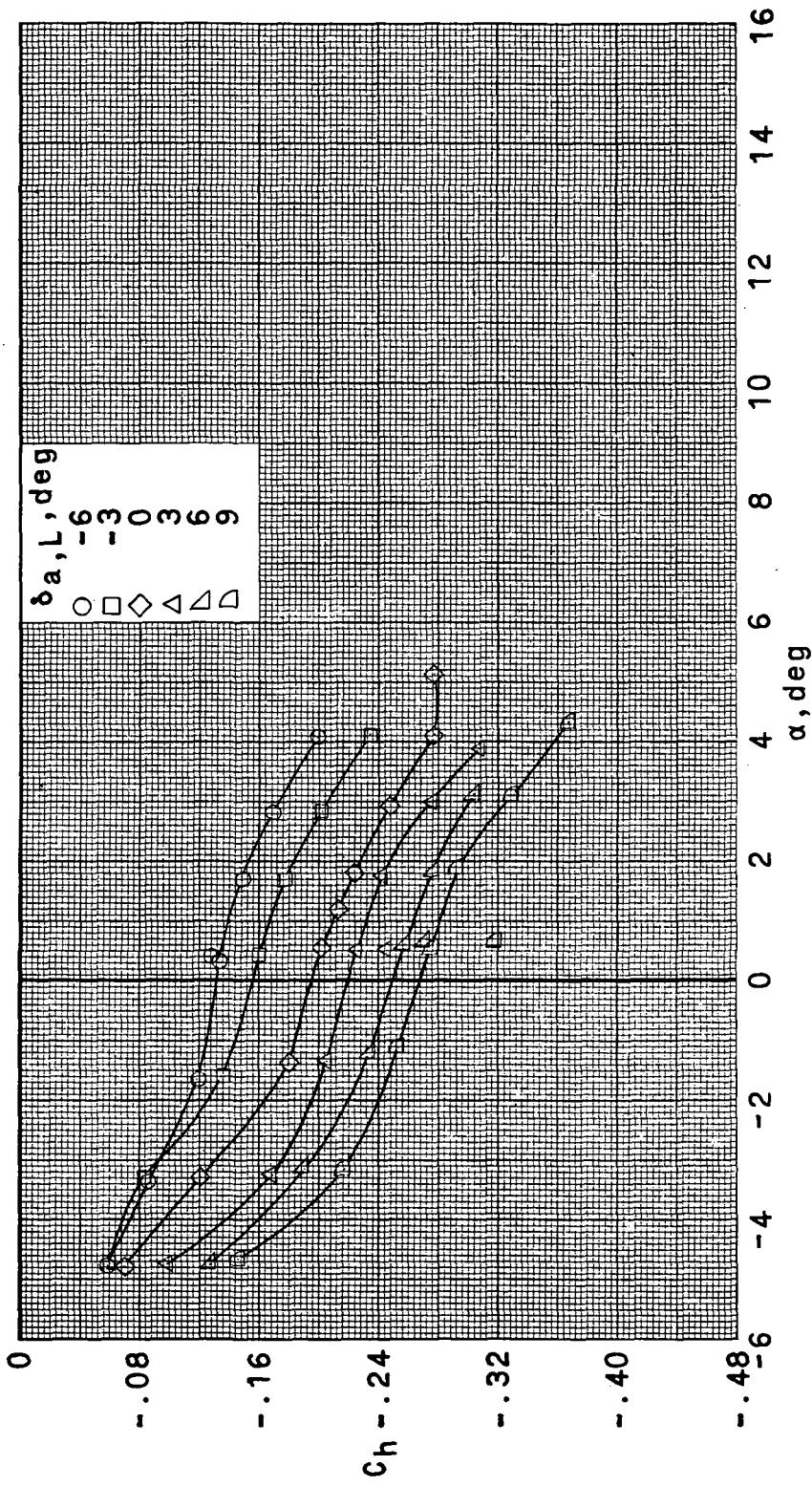
Figure 26.- Continued.

~~CONFIDENTIAL~~



(d) $M = 0.73; R_{\bar{C}} = 3.86 \times 10^6$.

Figure 26. - Continued.



(e) $M = 0.76$; $R\bar{c} = 3.86 \times 10^6$.

Figure 26. - Concluded.

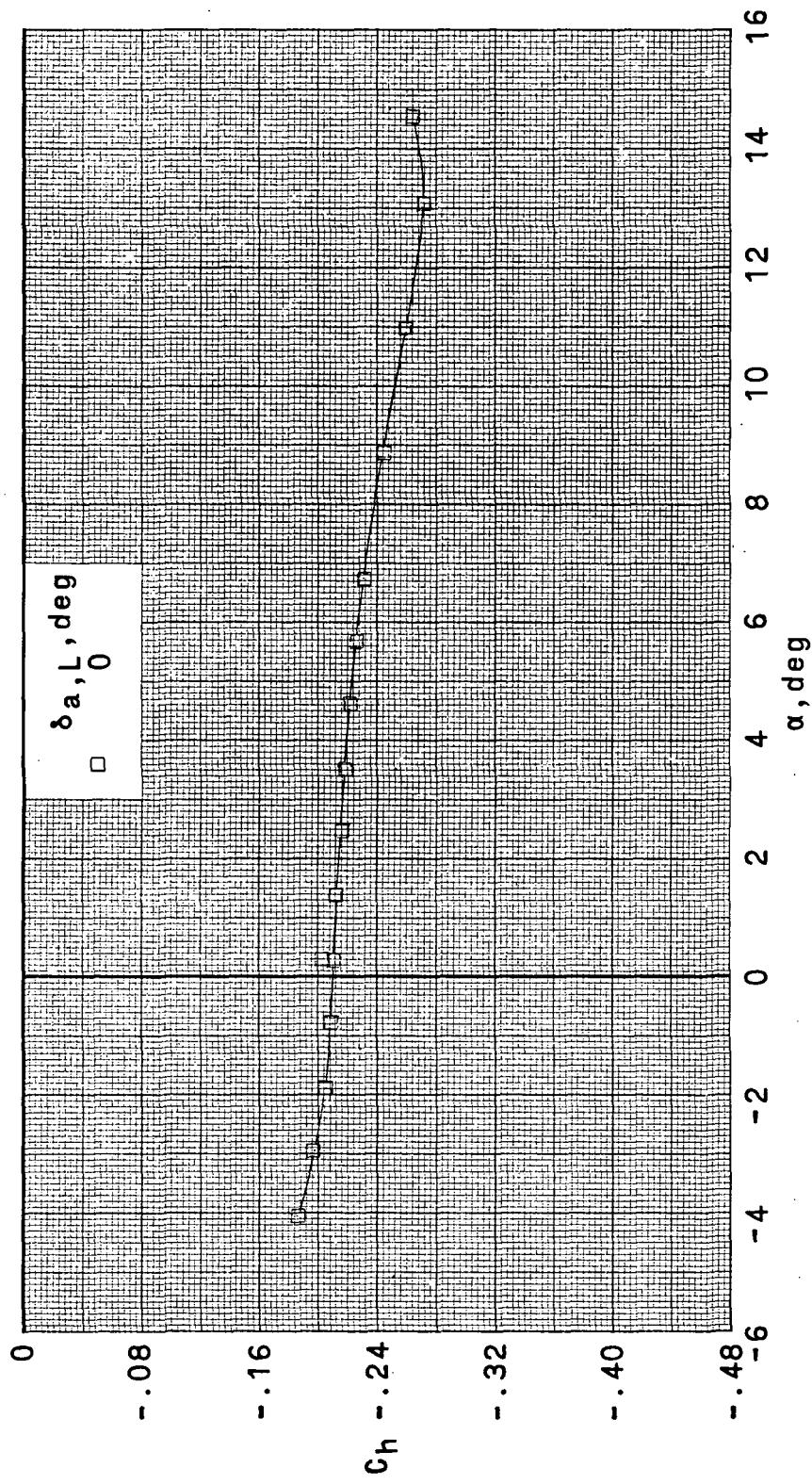
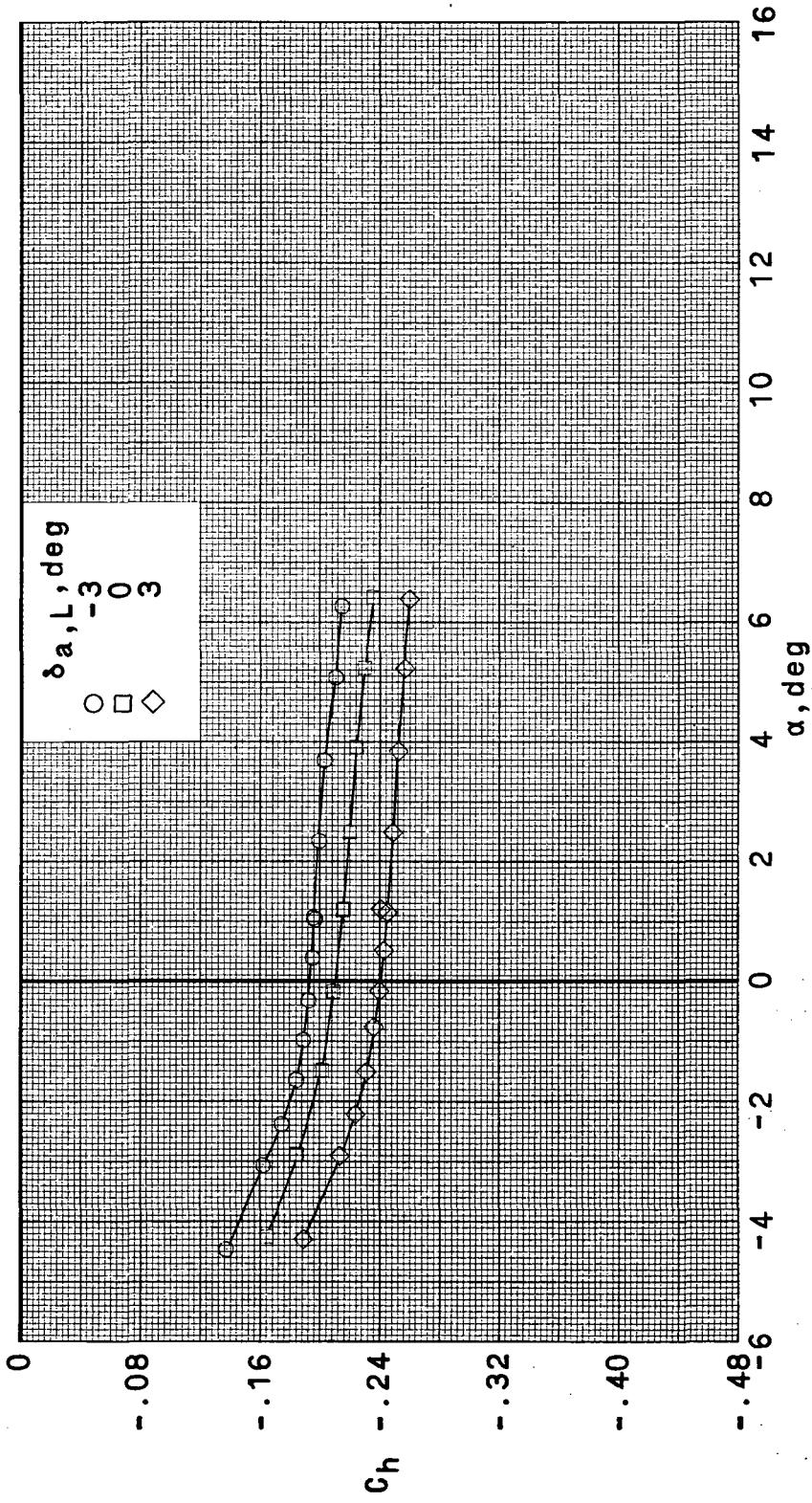


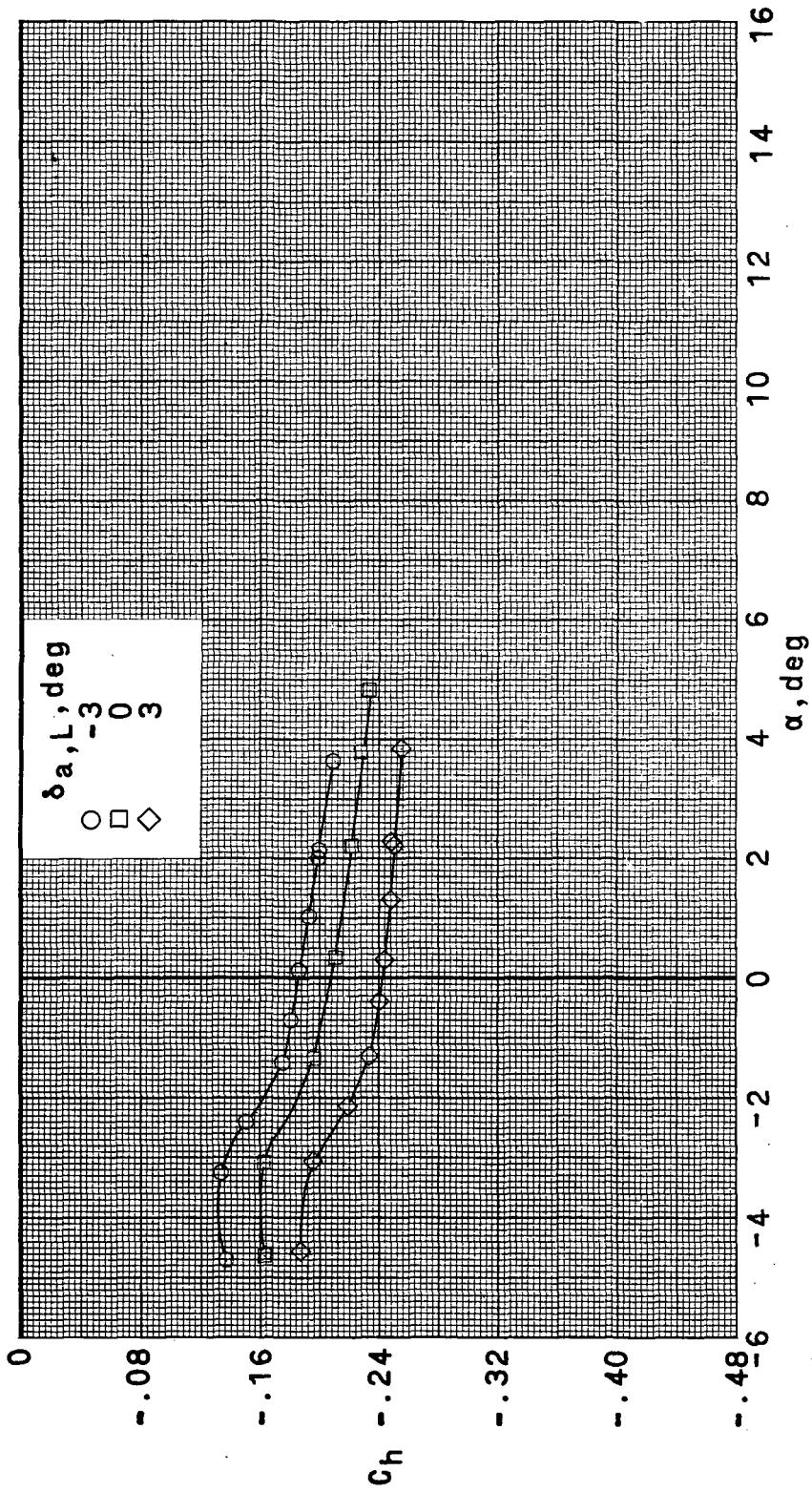
Figure 27.- Effect of angle of attack on aileron hinge-moment coefficients. $\delta_e = 0^\circ$; $i_h = 0^\circ$; $\beta = -5^\circ$.
 (a) $M = 0.30$; $R\bar{c} = 2.00 \times 10^6$.



(b) $M = 0.60; R_c = 3.33 \times 10^6$.

Figure 27. - Continued.

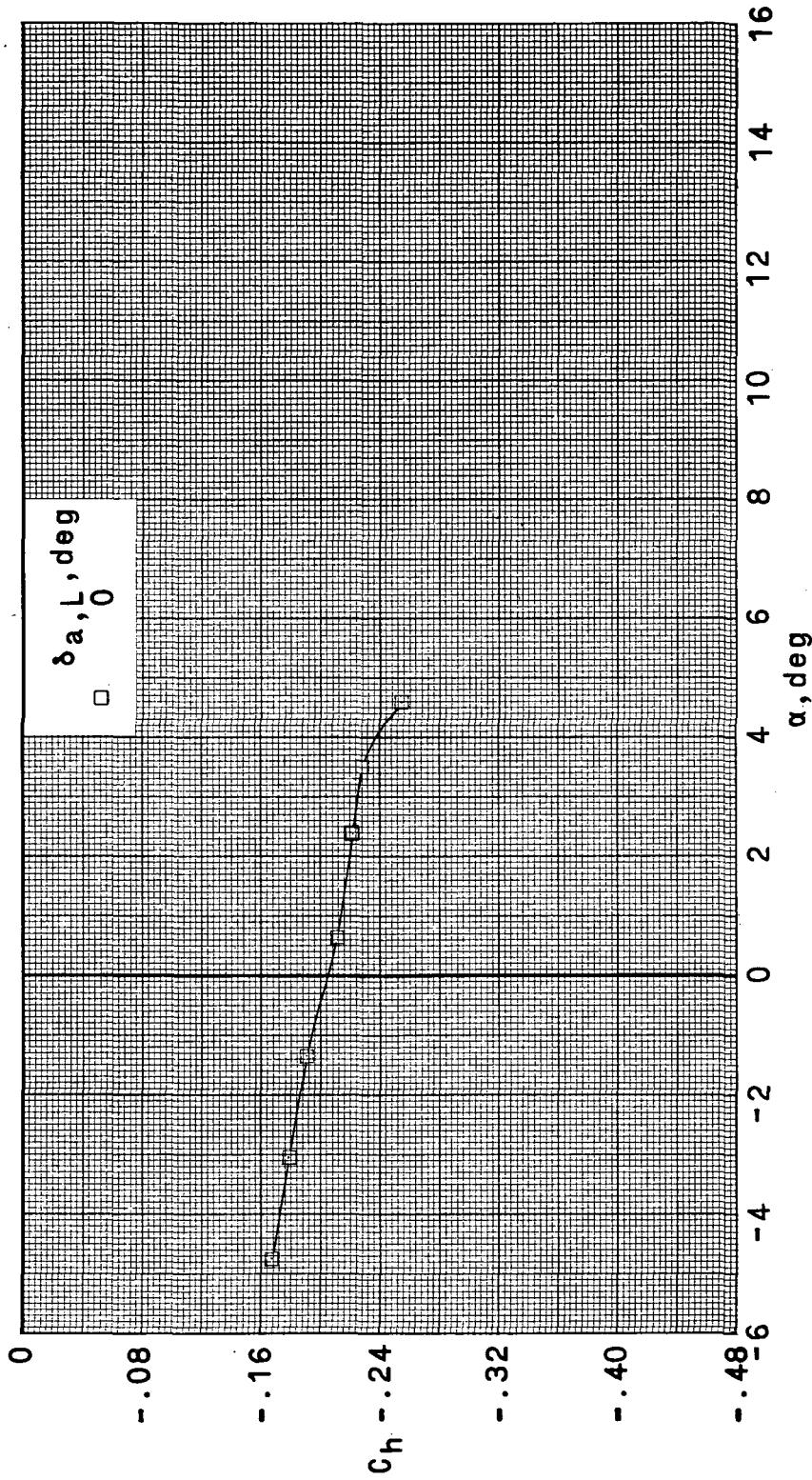
~~CONFIDENTIAL~~



(c) $M = 0.70$; $R\bar{c} = 3.86 \times 10^6$.

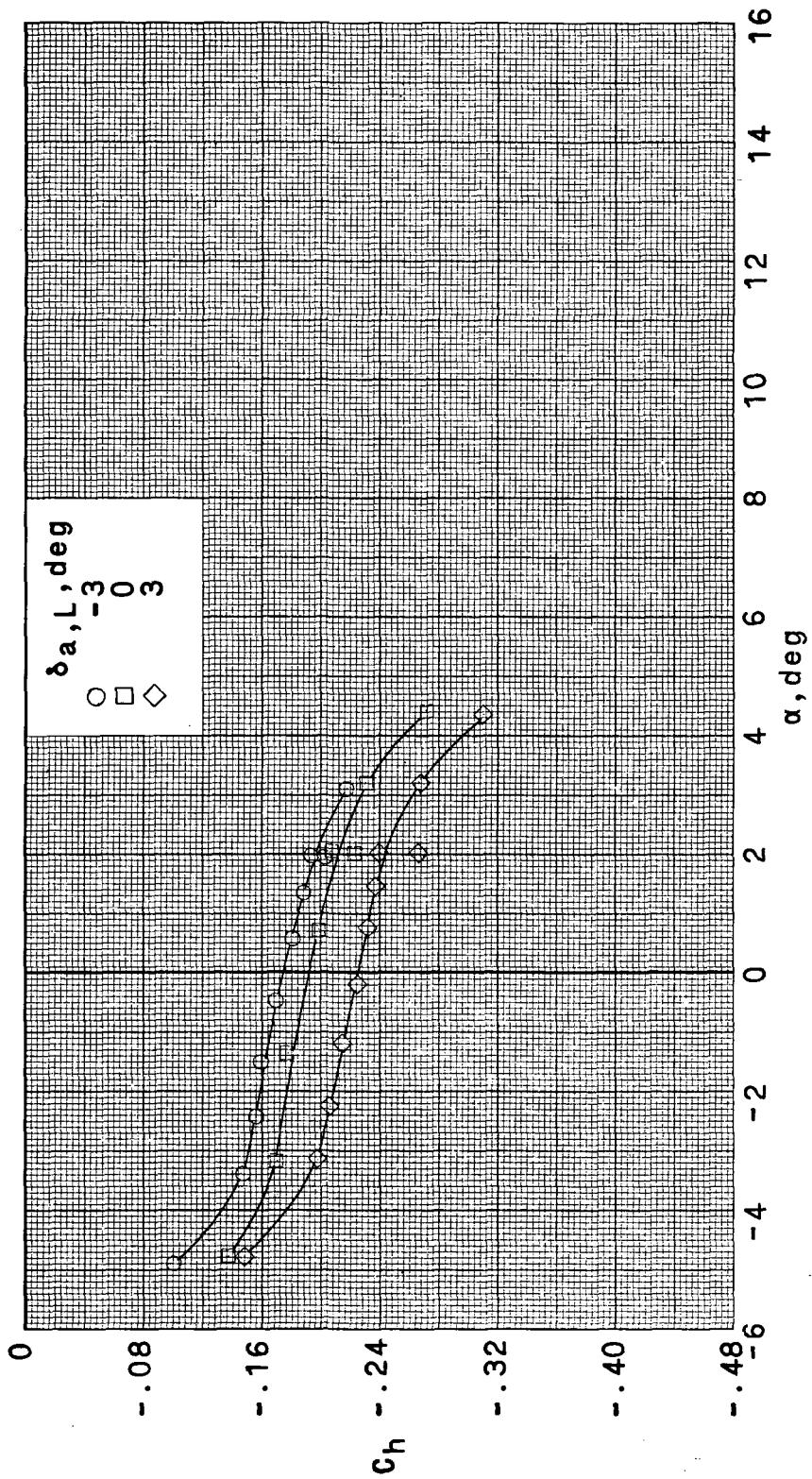
Figure 27.- Continued.

~~CONFIDENTIAL~~



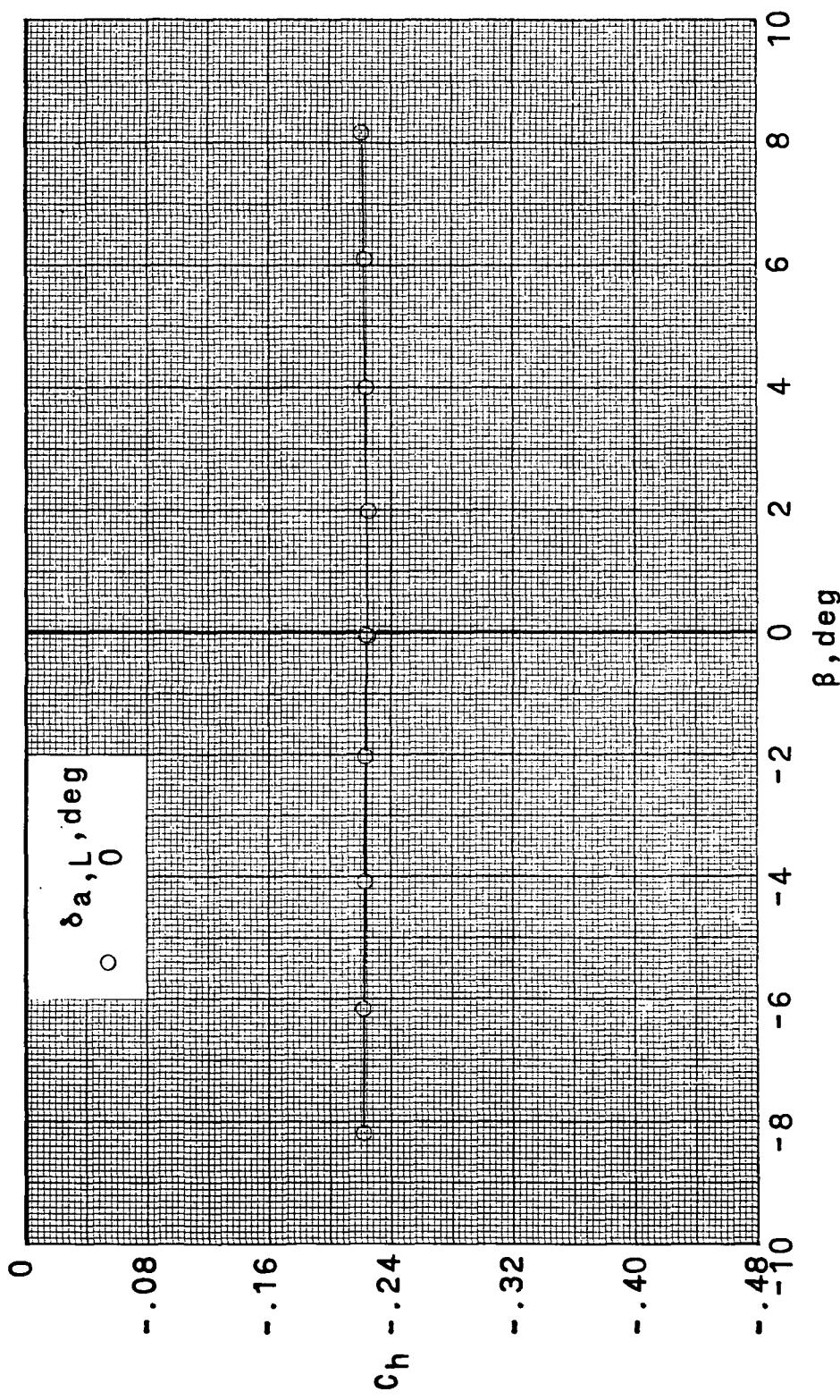
(d) $M = 0.73; R_C = 3.86 \times 10^6$.

Figure 27.- Continued.

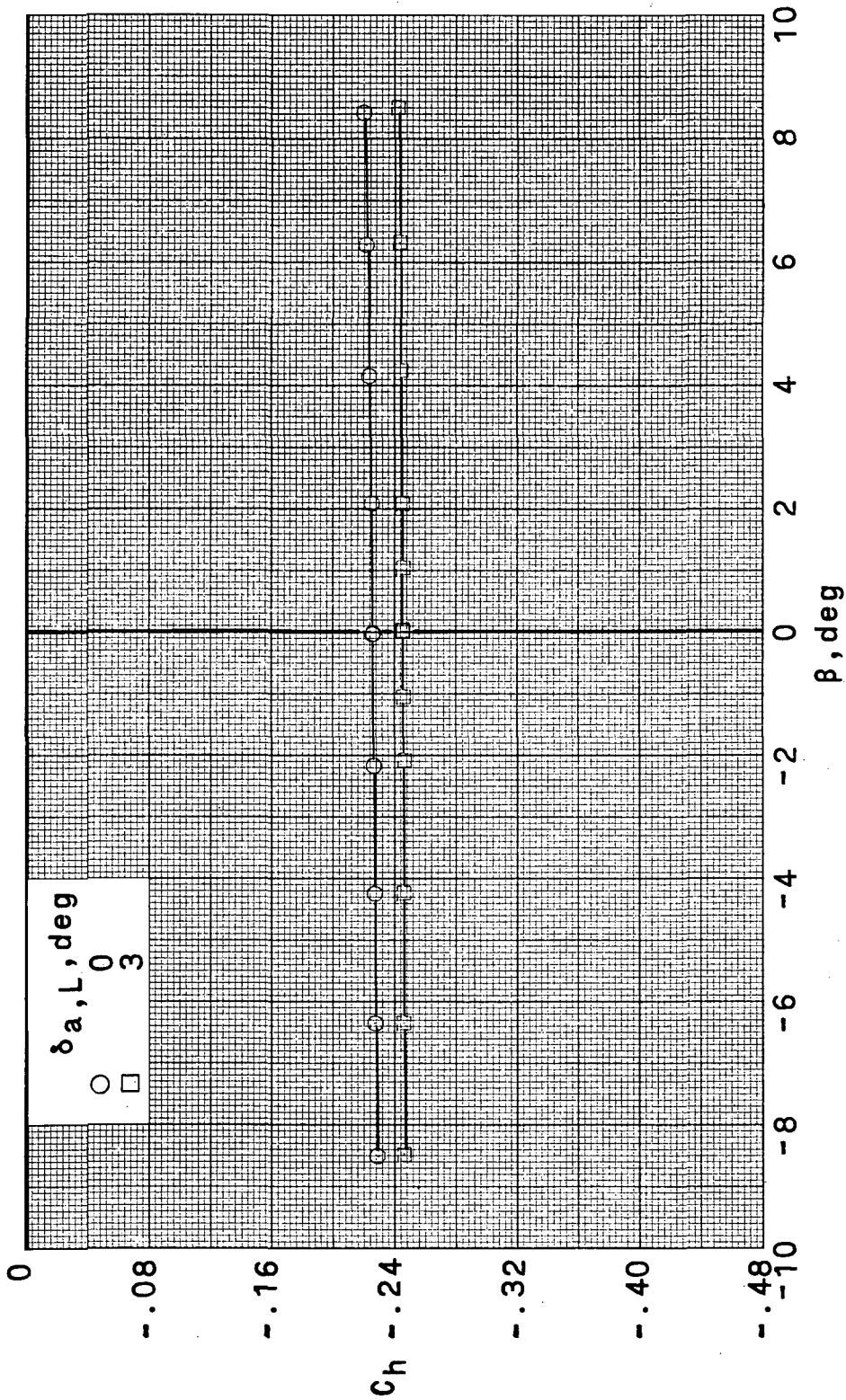


(e) $M = 0.75$; $R_E = 3.86 \times 10^6$.

Figure 27.- Concluded.

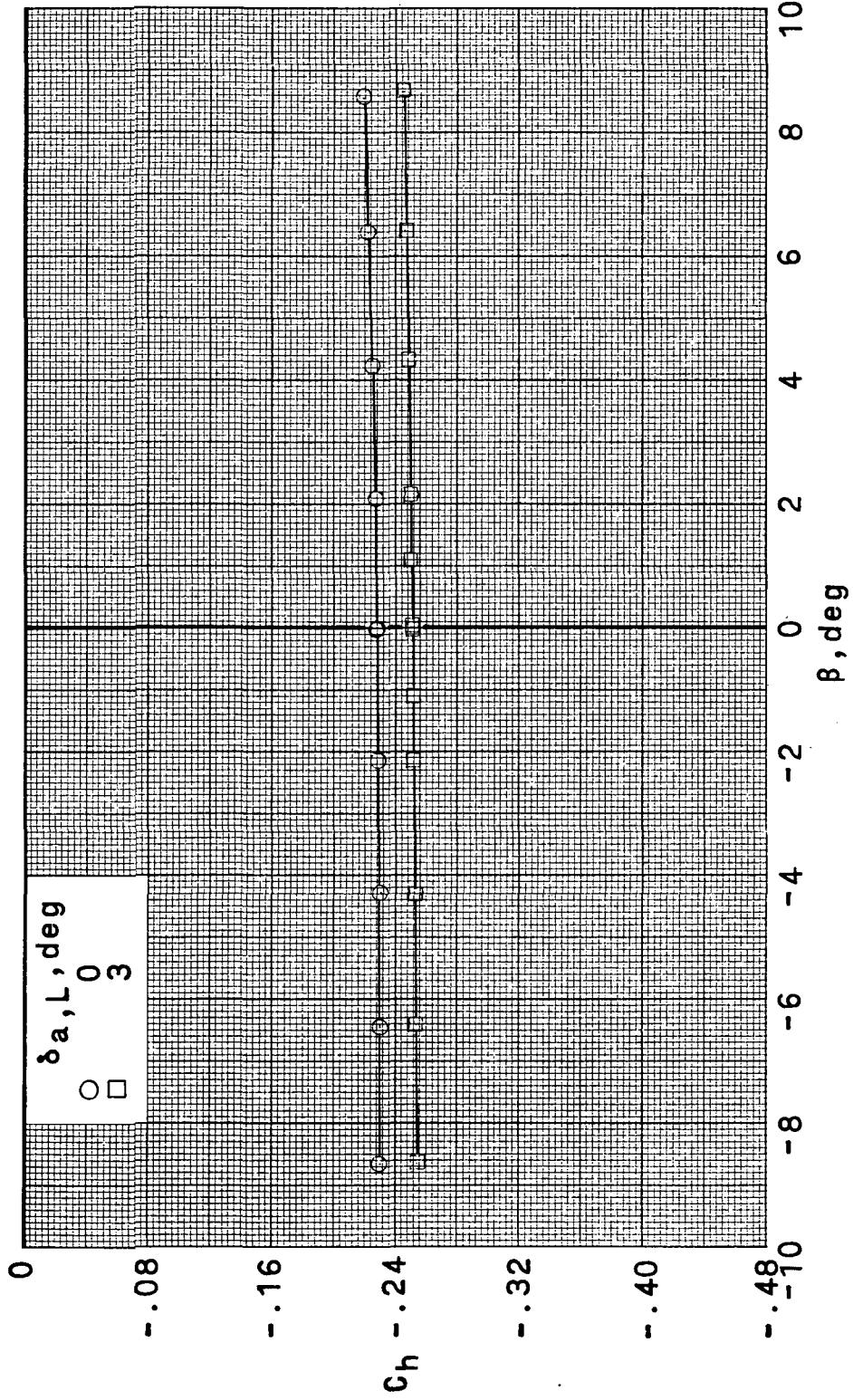


(a) $M = 0.30; \alpha = 0.30^\circ; R\bar{c} = 2.00 \times 10^6$.
 Figure 28.- Effect of angle of sideslip on aileron hinge-moment coefficients. $\delta_e = 0^\circ; i_h = 0^\circ$.



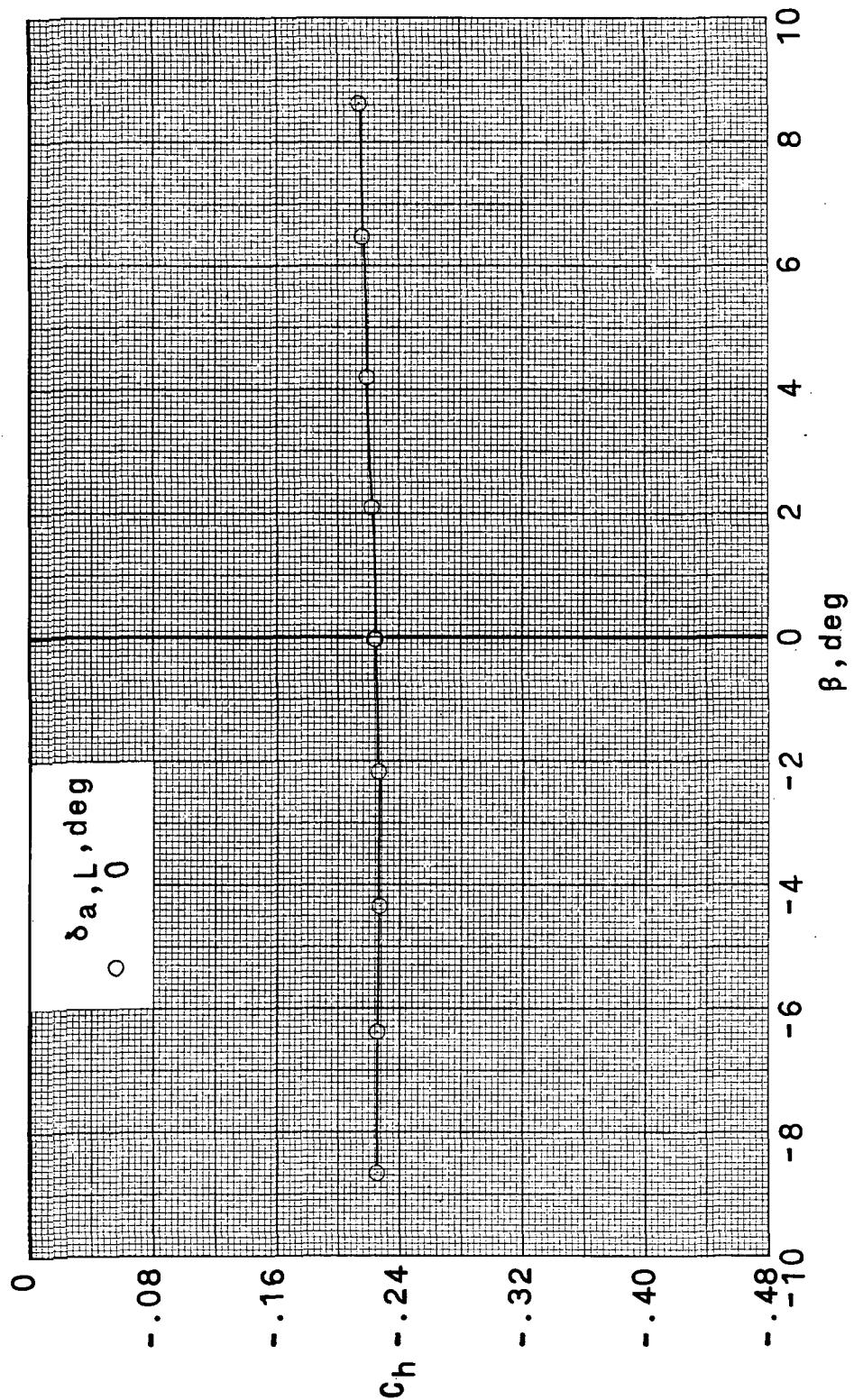
(b) $M = 0.60; \alpha = 1.30; R_C = 3.33 \times 10^6$.

Figure 28.- Continued.



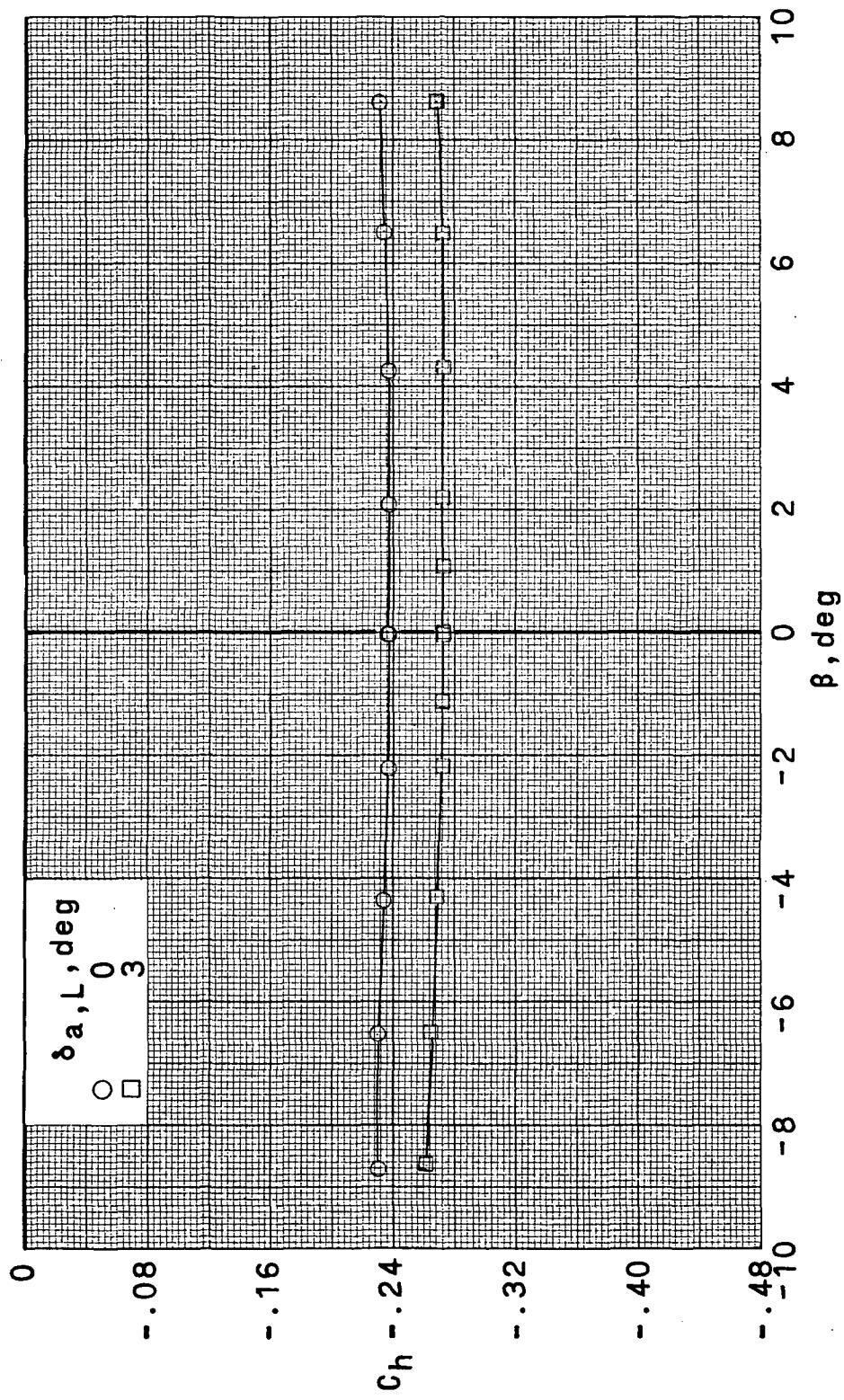
(c) $M = 0.70$; $\alpha = 2.40$; $R_c = 3.86 \times 10^6$.

Figure 28.- Continued.



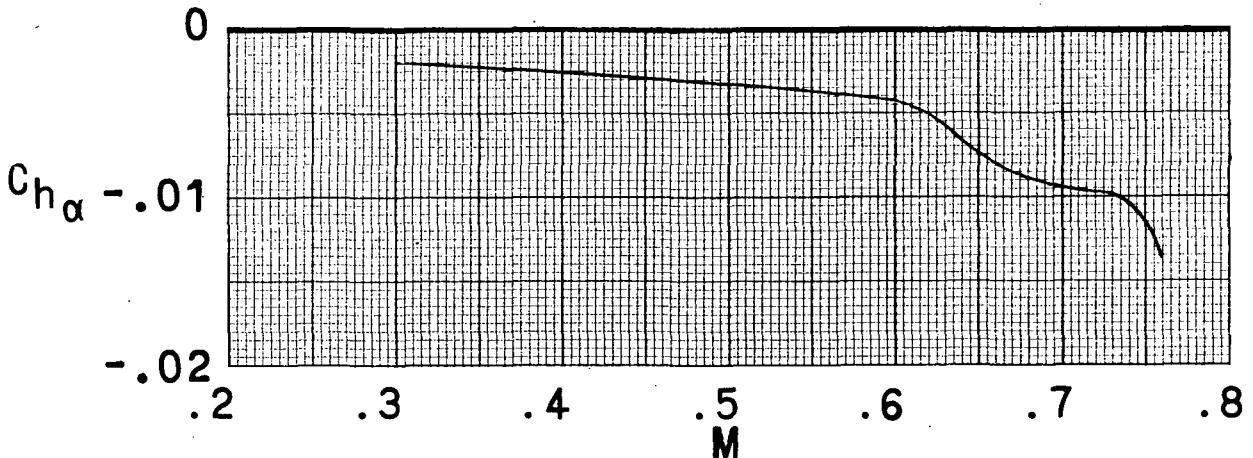
(d) $M = 0.73; \alpha = 2.4^0; R_C = 3.86 \times 10^6$.

Figure 28.- Continued.

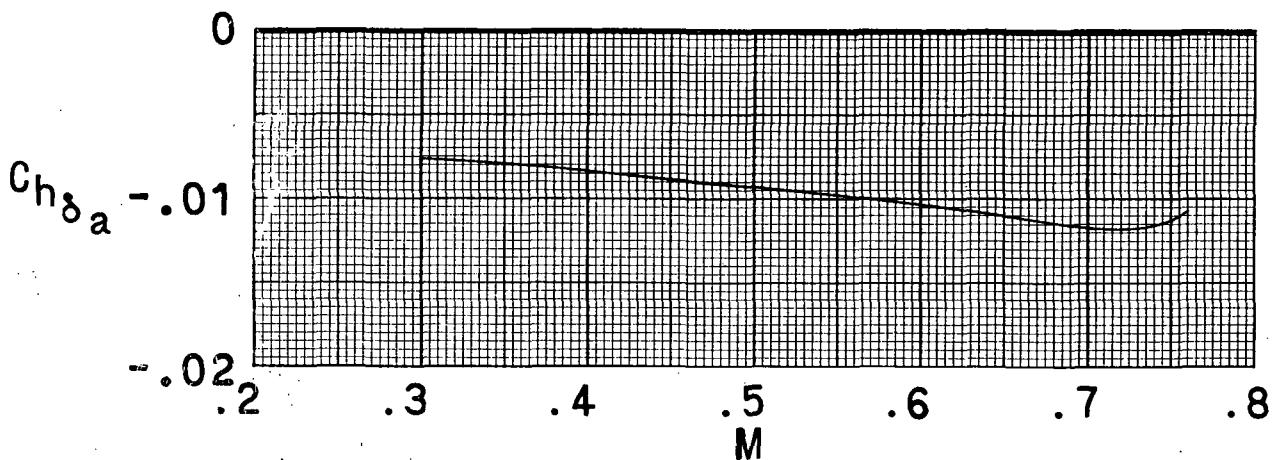


(e) $M = 0.76; \alpha = 2.0^\circ; R_c = 3.86 \times 10^6$.

Figure 28.- Concluded.



(a) $\alpha = 0^0$ to 1^0 ; $\delta_a = 0^0$.



(b) $\delta_a = -3^0$ to $+3^0$; $\alpha \approx \frac{1}{2}^0$.

Figure 29.- Variation of $C_{h\alpha}$ and $C_{h\delta_a}$ with Mach number. $\delta_e = 0^0$; $i_h = 0^0$; $\beta = 0^0$.

~~CONFIDENTIAL~~

~~CONFIDENTIAL~~

~~CONFIDENTIAL~~

"The aeronautical and space activities of the United States shall be conducted so as to contribute . . . to the expansion of human knowledge of phenomena in the atmosphere and space. The Administration shall provide for the widest practicable and appropriate dissemination of information concerning its activities and the results thereof."

— NATIONAL AERONAUTICS AND SPACE ACT OF 1958

NASA SCIENTIFIC AND TECHNICAL PUBLICATIONS

TECHNICAL REPORTS: Scientific and technical information considered important, complete, and a lasting contribution to existing knowledge.

TECHNICAL NOTES: Information less broad in scope but nevertheless of importance as a contribution to existing knowledge.

TECHNICAL MEMORANDUMS: Information receiving limited distribution because of preliminary data, security classification, or other reasons.

CONTRACTOR REPORTS: Scientific and technical information generated under a NASA contract or grant and considered an important contribution to existing knowledge.

TECHNICAL TRANSLATIONS: Information published in a foreign language considered to merit NASA distribution in English.

SPECIAL PUBLICATIONS: Information derived from or of value to NASA activities. Publications include conference proceedings, monographs, data compilations, handbooks, sourcebooks, and special bibliographies.

TECHNOLOGY UTILIZATION PUBLICATIONS: Information on technology used by NASA that may be of particular interest in commercial and other non-aerospace applications. Publications include Tech Briefs, Technology Utilization Reports and Notes, and Technology Surveys.

Details on the availability of these publications may be obtained from:

**SCIENTIFIC AND TECHNICAL INFORMATION OFFICE
NATIONAL AERONAUTICS AND SPACE ADMINISTRATION
Washington, D.C. 20546**

~~CONFIDENTIAL~~